Hybrid Fuel Cell Vehicle Powertrain Development Considering Power Source Degradation

by

Matthew Burgess Stevens

A thesis
presented to the University of Waterloo
in fulfillment of the
thesis requirement for the degree of
Doctor of Philosophy
in
Chemical Engineering

Waterloo, Ontario, Canada, 2008

AUTHOR'S DECLARATION

I hereby declare that I am the sole author of this thesis. This is a true copy of the thesis, including any required final revisions, as accepted by my examiners.

I understand that my thesis may be made electronically available to the public.

Abstract

Vehicle design and control is an attractive area of research in that it embodies a convergence of societal need, technical limitation, and emerging capability. Environmental, political, and monetary concerns are driving the automotive industry towards sustainable transportation, manifested as increasing powertrain electrification in a gradual transition to fossil-free energy vectors. From an electrochemical degradation and control systems perspective, this transition introduces significant technical uncertainty. Initial indications are that the initial battery designs will have twice the required capacity due to degradation concerns. As the battery is a major contributor to the cost of these vehicles the over-sizing represents a significant threat to the ability of OEMs to produce cost-competitive vehicles. This potential barrier is further amplified when the combustion engine is removed and battery-electric or fuel-cell hybrid vehicles are considered.

This thesis researches the application of model-based design for optimal design of fuel cell hybrid powertrains considering power source degradation. The intent is to develop and evaluate tools that can determine the optimal sizing and control of the powertrain; reducing the amount of over-sizing by numerically optimization rather than a sub-optimal heuristic design.

A baseline hybrid fuel cell vehicle model is developed and validated to a hybrid fuel cell SUV designed and built at the University of Waterloo. Lithium-ion battery degradation models are developed and validated to data captured off a hybrid powertrain test stand built as part of this research. A fuel cell degradation model is developed and integrated into the vehicle model.

Lifetime performance is modeled for four hybrid control strategies, demonstrating a significant impact of the hybrid control strategy on powertrain degradation. A plug-in variation of the architecture is developed. The capacity degradation of the battery is found to be more significant than the power degradation. Blended and All-electric charge-depleting hybrid control strategies are integrated and lifetime performance is simulated. The blended charge-depleting control strategy demonstrated significantly less degradation than the all-electric strategy. An oversized battery is integrated into the vehicle model and the benefit of oversizing on reducing the battery degradation rate is demonstrated.

Acknowledgements

I have had an incredible graduate experience, due heavily to the dedicated and passionate people I have been fortunate enough to collaborate with over the past four years. Dr. Michael Fowler's direction has guided me through the knowledge process and supported my complimentary pursuits during this development process. This ability to direct my research in a direction that is both of interest and one that I believe has impact was fundamentally enabled by Dr. Fowler as well as NSERC's support.

The University of Waterloo Alternative Fuels Team has been a major part of my university experience and is subsequently embedded in this thesis. Dr. Roydon Fraser's support and guidance over the years has been a key driver for the team's success. There has been a vast number of team members that I have learnt from over the years, the short version of the list includes Chris Mendes, Mike Wahlstrom, Jen Bauman, Chris Lawrence, Erik Wilhelm, Chris Haliburton, Kuo-Feng Tong, Dave Shilling, Taylor Mali, Alain Boutros, Dan Sellan, Charles Hua, and James Goh. The lengthy list of competition sponsors, led by General Motors, US Department of Energy, Argonne National Labs and Natural Resources Canada, were the reason that we had the resources to work on such a project. Tom Ender's mentoring, support, and willingness to "go up to bat" for us was an excellent lesson in what a great manager is. Dick Kauling's guidance was very helpful in ensuring our design philosophy met our design objectives. And I would be remisced if I didn't highlight the passion of Kristen De La Rosa to the competition, the students, and the spirit of the competition. I will forever cherish the 4am's the week before competitions, being surrounded by a team of people solely motivated by a passion for the project. In addition, the opportunity to collaborate with the team at Argonne National Laboratory and to test the vehicle on their dynamometer was instrumental to this research. Thanks to Henning Lohse-Busch, Steve Gurski, and Richard Carlson for their time and expertise.

I would also like to thank Dr. Ali Elkamel, Dr. Hector Budman, Dr. Zhongwei Chen, and Dr. Doug Nelson for your input and review of my research. The mentorship and opportunity provided by John Bell has been instrumental in developing an understanding and appreciation for the entrepreneurship process, and for that I am eternally grateful.

I am grateful to my labmates, Jeff Gostick and Sumit Kundu for their time, expert advice, and for reminding me I have to publish more. And Sumit thank you for letting me use your equipment. I am also grateful to the coop and 4th year students I was fortunate enough to supervise, your contributions to the design and build of the hybrid test stand were significant.

Lastly, and most importantly I would like to thank my family – my aunts and uncles, Dina, and my parents. Dina, thank you for being so incredibly supportive throughout the entire process, despite having countless nights and weekends sacrificed to UWAFT and the lab, and for being a personal cheerleader through the more strenuous times. Mom, your unconditional love and support has allowed me to tackle the most challenging of pursuits. And to my dad, for never tiring of the "quiz-master" and in that fostering what would become an eternal passion for knowledge.

to mom and dad

Table of Contents

Appendices

List of Figures

List of Tables

Chapter 1

Introduction

Environmental, political, and monetary drivers have aligned on the need for sustainable transportation, requiring a long-term transition to fossil-free energy vectors [1,2]. This transition will be evolutionary with many experts predicting a continual increase in the electrification of the powertrain in passenger vehicles [3-5]. In technology terms, this evolutionary path includes gradual and deliberate steps from conventional powertrains, to hybrid powertrains, to plug-in hybrid powertrains, to a final state incorporating a combination of plug-in fuel cell and battery-electric propulsion [6].

Powertrain electrification has been initiated through the introduction of the currently available charge-sustaining hybrids. The vehicles draw all their energy from a power source onboard the vehicle that is refueled by a liquid or gaseous fuel. These vehicles have permitted the initial investigation of the electrochemical, electromechanical, and control systems required for hybrid powertrains [7,8]. Technical uncertainty about battery degradation has required that in the design of current hybrid systems that fuel consumption be sacrificed to ensure powertrain reliability and durability [9]. A consequence has been battery pack over-sizing and minimization of control algorithm sophistication. Correspondingly, the initial generations of charge-sustaining hybrids have yet to realize the full hybrid benefit; however, technological and operational uncertainty is being reduced and subsequent designs are extending the hybrid utilization.

The next transition in the electrification continuum is the introduction of charge-depleting hybrids, commonly referred to as plug-in hybrids. These vehicles plug-in to an electrical distribution grid and draw energy to recharge a battery pack. From an electrochemical degradation and control systems perspective, this transition introduces significantly more technical uncertainty than the charge-sustaining hybrids [10-12]. The main sources of uncertainty include the effect of deep cycling large battery packs and variation of real-world

duty cycles. Initial indications are that the battery designs will have twice the required capacity due to degradation concerns and uncertainty [13]. As the battery is a major contributor to the cost and weight of these vehicles the over-sizing represents a significant threat to the ability of Original Equipment Manufacturer (OEM) to produce cost-competitive vehicles. This potential barrier is further amplified when the combustion engine is removed and battery-electric or fuel-cell hybrid vehicles are considered.

The over-sizing design approach is shown schematically in Figure 1. A minimum End-Of-Life (EOL) performance requirement is defined for a given operating time. Anticipated degradation rates are then considered and used to back-calculate the required Beginning-Of-Life (BOL) performance required to ensure the EOL requirement is achieved. In cases where there is additional concern regarding the degradation window's accuracy, an additional margin for design robustness is added to the BOL performance requirement. The BOL performance determines the volume, mass, and cost of the component being considered and frequently results in actual EOL performance significantly exceeding the actual EOL specification.

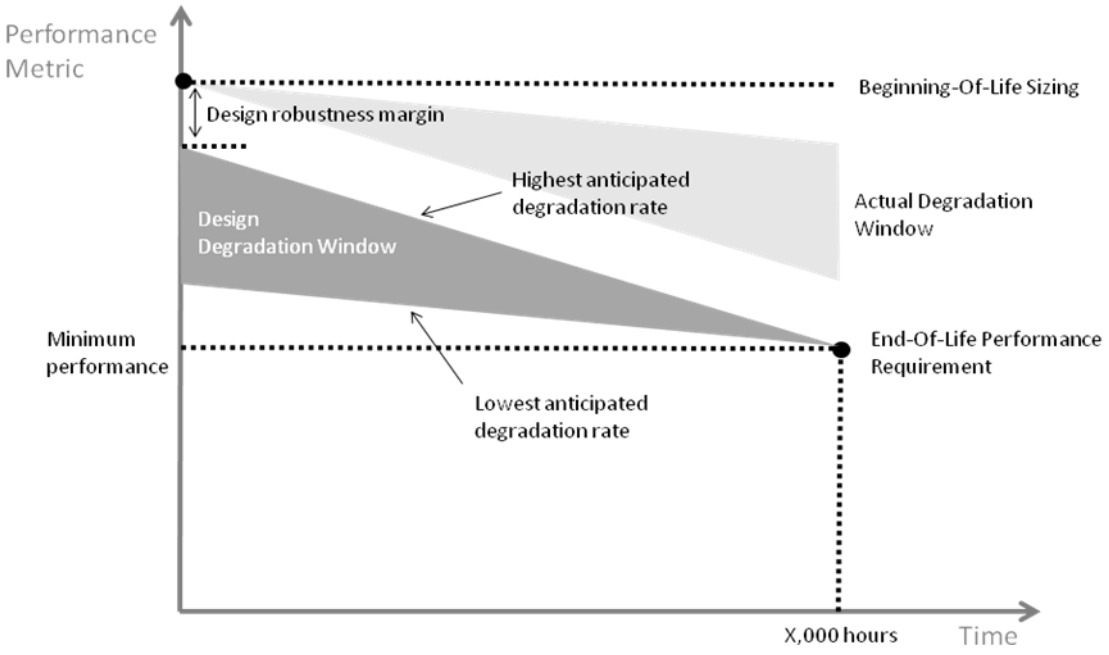

Figure 1 –Schematic of backwards-facing component sizing process

For hybrid powertrains this process is complex as there is significant interaction between the BOL sizing and both the degradation window and the vehicle dynamics. A larger battery capacity in a hybrid fuel cell vehicle implies smaller State-Of-Charge (SOC) swings thereby

reducing the expected degradation rate; however, this benefit is counteracted by the fact that a larger battery increases the vehicle mass, the subsequent energy requirements, and potentially increases the SOC swings. In addition, there is significant uncertainty about the duty cycles that components will be exposed to in charge-depleting operation. As a result, the common practice is to err on the side of battery over-sizing, as shown in Figure 2. This over-sizing results in significantly higher production costs.

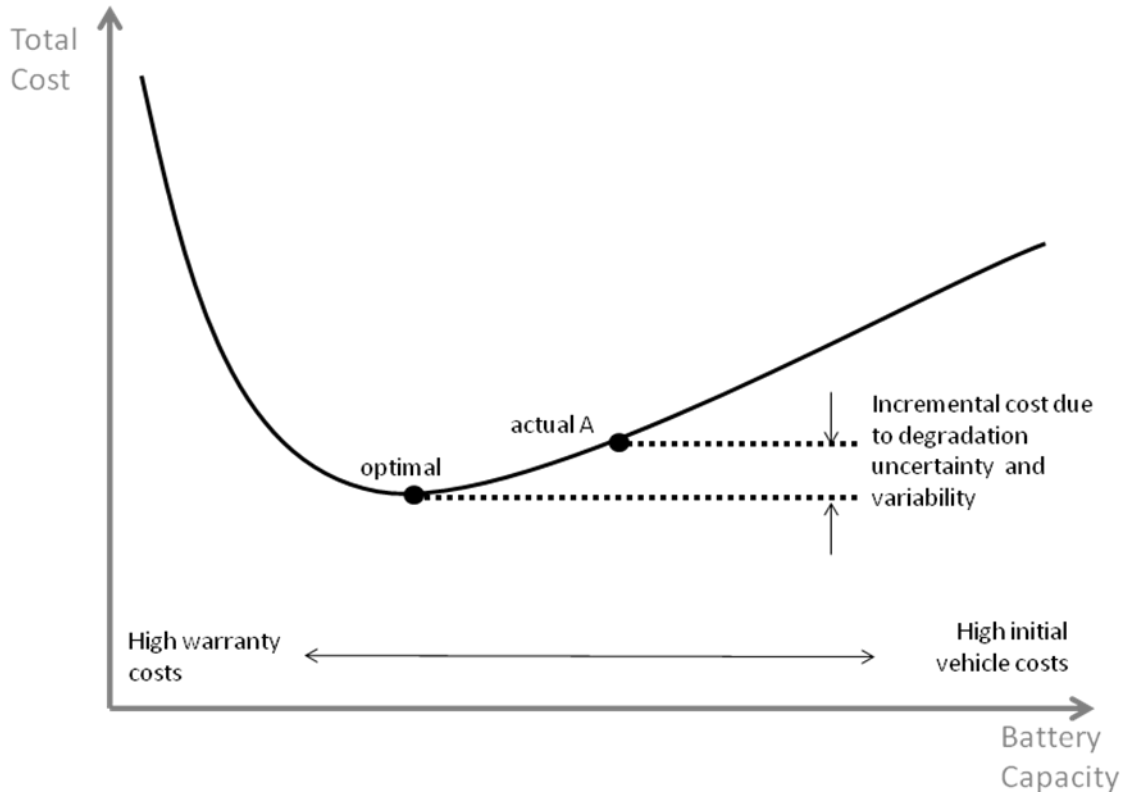

Figure 2 –Schematic representation of the cost due to degradation uncertainty and variability for the battery capacity case.

Fuel cell system price estimates range widely and are continually improving. As an example, Jeong published fuel cell system pricing to be $1200/kW in 2002, while Ahluwalia published in 2008 that including reasonable volume estimates that the cost had reduced to $108/kW [3,14]. For lithium ion batteries designed for charge-depleting the estimates range from $270-420/kWh according to Kromer and 427-455$/kWh according to Williams [2,5]. Using the lowest cost estimates a hybrid fuel cell vehicle that has a fuel cell that is oversized by 20kW with 8kWh excess battery capacity would increase the car manufacturers cost by over $4,300 per vehicle. Using cost estimates at the high end of the published ranges the incremental cost to the car

manufacturer exceeds $10,000. Clearly oversizing of components will be a significant barrier to producing cost-competition vehicle. In addition, the oversizing results in a significant increase in vehicle mass and powertrain volume, which introduces packaging complications.

In order to reduce the BOL battery and fuel cell sizing, two improvements must be achieved. First, the component degradation rate must be minimized. Second, confidence must be increased about the accuracy of the degradation rate to reduce the amount of oversizing required. Both improvements require a comprehensive understanding of the factors that cause and accelerate component degradation. Degradation mechanisms, and subsequently the operation factors that accelerate degradation in lithium ion battery and hydrogen fuel cells are becoming increasingly understood. Subsequently this knowledge permits the development of causal battery and fuel cell degradation models that simulate component degradation given sizing and control decisions; both of which combine with demand cycles to determine the operating conditions of the components. Therefore it is important to integrate component degradation information in to vehicle modeling so that component sizing and control parameters can be optimized.

Fortunately, the technical uncertainty resulting in oversizing has coincided with the maturation of new design tools and methodologies. Model-based design has recently expanded from the aerospace and nuclear energy sectors into the automotive design space. Model-based design has been enabled by cost-effective simulation tools achieving sufficient fidelity [15]. The progression from vehicle modeling, software-in-the-loop, hardware-in-the-loop, component-in-the-loop (also referred to as bypass testing), to vehicle testing allows for accelerated development and evaluation of design and control decisions [16]. This thesis developed the use model-based design tools to incorporate powertrain component degradation into sizing and control decisions for hybrid fuel cell vehicles.

In this work, to incorporate component degradation into the model-based design methodology the following has been performed:

- a hybrid hydrogen fuel cell SUV vehicle was designed and built at the University of Waterloo. This is one of first successfully student built fuel cell passenger vehicles,
- A baseline vehicle model is developed and validated to dynamometer performance of the hybrid fuel cell SUV (one of the first fuel cell vehicles to be tested at Argonne

National Laboratory (ANL) one of the leading international hybrid vehicle research centers),

- a scaled hybrid fuel cell vehicle test stand was built to allow for accelerated testing for lithium ion batteries,
- a causal battery degradation model was developed for a lithium ion ($LiFePO_4$ cathode)chemistry is developed and validated to data from the scaled hybrid powertrain test stand,
- a causal fuel cell degradation model was developed,
- the causal component degradation models was integrated into the baseline vehicle model to create a hybrid fuel cell vehicle model that degrades based on design parameters and operating conditions,
- various control strategies were compared to evaluate lifetime performance,
- the impact of component sizing is introduced within the framework of lifetime performance, and
- a real-time hybrid control strategy was evaluated that includes an estimated degradation cost in addition to powertrain efficiency and battery management.

While the focus is on hybrid fuel cell and plug-in fuel cell architectures the intent is that the majority of the results will be simultaneously useful for the earlier stages in the electrification process, specifically charge-depleting internal combustion engine (ICE) hybrids.

1.1 Research Contributions

This research contains a number of novel contributions to the publically available body of knowledge. Specifically,

- A validated charge-sustaining hybrid fuel cell vehicle model. The most similar information available to date is based upon a Virginia Polytechnic Institute and State University paper that was submitted and presented at SAE World Congress. Unfortunately the vehicle fuel cell had a failure prior to dynamometer testing resulting in an inability to complete charge-sustaining operation during testing. While there have been numerous papers presenting the overall performance of hybrid fuel cell automobiles and buses, these papers either exclusively state the overall performance or

provide overall and component performance curves but lack component model parameters and degradation considerations.

- A causal degrading hybrid fuel cell vehicle model. PSAT uses a causal structure to accurately model BOL performance. No vehicle modeling software that incorporates component degradation was found.
- Optimization of a hybrid fuel cell powertrain considering component degradation. There are a small number of very recent papers that discuss optimal powertrain sizing and control of hybrid fuel cell vehicles; however, none consider component degradation.
- The majority of published real-time hybrid control strategies are based upon efficiency estimations and battery management. Although a couple references include anecdotal references to ensuring small battery State Of Charge (SOC) variations for durability reasons, no papers explicitly include degradation in the real-time control strategy.

1.2 Thesis Structure

This thesis is divided into four main sections. Chapter 2 introduces the current state of literature on hybrid fuel cell architectures, control, simulation and performance as well as component degradation. Chapter 3 covers the baseline vehicle design and build as well as the baseline vehicle model development and validation. Chapter 4 investigates component degradation and develops a causal battery degradation model based upon experimental data.

Chapter 5 integrates the component degradation models into the validated baseline hybrid fuel cell vehicle model and evaluates the impact of component sizing and control strategy on the lifetime performance of the vehicle.

Chapter 2

Background and Literature Review

Researching power source degradation and design of hybrid fuel cell vehicle powertrains requires an understanding of the literature in four distinct areas. Those areas include:

- Vehicle dynamics and powertrain efficiency
- Hybrid powertrain design and control
- Batteries and fuel cells performance and degradation
- Model based design and optimization

The following sections will discuss each of these four areas in their entirety. A background in fundamental vehicle dynamics is presented first as it is required to understanding the vehicle-level impacts of design decisions and operating conditions – including tradeoffs between alternative hybrid powertrain architectures. Internal Combustion Engine (ICE) based hybrid architectures are presented and then compared to fuel cell based hybrid architectures. The comparison is performed because there are common operating modes and knowledge derived from the ICE based hybrid architecture provides insight into possible benefits in fuel cell based architectures. Considerations that are specific to fuel cell based architectures are then discussed, including the location and topology of power electronics. Following the architecture-level discussion, component-level knowledge is presented for both fuel cells and batteries. The current state of knowledge on performance, degradation behavior and mechanisms, factors accelerating degradation, and component models is discussed. Finally, the application of model based design for hybrid powertrain design is reviewed. A particular focus is placed on the use of

optimization techniques to determine sizing and control parameters from vehicle models. In conclusion, the thesis is defined within the scope of the existing literature.

2.1 Vehicle Dynamics, Powertrain Efficiency, and Fuel Displacement

The motivation for advanced vehicle propulsion is based upon the pursuit of sustainable transportation, which is primarily driven by the need to reduce fossil fuel use [1]. In the context of vehicle design, a reduction in fossil fuel use can be achieved through one of three, often inter-related, mechanisms. These three include reducing in the at-road energy required, increasing the powertrain efficiency to reduce the at-tank energy required given an at-road energy requirement, and utilizing an alternative fuel with reduced fossil fuel demand [7,8]. These three mechanisms are illustrated graphically in Figure 3 –Three options for improving vehicle powertrain sustainability.

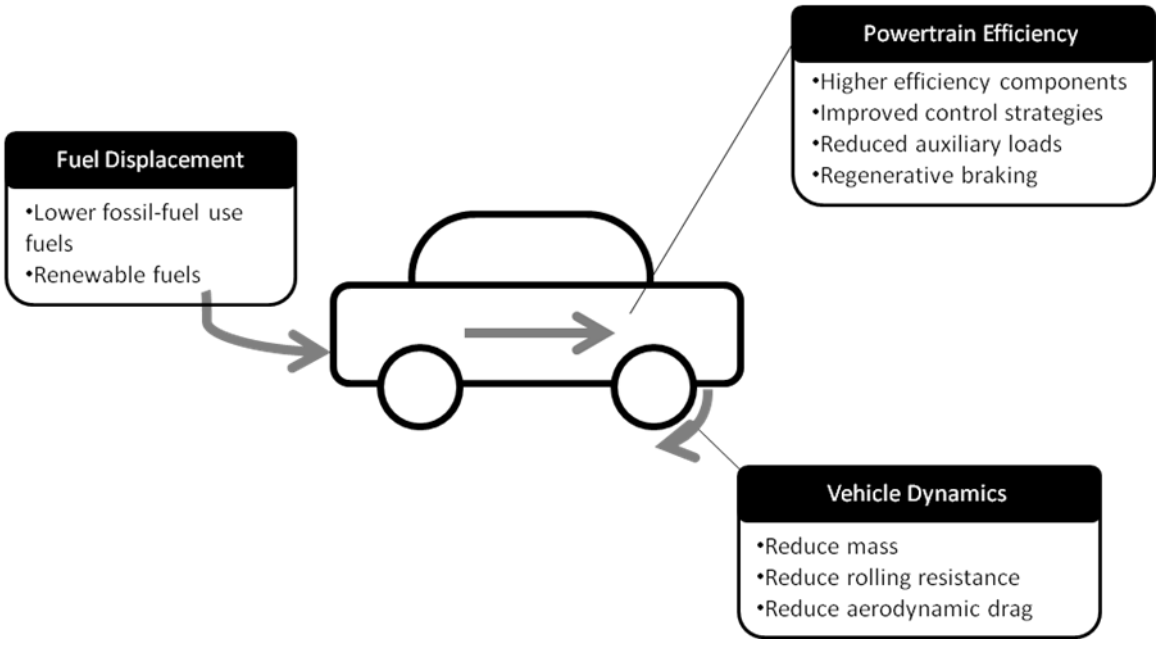

Figure 3 –Three options for improving vehicle powertrain sustainability

The output (at-road) energy requirement is a function of the drive cycle and vehicle dynamics [11,17]. The drive cycle impact is derived from the effects of distance, speed, stop/start content, and idling on energy demand. These factors are governed by driver behavior (i.e. aggressive acceleration and braking), road design, and traffic congestion. While these factors are significant, they are focused on road design and driver psychology and are therefore outside the scope of research on vehicle design. Standard speed versus time drive cycles utilized for

vehicle characterization will be employed and the effects of vehicle dynamics on at-road energy demand will be focused on exclusively.

Improving vehicle dynamics can be achieved by reducing the aerodynamic drag, rolling losses, or vehicle mass [8]. The generally accepted equations for calculating aerodynamic drag, rolling loss, and force required for grade and acceleration are as follows in equations 1 - 4:

$$F^{aero} = \frac{1}{2} C_D \rho_a A_f v^2 \quad (1)$$

$$F^{roll} = C_{rr} mg\, cos(\theta_v) \quad (2)$$

$$F^{grade} = mg\, sin(\theta_v) \quad (3)$$

$$F^{accel} = ma = m\frac{dv}{dt} \quad (4)$$

The aerodynamic drag, rolling resistance, and force to overcome gravity/grade are generally considered the three primary drag forces. The name is a slight misnomer for the grade force as the force is directed in the direction of travel when θ_v is negative during declines. The acceleration force is derived from Newton's second law and is equal to the balance of forces on the vehicle as described below:

$$F^{accel} = \Delta F^{veh} = F^{wh} - F^{grade} - F^{drag} = F^{wh} - F^{grade} - F^{aero} - F^{roll} \quad (5)$$

Equation 5 introduces the F^{wh} term which represents the force exerted by the powertrain and brakes at the wheel, translated to the longitudinal direction of travel. The instantaneous power requirement and total energy demand for a given time interval can be calculated from:

$$P^{wh} = F^{wh} v \quad (6)$$

$$E^{wh} = \int P^{wh} dt = \int \left(m\frac{dv}{dt} + \frac{1}{2} C_D \rho_a A_f v^2 + C_{rr} mg\, cos(\theta_v) + mg\, sin(\theta_v) \right) v dt \quad (7)$$

If during the time interval under consideration the vehicle's initial and final velocities and heights are equal, the simplifications can be made:

$$\int \frac{dv}{dt} dt = 0\ ;\ \int sin(\theta_v)\, dt = 0; \int cos(\theta_v)\, dt = 1;$$

Given that E^{wh} is a linear function of P^{wh}, the resulting simplified calculation for at-wheel energy demand is given by:

$$E^{wh} = \int P^{wh} dt = \int F^{wh} v dt = \int \left(\frac{1}{2} C_D \rho_a A_f v^2 + C_{rr} m g \right) v dt \quad (8)$$

Equation 8 clearly demonstrates that a reduction in vehicle mass or cross-sectional area will result in a reduction of at-road energy demand. Correspondingly an increase in either mass or cross-sectional area will increase the at-road energy demand. As conventional vehicles have reasonably consistent powertrain efficiencies, an example of the impact of reducing output requirements is the difference between the energy used by a Sport Utility Vehicle (SUV) versus a subcompact travelling the same route. The lower fuel consumption of the subcompact is primarily due to the lower vehicle mass and aerodynamic drag.

Reducing the output energy requirement of the powertrain is an effective method for reducing energy use as the energy reduction is compounded by powertrain efficiency to reduce overall energy use. In that context, it is the at-tank energy requirement that is of greater interest. The at-tank power and energy requirement can be calculated from:

$$P^{tank} = \frac{P^{wh}}{\epsilon^{pwt}} \quad (9)$$

$$E^{tank} = \int \frac{P^{wh}}{\epsilon^{pwt}} dt \quad (10)$$

Where ϵ^{pwt} represents the instantaneous powertrain efficiency, which is defined as the ratio of the mechanical power delivered at the drive wheels divided by the chemical power delivered from the power source. In conventional vehicles this input chemical power represents the chemical energy flux of gasoline injection. In an all-electric vehicle using a lithium ion battery this chemical power represents the lithium de-intercalation/intercalation flux.

The powertrain efficiency is heavily dependent on the output power requirement and the state of the powertrain. The relevant powertrain state variables are dependent on the powertrain type. In hybrid vehicle powertrains, the battery State-Of-Charge (SOC) is a key state variable. The resulting efficiency is therefore power and time variant and can be summarized by:

$$\epsilon^{pwt} = \boldsymbol{f}(P^{wh}, X^{pwt}, t) \quad (11)$$

Where X represents a state array that includes relevant state variables such as SOC and temperature. Since the powertrain efficiency is a function of output power, the E^{tank} is not a linear function of P^{wh}, therefore the simplified energy calculation from Equation 8 is not an acceptable simplification. Grade and acceleration effects must be included in the calculation of at-tank energy requirements. Qualitatively, this can be explained by comparing two drive cycles. Both drive cycles have equivalent speed-time curves and begin and end at the same point; however, one curve includes significant grade variations while the other is on a perfectly flat surface. While the overall at-wheel energy requirement for both cycles is equivalent, the distribution of at-road power differs significantly between the two cycles. As a result, the operating points and subsequent powertrain efficiency will differ, resulting in different at-tank energy requirements. Therefore, the at-tank energy must include the grade and acceleration terms, as given by:

$$E^{tank} = \int P^{wh} dt = \int \frac{\left(m\frac{dv}{dt} + \frac{1}{2}C_D\rho A v^2 + C_{rr} mg\cos(\theta_v) + mg\sin(\theta_v)\right)v}{\epsilon^{pwt}} dt \quad (12)$$

The powertrain efficiency can be improved through improving component efficiency, component sizing to improve the operating location within the component efficiency behavior, or employing higher efficiency charge-sustaining hybrid architectures that enable regenerative braking. By definition, charge-sustaining hybrids continue to derive all the energy from the liquid fuel (i.e. gasoline), temporarily storing energy in the battery to improve the operating of the powertrain components and to recapture energy during braking events [18].

Using an alternative fuel displaces fossil fuel use by removing or reducing fossil fuel from the vehicle's energy vector. Additional analysis is required when electricity is displacing gasoline as most generation compositions of electricity grids include fossil fuel components [1,2,19].

Vehicle dynamics, powertrain efficiency, and alternative fuel utilization are not independent. For instance, while hybrid powertrains generally improve powertrain efficiency the additional components generally increase the vehicle mass thereby increasing the at-road energy requirements. As a result, comprehensive analysis of any design decision must include the evaluation of interactions between these three mechanisms. This thesis is focused on optimizing powertrain efficiency given a hydrogen-based powertrain integrated into Sport Utility

Vehicle (SUV). Understanding the interplay between vehicle dynamics and powertrain efficiency is important to understand the application hybrid powertrain design and control as introduced in the next section. In addition, comprehending the complexity of equation 12, specifically the ability to calculate powertrain efficiency is important in appreciating the value of model-based design, as will be discussed later.

2.2 Hybrid Vehicle Design and Control

Hybrid vehicles introduce a number of additional degrees of freedom to the designer. For a given set of vehicle performance requirements; the hybrid architectures, components types, component sizing, and control algorithms are all design variables [7,8]. The architecture selection and component sizing is heavily driven by the energy storage selection. The hybrid architecture establishes the modes of operation and the physical connections. The component type and sizing impacts the system's dynamic performance, coupling mechanisms, and establish the fundamental behavior of component degradation. During vehicle operation the control strategy determines the i) mode of operation, within those permitted by the vehicle architecture, and ii) the power division, within the operating limits of the component type and sizes. ICE based hybrid architectures are presented and compared to a fuel cell hybrid architecture. Considerations for power electronic location and topology are then discussed for the hybrid fuel cell vehicle case. While there is interaction between architecture selection, control decisions, and the performance characteristics of the powertrain components, the architecture and control literature is presented initially and component-specific information on fuel cells and batteries is discussed in the section 2.3.

2.2.1 Hybrid Architectures

Hybrid powertrains are defined by the availability of two power sources within the drive train, which can include: internal combustion engines (ICE), fuel cells, or Energy Storage Systems (ESS). The two most common ESS types are batteries and ultracapacitors [20]. The main hybrid architectures employing internal combustion engines (ICE) are summarized in Figure 4. Series fuel cell hybrid is also presented in Figure 4 for comparison.

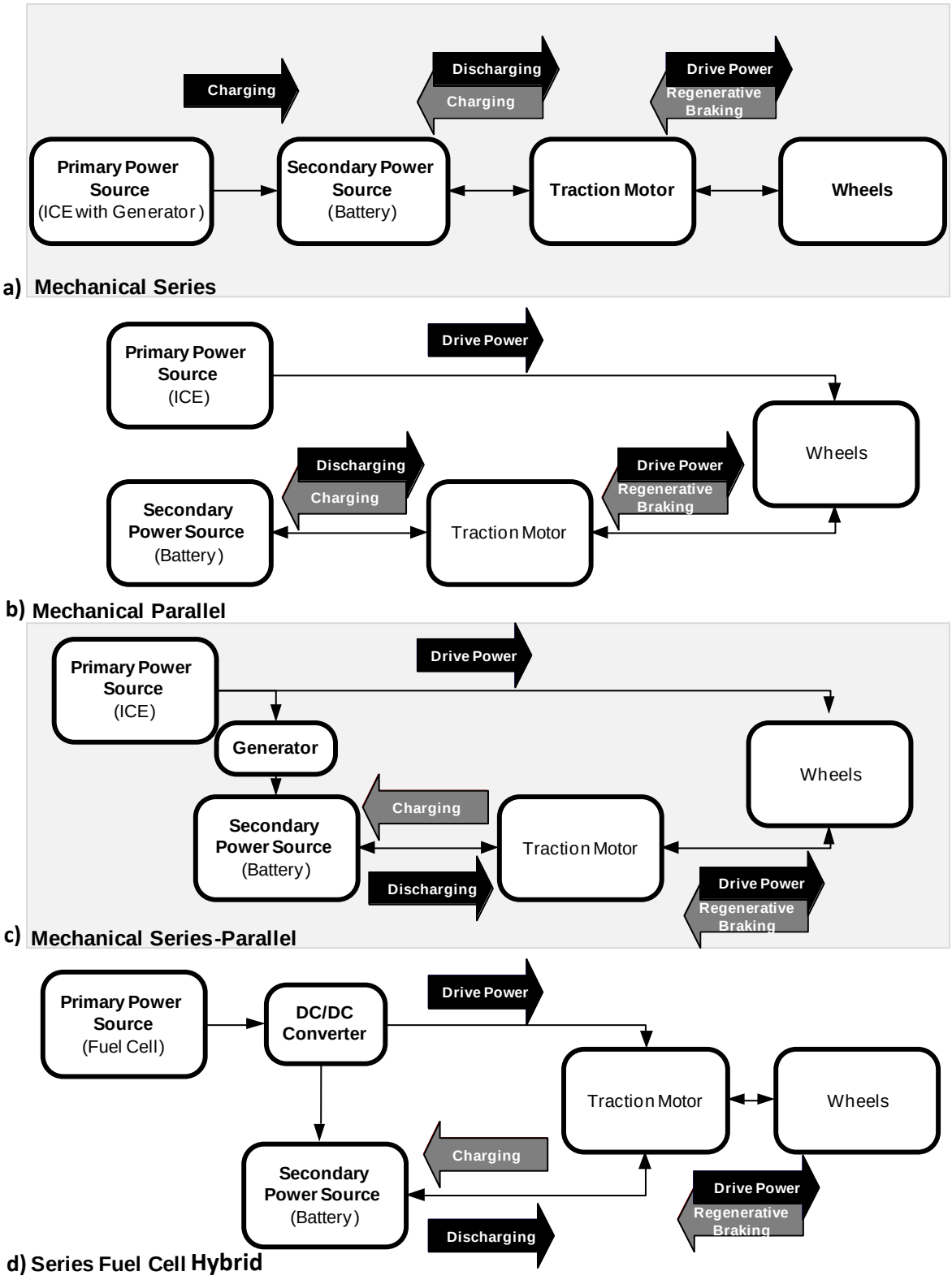

Figure 4 - Schematic of a) Series, b) Parallel, c) Series-Parallel, and d) Series Fuel Cell Hybrid Configurations With Operational Modes

ICE series hybrid systems are common for locomotive diesels; however, most of the diesel locomotive applications do not include an ESS. This type of configuration is ideal for applications that have a fairly constant duty cycle and a primary energy source with low efficiency operating regions [21]. An additional benefit of this architecture is the replacement of mechanical powertrain linkages with electric powertrain linkages that are significantly easier to route. This configuration allows for the primary power source to operate at or near a maximum efficiency point, however, the ESS must be of sufficient capacity to store all the required energy, and of sufficient power to provide the required power to the motors. An example of a series ICE/ESS topology that is under development for the automotive industry is an electric vehicle with range extender topology known as the Chevrolet Volt [13]. A benefit of the range extended variation of this topology is that the electric motor is capable of delivering all traction power requirements, thereby eliminating the power-limited operation of parallel ICE/ESS configurations that are often unable to complete hard accelerations in all-electric mode. Since the motor is the only direct connection to the wheels, the motor must be capable of providing all power required to meet the desired acceleration rate and speed profile, resulting in the a motor sizing that is significantly larger than the average power needs. A larger motor also results in increased cost and mass.

Parallel ICE/ESS configurations allow for both the traction motor and the engine to provide torque to the wheels. Within the classification of parallel hybrid there is a further subdivision between heavy and weak hybrid designs. The term 'heavy hybrid' refers to the amount of power available from the traction motor. The available power of the traction motor is the limiting of the traction motor and ESS power capability. In a heavy hybrid the traction motor is of sufficient power to act as the primary torque source in common operational modes. By comparison, 'weak hybrids' which provide less than 10% of traction power only allow for initial launch allowing engine shut-off during idling, limited regenerative breaking, and the addition of a small amount of torque during high acceleration modes. Weak hybrids are sometime referred to as load tracking or load-following hybrids. Heavy hybrids provide improved economy and efficiency when compared to weak hybrids; however, they are inherently more expensive as a larger ESS and larger electrical traction motors are required [7].

For both parallel ICE/ESS and series ICE/ESS hybrids there are charge-sustaining and charge-depleting designs. Charge-sustaining describes a powertrain and control strategy in which the

powertrain self-regulates the ESS state of charge so no external charging is required – no 'plugging in' of the vehicle to an electrical grid to charge the battery. In this design all the energy ultimately comes from the primary power source or fuel, while some energy is temporarily stored in the ESS. In a charge-depleting design, commonly referred to as a plug-in hybrid, the vehicle requires both refueling and electrical re-charging from the electrical grid. The additional task of charging the ESS is often justified by the potential for zero emission operation, and the fact that the battery-motor combination can achieve efficiencies in excess of 80%, compared to conventional ICE powertrain efficiencies of 20-25% [22]. Charge depleting designs generally require significantly larger batteries as they are exposed to prolonged high power draws (which also entail advanced cooling and thermal management with battery packs).

While hybridization of a powertrain repeatedly results in efficiency gains, the benefits do not always outweigh the impact of the additional mass, costs and complexity. Miller investigated the hybridization of a fuel cell locomotive, and found that the fairly constant duty cycle resulted in marginal gains due to hybridization insufficient for justifying the additional mass and cost [7]. The duty cycles present in an automobile drive cycle have significantly more fluctuation (and braking) which does, more often, justify the use of a hybrid powertrain. The ratio of average power to peak power is a good indicator of hybridization benefit. Applications with low average power to peak power ratios will benefit significantly from hybridization.

The series-parallel configuration allows for the benefits of both the series and parallel configuration. In the mechanical hybrid system this requires additional weight in cost due to the requirement of an additional generator and a complex torque splitting device, commonly a planetary gear set. The series fuel cell hybrid powertrain can provide all the operation model of the mechanical series-parallel configuration without the requirement of planetary gear set or generator. The series fuel cell configuration allows for the following operational modes:

- Electrical power to the motors from both the fuel cell and the secondary power source (ESS) to provide high power potential,
- Regenerative braking to recover and store energy in the secondary power source with the associated efficiency gains in system efficiency,
- Electrical power to the motors from the fuel cell alone thus benefiting from rapid refueling and the extended range of a refuelable energy sources, and
- Charging of the secondary power source directly from the fuel cell.

Additional information on the mechanical hybrid architectures can be found in the texts by Miller, Guzzella, and Wishart [7,8,23]. While this research focuses on the series fuel cell configuration, the framework will be almost completely transferable to series-parallel ICE. There are; however, architecture considerations that are unique to hybrid fuel cell powertrains. The number of energy storage systems and location of power electronics within the structure has a significant impact on the system behavior, control loops, and power electronic topologies. Hybrid fuel cell architectures generally consist of one or two energy storage systems. In the case of a single energy storage system either a battery or ultracapacitor system is selected. Configurations for the single energy storage architecture are illustrated in Figure 5. In all cases there is assumed to be a diode on the fuel cell output to ensure there is not possibility of reverse current polarizing the fuel cell stack.

The energy storage voltage bus configuration consists of a DC/DC converter attached to the fuel cell. A major benefit of this topology is that the DC/DC converter is unidirectional, resulting in fewer components and simpler control. The converter can be boost, buck, or buck-boost depending on the voltage characteristics of the fuel cell and energy storage. Boost or buck designs can achieve higher efficiencies than their buck-boost counterparts; however, buck-boost converters are less susceptible to having operating ranges limited by the voltage behavior of the energy storage system. A drawback of this configuration is that in a charge-sustaining powertrain all energy passes through the DC/DC converter and is therefore subject to its efficiency loss. In charge-depleting operation this topology is ideal as no energy in the energy storage pathway is subject to conversion losses.

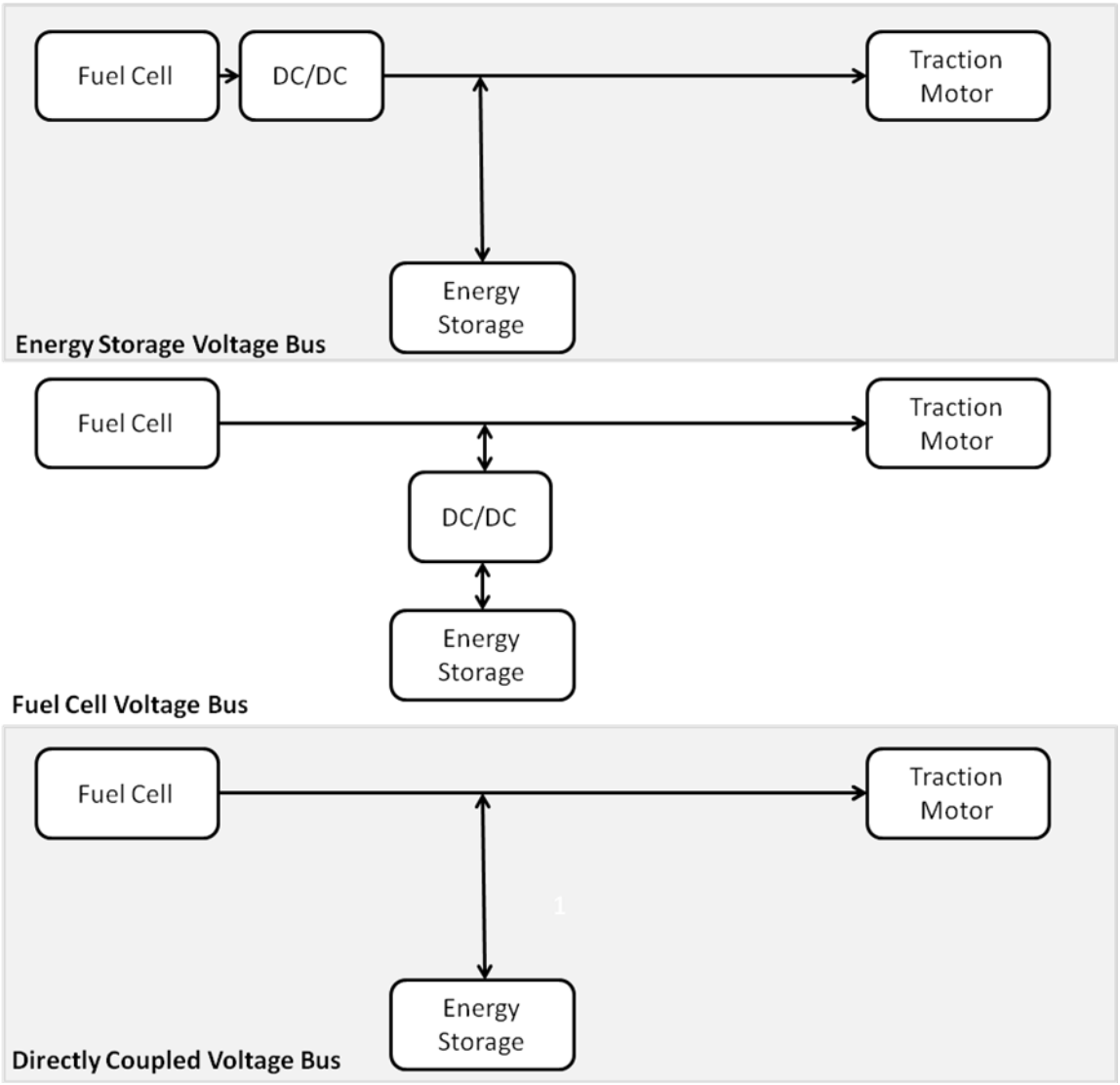

Figure 5 – Hybrid Fuel Cell Powertrain Architectures for Single Energy Storage

The fuel cell voltage bus configuration requires a bidirectional DC/DC converter on the energy storage system. For a similar power and current level, the bidirectional topology is generally heavier, more expensive, and lower efficiency that the unidirectional topology. For charge-sustaining operation in this configuration; however, not all energy passes through the DC/DC converter and is therefore subject to conversion losses. In addition, a smaller DC/DC converter can be used for charge-sustaining operation. Unfortunately, in charge-depleting operation all energy in the energy storage pathway is subject to the conversion losses. Similar to the energy storage voltage bus configuration, the converter can be of buck, boost, or buck-boost type and

has the same tradeoffs as discussed above. An additional drawback of this configuration is related to operational robustness regarding DC/DC converter failure. If the failure occurs during a regenerative braking event the high voltage bus becomes effectively without storage. The concern is that it is unlikely that the system could respond quick enough to avoid a system overvoltage.

The directly coupled voltage bus configuration consists of no DC/DC converters, with the fuel cell and energy storage coupled directly together. Kim et al. have evaluated this topology given the benefit of this topology of elimination of a DC/DC converter, eliminating its associated mass, volume, efficiency loss, and cost [24]. The drawback is the complete elimination of the ability to control the division of power, as the power split is determined exclusively by the native voltage characteristics of the fuel cell and energy storage. While theoretically plausible, there is significant concern about real-world viability of this configuration. Specifically, the voltage characteristics of the components vary significantly during operation as a function of SOC, temperature, and pressure as well as over the component's lifetime. Even if the component voltages can be coordinated/managed at their beginning of life the system will become unbalanced and will have no way to compensate for uneven increases in internal resistance manifested as voltage decay over the system's life.

Due to the differing characteristics of battery and ultracapacitor packs two energy storage configurations have also been considered. Battery packs provided large amounts of energy storage, while ultracapacitors provide a long lifetime, high efficiency, and high power capabilities. Configurations using both energy storage types permit for combining the benefits of each type and have been evaluated extensively by Bauman and Kazareni [25]. The drawback is the additional complexity, cost, and mass. Two energy source hybrid fuel cell configurations are shown schematically in Figure 6.

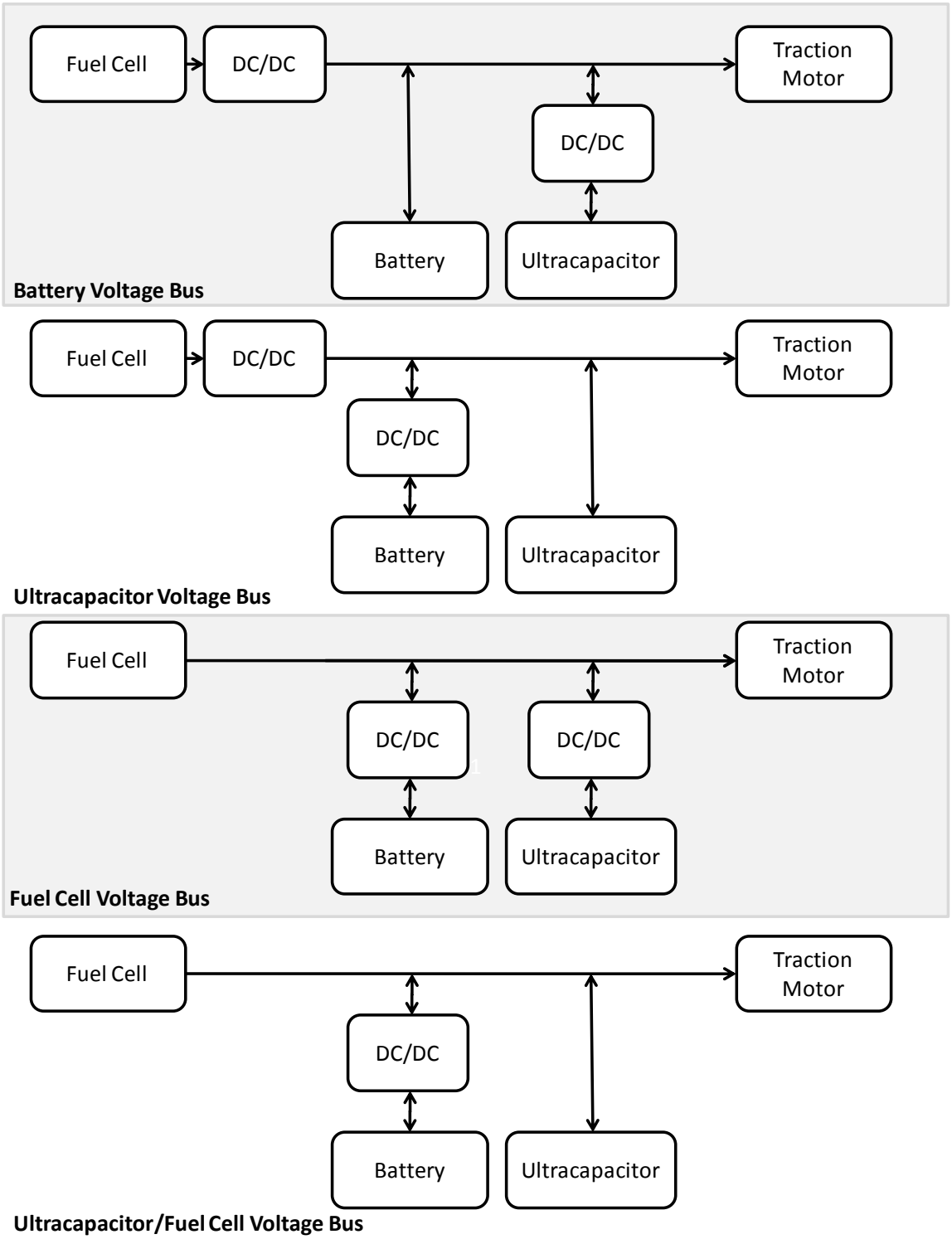

Figure 6 - Hybrid Fuel Cell Powertrain Architectures for Double Energy Storage

The majority of the factors to consider for configurations with two energy storage devices are the same as single storage device configurations. The key consideration that is unique to double

storage configurations is the selection placing the DC/DC converter on the battery or the ultracapacitor pack. Benefits of placing the DC/DC converter on the ultracapacitor pack are that the high voltage bus exhibits relatively flat voltage behavior due to the battery voltage characteristics and that during charge-depleting operation the battery pathway has no conversion losses. Benefits of placing the DC/DC converter on the battery pack are that the ultracapacitor can rapidly accept regenerative braking energy and the regenerative braking round trip efficiency can be very high. It is also possible to directly couple the fuel cell to the ultracapacitor pack without the integration of a DC/DC. In the directly coupled system the diode (not shown) on the fuel cell output results in the ultracapacitor voltage behavior controlling the bus behavior when the voltage exceed the fuel cell open circuit voltage. At voltages below the fuel cell open circuit voltage the bus voltage and power flow is controlled by the characteristics of both the ultracapacitor pack and the fuel cell. In this architecture the DC/DC can be used to control the ultracapacitor pack SOC to provide a level of control. While the two energy storage devices provide additional capability and response, the benefits must be balanced with the cost and complexity of these systems.

Evidently there are a number of configuration options within the series hybrid fuel cell architecture. The research performed herein exclusively considers the energy storage voltage bus configuration with single energy storage based upon the following factors:

- **Capable of high system efficiencies**. Allows for a high efficiency unidirectional DC/DC topology. During charge-depleting operation there are no conversion losses for the energy storage pathway.
- **High system robustness**. Energy storage is directly coupled to the motor controller. As a result DC/DC converter failure does not render the high voltage bus storageless.
- **Highly controllable**. Even using a boost or a buck DC/DC converter topology, a well designed system retains a wide operating range for both the fuel cell and energy storage.
- **Relatively low system complexity and cost**. Costs and mass associated with a second energy storage system and subsequent power electronics are not required.

Charge-sustaining operation is the primary focus for the initial research described herein, with inclusion of charge-depleting operation considered in section 5.2. As will be described in the

following chapter, charge-sustaining and charge-depleting designs for a given architecture require different approaches for optimal component sizing and control.

2.2.2 Hybrid Component Sizing

One of the initial design decisions to be made following the selection of hybrid architecture is the type of ESS to be used. The two common options for the energy storage system are batteries and ultracapacitors. Hydraulic hybrid systems are also under development as an ESS option, however to date these systems remain in early stages of research and development [26,27], and have experienced mechanical failures in practice. Within the battery category there are a number of battery chemistries available. The most common chemistries under development for hybrid vehicles are based upon Nickel Metal Hydride (NiMH), Lithium Ion (Li-Ion), and Lithium Polymer (Li-Pol) systems [7]. The power and energy densities of lead-acid batteries are too low to be considered for hybrid vehicle operation [28]. Ultra-capacitors generally exhibit much higher specific powers than battery technologies; however, batteries exhibit much higher energy capacities. The performance differences between ESS types are provided in Table 1[29,30]. The lifetime cycles quoted are heavily dependent on the duty cycle, which will be described in significant more detail in the next section.

Table 1 - Comparison of Specific Power and Energy for Energy Storage Systems

Metric	Lead-Acid	NiMH	Li-Ion	Ultracapacitor
Specific Power (W/kg)	358	704	1,222	10,000
Specific Energy (Wh/kg)	25	49	91	9
Shallow-cycle Lifetime (cycles)	100,000	200,000	200,000	500,000*
Deep-cycle Lifetime (cycles)	Moderate	Low	High	500,000*
Cost	Low	Medium	High	High

*Due to low energy capacity of ultracapacitors, differentiation between shallow and deep cycling not applicable

Ragone plots provide a useful visualization tool for comparing ESS technology's respective energy and power densities [31]. A representative battery Ragone curve is illustrated in the inset of Figure 7. Christen has described a method to combine Net Present Value analysis with Ragone plots to size energy storage components [32]. The method is premised on the fact that a given component is not a point but rather a curve on the Ragone plot as a function of the operating conditions. If the component is operated higher powers the capacity is decreased.

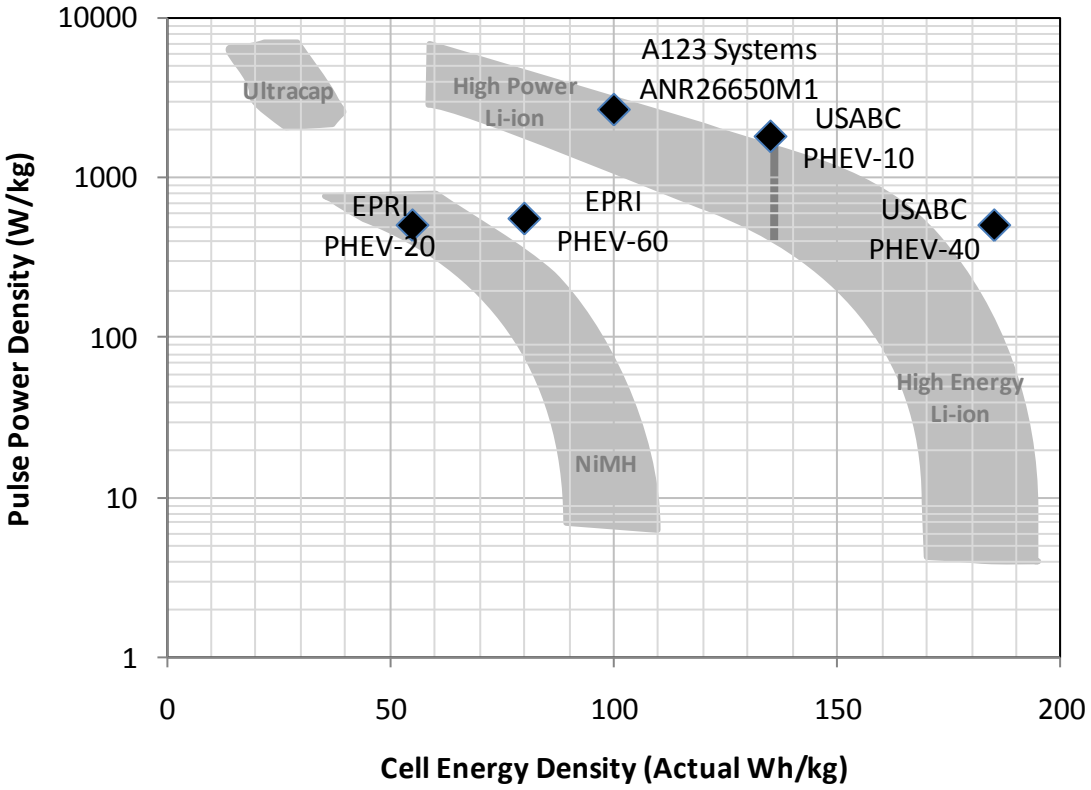

Figure 7 – Modified Ragone plot for various energy storage systems. Performance targets from the US Advanced Battery Consortium and Electric Power Research Institute (EPRI) are plotted as well as the coordinates for an A123 ANR26650M1 battery.

W. Gao et al [22] have published a detailed comparison between batteries and ultra-capacitors for fuel cell hybrids. Gao found that in simulations charge sustaining hybrids with the high specific power ultracapacitor packs outperformed the high energy capacity battery packs in both acceleration and mileage. While standard vehicle operation for a charge-sustaining hybrid did not require the energy capacity of the battery pack, Gao concluded though that ultra-capacitors could exhibit complications during initial vehicle start up if the fuel cell or any onboard reforming system required a significant amount of time to spool. Spooling time refers to the time required for the system to prepare to deliver full power.

Similar results were obtained by Burke in a later study that incorporated advancements in energy storage technology and included considerations for charge-depleting hybrids [20]. Burke did not consider cost explicitly, but did conclude that the energy storage technologies have achieved sufficient energy and power densities to be technically feasible, in addition to the following conclusions:

- an All-Electric Range (AER) for a charge-depleting hybrid is possible with a relatively small lithium-ion battery pack,
- charge-sustaining Hybrid Electric Vehicles (HEV) can provide a >50% fuel consumption improvement over conventional ICE vehicles, and
- fuel cell hybrid vehicles can provide a 200-300% fuel consumption improvement over conventional ICE vehicles.

Burke [20] also discussed energy storage sizing to be based upon the architecture and intended operation, suggesting that:

- **charge-sustaining hybrid** ESS' are sized based upon peak power requirements,
- **charge-depleting hybrid** ESS' are sized upon a combination of peak power and capacity,
- and **electric vehicle ESS'** are sized based upon capacity, calendar, and cycle life.

For parallel ICE/ESS architectures, a term called Electric Fraction (EF) is used for sizing of the components. EF relates is the percentage of traction electric motor power that makes up to the total powertrain power. In the ICE/ESS topology, the engine is downsized according to the degree of hybridization. Standard engine downsizing and EFs for various hybridizations are provided in Table 2. As previously mentioned, the total power requirement is set for performance, in particular acceleration. Therefore, the primary electric torque of the hybrid system must augment the reduced torque from downsizing the ICE [22]. The corollary in a fuel cell hybrid is that the ESS must be sized large enough so that the ESS power combined with the downsized fuel cell system generates sufficient power to the motors, which in turn provide the torque required for adequate vehicle performance.

Table 2 - Engine Downsizing and Electric Fraction for Various Levels of Vehicle Hybridization

Hybridization	**Engine Downsizing**	**Electric Fraction (EF)**
None – Conventional	None	<1%
Weak Hybrid	<10%	1-10%
Strong Hybrid	10-30%	10-50%
Electric Vehicle	N/A	100%

The energy rating of the energy storage system is a significant function of the sizing of the fuel cell and the control strategy. Smaller fuel cell power systems will require increased durations of higher power demands, therefore, requiring additional electrical capacity. As this is also a function of control, the energy capacity requirement is discussed further in the following section.

As discussed in the previous section, an energy storage bus voltage configuration under charge-sustaining operation is the initial powertrain of interest, with subsequent work considering charge-depleting operation. Given the characteristics described above, a NiMH-based ESS was used in this work for the initial charge-sustaining research, with Lithium-based ESS considered when the powertrain is extended to include charge-depleting operation. Ultracapacitor based ESS' are not considered due to prohibitively low energy storages eliminating the technology as a feasible technology for charge-depleting operation.

Optimal selection of the ESS type and component sizing is strongly dependent on a number of variables, including: the expected drive cycles, vehicle physical characteristics affecting rolling losses and aerodynamics, and control strategies significantly affect power requirements. As previously discussed, powertrain component selection and sizing is further complicated by the significant interaction between energy storage mass, which in turn impacts vehicle dynamics and power requirements. The resulting optimization includes a number of multi-factor interactions which requires significant modeling in order to map the design space. As mentioned, the hybrid control strategy has a significant impact on both power and energy

requirements. Common hybrid control strategies will be discussed further in the following section. It is important to note that in current real-world applications there exists limited availability of energy storage devices of automotive sizes. As a result, the optimal values can be identified but component availability becomes a significant consideration for designing actual powertrains.

2.2.3 Hybrid Fuel Cell Vehicle Control, Charge-Sustaining

Powertrain control is commonly divided into two abstraction layers; low-level control and supervisor control. Low-level control focuses on maintaining component stability and to achieve the set points determined by the supervisor control.

In the context of a fuel cell power system, low-level control manages the fuel cell system auxiliaries to ensure that reactant flow, relative humidity, temperatures, pressures, stoichiometric values, and coolant flows are kept to required operational ranges [33]. This low-level system control is general developed by the fuel cell system manufacturer as it is a function of fuel cell stack, composition, and specific stack materials and design. In the context of a DC/DC converter, the low-level control will consist of a PI loop determining a Pulse-Width Modulation (PWM) duty cycle that drives an Insulated-Gate Bipolar Transistor (IGBT), causing the required DC boost to achieve the fuel cell current set point determined by the supervisory control. Supervisory control required by hybrid fuel cell powertrain designers focuses on 1) identifying driver intent, 2) determining torque set points, and 3) managing energy and power between the two power sources. The third objective is referred to as the hybrid control strategy.

To provide an overall description of the control system, a simplified control schematic for a hybrid vehicle is provided as Figure 8. The primary controller is the driver who is seeking a vehicle speed target. The driver interprets the difference between speed target and actual speed and depressed the throttle and brake pedals accordingly. These two pedals can be considered to be one torque request, with the throttle position representing the positive torque requests and the brake pedal representing the negative torque requests.

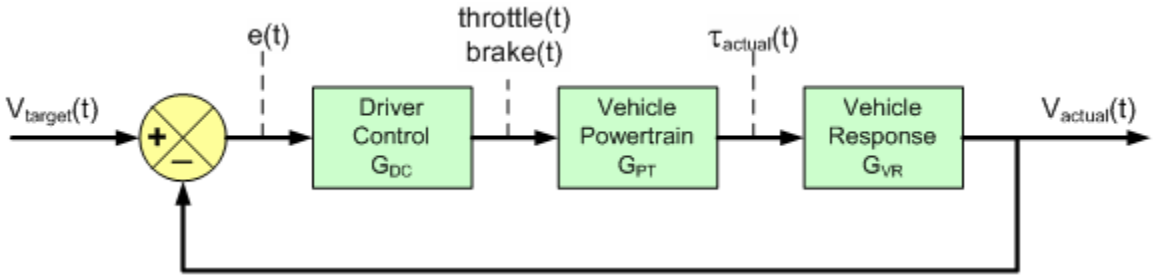

Figure 8 - Simplified Vehicle Control Schematic

The powertrain controller then interprets the throttle and brake pedal positions and correspondingly manages the power, torque, and energy levels of powertrain. The location of the supervisory hybrid control strategy within the overall vehicle controls is illustrated in Figure 9.

The simplified series fuel cell hybrid architecture is provided as Figure 10. As illustrated above the parasitic and traction motor power demands are a function of the drive cycle, driver, and powertrain controls. At a given time step the supervisory hybrid control has one Degree Of Freedom (DOF) for the power sharing between the fuel cell and the battery. Therefore, setting the fuel cell current for a specific system fixes the battery current.

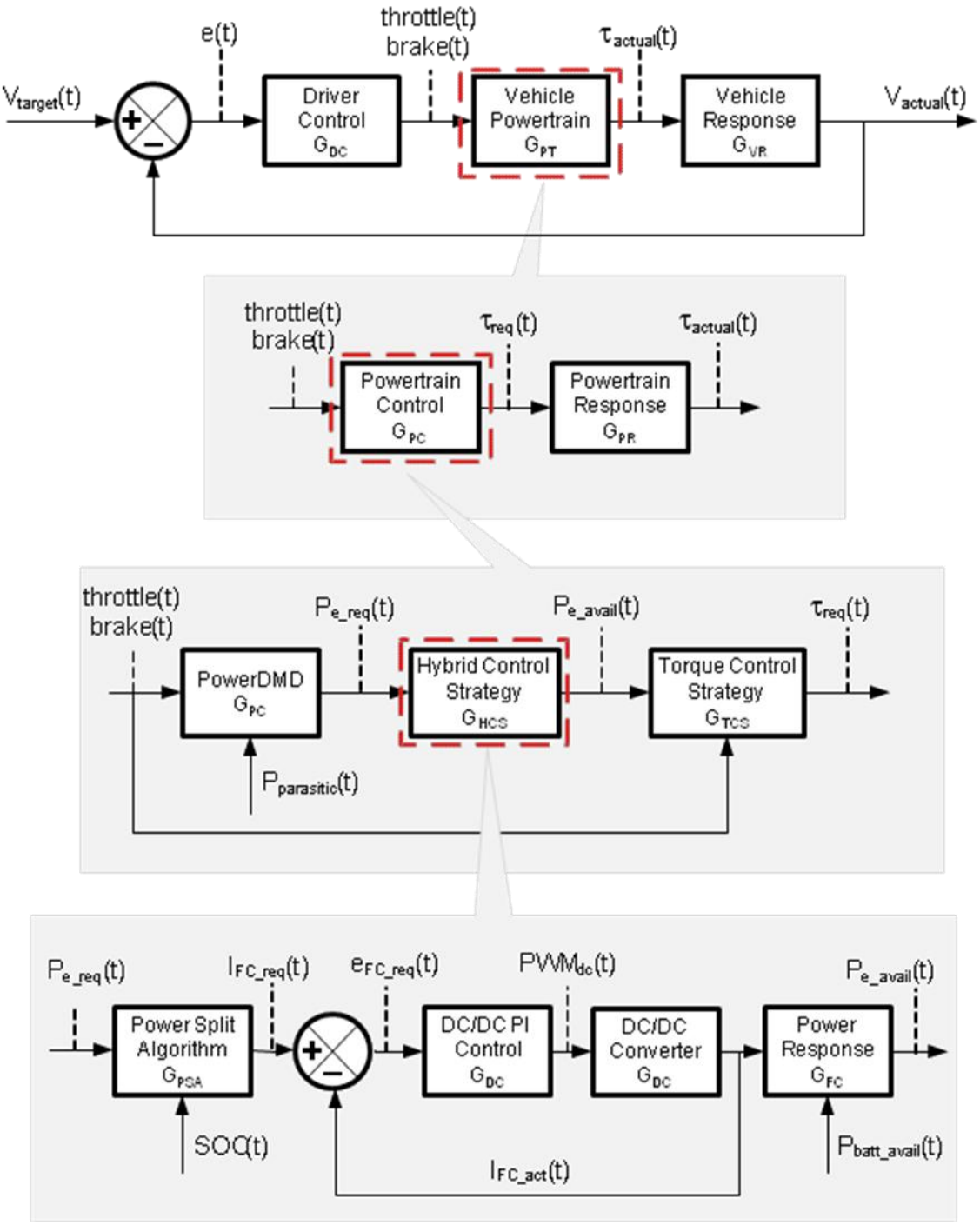

Figure 9 - Fuel Cell/Battery Hybrid Vehicle Control System

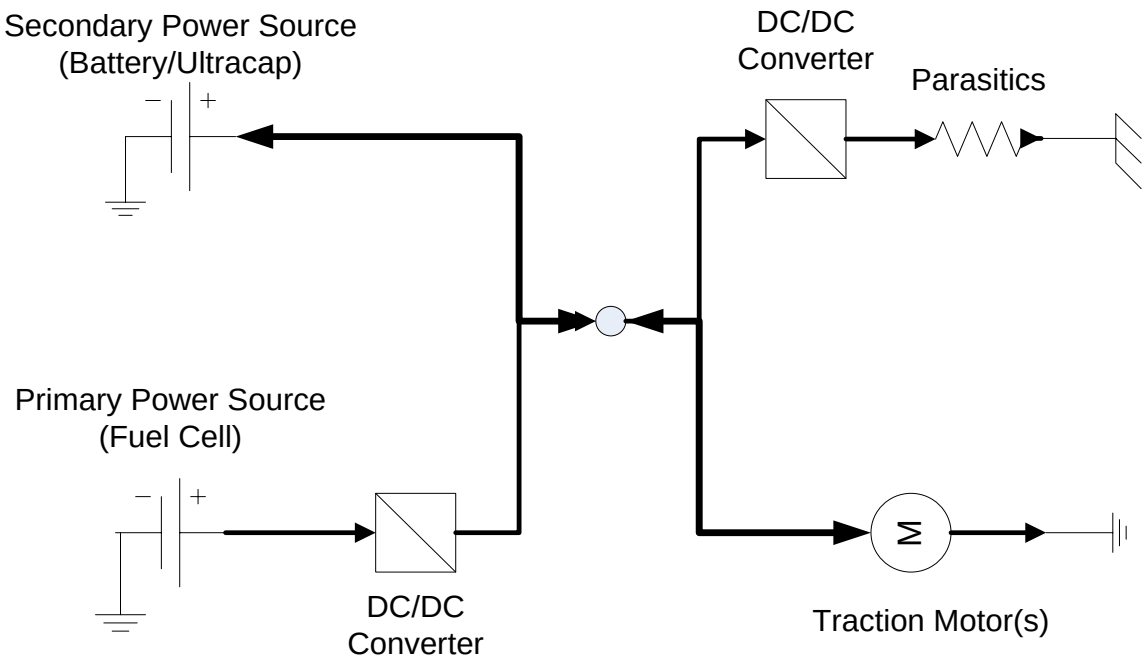

Figure 10 - Schematic of Series Fuel Cell Hybrid Vehicle

In the hybrid configuration, the total power demand can be satisfied for an infinite number of power splits between the two power sources. The designer can therefore use the hybrid control strategy to change the duty cycles of the individual power sources and the resulting stresses on the component. Figure 11 clearly illustrates the significant difference of the power demands for the primary and secondary power sources for load-leveling and load-following control strategies. In both of these strategies, the intent is that given a predefined time horizon the system is charge-sustaining, meaning the net battery pack SOC does not exhibit a continuous decreasing trend. Functionally, charge-sustaining means that the vehicle is never plugged in, as all energy is ultimately derived from the hydrogen fuel.

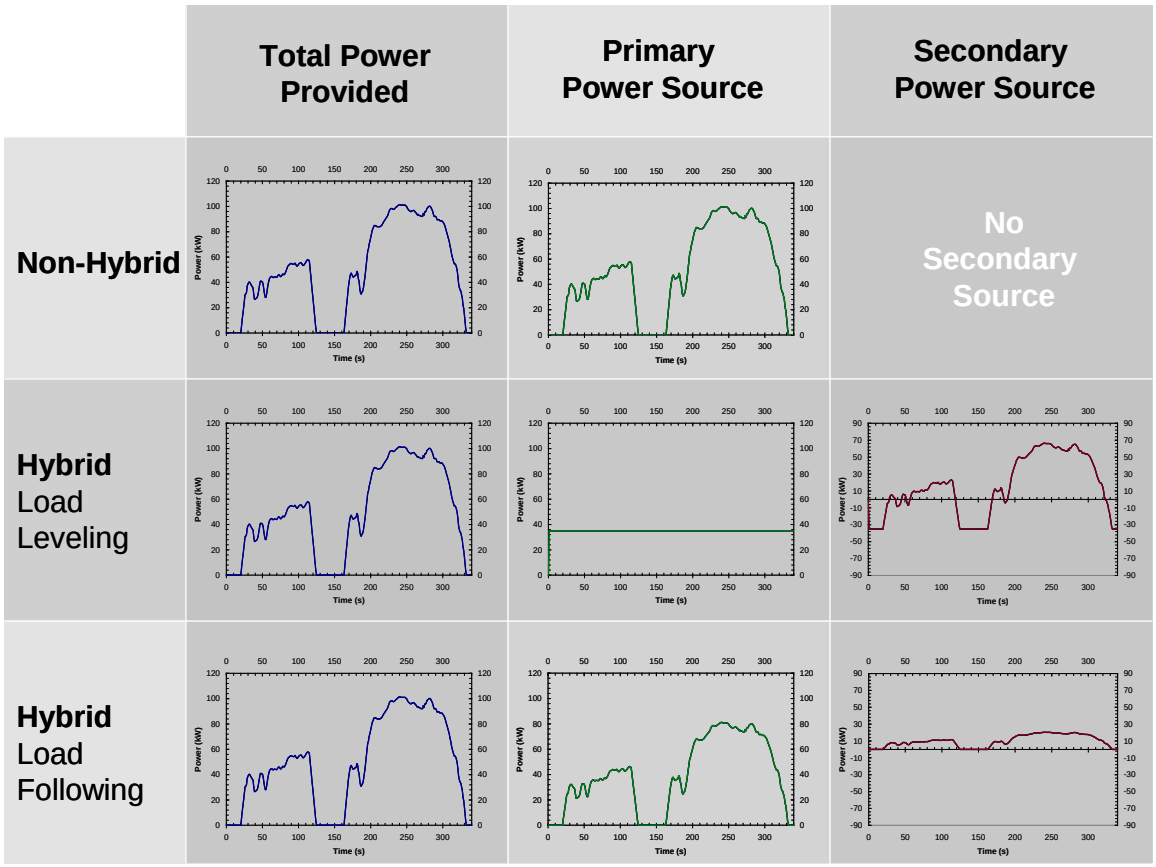

Figure 11 - Comparison of Operation Power Demands for Non-hybrid, Load-leveling hybrid, and Load-following Hybrid Powertrains

The hybrid control strategy, in conjunction with component sizing, determines the operational parameters and component duty cycles. A number of studies of varying complexity have investigated the impact of a variety control strategies on vehicle performance [34-47]. Three common hybrid control strategies discussed for hybrid systems in literature are:

Load leveling: utilizes the secondary power source as load leveling to enable the primary power source to operate continuously within a narrow, high efficiency operating range. This allows high efficiency and significant downsizing of the primary source, but results in low efficiency of the secondary power source and high power and capacity requirements of the secondary source.

Load following: utilizes the secondary power source only to augment the primary system and to provide improved transient response. The primary source trails the power demands with a

slight delay. This allows for smaller and high efficiency operation of the secondary power source at the cost of a larger primary power system and potentially reduced primary source efficiency.

Rule based: operates the primary source only when it can operate at a high efficiency point due to high power demands or lower secondary source state of charge. The secondary source provides power until it reaches a low state of charge value and then the primary source turns on to charge the battery. This provides a balance between the efficiency of the primary and secondary sources and limits the power requirements of the system. This control does require a larger capacity secondary power source.

These three control strategies have been simulated and evaluated for a 2kW hybrid fuel cell bench top setup by Corbo et al [35-37]. The resulting battery (secondary power source) state of charge is provided in Figure 12 for the three strategies. As can be seen, the load-leveling strategy results in significant state of charge swings, while the rule-based control results in a moderate state of charge swing, and the load-following strategy results in very little power swing. A limited number of additional studies have developed and simulated more complicated control algorithms for fuel cell hybrid vehicles, including a stochastic dynamic programming algorithm [45,14,48].

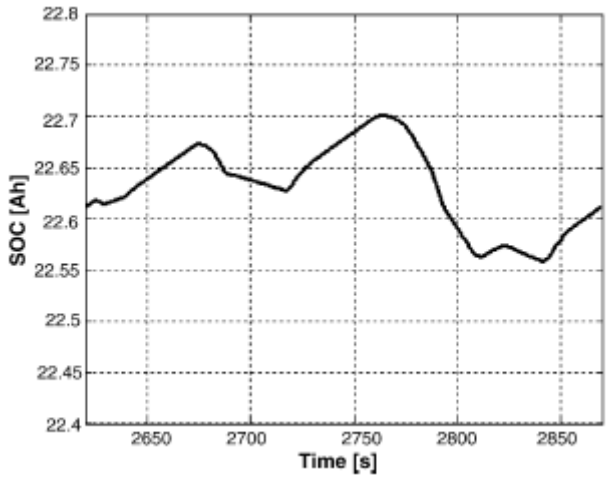

A) Load Levelling Control

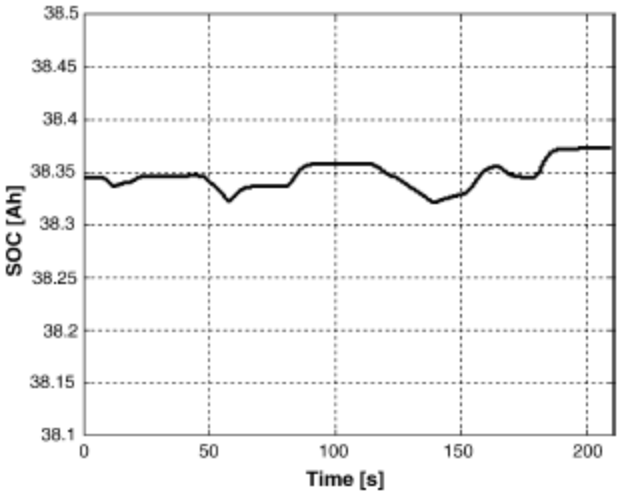

B) Load Levelling Control

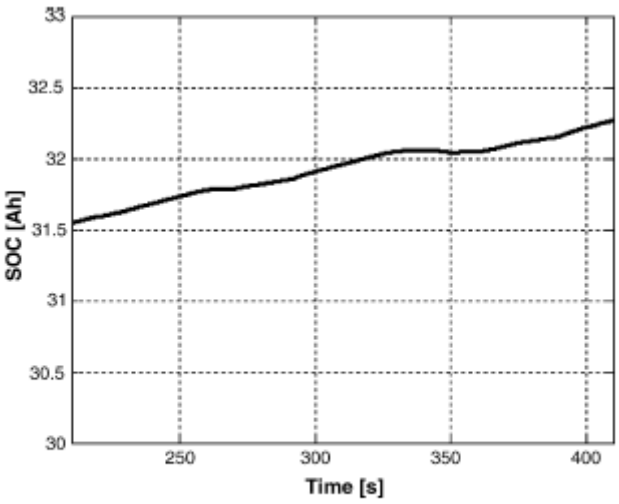

C) Rule Based Control

Figure 12 - State of Charge During the European 40 Drive Cycle for a) Load-leveling Control, b) Load-following Control, c) Rule-Based Control [35]

SOC swing has been proven to have a significant impact on battery degradation rates, which is discussed further in the next section. As described above and clearly demonstrated in Corbo's papers [35-37], hybrid control strategies can result in significantly different operating conditions for the individual components for a given vehicle performance. It can therefore be concluded that for a given performance the control strategy can result in significantly different degradation rates of the powertrain.

None of the studies described have explicitly integrated considerations of component degradation. At the vehicle design layer of abstraction the discussion of durability is limited to general references to reducing large transiency in the fuel cell duty cycle and state-of-charge swing of the battery. None of the control papers formally integrate component degradation into the vehicle operation, define a causal degradation model, or permit quantifiable degradation comparison between design decisions.

Gokosan [49] and Wu [27] have published papers on hybrid control development for ICE based hybrids with simulated data on performance and efficiency for military and delivery vehicles respectively.

An advanced control strategy that has been introduced by Johnson [50] and a team at the National Renewable Laboratory utilizes an 'impact function', which in other papers is referred to as a 'cost function'. The proposed control strategy was for an ICE/battery parallel hybrid configuration which balances estimated engine efficiency, emissions, and implied motor/battery efficiency as implied by future state of charge. The control strategy calculates an "impact" value for a variety of power splits between the battery and the ICE and selects the power split with the lowest "cost". The impact, akin to a cost, allowed for simultaneous consideration of multiple control objectives. While the impact terms are not applicable for the series fuel cell hybrid, the cost function control strategy algorithm introduces a method for incorporating numerous control objectives into the real-time selection of the power division.

Optimal selection and tuning of the control strategy and evaluation of the interaction with the powertrain selection on vehicle performance requires significant investigation. This further amplifies the need for accurate models and advanced simulation tools to research these interactions and developments.

2.2.4 Hybrid Fuel Cell Vehicle Control, Charge-Depleting

Charge-depleting operation introduces an additional complexity to the control requirements. The charge-depleting operation is defined as the initial mode of operation that has a characteristic decline in battery State-Of-Charge (SOC). Once a minimum SOC is reached, the control strategy converts to a charge-sustaining mode for subsequent vehicle operation [51]. A schematic representation of charge-depleting and charge-sustaining modes is provided as Figure 13. While a negligible number of studies have focused on fuel cell charge-depleting hybrids, there exists a significant amount of recent publications evaluating control and sizing strategies for charge-depleting ICE/ESS hybrid architectures [52,53].

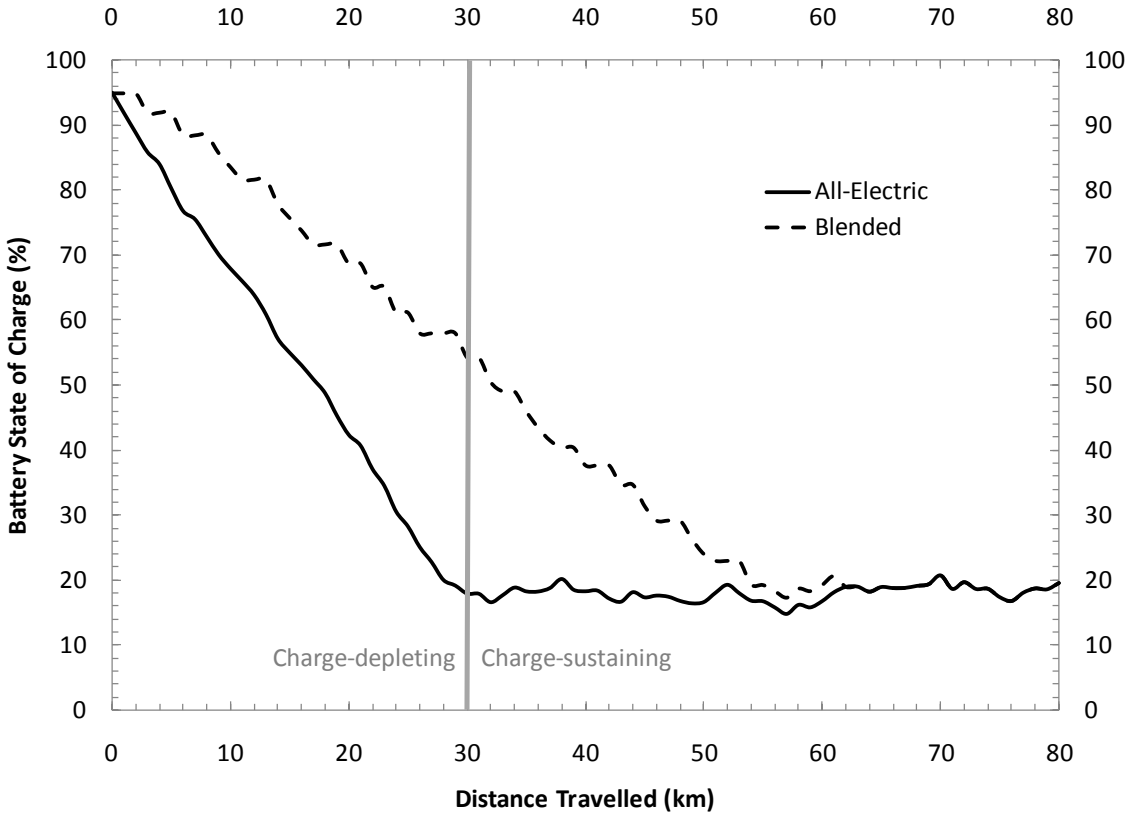

Figure 13 – Schematic representation of battery SOC versus distance depicting charge-depleting and charge-sustaining modes for All-Electric and Blended strategies

Freyermuth utilized PSAT to compare series, parallel, and series-parallel architectures for both 10 and 40 mile All-Electric Ranges (AER) [52]. The engine was sized to meet the gradeability requirement of the vehicle. The battery and motor powers were selected to match the maximum required power draw during the Urban Dynamometer Driving Schedule (UDDS) during

all-electric operation. The battery capacity was selected to satisfy the AER requirement. During all-electric operation the parallel and series-parallel architectures exhibited slightly better fuel consumption performance than the series hybrid. The deviation; however, is likely due to the significantly larger engine in the series architecture as a result of the sizing algorithm. During blended operation the series-parallel exhibited the lowest fuel consumption.

The two main control strategies that are being considered for ICE/ESS charge-depleting operation are all-electric operation and blended operation, which are shown in Figure 13. The all-electric operation utilizes the battery system exclusively until the minimum SOC threshold is reached, whereas the blended operation permits opportunistic utilization of the ICE at high efficiency points. Sharer utilized Powertrain System Analysis Toolkit (PSAT) to investigate powertrain efficiencies for all-electric operation as compared to blended operational strategies and concluded that the blended operation can result in higher overall powertrain efficiencies [53].

As the hybrid fuel cell architecture approximates the series-parallel ICE/ESS hybrid with respect to modes of operation, Freyermuth's results imply that it is an ideal architecture for a charge-depleting operation. Sharer's results suggest that a blended charge-depleting strategy will generate the lowest fuel consumption values for the hybrid fuel cell vehicle. None of the studies to date have considered the durability impacts of the charge-depleting operation or specific control strategy. In addition, it is important to evaluate the architectures and charge-depleting control strategy for fuel cell operation due to the differences in partial load efficiency behavior between fuel cells and combustion engines.

2.3 Electrochemical Power Sources

While battery technology has undergone two centuries of development, the recent advancements in battery technology for vehicle systems represent preliminary advancements in a nascent industry. Nickel-metal hydride chemistries have been successfully deployed in current hybrid vehicles and lithium-based chemistries have been developed by heavy utilization in the mobile electronics market [12]. While initial hybrids have allowed for the development of periphery components, controls, and technology, nickel-metal hydride's inability to provide sufficient lifetime performance during deep-cycling negates the chemistry as a viable option for electrification beyond charge-sustaining configurations. Similarly, the majority of lithium

chemistries developed for the mobile electronics market are considered unsafe for vehicular application due to thermal sensitivities. Despite the significant amount of development required for lithium cells, no chemistry has successfully displaced lithium-based technology as the expected standard for near-term charge-depleting applications.

Battery technology for plug-in operation is further complicated by an a priori requirement for cell and pack design. Design and lifetime performance projections require duty cycle and environmental operating conditions to be inputs to the design process. Battery duty cycles for plug-in vehicle operation are highly variable, vaguely understood, and fundamentally dependent on the hybrid control algorithm. Successful design of battery packs for the next transition in the evolutionary path requires an improved understanding of application and the control algorithms that will be employed.

Fuel cell technology has progressed significantly in the last decade with significant improvements in reliability, durability, and performance over a wide temperature operation range. The primary limitations to fuel cell technology adoption for vehicular applications are cost, reliability, durability, and hydrogen infrastructure requirements. Similar to the battery technology profile, the fuel cell durability is heavily dependent on the load profiles and is a function of the hybrid control algorithm.

The following sections will detail the existing literature on lithium ion batteries and fuel cells. The Beginning-Of-Life (BOL) characteristics and models will be presented. In addition, the degradation mechanisms, models, and evaluation techniques developed in the literature are discussed.

2.3.1 Fuel Cells

Fuel cells were initially discovered in 1839 by Sir William Grove [54]. Knowing that hydrogen gas would be evolved under the presence of electrical current, Grove hypothesized that the reverse process could be achieved. Grove successfully demonstrated the generation of electrical current by reacting hydrogen and oxygen in the presence of a catalyst, and fifty years later in 1889 Ludwig Mond and Charles Langer demonstrated the first fuel cell in its current form [55].

The fuel cell itself is an electrochemical device that converts chemical energy into electrical energy. While there are a number of types of fuel cells, each distinguished by their electrolyte, the Polymer Electrolyte Membrane Fuel Cell (PEMFC) are the primary fuel cell under

development for the automotive market. PEMFC are considered to be the most suitable for the automotive market due to their solid state design, low operating temperature, quick start up times, as well as their ability to respond to rapid load changes [56].

The fuel cell half-cell and overall reactions for a PEMFC are:

Anode: $H_2 \xrightarrow{Pt} 2H^+ + 2e^-$ (13)

Cathode: $2H^+ + 2e^- + \frac{1}{2}O_2 \xrightarrow{Pt} H_2O$ (14)

Overall: $H_2 + \frac{1}{2}O_2 \xrightarrow{Pt} H_2O$ (15)

The PEMFC consists of three main components: the bipolar plates, Gas Diffusion Layer (GDL), and the Membrane Electrode Assembly (MEA) [14,57]. Some sources consider the GDL as part of the MEA, as some newer MEAs have the GDL integrated. Without the GDL, the MEA consists of two electrodes separated by a polymeric membrane. The most common membrane material is a perflourosulfonic acid (PFSA) based ionomer, almost exclusively marketed by Dupont under the name Nafion™ [58]. The molecular structure for the membrane is provided as Figure 14. Newer MEA's often include a micro-porous layer on the electrode, which is believed to improve reaction kinetics.

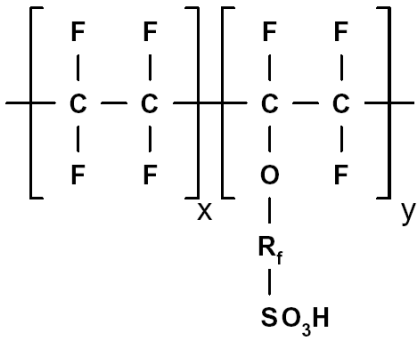

Figure 14 - Molecular Structure of PFSA [58]

The cell components are then assembled in repeated cells in the following order:

bipolar plate → GDL → MEA → GDL → bipolar plate → GDL → …

Collector and end plates are added on the end of the repeated cell structure. The collector plate acts as the primary connection to the external circuit, while the end plates provide mechanical strength and compression to the stack [54]. There are a number of additional components required for continual operation of a fuel cell. These components include those required to pressurize, supply, heat, and humidify the incoming reaction streams. On the anode stream, these components include anode supply manifolding, humidifier, and recirculation pump. The associated components on the cathode stream include an air blower, supply manifolding, humidifier (e.g. enthalpy wheels, hydrators), and exhaust manifolding. A coolant loop with pump and radiator is also required in addition to significant sensor and control circuitry. A schematic of a fuel cell power module is provided as Figure 15.

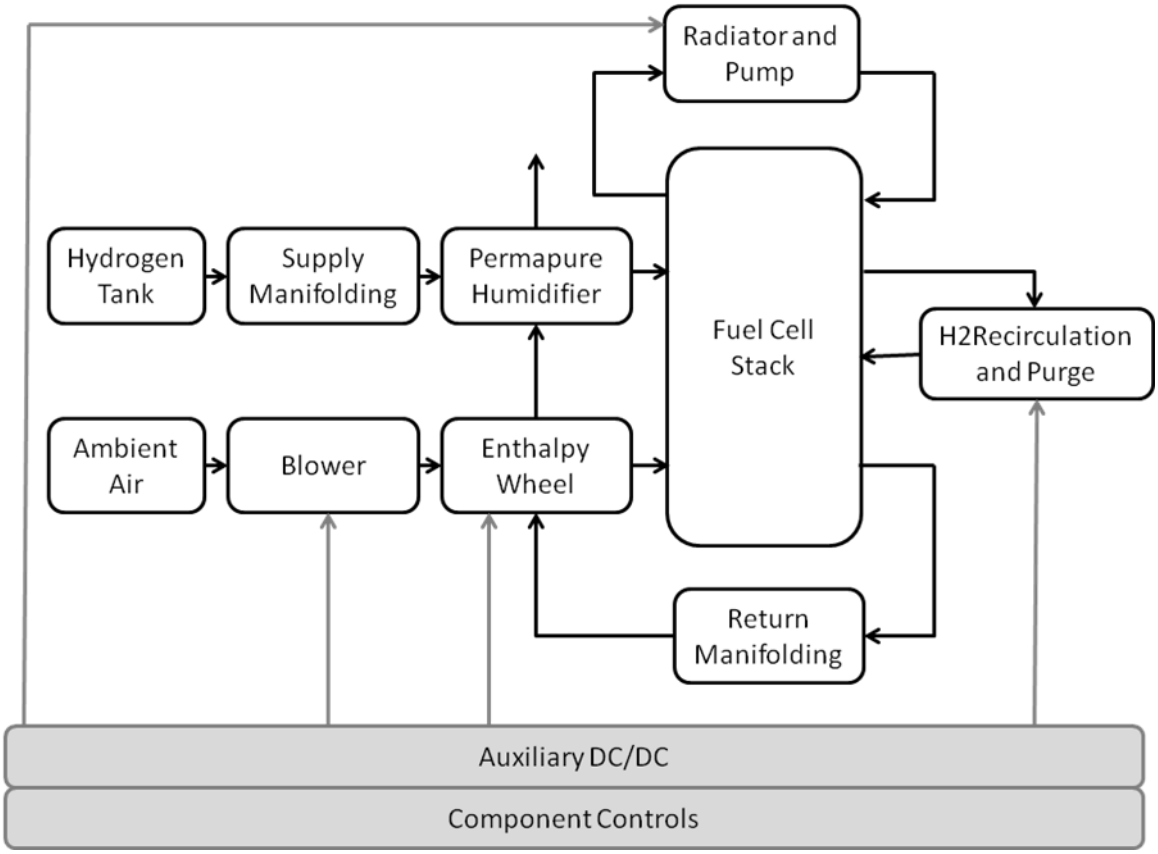

Figure 15 - Schematic of fuel cell power system similar to the one used in this work

Characteristic fuel cell stack and auxiliary load power for a fuel cell power module are plotted as a function of output current in

Figure 16. The details of the fuel cell stack output curve are described in the next section; however, what can be derived from this system level view is that a stack operating at a highest

efficiency at low current draw is counterbalanced by higher relative power draws of the auxiliaries.

The net power output of the fuel cell power module is the stack output power decreased by the auxiliary load power. The impact of auxiliary loads not scaling directly with the stack power curve is a steep drop in net output power at low output powers. This difference between stack and net power module efficiencies is demonstrated in Figure 16 and Figure 17 respectively. The efficiencies are defined as:

- **Stack efficiency:** electrochemical efficiency defined as the ratio of output voltage to the reversible stack voltage.
- **Module efficiency:** power efficiency defined as the ratio of output power (the product of voltage and output current) divided by the chemical flux of hydrogen supplied.

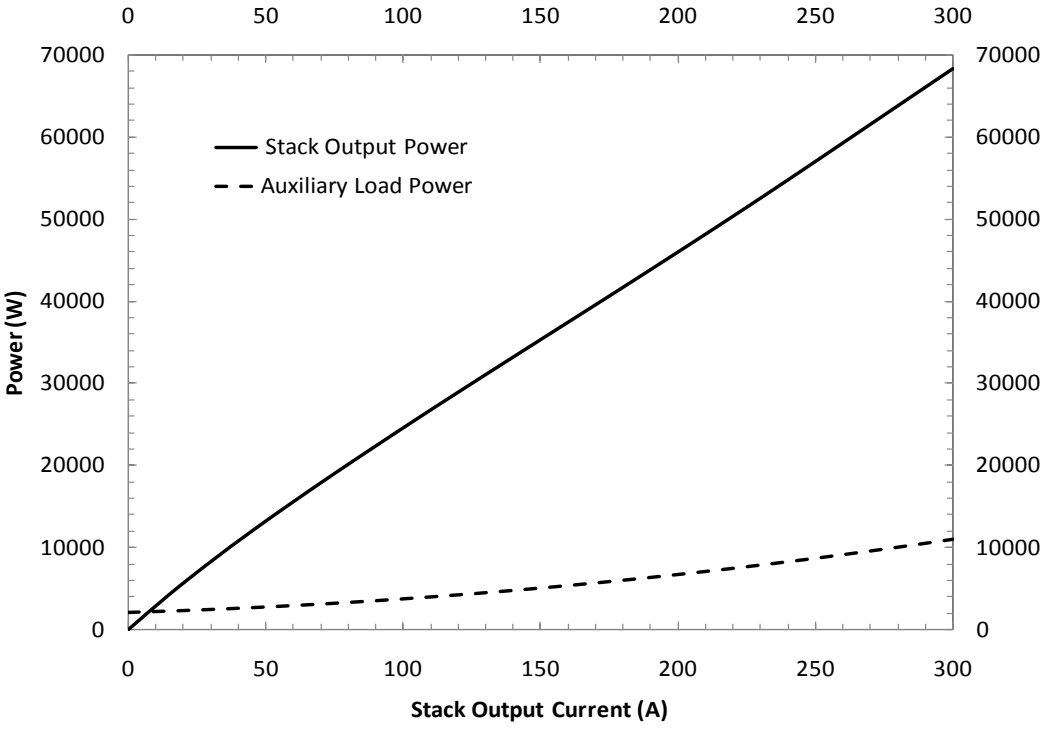

Figure 16 - Fuel cell stack power output and auxiliary load power

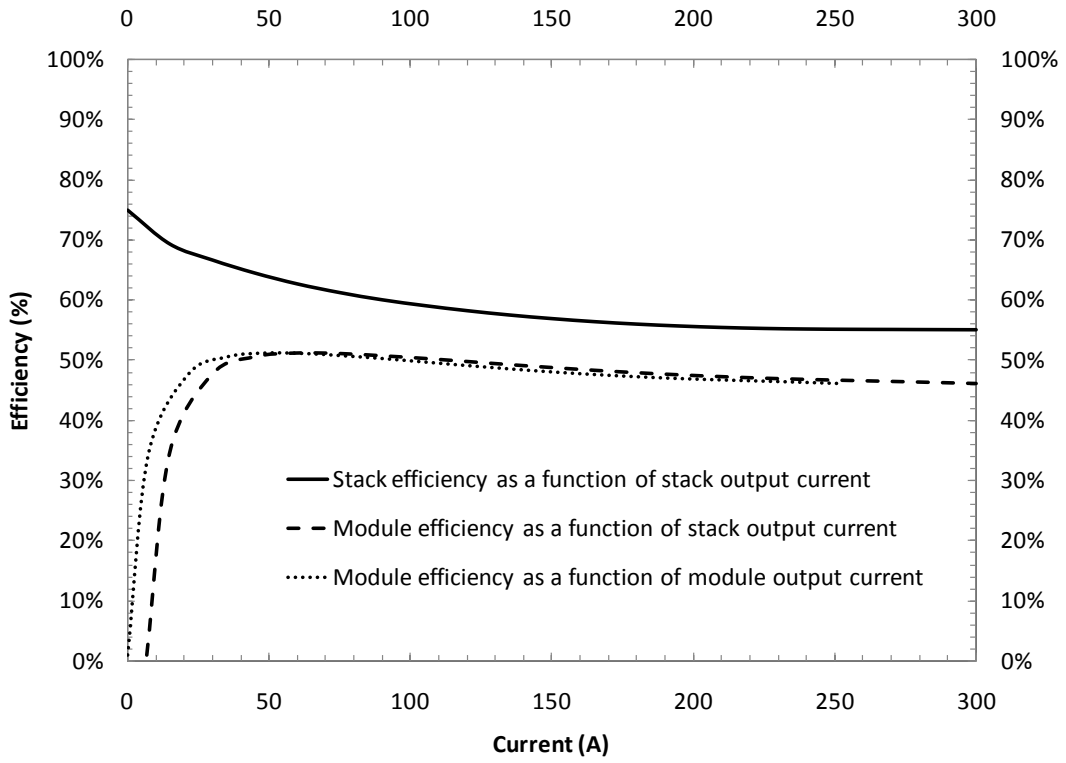

Figure 17 Fuel Cell Stack and Module Efficiencies

A thorough understanding of fuel cell power module performance requires a comprehensive understanding of single cell and fuel cell stack behavior. The next section will discuss single cell operation and modeling, with the subsequent section reviewing the current literature on fuel cell degradation.

2.3.1.1 Fuel Cell Performance and Beginning-of-Life (BOL) Models

Numerous empirical, semi-empirical, and mechanistic models are available for describing fuel cell behavior [59]. Separate reviews of the most significant models up to 2008 have been published by Haraldsson, Biyikoglu, Cheddie [59-61].

The first semi-empirical models of fuel cell performance were published by both Amphlett and Kim in 1995 [62-64]. Both models calculated cell voltage as a function of current by a general equation of the form:

$$V = V_0 - \eta_{act} - \eta_{ohmic} \tag{16}$$

This parametric form was later refined by Mann in 2000 into what is currently known as the Generalized Steady-State Electrochemical Model (GSSEM) [65]. In should be noted that mass transfer losses are integrated into the activation and ohmic overvoltages. The V_o term represents the thermodynamic equilibrium potential, which can be calculated from the Nernst Equation:

$$V_o = E_0 - \frac{RT}{nF} ln\left[p_{H_2}^* \left(p_{O_2}^*\right)^{0.5}\right] \tag{17}$$

The activation overvoltage represents the loss of potential associated with the kinetics of the reaction. In the context of a fuel cell, the reaction kinetics for the hydrogen oxidation at the anode are significantly faster and resistive than the oxygen reduction at the cathode [62]. Within the GSSEM, the activation overvoltage is calculated as a lump sum equation derived from the sum of Butler-Volmer equations for the anode and cathode, resulting in the following structure:

$$\eta_{act} = \xi_1 + \xi_2 T + \xi_3\left[ln\left(c_{O_2}^*\right)\right] + \xi_4 T[ln(i)] \tag{18}$$

The ohmic resistance represents the resistance to proton transfer in the membrane and electron transfer in the electrodes and collector plate. The ohmic resistance is defined by following equation:

$$\eta_{ohmic} = i(R^{electronic} + R^{proton}) \tag{19}$$

The total resistance to proton diffusion can be calculated using membrane thickness, cross-sectional area, and membrane resistance by the equation:

$$R^{proton} = \frac{r_M l}{A} \tag{20}$$

Where the membrane resistance is given by the equation:

$$r_M = \frac{181.6\left[1 + 0.03\left(\frac{i}{A}\right) + 0.062\left(\frac{T}{303}\right)^2\left(\frac{i}{A}\right)^{2.5}\right]}{\left[\lambda - 0.634 - 3\left(\frac{i}{A}\right)\right]\exp\left(4.18\left[\frac{T-303}{T}\right]\right)} \tag{21}$$

The λ term in equation 21 is used as a fitting parameter that affected by the preparation method, humidification, and age of the membrane. The value has been observed to reach 14 in 100% saturated conditions and as high as 24 in supersaturated conditions [65,66].

A common graphical representation of a fuel cell is a polarization curve. A representative polarization curve is provided as Figure 18. The curve contains three distinct regions. The first region exhibits rapid voltage drop as a function of current density and is associated with activation losses. The second region exhibits a linearly decreasing voltage as a function of current density and is associated with the ohmic losses that can be approximated using Ohm's Law. The third and final region is at high current densities, exhibits a rapid and accelerating decrease in voltage and is associated with the mass transfer limitations of the cell. As shown in Figure 19 all three mechanisms are present throughout the entire polarization curve; however, the region is labeled by the significant phenomena in that region.

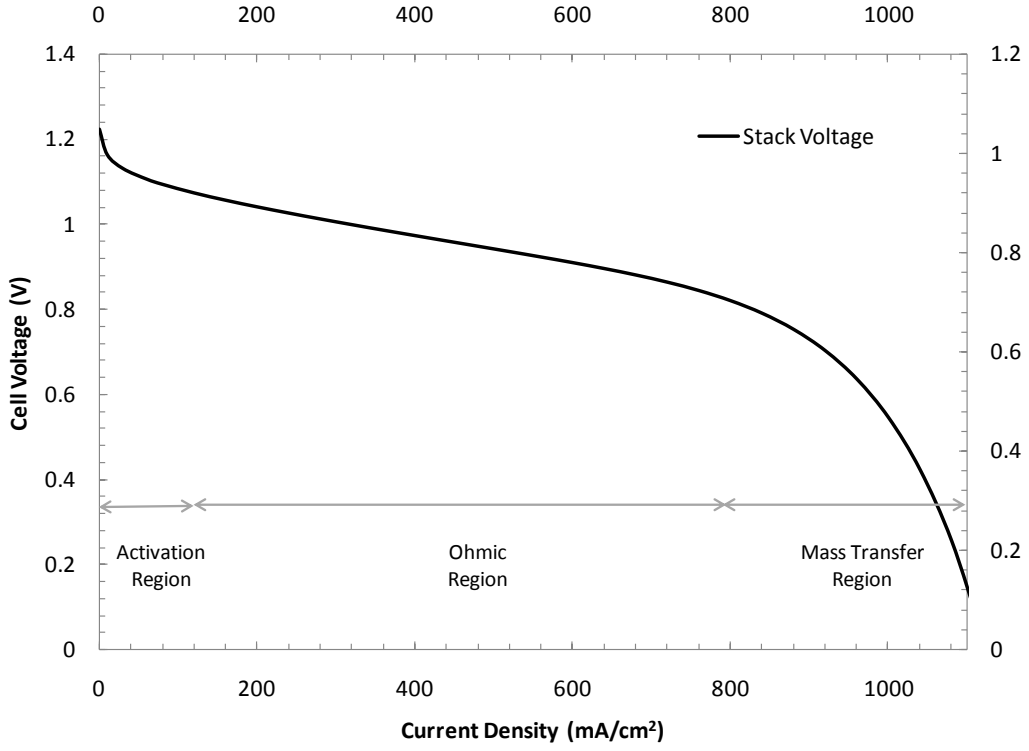

Figure 18 – Beginning Of Life (BOL) polarization curve for a single fuel cell

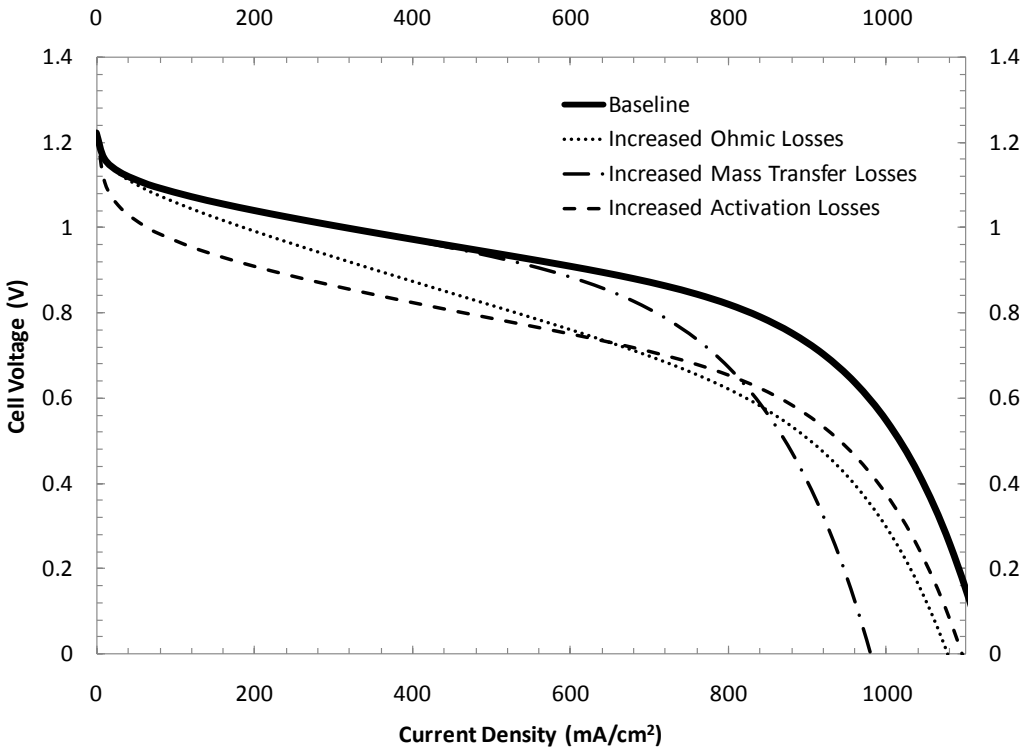

Figure 19 – Fuel cell polarization curve illustrating activation, ohmic, and mass transfer degradation mechanisms

As discussed previously, a number of individual cells are combined in series to form a fuel cell stack. More recent models have been developed that model stack performance, integrating pressure loss and heat effects across the stack [67,68]. Students working for Peng and Stefanopoulou's research team at the University of Michigan have developed full fuel cell system and limited control models [33,47]. These control models are also for high pressure fuel cells that have been primarily abandoned in the automotive market [33,69-71]. While models are interesting for initial cell, stack, and power module performance estimates, the intent of this research is to extend these models to include the impact of operating conditions on degradation. To that effect, fuel cell degradation is presented in the next section.

2.3.1.2 Fuel Cell Degradation

Fuel cells degrade over time and operation [72]. The Department of Energy's target for fuel cell lifetime under load cycling conditions is 2000 hours for 2010 and 5000 hours for 2015[73]. Degradation in fuel cells is often referred to as voltage degradation as the voltage for a given current draw reduces over time in service. The degradation is a combination of irreversible and

reversible degradation. Observing the change in polarization curve over fuel cell operation is valuable as the curve provides insight into the dominant degradation mechanisms. Specifically, a degradation mechanism that increases activation losses will result in a downwards translation of the polarization curve. Increased resistance to proton or electron transfer will increase the ohmic losses, therefore increasing the negative slope of the linear region of the polarization curve. An increased resistance to mass transfer within the cell will result in an earlier 'dip' of the curve due to earlier onset of the mass transfer limitation. Representative curves comparing a baseline polarization curve with curves demonstrating activation, ohmic, and mass transfer degradation is provided as Figure 19.

A number of studies have been published that provide voltage degradation observations for a wide variety of operating conditions. Maximum operating hours using a constant current draw of over 10,000 hours have been published, with a maximum operating time of over 60,000 hours reported by GE [74-76]. The voltage degradation rate for a cell operated at a consistent 800 mA/cm^2 is shown in Figure 20 with diagnostics occurring every 500 hours. Significant reversible degradation rates are observed as a result of reversible catalyst oxidation, which is removed during the diagnostics tests at the 500h intervals.

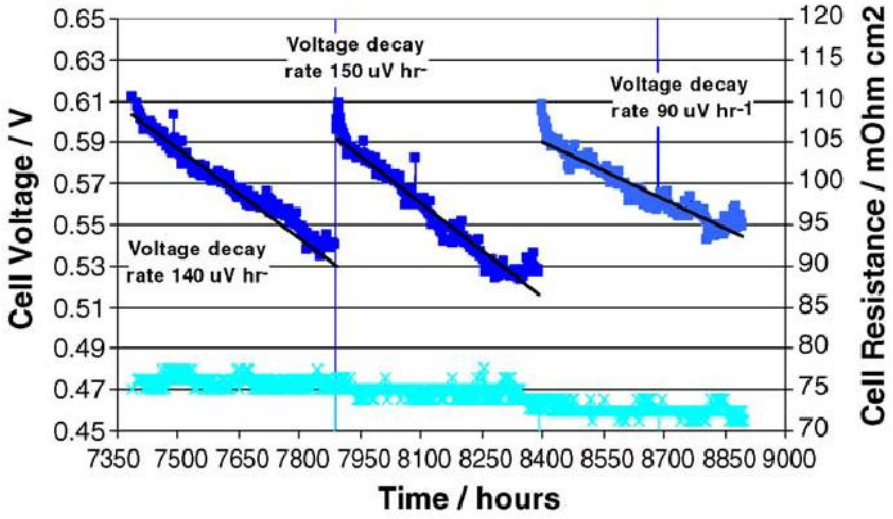

Figure 20 - Voltage Degradation Rates with Diagnostics at 500h Intervals [74]

The reversible degradation is believed to be due to MEA performance degradation from operating conditions such as hydration conditions (i.e. flooding or dehydration of the membrane) and reversible materials change such as formation of Pt oxides. The diagnostics

performed every 500 hours operated the cell at high current densities, which are presumed to have reduced the Pt-oxides, returning the Pt to full activity, as well as improving the water management of the cell. In the context of hybrid fuel cell vehicle operation the reversible degradation is unlikely to be significant as the transient nature of the duty cycles will permit continual reduction of any reversible effects. The irreversible degradation of the cell is demonstrated as a function of operational time in Figure 21 and polarization curve form in Figure 22. The ageing trend observed in Figure 22 clearly exhibits downward and downward-leftward translations, implying both activation and ohmic degradation mechanisms are contributing to the voltage decay.

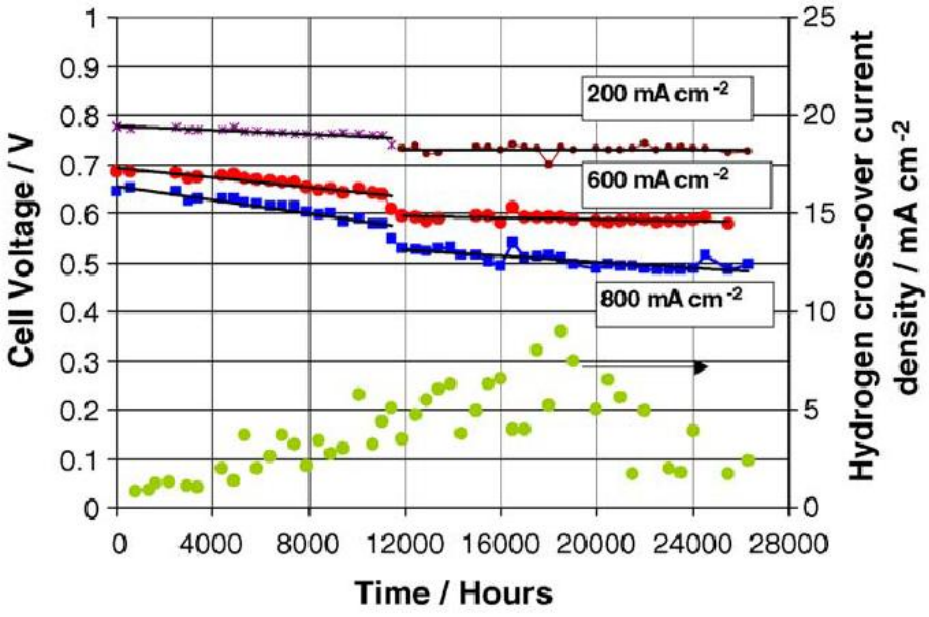

Figure 21 - Irreversible Degradation Rates at Various Current Draws [74]

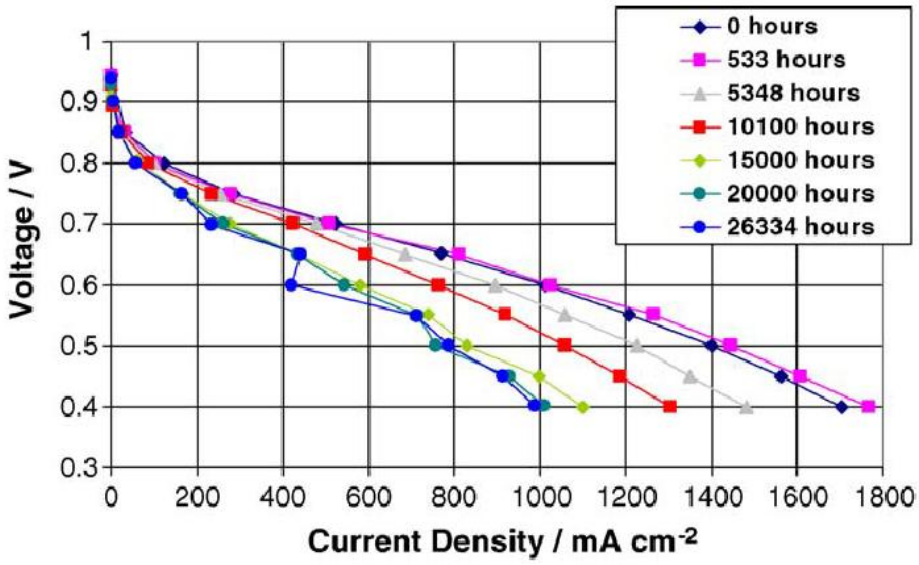

Figure 22 – Polarization Curves with Irreversible Degradation at Various Hours of Operation [74]

Reduction in effective electrochemical catalytic active area, reduction of proton conductivity of the membrane, and increasing membrane impedance have all been found to contribute to the irreversible voltage degradation [77-79]. An excellent summary of major degradation studies up until 2007 was published by de Bruijn et al [80]. Within the steady state testing, both high and low temperature extremes exhibited higher degradation rates. Disregarding the extreme temperature accelerated aging tests and one outlier, the steady state experiments demonstrated voltage decay rates ranged between 1 and 30 μV/hr. Three of the four cyclic testing experiments demonstrated significantly higher voltage decay rates, ranging between 45 and 210 μV/hr. The results imply that temperature extremes and cyclic loads accelerate voltage decay.

As shown in Figure 22, the voltage decay is dependent on the current density the voltage is evaluated at. Therefore the results in Table 3 do not provide a complete understanding of the change in the voltage-current relationship as the cell ages. The results do; however, permit preliminary evaluation of operational impacts on voltage decay. A summary of the accelerating operating conditions and their corresponding degradation mechanisms is provided as Table 4.

Table 3 – Summary of PEM fuel cell degradation studies (adapted from de Bruijn et al [80])

Test Cycle Type /Researcher	Current Densities (mA/cm^2)	Cell Temperature (ºC)	Voltage Decay Rate ($\mu V/hr$)
Steady State			
St-Pierre	1076	75	1
St-Pierre	538	75	1.4
St-Pierre	861	75	1.3
Yoshioka	259	75	1.5
Cleghorn	800	70	6.4
Ferriera	0	80	20
Ferriera	200	80	25
Nakayama	300	80	28
Miyoshi	300	80	29
Wood	550	80	33
Endoh	200	120	75
Wahdame	500	55	95
Liu	1060	80	180
Cyclic			
Yamazaki	150-300	70	2.5
Wahdame	0-700	55	45
Nakayama	0.01-300	80	75-114
Miyoshi	0.01-300	80	210

Table 4 – Operational conditions' impact on dominant degradation mechanisms for PEM fuel cells (adapted from de Bruijn et al [80])

Operating Behavior / Condition	**Degradation Mechanism**
Load Cycling /Humidity cycling	Mechanical wear of membrane
Load Cycling /Potential cycling	Platinum particle growth in the cathode Platinum dissolution in the cathode
Load Cycling /Open circuit voltage	Chemical degradation of the membrane via radical attack
Load Cycling /Start-stop cycles	Carbon corrosion in the electrodes
High Temperature	Chemical degradation of the membrane via accelerated kinetics of radical attack reaction

Load cycling contributes to a number of operation conditions that accelerate fuel cell degradation. Understanding the relationship between operating conditions and degradation mechanisms allows for the development of causal degradation models; models that degrade as a function of the operating conditions. The next section discusses the development of both non-casual and casual fuel cell degradation models.

2.3.1.3 Fuel Cell Degradation Modeling

Fowler et al[77] proposed a method to integrate this degradation into the GSSEM discussed above. Fowler proposed the use of the λ term as a fitted age parameter in the modified form:

$$r_M = \frac{181.6\left[1+0.03\left(\frac{i}{A}\right)+0.062\left(\frac{T}{303}\right)^2\left(\frac{i}{A}\right)^{2.5}\right]}{\left[\lambda_{age}-0.634-3\left(\frac{i}{A}\right)\right]\exp\left(3.25\left[\frac{T-303}{T}\right]\right)} \quad (22)$$

Where:

$$\lambda_{age} = \lambda_o + \lambda_{DR} * age \quad (23)$$

To date no research has been published on the impact of operating parameters on λ_{DR}. This research will develop a causal degradation model that will determine λ_{DR} as a function of operating conditions. Understanding this relationship allows for the evaluation of vehicle design decisions and the development of control algorithms could decrease degradation rates.

In summary, a number of detailed mechanistic and semi-empirical models are available for single cells. A limited number of simplified models are available for fuel cell stacks, and even less models are available for full fuel cell power systems. The full system models are primarily 0-D models with generalized thermal and water transfer models.

While both reliability and durability are of significant interest, this research focuses on durability. In this context reliability is the catastrophic failure of the fuel cell requiring immediate removal from service (likely to the catastrophic failure of a membrane). Data available on fuel cell reliability is reasonably limited, and as such is not considered in detail in this work.

2.3.2 Battery

Energy storage systems (ESS) that have the most significant research effort for hybrid vehicle applications include NiMH, Li-Ion, Li-Polymer, and ultra-capacitor packs [20]. As previously described, the NiMH chemistry is considered and integrated into the charge-sustaining baseline hybrid fuel cell vehicle model while all subsequent models will consider Li-Ion chemistries as Li-Ion represents the future technology selection for hybrid applications. This section introduces the fundamentals of battery degradation and relevant research available related to automotive application of these chemistries.

The voltage-current behavior of NiMH and Li-Ion chemistries exhibits the same trends as a fuel cell polarization curve. Since the balance of plant for a battery is limited to control and coolant circuits, the battery pack efficiency curve more closely resembles a fuel cell stack curves than fuel cell power module curves. Due to the similarity the BOL performance curves are not repeated for battery packs in this background section. Batteries do exhibit significantly different degradation behavior, the dominant degradation mechanisms and effects are introduced in the next section.

Various targets for battery performance in hybrid vehicles have been presented. In the work by Christophersen, the performance goal was 15 years of service, cycle life depending on power-assist ratings – 240,000 cycles at 60%, plus 45,000 cycles at 80%, plus 15,000 cycles at 95% of rated power (80%/15%/5% split of the 300,000 total cycles)[81]. Cycles are defined by an engine-off, vehicle launch, vehicle cruise, and finally a regenerative braking event. The FreedomCAR target for Power-Assist Hybrid Electric Vehicles is a minimum of 300,000 25-Wh cycles, for a total of 7.5MWh delivered [82]. For batteries intended for 40-mile range PHEVs the lifetime target is 5,000 charge-depleting cycles for a total energy delivery of 58 MWh in addition to 300,000 charge-sustaining cycles [83].

2.3.2.1 Battery Degradation

Batteries exhibit two forms of degradation: capacity fade and power fade. Capacity fade represents a gradual loss in energy capacity for a given current. Power fade represents a gradual increase in battery impedance, and subsequent decay in apparent voltage for a given current. Capacity fade is generally measured in Amp-hours while power fade is measured in Volts.

For a hybrid fuel cell vehicle with the DC/DC converter on the fuel cell, both capacity and power fade each have two major implications. For capacity fade, the first is that a decrease in useable capacity represents larger State-Of-Charge (SOC) swings in charge-sustaining operation for a given drive cycle, further contributing to accelerated degradation as will be discussed below. Secondly for capacity fade, the battery capacity has a direct correlation to charge-depleting range of the vehicle. Considering power fade, the first implication is that the minimum and maximum high voltage bus limits will be achieved at lower battery discharge and charge currents respectively. As a result, the maximum discharge and charge power of the battery is reduced, resulting in less power available during accelerations and less ability to recapture power during regenerative braking. Since the drive cycle and vehicle dynamics determine the required power, the second implication of power fade is a further decrease in useable battery capacity as a given power will require additional current to compensate for a lower terminal battery voltage.

A number of papers have been published on the durability of NiMH batteries [84-86], including papers focused on the use of Electrochemical Impedance Spectroscopy (EIS) to determine degradation modes [87-89]. One of the degradation modes identified through EIS was the

formation of permanent oxides during the “overcharging” of the battery pack at high SOC. As previously discussed, NiMH chemistries are viable options for charge-sustaining operation but are unable to exhibit sufficient cycle life for serious consideration in charge-depleting applications. As a result, the charge-sustaining baseline vehicle model will be developed using a NiMH battery pack; however, subsequent studies will utilize a Lithium Ion battery pack model as the lithium chemistry is the predominant front-runner for future charge-sustaining and charge-depleting applications.

Due to heavy penetration in the consumer electronics market, large research efforts have been focused on understanding the mechanisms of degradation in lithium ion batteries. The knowledge derived from these research efforts is strongly beneficial for developing the battery technology for automotive application; however, there are two main limitations that must be considered when reviewing consumer electronics focused research. First, a large portion of the research is focused on lithium cobaltate cathode chemistries, which are not feasible for vehicular application due to safety concerns regarding potential thermal runaway failure modes. Subsequently, only the conclusions related to the anode, electrode, and diagnostic methods are relevant for automotive application. Secondly, vehicular applications entail a vastly different duty cycle than consumer electronic applications with significantly higher pulse discharge rates, and consumer electronic batteries are generally maintained by the user at a high state of charge. The results must be extended to anticipate higher discharge rates for accurate considerations of performance within a vehicle. Although not providing completely transferable conclusions, the body of research on lithium chemistries does provide valuable insights and is subsequently presented herein. In addition, a few seminal studies investigating lithium ion battery degradation in automotive-focused have recently been published and are also discussed. A thorough review of a large number of lithium battery degradation studies has been performed by Kanevskii [90]. A summary of major lithium ion degradation studies is provided as

Table 5

Table 5 – Summary of Major Degradation Studies for Lithium Ion Batteries

Degradation Type		Degradation Rates	Degradation Mechanisms	Accelerating factors
Calendar-life	Power Fade	4.20 Ω-cm^2/day @ 70ºC [91] 0.22 Ω-cm^2/day @ 55ºC [92] 43% at 68 weeks @ 45ºC [93]	lithium-ion transport and charge-transfer kinetics at the cathode Increased resistance to ion transfer in the cathode, caused by oxide surface film.	Temperature SOC
	Capacity Fade	0.338 %/day @ 55ºC [92] 0.064-0.194 %/day @ 55ºC [94] 0.027 %/day @ 45ºC [95] 0.049-0.112 %/day [90] 0.0-0.082 %/cycle [96]	Depletion of cyclable lithium and reduction in rate capability	Temperature Test Current SOC
Cycle-life	Power Fade	15.2% for 300,000 L-HPPC cycles[97] 51% for 1,140,000 25 Wh Power Assist cycles ([93] 8.2% at 125,000 25 Wh Power Assist cycles ([93] 0.041-0.092 %/cycle [98] 0.00051-0.0000478 %/cycle [99]	Increased resistance due to the build-up of the SEI with aging	Temperature Charging Rate Discharging Rate EOCV EODV SOC window
	Capacity Fade	0.0425 %/cycle @ 22ºC [92] L-HPPC (300,000 cycles)[97] -15.3 % @ 30 ºC -13.7 % @ 40 ºC -11.7 % @ 50 ºC 34% for 1,140,000 25 Wh Power Assist cycles [93] 3.8% at 125,000 25 Wh Power Assist cycles ([93] 20% for 500 cycles [90] 0.046-0.415 %/cycle @ 5-45ºC 0.032-0.056 %/cycle [98] 0.044-0.069 %/cycle [100] 0.024-0.048 %/cycle [96] 0.125 %/cycle [101]	Impedance build-up on electrodes	Temperature Charging Rate Discharging Rate EOCV EODV SOC window

There are significant challenges when interpreting the results of Table 5 and most degradation studies in general. The capacity fade measurements are dependent on the test current,

temperature, and definition of start and end point. Power fade measurements are also dependent on the test current, temperature, and the State Of Charge of the battery during the test. While these challenges limit the ability to derive quantifiable relationships between operational factors and degradation, qualitative relationships may be obtained. Key degradation variables include, state-of-charge, energy throughput, and pulse power levels [81]. To permit comparable results for automotive batteries, common test procedures have been developed for testing.

For automotive application, Reference Performance Tests (RPT) are a set of tests designed for battery characterization. Battery capacity is determined from a 1C discharge rate at 20°C between the manufacturer's defined SOC windows and the power fade can be calculated by the impedance during the Hybrid Pulse Power Characterization (HPPC) tests. HPPC test includes of a 10s 5C discharge, 40s hold, and a 10s 3.75C discharge, repeated at 10% SOC intervals except at 0 and 100% SOC. The SOC% increments are based upon BOL battery capacity. There exists low (L-HPPC) and medium (M-HPPC) variations that can be utilized to test performance of weaker hybrid powertrains. Christophersen; however, determined that RPTs contributed to battery degradation [93]. As the intent of the RPTs is to evaluate the state of the battery without significant altering the battery it is clearly undesirable to utilize RPTs that cause significant degradation. As a result the Minimum Pulse Power Characterization (MPPC) profile was developed, which consists of the same three components as the HPPC except it is only evaluated at SOCmax and SOCmin. SOCmax and SOCmin represent the extreme SOC values expected under normally operating conditions. A major difference between the MPPC and the HPPC is that as the battery ages the test points for MPPC are based upon voltage set points rather than BOL battery capacity. A summary of Christophersen's degradation results for various RPTs is provided in Figure 23.

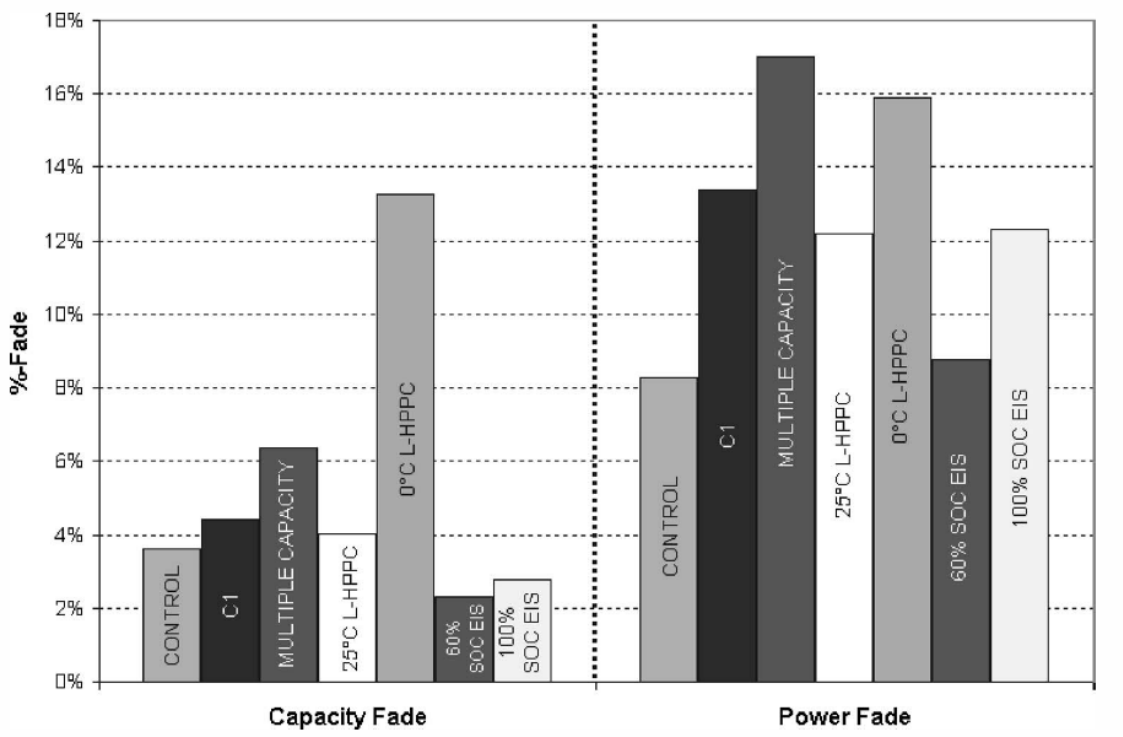

Figure 23 – Degradation caused by Reference Performance Tests (RPTs) [93]

The Technology Life Verification Test (TLVT) manual develops methods to predict a battery's 15 year lifetime based upon one to two years of accelerated testing [102]. Assessment of battery state and life requires accurate measurements. Christophersen has proven that battery resistance measurements are path dependent, showing different resistances between charge and discharge approaches to the test point and a heavy impact on charge rates [81]. Approaching the test point using discharge is recommended as the discharge measurements was found to be less rate dependent than approaching the test point by charging. Dubarry has also described the inherent inaccuracy of SOC measurements; defining commonly accepted battery SOC measurements as engineering-SOC (e-SOC) as opposed to the thermodynamic-SOC (t-SOC)that represents the actual state of the electrodes [103]. Dubarry suggests that thae current methods are insufficient and stresses the importance of developing e-SOCs that provide an accurate estimate of t-SOCs.

Three main results have been therefore introduced:

1. A significant number of degradation studies have been performed on lithium chemistries. These results have shown that capacity and power fade is affected by

temperature, SOC window, EOCV, EODV, charge current, and discharge current. A limited amount of testing has been performed using automotive test cycles.

2. Reference Performance Tests (RPTs) have been developed to allow for standardized evaluation of battery performance intended for automotive application. Unfortunately these tests have been found to cause significant degradation. Newer standardized performance tests are being developed that have less detrimental impact.
3. The tests have been found to be path dependent and are sensitive to SOC calculation errors (e-SOC approximation of t-SOC). Lifetime approximation methods are therefore limited by the accuracy of the measurements.

The results reflect the relatively nascent state of lithium-ion battery pack testing for hybrid powertrain applications. The results also support the need for advanced simulation tools that are flexible and that allow for the evaluation of SOC calculation errors and the impact of RPTs. These simulation tools must incorporate the factors that have been found to impact degradation rates. The current understanding of the impact of these operational factors and the degradation mechanisms must now be introduced. To allow for an understanding of the degradation mechanisms the structure of a lithium ion degradation models are presented at the beginning of Chapter 4.

The fuel cell and battery causal degradation models developed are integrated into an overall vehicle model. The vehicle model can then be utilized within a model-based design process to allow evaluation of powertrain sizing and control.

2.4 Model-Based Design

Accelerated development cycles and compliance with stringent regulatory requirements are driving the increased use of models during the design and realization process [15,104]. The ability to model and simulate hybrid powertrains allows for the determination of whether the system meets requirements using virtual rather than physical prototypes. In addition, the model based design processes enhance communication between design teams by promoting collaboration at all stages of the overall design process. Design models can be incrementally extended to include increasing implementation detail, including benchtop results and latency of real-time systems and control communication networks. Use of these virtual prototypes in the form of models permits the validation of multiple design alternatives, optimization of the

design, and identification & elimination of control logic errors prior to implementation. In addition, the newest model-based design tools can also generate prototype and production code from a model automatically, significantly decreasing development time generally required for embedded coding.

The use of accurate plant and control models allows for the evaluation and optimization of the powertrain with respect to design objectives. Hybrid powertrain designs include a number of additional degrees of freedom for the design, and as such, the use of model based design for these complex systems is required as the conventional build and trial approach would be cost prohibitive and time consuming.

The work described herein incorporates a design process based upon the model based design philosophy. The plant and control models are developed and evaluated in Matlab/Simulink, allowing for extensive simulation of vehicle performance. The benefits of model based design are extended to final application as a Motohawk ECU565-128 pin controller is used as the primary vehicle controller in the prototype fuel cell/battery hybrid vehicle. Motohawk is selected primarily for its ability to use auto-generated code created directly from a Simulink model, thereby allowing for a developed Simulink control algorithm to be compiled into machine code targeted for the controller. Thus the Motohawk controller is a new and innovative 'model-based design tool'. This project demonstrates the use of models incorporated from the initial powertrain design, to the control algorithm development, to final vehicle implementation of the hybrid powertrain.

The integration of causal degradation models for the battery and fuel cell systems allow for the evaluation of design decisions on vehicle lifetime performance. Specifically, the impact of component sizing and control strategy decisions can be evaluated. Using an optimization loop, the vehicle design can then be optimized to maximize overall lifetime performance. The structure of the modeling software and historic application of optimization of model-based design powertrains is described in the following sections.

2.4.1 Modeling Software Structure

Hauer generated a requirement list to be used to evaluate available software platforms for fuel cell vehicle simulation [105]. The primary requirement was that the software structure be a causal architecture, as a non-casual architecture was considered to lack physical or

mathematical soundness as it requires substantial overhead to ensure operation is not outside of physical limits. The non-causal architecture is often referred to as a "backward-facing" simulation approach due to the fact that the vehicle's wheel speed is set to be the desired speed and the powertrain operating points are determined in a backwards fashion. Correspondingly a causal vehicle architecture is often referred to as "forward-facing" as a desired speed is put through a driver model that determines a vehicle torque request, which is then passed through control algorithms to determine powertrain torque and power requests, which are then passed through component models. The forwards-facing approach allows for the integration of the driver and control strategies and has an inherently simpler structure for ensuring that components do not operate outside their feasible limits. In addition, the forward-facing approach allows for the evaluation of the capability of a vehicle to achieve a given drive cycle.

To ensure mathematical accuracy Hauer determined that the maximum simulation time step must not exceed $1/10^{th}$ the fastest time constant of interest [106,107,105]. Pukrushpan listed the time constants of the relevant phenomena within a fuel cell power module; determined which phenomena were fast enough to approximate using steady-state models and set his maximum simulation step to not exceed $1/10^{th}$ of the fastest phenomena that was not approximated by a state-state system [33].

Two main software packages developed for hybrid vehicle simulation are Advisor and Powertrain System Analysis Toolkit (PSAT) [108]. Both Advisor and PSAT are modular frameworks that include a number of hybrid architectures and component models. Advisor is an older software package that is non-causal, or backward-facing as previously discussed. This approach does not include transient behaviour of the powertrain components and does not facilitate control strategy development. PSAT is a forward-looking model that includes a driver model which attempts to achieve the required duty cycle via the throttle and brake pedal signals. As discussed, this forward-looking approach incorporates transient behaviour and promotes hybrid control strategy development. AVL CRUISE is an alternative software package that is similar in structure to PSAT. PSAT is the package used for this work, selected due to its extensive component library and fuel cell hybrid topologies.

While PSAT provides the ability to model performance over various duty cycles and control strategies there are some major limitations in the existing models. Some of the specific limitations include:

- No evaluation of some physical phenomena such as voltage dynamics,
- Over simplified fuel cell component model with only a look-up table relating hydrogen consumption for an older fuel cell stack to power (quasi steady state),
- Only beginning-of-life performance. No inclusion of degradation and ageing effects,
- Over simplified DC/DC converter with no dynamics and a fixed efficiency, and
- Only available control strategy for the series fuel cell topology is a simple rule-based strategy.

While PSAT provides an initial series fuel cell vehicle model, there exist significant limitations of the model to accurately represent the performance of fuel cell vehicles, especially over the lifetime of the vehicle. Improving the accuracy and extending the software to model lifetime performance is performed herein.

2.4.2 Hybrid Fuel Cell Vehicle Models

A variety of hybrid fuel cell vehicle models have been previously developed. The previous models can be categorized into either an aggregate of general component models for general evaluation or models developed to simulation a specific prototype hybrid fuel cell vehicle.

One of the first generic hybrid fuel cell vehicle models was developed, and later improved, by Boettner [69-71]. The control of the system was then extended by Pukrushpan for a similar vehicle architecture [33]. Both of Pukrushpan and Boettner's models utilized on-board reformers for creating hydrogen. A significant portion of foci were on the development and optimization of the control of the reformer. On-board reforming has been generally rejected as a candidate for current hybrid fuel cell powertrains; therefore these models represent a baseline for hybrid fuel cell vehicle modeling but are of limited utility. A non-reformer hybrid fuel cell vehicle models have also been developed and evaluated in ADVISOR in separate studies by Gao and Burke comparing the use of batteries and utracapacitors as the energy storage [20,22]. Due to the limitations of backward-facing simulations as previously described, Hauer developed a generic hybrid fuel cell vehicle model for non-reformer and reformer vehicles named FCV-Sim [106,107]. Later variations of Hauer's models focused on the non-reformed architectures were developed by Moore [109-111]. An ADVISOR based fuel cell model was developed by Maxoulis that investigated the impact of fuel cell design parameters on vehicle performance for a variety of driving cycles [56].

Within the PSAT framework one of the initial models was developed by Ahluwalia [34]. Ahluwalia developed initial sizing heuristics and evaluated an initial hybrid control strategy based upon a tiered SOC management algorithm. For Ahluwalia's models the time constant of the fuel cell power module was declared to be <1s for a 10-90% step in rated power output. Energy storage requirements were investigated by Rousseau using a PSAT-GCTool hybrid fuel cell vehicle model, determining that energy storage sizing should be based upon regenerative braking and fuel cell efficiency curve considerations [112].

These generic models provide valuable insights into general behavior and performance of these vehicles. Due to their generic nature they do not allow for model validation and are therefore incapable of ensuring model accuracy. The models developed to simulate a specific prototype vehicle can be validated to actual vehicle performance, thereby allowing for greater confidence in the accuracy of these complex system models.

One of the first hybrid fuel cell passenger vehicle models intended to represent an actual vehicle prototype was published by Ogburn [113]. The model was based upon Virginia Tech's submission into the Department of Energy's (DoE) FutureCar Challenge and was developed upon the ADVISOR software platform. The model was improved and validated using dynamometer testing of the vehicle. This ADVISOR model was later extended to a Sport-Utility-Vehicle (SUV) by Gurski for a subsequent phase of the DoE competition [39]. Although modeled in ADVISOR, and therefore subject to the inaccuracies of backward-facing simulation, these models provide a value baseline for the work performed. An additional model developed for a prototype hybrid fuel cell vehicle was described by Schell to simulate DaimlerChrysler's Natrium concept car using sodium borohydride hydrogen storage [45].

Extending the scope to heavy-duty passenger vehicles, a number of models have been developed and validated for hybrid fuel cell buses in separate papers by Jia, Ouyang, and Kim [24,42,114]. In particular, Ouyang's paper describes in detail the real-world performance of two buses with different powertrain topologies and control strategies.

Clearly, a number of hybrid fuel cell vehicle models have been developed in both causal (forward-facing) and non-causal (backward-facing) software structures. A small number of these models have been validated to real-world performance. With the exception of an anecdotal evaluation of fuel cell degradation by Ouyang, none of the papers have discussed

component degradation. None of the papers have included degradation models or considered charge-depleting operation.

2.4.3 Design Optimization

The use of a model-based design structure allows for the integration of an optimization algorithm to maximize vehicle performance by varying design parameters. This methodology was originally discussed for hybrid vehicle architectures by Assinis and Fellini [115,116]. Fellini optimized the component sizing for a series hybrid powertrain, namely the engine, motor, and battery rated power. The problem formulation was to maximize fuel economy subject to minimum performance constraints. Fellini combined combining ADVISOR and Turbocharged Diesel Engine Simulation (TDES) software and considered five optimization algorithms: Sequential Quadratic Programming (SQP), trajectory, complex, DIvided RECTangles (DIRECT), and Sequential Metamodel Optimization (SMO). Due to the noisy nature of the hybrid vehicle simulation results, the derivate-based optimization algorithms (SQP and trajectory) were eliminated from consideration. DIRECT and Complex algorithms resulted in nearly identical solutions, corresponding to 48.54 and 48.52 mpg respectively. The DIRECT algorithms was found to be more efficiency as the Complex algorithm required multiple restarts after the solution became stuck in an infeasible region.

Fellini's work was extended by Assanis, who utilized a gradient-based Sequential Quadratic Programming (SQP) optimization algorithm with the same ADVISOR/TDES combination to determine motor, engine, and battery size [115]. Assinis performed the optimization for two separate optimization objectives, the first optimization maximized fuel economy given minimum acceleration requirements and the second optimization maximized acceleration given a minimum mileage requirement. Assinis performed the optimization for a variety of starting points determined using a Design Of Experiment (DOE) methodology and observed that the gradient-based nature of the SQP algorithm resulted in many optimizations being caught in local minima. Assinis identified that the work was preliminary, as thorough optimizations would have to consider control parameters and emissions in the optimization.

Simultaneous optimization of both sizing and control parameters was first presented by Wipke, varying four sizing variables and four energy management variables for a hybrid fuel cell vehicle [117]. Gradient and non-gradient optimization routines were compared, all integrated with a base ADVISOR vehicle model. The designs were also simulated over various drive cycles to

evaluate the sensitivity of the design to duty cycles. Similar to Assinis and Fellini, Wipke found that the gradient based routines were often caught in locally optimal solutions whereas globally optimal solutions were found by the slower non-gradient routines such as DIRECT. Wipke also found that the design was highly sensitive to the drive cycle used for evaluation.

In 2005, the optimization schemes employed Assinis, Fellini, and Wipke were integrated into a PSAT framework by Gao [118]. Gao evaluated DIRECT, Genetic Algorithm (GA), and Simulated Annealing (SA) algorithms for optimizing a parallel hybrid architecture. The Simulated Annealing algorithm is based upon the Metropolis probability criterion which can select less optimal points depending on the following equation:

$$P(f,T) = e^{\left[\frac{f_{new}-f_{current}}{T}\right]} \quad (24)$$

Similar to Wipke, the objective was to optimize fuel economy, given minimum acceleration, by varying sizing and control parameters. An additional Hybrid optimization algorithm was developed that utilized a non-gradient solver initially which converted to a gradient based solver to accelerate the solution once a near-optimal region was found. SA and DIRECT performed well, while the Hybrid algorithm was the fastest.

Fuel cell power module design parameters were optimized by Han using a similar approach by combining a detailed fuel cell model with a vehicle model derived from mainly ADVISOR component models [119]. Bauman evaluated fuel cell-battery, fuel cell-ultracapacitor, and fuel cell-battery-ultracapacitor combinations by utilizing a discrete step optimization algorithm with a simplified vehicle model [25]. An overall review of optimization methods for vehicle design was published by Gobbi [120].

A number of studies have developed and evaluated optimization techniques for sizing and controls of hybrid vehicles, which have identified noise-tolerant methods are required. A subset of these studies have included hybrid fuel cell architectures. No studies to date have included considerations of performance over the lifetime of the vehicle.

Chapter 3

Baseline Hybrid Fuel Cell Vehicle

This chapter presents the design of a baseline hybrid fuel cell power train, including both component sizing and control, which used an innovative model based design strategy. The powertrain is then built and subjected to dynamometer testing. The initial vehicle models used in the design phase are revised using two sets of dynamometer testing data to validate the model. The improved vehicle model is then validated using a different set of dynamometer data. Finally, different control strategies are evaluated using the validated vehicle model.

3.1 Model-Based Design without Degradation Considerations

The precursor to model-based design considering component degradation is model-based design without considering degradation. As discussed in the literature review, there were not any hybrid fuel cell vehicle models or datasets that had been sufficiently validated and used current technology. To develop a validated hybrid fuel cell vehicle model with current technology a model-based design process was developed and employed for the powertrain design of a Sport Utility Vehicle (SUV) using the best available models. The vehicle design that was nearest the optimal design values using procurable components was built and used to improve and develop a validated baseline hybrid fuel cell vehicle model. Note, at the time of development of the vehicle there were not 'available' fuel cell stack (either commercially available or available to research institutions in general), and construction of a stack in this power range was definitely beyond the capability of any academic institution; as such any availability of the fuel cell components in this power range in general was extremely unique.

This section summarizes the work performed to map the design space to allow a structure for decision processes to understand the trade-offs between various powertrain design decisions and their impact on performance metrics such as acceleration and mileage. The results of the

simulations were then used to generate equations relating vehicle performance to powertrain design decisions. The developed model then provided the primary powertrain model with which controls and degradation models were then based.

3.1.1 Evaluation of Storage Technology and Component Sizing

For an accurate comparison of architectures, optimal designs for each architecture scenario must be obtained for a common platform. This results in a modeling dilemma between individual architecture optimality and common platform variability. An example is the decision to consider two-wheel or four-wheel drive selection. For instance, the packaging and integration of multiple electric motors to power a vehicle is fairly practical or often preferred for efficiency and packaging reasons. Contrarily, the use of two or four combustion engines on a vehicle is impractical. The decision is whether to maintain a common two-wheel or four-wheel drive architecture, or to allow for the architecture analysis process to select the optimal configuration. For this study, two-wheel vehicle configurations are assumed for all powertrains using the 2005 Chevrolet Equinox platform for vehicle dynamics. Battery and ultracapacitor systems are evaluated. The four types of hybrid configurations considered are parallel, series, parallel-series, and split. The split configuration is a slight modification of series-parallel configuration. A rule-based control logic was used for all work.

Over 400 hundred simulations have been performed to understand the impact of various hybrid architectures and sizing. The process utilized a model initially generated from Powertrain Simulation and Analysis Toolkit (PSAT) and which has been heavily modified to reflect actual components available. The development and selection of the initial models is not presented herein due to the preliminary nature of those models.

From a preliminary Design of Experiment (DOE) series of simulations the optimal parallel hybrid configuration exhibited the best performance metrics for ICE hybrid powertrains. Based upon these results, the second design of experiment study was developed to focus the models on the optimal regions for design sizing selections within the design space as identified in the initial study. The factors and levels evaluated are summarized in Table 6. The engine and fuel cell powers represent the peak net output power values for the respective technology. The maximum motor efficiency was used in combination with PSAT's motor scaling algorithm that multiples the entire efficiency map by the ratio of the new maximum efficiency values to the original efficiency value. Motor gearing was not considered in this study but was later found to

be a significant variable tied to the usefulness of the motor power rating. For simplicity the ESS cell count was maintain the number parallel strings required for the lowest cell count. For instance, the series fuel cell with nickel metal hydride simulations included two parallel strings with all incremental cell counts added in series. As PSAT models the connections as power buses rather than voltage buses the simulation could complete despite impractically high voltages present at higher cell counts. The result is an overestimation of voltage losses for high cell counts as the current would be divided among a larger number of parallel strings; however, as the ESS losses did not represent a significant portion of the overall energy consumption this simplification had minimal impact and allowed for simpler simulation setup. As the cell count increased the effective voltage of the pack increased the amount of power delivered at the maximum current value increased. In addition, the current required for a given amount of power delivered decreased, increasing the useable energy of the pack. Refined simulations would include a consideration of real-world voltage limits in selecting the series-parallel combination for each cell count.

The results of the simulations were utilized to generate parametric equations describing vehicle performance metrics as a function of the factors listed in Table 6. A plot representing one of the developed models is provided as Figure 24. The figure illustrates the parabolic behaviour of the mileage around the optimal design point.

Table 6 - Design of Experiment Factors and Levels for Hybrid Powertrain Sizing Study

Vehicle Type	Engine/ Fuel Cell Power (kW)	Motor Power (kW)	Scaled Maximum Motor Efficiency (0,1)	Number of ESS Cells
Series Fuel Cell Hybrid with Ultracapacitor Pack (FC_UC)	25.0	60.0	0.950	120
	34.1	73.2	0.960	168
	47.5	92.5	0.970	240
	60.9	111.8	0.990	312
	70.0	125.0	1.000	360
Series Fuel Cell Hybrid with Nickel Metal Hydride Battery Pack (FC_NiMH)	10.0	60.0	0.950	200
	20.0	75.0	0.963	255
	30.0	90.0	0.975	310
	40.0	105.0	0.988	365
	50.0	120.0	1.000	420
Series Fuel Cell Hybrid with Lithium Ion Battery Pack (FC_LI)	10.0	60.0	0.950	240
	20.0	75.0	0.963	311
	30.0	90.0	0.975	383
	40.0	105.0	0.988	454
	50.0	120.0	1.000	525
ICE Diesel Parallel Hybrid with Nickel Metal Hydride Battery Pack (ICE_NiMH)	45.0	52.2	0.950	168
	52.2	57.5	0.963	265
	57.5	62.8	0.975	336
	62.8	68.1	0.988	407
	70.0	70.0	1.000	504

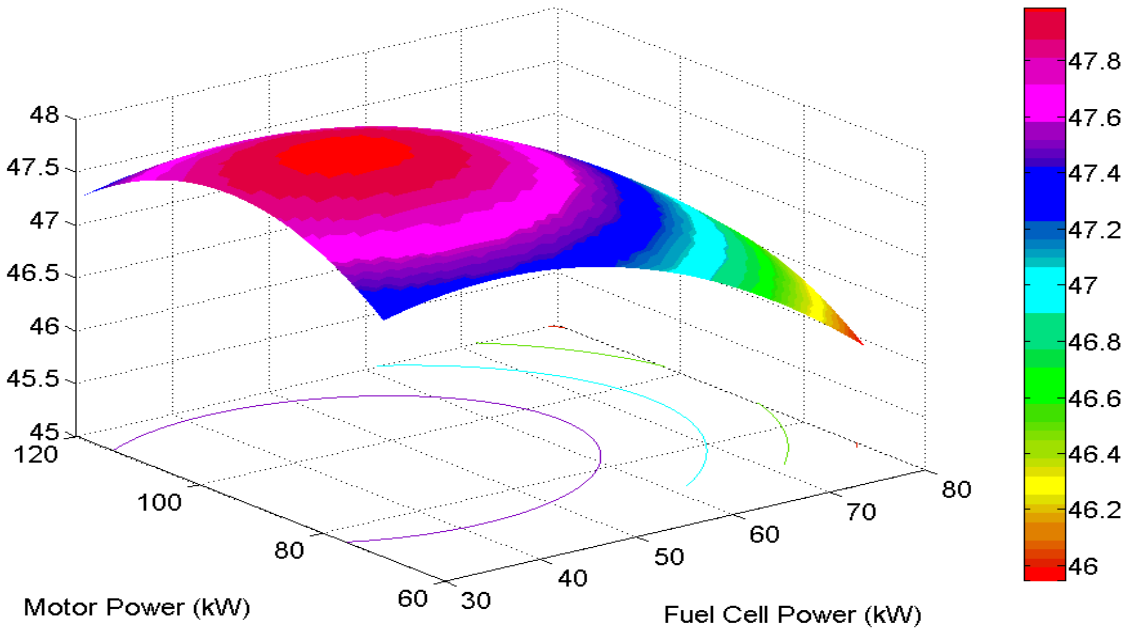

Figure 24 - Vehicle Mileage As A Function of Motor and Fuel Cell Power (kW)

The developed equations were incorporated into a non-linear optimization based on a balance of vehicle acceleration, mileage, and mass. The results of the optimization with the associated performance metrics are provided in Table 7. The noted mileages were not accurate to the final vehicle models as parasitic power losses within the powertrain were not accurate (i.e. there was little date data available to represent these loses). Specifically, the parasitic power draws were significantly undersized, being a fixed 800W draw as compared to the ~4,000W required in an actual fuel cell vehicle as determined during the build phase. The effect of additional parasitic load is presumed to be similar for all fuel cell powertrains considered and therefore the resulting offset is relatively similar for those three powertrains under review. The anticipated parasitic draws for the ICE-based powertrain are significantly less than those for the fuel cell powertrain; however, given the large difference in fuel efficiency the lower parasitic loads for the ICE derivation would not alter the overall conclusion.

Table 7 - Powertrain Optimal Sizing and Effective Performance Metrics

	Parameter	Fuel Cell Ultracapacitor	Fuel Cell Nickel Metal Hydride	Fuel Cell Lithium Ion	Biodiesel ICE Nickel Metal Hydride
Inputs	Engine/Fuel Cell Power (kW)	46.0	32.5	63.0	70.0
	Motor Power (kW)	86.6	93.4	116.0	58.0
	Peak Motor Efficiency (%)	98.0	98.0	98.0	98.0
	Number of ESS Cells	240	240	320	346
Outputs	IVM-60 mph (s)	7.6	9.0	8.7	12.1
	50-70 mph (s)	5.4	5.1	4.9	11.8
	Combined Energy Use (Wh)	10881	8994	9446	19850
	Mileage (mpge)	55.2	66.3	60	29.8
	Fuel Cell/Engine Efficiency	50.2	51.9	51.2	37.4
	Motor Efficiency (%)	84.6	88.0	85.9	72.2
	Mass (kg)	1952.1	1978.7	1861.6	2253.5

A fuel cell/NiMH hybrid vehicle was selected based upon available components and the optimization presented above. The component selection was performed by selecting the fuel cell power rating as close to the 32.5kW optimal value as possible given available fuel cells. It is important to note that the analysis did not include considerations for towing and driving over extended grades, as both require a larger primary power rating or a larger capacity energy storage system. As only 10kW, 20kW, and 65kW power modules were available, the 65kW Hydrogenics fuel cell power module was selected. The optimization was rerun with the fuel cell power set to 65kW. The resulting optimization identified an optimal NiMH power rating of ~65kW and since 60kW and 70kW Cobasys battery packs were available the 70 kW battery pack

was selected. The 70kW pack was later replaced with the 60kW pack due to voltage limit issues as a result of a narrower motor input voltage limit than originally anticipated. The motor power requirement was achieved by selected two identical Ballard 67kW peak traction motors, one motor per axle. These motors were available and within the budget for the actual vehicle construction. A custom design and built boost DC/DC converter by UWAFT's electrical team was designed and built to control the fuel cell power and boost the voltage. A simplified schematic of the powertrain is provided as Figure 25.

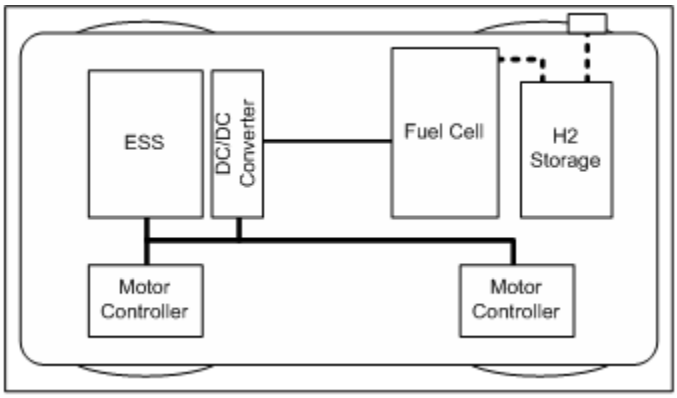

Figure 25- Schematic of Fuel Cell/Battery Hybrid Powertrain

These simulation results provide significant insight into the fuel cell vehicle performance as a function of storage technology and component size. The results also suggest a significant fuel efficiency advantage of the fuel cell based powertrains as compared to the ICE based powertrains. It is important to note that in a head-to-head competition of this hybrid fuel cell vehicle against hybrid ICE vehicles did not demonstrate this result. A significant reason for this variation was that the actual performance of the hybrid fuel cell vehicle did not achieve the performance values obtained through simulation. Performance of the actual vehicle is described in detail in section 3.3.

At this time in the model based design process this evaluation lacked co-optimization of control strategy. As a rule-based control strategy is used for all configurations, the results are not fully optimized as there is an interaction between powertrain sizing ratios and control. Certain control strategies exhibit improved performance for certain secondary/primary power source fractions. These control strategies are discussed further in the following section.

3.1.2 Hybrid Control Strategy Development and Optimization

As described in the background, the objective of the hybrid control strategy (HCS) is to split power demand between the fuel cell and the battery pack in a fashion that maximizes fuel economy and vehicle performance, while minimizing hydrogen purging. The HCS achieves this objective by:

- Maximizing powertrain component efficiency,
- Targeting a SOC set point for the battery, and
- Maximizing system reliability and durability by limiting start/stop cycles, and maintaining SOC in a limited range, and controlling torque.

Five supervisory control strategies have been evaluated based upon the hybrid fuel cell vehicle described above. These strategies are separated into two categories: the first three are feed-forward and combined feed-forward/feed-back calculating while the last two are of unique to vehicle design 'cost function' based control types. The control strategies are labeled A to F and are described in the following section.

3.1.2.1 Simple Hybrid Control

The first three control strategies were considered first due to their simplicity of design and implementation. The forward calculating strategies utilize a single line calculation to determine the power split based upon current operating conditions. The slightly more complicated cost function based strategies calculate a "cost term" for an array of power splits and selects the split with the lowest associated cost.

A *– Open Loop Model Predictive Load Following Control*

The objective is to use a model predictive control approach to calculate the required fuel cell power demand to provide all the power requested by the driver. Specifically, the required electrical power for the motor is calculated using driver torque demand, vehicle speed, and the appropriate gear ratios. The required electrical power from the fuel cell is then calculated based upon assumed:

- Energy pathways (described in detail in cost based control strategy section),
- Component efficiencies, and
- Regenerative braking capabilities.

The battery pack compensates for deviations between the actual power demand and the power provided by the fuel cell. These deviations are a function of both the transient response of the fuel cell and errors in the assumptions. This control strategy demonstrated that the vehicle could not operate on the road with driver interface as the control system does not compensate for errors resulting in unsafe battery states.

B *– Closed Loop Model Predictive Load Following Control*

Same approach as control strategy A, with the exception that a SOC feedback loop is added. The fuel cell power determined from strategy A is adjusted based upon the deviation between actual SOC and target SOC.

$$P_{FC\_dmd\_adjust} = \frac{(SOC_{actual} - SOC_{target}) * E_{battery\_capacity}}{t_{int}} \quad (25)$$

t_{int} is a tuning variable which denotes the time required at the calculated power adjustment to achieve the target SOC. The lower the value of t_{int} represents a more aggressive SOC correction.

C *– Rule based control (also known as Thermostat control)*

This strategy is a default control strategy in PSAT. The strategy is primarily rule based in that, as long as the SOC is within an acceptable range, the fuel cell will only operate if the power from the battery pack is insufficient to meet the demand from the motors or if the fuel cell can operate at optimal efficiency. The result is that the battery pack is used for the majority of the power until SOC decreases to a lower limit, and then the fuel cell operates at a high efficiency point to charge the battery pack up to a high SOC level. Note that this strategy results in significant degradation of the battery pack due to wide SOC swings.

3.1.2.2 Cost Based Control Strategy

The two cost based control strategies are very similar and therefore the cost based approach developed below is common to both strategies. The approach used to consider the three objectives simultaneously is a modified version of a control concept published by Johnson and discussed in the background section for parallel combustion hybrid vehicles [50]. The method incorporates a cost function that sums associated “costs” for the three objectives and selects the power split with the lowest overall cost. A schematic representation of the HCS is provided as Figure 26. Due to computational limitations imposed by real-time implementation on a

vehicle controller, it is computationally prohibitive to solve the cost function for the optimal value. A viable approach that was adopted is to calculate the costs for ten power split values within the feasible range and select the split with the lowest cost.

The first cost based control strategy includes two terms, while a third term is included in the second cost function based strategy. The equations for each term in the cost function are described in detail later. The intent is to integrate a maximization of powertrain efficiency, minimization of component degradation, and targeting of SOC within one equation. The first term assigns a lower cost for higher instantaneous powertrain efficiency. The second term assigns lower costs for power splits that result in SOC values closer to the target value, and the last term assigns lower costs to infrequent fuel cell start-stop toggling.

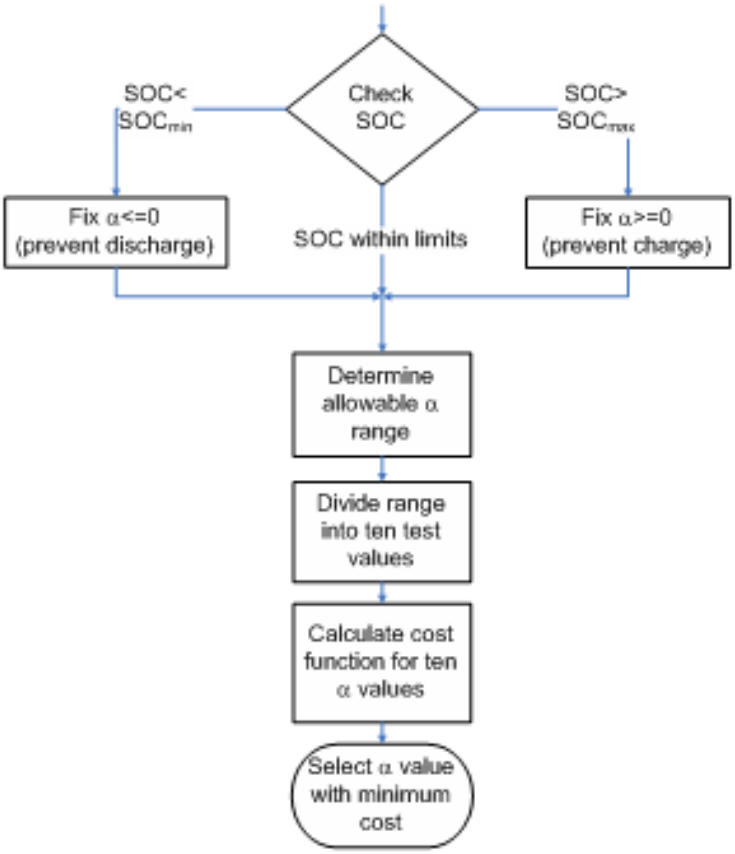

Figure 26 - Hybrid Control Strategy Schematic for Cost Based Function

The cost function for the optimization is defined as:

$$Cost = \frac{\beta_1}{\gamma_1} Eff(\alpha) + \frac{\beta_2}{\gamma_2} SOC(\alpha) + \frac{\beta_3}{\gamma_3} FCsw(\alpha) \tag{26}$$

Symbols β_i and γ_i correspond to the weighting and normalization values respectively for each objective. The γ_i value represents the largest value for cost i for the ten α values. The objective of the γ_i is to normalize all costs to a 0 to 1 scale, thereby compensating for order of magnitude differences between individual costs. The β_i values represent the weightings of the various cost terms. For initial development all β_i were set to one. The intent is that β_i be dynamic in order to be able to adapt the control strategy simply over the life of the vehicle and for different drive types. For instance, β_3 could be increased as the vehicle ages to improve reliability and durability as the power module becomes more sensitive to state cycling. In addition, β_2 could be increased in a trailer towing mode to increase the importance of having sufficient energy stored in the battery pack to overcome sustained power demands. The objective of the cost function is to provide a mathematical formulation that provides flexibility while seeking high powertrain efficiency, a relatively consistent battery pack SOC, with minimal fuel cell switching.

The cost function is written as a function of α, which corresponds to the power split provided by the battery as defined by:

$$\alpha = \frac{P_{Batt}}{P_{Motor,Elec}} \quad ; \quad (1-\alpha) = \frac{P_{FC}}{P_{Motor,Elec}} \tag{27}$$

The values of α can be positive or negative. Negative α designates states where the battery pack is being charged by the fuel cell. α=0 is the case where all power is provided by the fuel cell, while α=1 denotes cases where all power is provided by the battery pack. Values between 0 and 1 denote cases where the power is provided from both the battery pack and the fuel cell. The limits on α are as follows:

$$\alpha_{\min} = \max\left(\frac{P_{Motor,Elec} - P_{FC\_Max\_Avail}}{P_{Motor,Elec}}, \frac{-P_{BattChg\_Max\_Avail}}{P_{Motor,Elec}}\right) \tag{28}$$

$$\alpha_{\max} = \min\left(\frac{P_{BattDsc\_Max\_Avail}}{P_{Motor,Elec}}, 1\right) \tag{29}$$

The minimum α value is limited by the maximum of:

- Power the fuel cell can provide in addition to the power demand by the motor, and
- Power the battery pack can accept for charging.

The maximum α value is limited by the minimum of:

- Power the battery pack can deliver during discharge, and
- One (1), i.e. since the fuel cell cannot accept power, the battery pack can't delivery more power than the motor(s) require.

For the efficiency term, the two energy pathways must be considered: either energy from the fuel cell is conditioned by the DC/DC converter and is delivered directly to the motor, or the conditioned energy charges the battery pack and is delivered to the motor during battery discharge at a later time. There are two cases for the efficiency function:

Case 1: $\alpha \geq 0$ (All Battery if $\alpha=1$, power splitting if $0<\alpha<1$)

$$Eff(\alpha) = -(\frac{P_{Motor,Elec}}{P_{FC}})\varepsilon_{FC}\varepsilon_{PC} - (\frac{P_{Batt}}{P_{FC}})\bar{\varepsilon}_{FC}\bar{\varepsilon}_{PC}\varepsilon_{BC}\bar{\varepsilon}_{BD} \quad (30)$$

Case 2: $\alpha \leq 0$ (All Fuel Cell if $\alpha=0$, regen if $\alpha<0$)

$$Eff(\alpha) = -(\frac{P_{Motor,Elec}}{P_{FC}})\varepsilon_{FC}\varepsilon_{PC} - (\frac{P_{Batt}}{P_{FC}})\bar{\varepsilon}_{FC}\bar{\varepsilon}_{PC}\varepsilon_{BC}\bar{\varepsilon}_{BD} \quad (31)$$

The symbol ε_i denotes the instantaneous efficiency of the component/function i, and $\bar{\varepsilon}_i$ denotes time averaged efficiency for the component/function i. The efficiencies are obtained from lookup tables corresponding P_{FC} and P_{Batt} to the component efficiency specific to the component implemented on the vehicle platform. The SOC targeting term is calculated as:

$$SOC(\alpha) = abs(SOC_{after\_proposed\_alpha\_used} - SOC_{target}) \quad (32)$$

A possible extension would be to have the SOC target value vary as a function of vehicle speed. The intent would be to lower the SOC target when traveling at high speeds to prepare for the large amount of regenerative braking energy, and to have a higher SOC at low speeds to prepare for the significant amount of energy required for a potential acceleration. When considering a variable SOC target the time and energy required for a given chance in SOC must be considered. The Cobasys pack evaluated as part of this work had an 8.5Ah rating, meaning a 10% SOC swing

represents approximately 0.85Ah or 3060As. Under an acceleration condition requiring 50kW of battery power the current draw would be in the range of 250A. A 250A discharge sustained for ~ 12s would represent a 10% change in SOC and would approximately represent a full acceleration from initial vehicle movement to highway cruising speeds. The SOC target could also be varied as a function of the current acceleration or deceleration of the vehicle; however, the order of magnitude analysis demonstrates that the SOC only varies significantly (10%) for full accelerations or decelerations.

In the initial work the component degradation term was represented by a FC switching cost term. In Chapter 4 battery degradation will be investigated in addition to a refinement of the fuel cell degradation model based upon current data. The rationality for using the fuel cell switching as the driver for degradation is due to the mechanical and hydration stresses on the membrane caused by the large transients during start-up and shut-down. To be specific, it was assumed that the thermal and hydration expansion of the membrane during start-up and shut-down of the stack was the critical factor leading to membrane and fuel cell stack failure [80]. The initial fuel cell degradation as a function of fuel cell switching is calculated as:

$$FCsw(\alpha) = \exp(-fcstate\_duration) * fc\_switch \quad (33)$$

The variable 'fcstate_duration' represents the time spent in the current fuel cell state (standby/on). 'fc_switch' is a binary variable that is equal to 0 if the state was not changed and is equal to 1 if the fuel cell state is changed. This was the initial form of interpreting degradation into the control logic. While other control strategies have included "minimum time on" constraints to eliminate excessive fuel cell state switching, this strategy permits the evaluation of the impact of switching in balance with SOC targeting and instantaneous efficiency simultaneously.

The cost function is solved in real-time for multiple α values within the limits, and the α value that provides the lowest cost function is chosen. In addition to a target SOC, there are also SOC operating limits. Prior to considering the cost function the current SOC of the battery is considered. If the SOC exceeds the SOC_{max} limit, α is constrained to be greater than 0 so that regenerative braking is prevented as this would cause battery damage and could be a safety risk. If the SOC is lower than the SOC_{min} limit, α is constrained to be lower than 0 so that battery discharge is prevented, which would also cause battery damage.

As alluded to previously, a secondary drive mode could be added to improve towing performance, which is a 'customer' requirement for a sport utility platform. The trailer towing mode will use the normal mode of operation with two modifications: the SOC_target is increased, and the weighting for the SOC(α) term (β_2) is also increased. This will result in increased demand from the fuel cell power module. These modifications allow for an elegant approach that uses a common platform for both modes of operation, while accommodating for the high energy requirements of the trailer towing event. This mode would be initiated by a driver input via a tow-mode request button. Note that this overall control strategy could also be customized for other potential customer operational modes, for example: high performance mode, parental control for limited powers and speeds, or urban short range operation. These extensions are introduced to highlight the flexibility of both the algorithm and the model-based design process; however, it should be noted that these additional operating modes are outside the scope of this thesis and therefore not discussed further herein.

In the Johnson paper from which basic concept for this approach has been originated, the intent was to balance the energy consumption and the vehicle emissions. However, with respect to the hybrid fuel cell vehicle utilized in this work, the only expected volatile emission from the vehicle is a small amount of hydrogen purged when the fuel cell state is switched from the Standby to Run mode, which is a limitation of the specific power module technology. The HCS addresses emission reduction by including the fuel cell switching term in the costing function thereby reducing the Standby to On toggling. No other emissions are anticipated during normal operation except simple water vapour. The HCS ensures safe operation within component limitations, while optimizing for the powertrain efficiency, SOC targeting, and fuel cell state switching.

D *– Cost Based Control without Degradation*

The first cost based control strategy includes the powertrain efficiency and SOC targeting terms, but omits the state switching cost term described above. The resulting cost equation is:

$$Cost = \frac{\beta_1}{\gamma_1} Eff(\alpha) + \frac{\beta_2}{\gamma_2} SOC(\alpha) \tag{34}$$

E – Cost Based Control with Degradation Proof-of-Concept

This strategy incorporates all three cost terms described in Equation 26. The benefits of the state switching term were not expected to be observable in the PSAT results, as start-of-life performance is simulated and hydrogen purging is not included. The intent is to quantify the decrease in start-of-life performance due to the state switching term. The inclusion of the degradation term further constrains the operating range within which the control strategy is optimizing across. As such, a reduction in initial vehicle performance is to be expected. The overall intent is that the benefits of improved end-of-line performance far exceed any minor reductions in beginning-of-life performance.

The simulation results are summarized in Table 8. The fuel cell efficiency represents the ratio of net module energy output divided by chemical energy input in the form of hydrogen. DC/DC efficiency represents the sum of the product of the DC/DC output current and voltage divided by the sum of the product of the DC/DC input voltage and current over the course of the drive cycle. The battery pack efficiency is defined as the sum of product of the battery output voltage and current divided by the change in chemical potential of the battery as calculated from the chance in SOC. Similar to control strategy A, the benefit of control strategy B is the inherent simplicity. As opposed to strategy A, this approach does include SOC correction and therefore is significantly more practical in real-world application. The strategy, however, does not consider efficiencies or fuel cell state switching, both of which are significant to overall performance. In all five cases the battery and fuel cell operated at maximum output powers during the Wide-Open-Throttle acceleration resulting in the same acceleration performance.

Table 8- Vehicle Performance Results for Five Hybrid Control Strategies for the TripEPA Combined Drive Cycle and Acceleration Time for a Wide-Open-Throttle (WOT) Acceleration

Performance Metric	Control Strategy				
	A	B	C	D	E
Fuel Cell Efficiency (%)	48.2	47.0	47.6	54.1	52.7
DC/DC Efficiency (%)	90.3	90.4	88.3	90.4	90.4
Battery Pack Efficiency (%)	96.8	97.0	60.3	94.8	93.9
Vehicle Mileage (mpge)	52.2	50.4	45.9	57.0	55.5
0-60mph Acceleration Time (s)	8.0	8.0	8.0	8.0	8.0

Control strategy C is relatively simple and ensures fuel cell operation is near optimal efficiency. However, the strategy causes the vast majority of the energy to pass through the battery pack, introducing significant charging and discharging losses, and large SOC swings. Large SOC swings on the battery pack also accelerate battery pack degradation and cause the battery pack to operate in lower efficiency regions. The battery pack SOC and efficiencies for control strategies A, B, and C are provided as Figures 23 and 24 respectively. Control strategy A's lack of SOC targeting is evident in Figure 23 as the SOC gradually increases throughout the simulation. Control strategy B's SOC remains near 0.6 while Control strategy C's SOC oscillates between 0.5 and 0.7. The impact of the oscillations and heavy power draw from the battery pack is evident in Figure 24 as the battery pack efficiency for control strategy C is significantly less than the efficiencies for strategies A and B. This lower battery pack efficiency average of 60.3% is the major factor resulting fuel economy being 45.9 miles per gallon equivalent, significantly lower than the other strategies. The higher fuel cell efficiency sought by control strategy C was significantly outweighed by the lowered battery pack efficiency. Evidently, an efficiency focused algorithm must include all the powertrain components.

The cost function in control strategies D and E consider all powertrain components. The impact of the system efficiency approach as compared to the individual component is evident in the 11 mpge difference in the mileage between control strategies C and D. The major improvement of

the cost based functions (D and E) is the significant increase in fuel cell average efficiency. The reduction in performance in the introduction of the state switching term in control strategy E had a minimal impact of approximately 1.5 mpge.

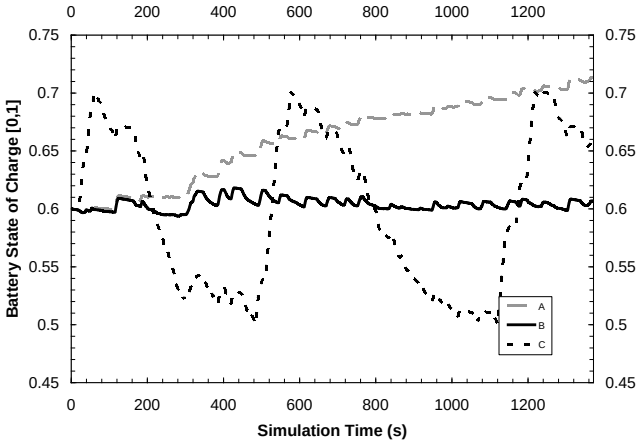

Figure 27- Battery State of Charge for Strategies A, B, and C

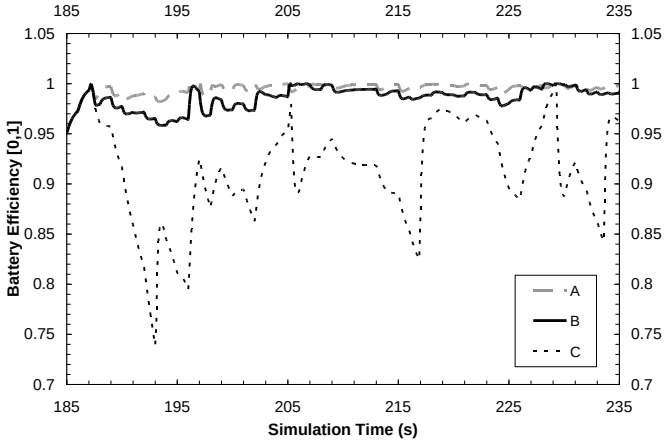

Figure 28 - Battery Efficiencies for Strategies A, B, and C

Although there is a slight decrease in beginning of life efficiency in the use of the state switching term in the cost function, the intent is to contribute to sustained performance over the lifetime of the vehicle. As shown in Figure 11, hybridization allows for the use of significantly different component duty cycles in order to provide the same overall power duty cycle. The significant impact of the hybrid control strategy on the duty cycle of individual components is demonstrated by the component metric comparison provided in Table 9. All power values provided represent net output power for the respective component. The additional use of the secondary power source in the rule based control strategy is evident in the 10,541W average

power draw compared to the 4,502W value for the cost function strategy and the state of charge swings between both control strategies. The cost function however exhibits higher average power draw changes, thereby exhibiting higher transient nature of the demand cycles.

Table 9- Comparison of Rule Based and Cost Function Control Strategies for the TripEPA Combined Drive Cycle

Metric	Rule Based		Cost Function	
	Battery	Fuel Cell	Battery	Fuel Cell
Average Power (W)	10,541	6,881	4,502	6,290
Maximum Power (W)	40,782	66,000	20,987	36,720
Standard Deviation Power (W)	15,961	17,066	6,678	9,120
Average Rate of Power Change (dW/dt)	3,568	1,476	5,633	2,745
State of Charge Minimum (%)	49.9%		59.9%	
State of Charge Maximum (%)	71.3%		62.1%	

These results show the successful development and evaluation of the control strategies in the simulated environment and the significant impact of the hybrid control strategy on the component duty cycle. Chapter 4 identifies the key metrics in the component duty cycles that accelerate degradation and Chapter 5 integrates the knowledge of Chapter 4 with the model-based methods evaluated herein. Prior to that, the following step is to integrate the control strategies onto a working fuel cell hybrid vehicle and to compare simulated and actual results.

3.2 Hybrid Fuel Cell Vehicle Build and Evaluation

The previous section used a model based design process to select components and develop control algorithms based upon pre-existing component models. These models were part of PSAT component library, developed based upon supplier datasheets, or by using a scaling algorithm to adapt an existing PSAT or datasheet based model to the desired size. While this approach allows for rapid evaluation, there exists a significant amount of uncertainty about the

accuracy of the results given the simplifications and approximations made in the control and plant models. The importance of this section is to validate both plant and control models. To this effect, actual data in a series fuel cell hybrid powertrain is required. The key deliverables of this section include:

- Hybrid fuel cell vehicle build and commissioning,
- Dynamometer testing of the prototype vehicle,
- Total power duty cycles for various drive cycles,
- Plant model validation, and
- Control model validation.

3.2.1 Vehicle Build and Validation Work Performed to Date

This work was performed as part of the University of Waterloo Alternative Fuels Team (UWAFT) competing in the North American Challenge X competition. The author of this thesis was team captain during the design phase (i.e. Year 1), co-team captain and controls lead during the build phase (i.e. Year 2), and control team member during the refinement phase (i.e. Year 3 and 4).

Series fuel cell powertrains are not commonly available and extensive work was required by UWAFT to create a prototype fuel cell hybrid vehicle. The selected powertrain components were selected by the process described in Section 3.1. The significant structural modifications performed by UWAFT are illustrated in Figure 29. The fuel cell power modules are located under the seats in the center section of the vehicle with the tank located in the rear section of the vehicle. The battery pack is located in the top of the hood compartment, above the DC/DC converter and the motor inverter and transaxle. The second motor inverter and transaxle are located at the rear of the vehicle. The vehicle after the build phase is shown as Figure 30. During the refinement phase control programming and the actual wiring was completely redone, and the vehicle was painted with a custom black paint job.

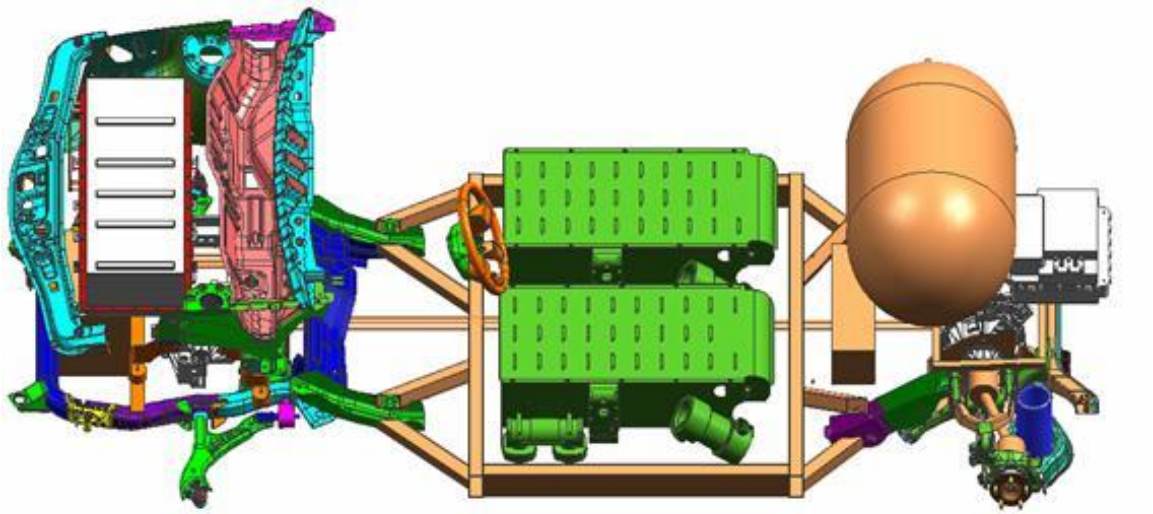

Figure 29 - CAD Model of Fuel Cell/Battery Hybrid

Figure 30 - Fuel Cell/Battery Hybrid Vehicle "Inukshuk"

To summarize, as shown in figures Figure 29 and Figure 30, this project involved the development, build and testing of a fuel cell passage vehicle based on a stock 2005 Chevy Equinox. The powertrain components are summarized in

Table 10. The 65kW of electrical power available from a Hydrogenics FCPM-65kW polymer electrolyte membrane fuel cell power module provided adequate power for efficient operation. The 65kW fuel cell power module is packaged inside of the vehicle in the floor area. This was

the only location with enough space to house the power modules while also allowing for five-passenger seating. The main structural frame rails were redesigned since the fuel cell power module support frame will also provide the support for the vehicle's structure.

Table 10 - Summary of powertrain components in the Inukshuk

Device	Make/Model	Specifications	
Fuel Cell Module	Hydrogenics HYPM 65kW	Max Net Power:	65kW
		Voltage Range:	190-300V
		Current Range:	0-350A
		Mass:	415kg
Hydrogen Storage	Dynetek ZM180	Max Pressure:	5000 psi
		Tank Capacity:	4.31kg H2
		Tank Weight:	92kg
		Tank Volume:	178L
DC/DC Converter	Custom UWAFT Design and Construction	Input Voltage Range:	190-300V
		Input Current Range:	0-350A
		Output Voltage Range:	300-385V
		Converter Type:	Boost
		Mass:	30 kg
Motors (2 units)	Ballard 312V67 transaxle	Peak Output Power:	67kW
		Continuous Power:	32kW
		Max Torque:	190Nm
		Mass:	84kg
Motor Controllers (2 units)	Ballard 312V67 controller	Full-Function Input Voltage:	230-360V
		Max Output Current:	280A RMS
Battery Pack	Cobasys/NiMHax 288-60	Voltage Range*:	276-336V
		Capacity:	8.5Ah
		Energy:	2.8kWh
		Mass:	85kg

**Open Circuit Voltage Range*

The architecture of the built vehicle incorporates two Ballard 312V67 traction motors and controllers, with one motor on each of the front and rear axles. The Ballard motors are 3-phase AC induction motors capable of delivering 67kW of peak traction power at high input voltages. The total theoretical output motor power is 134kW; however there is insufficient electrical power onboard to achieve the output power limits. Since the motor controllers are included with the motors, the custom control requirements for the vehicle control strategy involved only CANbus torque requests and coolant loop management. The motor controller contains an integrated inverter to connect the motor to the DC high-voltage bus. The rear of the vehicle required extensive modifications to house a second 65kW traction motor as well as the supports for a hydrogen storage tank. The battery pack was a Cobasys NiMHax 288-60 and includes an embedded controller. The battery pack is rated for 60kW at 35ºC and available peak power increases to 70kW as temperature rises to a limit of 50ºC. Due to packaging restrictions, the current vehicle integration strategy incorporates one Dynetek ZM180 tank. The integration included safe hydrogen tank mounting, hydrogen detectors, pressure, and temperature sensors. The DC/DC converter was a custom build (by another student [25]).

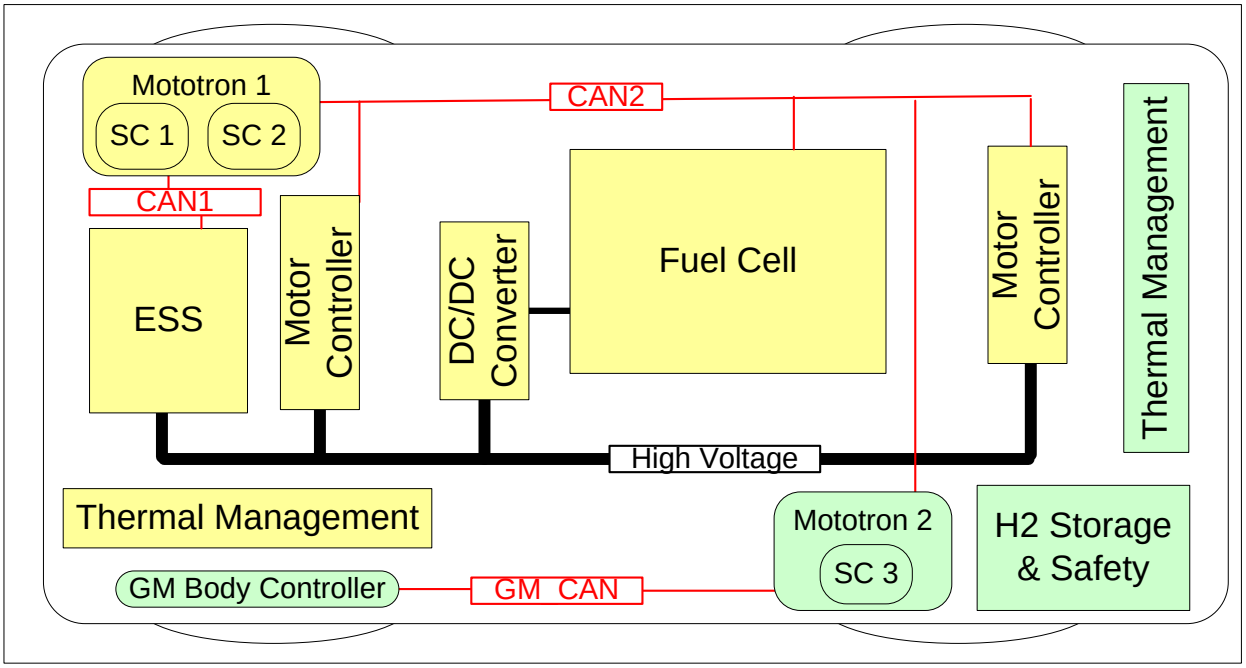

Figure 31 – Communication and Power Topology for Fuel Cell/Battery Hybrid Vehicle

The supervisory control was achieved through two MotoTron controllers that are based on the Motorola MPC555/565 PowerPC processor; the front controller is a ECM0565-128 while the rear controller is a ECM-555-80 controller. As shown in Figure 31, the front controller communicates with the battery on CAN1 and with the other powertrain components and rear controller on CAN2. The rear controller's second CAN channel is connected to the GM LAN network to allow for interfacing into the existing vehicle network and vehicle dashboard. In addition to powertrain control, vehicle integration required a number of additional control circuits, including:

- Four separate thermal loops (fuel cell loop, front motor and DC/DC loop, battery loop, and rear motor loop),
- Safety system monitoring (eight hydrogen sensors, inertia switch, and two Emergency Stops (Estop)),
- Fueling system monitoring and control,
- Interfacing to existing GM body controller to send dummy transmission and engine signals and to allow for feedback to the driver via the dash panel,
- System error checking and rationality checks, and
- Torque and traction control.

With the exception of the last item, the author of this thesis designed, programmed and wired the control circuits and control algorithms for the desired functionality. This specific setup and control of these systems is not specifically defined within the scope of this thesis and therefore is not discussed in detail. The two facts relevant to this thesis are that these control loops must also run on the actual MotoTron vehicle controllers running the hybrid control strategy, and that the Input/Output (I/O) of this system required that one controller be installed at the front of the vehicle and one at the rear. The 'pinouts' for the actual controllers for the two supervisory controllers are provided in Appendix A.

As described in section 3.1.1, a fuel cell/battery hybrid powertrain had been selected for integration into a Chevrolet Equinox vehicle platform. Since a model-based process was employed with Matlab/Simulink software products the hybrid control logic created and evaluated in PSAT (Powertrain System Analysis Toolkit which is Simulink software add-on) can be utilized for auto-generated code using Real-time Workshop and MotoTron controllers. This process allows the same Simulink code developed and evaluated in section 3.1.2 to be compiled

into target-specific and was flashed onto the real-time vehicle controllers. Upon initial testing in the vehicle parasitic/auxiliary power draws were found to average approximately 4,000W and peak at almost 6,000W. This was in stark contrast to the 800W value used in initial simulations. Note this observation leads one to conclude that the reduction of parasitic loads through better component design and intergrations remains a potential target for increased powertrain efficiency improvements in future fuel cell hybrid powertrains.

A significant amount of work was performed on the vehicle during the build and refinement phases. A large amount of time was devoted to debugging of the control wiring and non-hybrid control algorithms, including the rewiring of signal and power lines to reduce 'signal noise' causing communication errors. Due to a broken half-shaft (i.e. vehicle drive shaft) during testing (due to rapid torque spikes from the control systems) the slew rates and maximum torque saturations were decreased. Subsequently, the transient electrical power requirements during acceleration were decreased. Also, significant upper voltage limitations of the actual motor inverters were identified, resulting in regenerative braking being reduced and additional code being inserted in the hybrid control strategy to reduce overvoltage events that could not be tolerated by the motor. There were also two replacements of the Nickel-Metal Hydride battery as a result of battery failure (and a new model becoming available) and a battery controller failure. During testing in Arizona (Year 2) there was also a failure of the DC/DC due to tuning issues of the low-level DC/DC current PI loop. At this time the fuel cell blower was connected to the high voltage bus rather than start-up DC/DC boost converters to accelerate the fuel cell power module start-up process. While these failures are not discussed in detail these issues are presented as examples of issues relating to real-world testing and to underscore the value of a model-based design process when it reduces the number of prototype iterations required during a design process.

3.3 Experimental - Hybrid Fuel Cell Vehicle Testing

During the summer months the vehicle was driven around the university campus and a nearby emergency services test facility to allow for limited on-road testing. Intense on-road testing was performed during four periods, which listed chronologically includes two testing periods at General Motor's proving ground in Mesa, Arizona (year 2 and year 3), followed by a later test period at General Motor's proving ground in Milford, Michigan (year 3), and finally a road rally event between New York and Washington (year 4). Both testing periods in Mesa were plagued

with operational issues and were primarily focused on debugging. The testing at Milford was moderately successful but included numerous operational issues, with a persistent issue of regularly losing one of the two traction motors. The root cause of this issue was not found during the Milford testing period. The road rally testing period was very successful with the single motor issue being the sole operational issue. Dynamometer testing of the vehicle was done during two time periods. The first testing period was at Esso's environmental dynamometer test facility in Sarnia, Ontario prior to the Milford on-road test period (year 3). The second was at Argonne National Laboratory's Hydrogen Powertrain Test Facility in Argonne, Illinois following the road rally event described earlier (year 4).

While significant data sets were captured during the on-road testing in Waterloo, the four on-road test periods, and the two dynamometer test periods described, the refinement and validation of the component models will be focused exclusively on the testing at Argonne's dynamometer facility. The testing at Argonne represented the culmination of the four years of developing the vehicle and included the most reliable vehicle operation and most sophisticated data acquisition system. This facility provided the most controlled testing conditions and the most degraded state of the fuel cell stack. The models are refined using a set of Urban Dynamometer Driving Schedule (UDDS) and Highway Federal Emissions Test (HWFET) tests and are validated on a different set of UDDS/HWFET tests.

3.3.1 Interpretation of Dynamometer Data

Prior to the presentation of the data captured at Argonne's test facility, the interpretation and verification of key variables is first presented. The facility's Data Acquisition System (DAS) compiled results from five sources:

- Dynamometer control system,
- Emissions measurement system,
- Hydrogen delivery system,
- On-board CAN bus logging, and
- Additional Hioki voltage and current sensors.

The Hioki probes were installed on the high voltage bus to determine key values related to power flow in the powertrain. A portion of the probes provided were in duplicate to values reported by the vehicle control system sensors installed during this project (and reported of

over the Car Area Nework communication protocol - CAN) while others were values not captured via CAN. To ensure the accuracy of the measurements a rationality check for the Hioki and CAN reported measurements for motor currents was performed using the values as presented in Figure 32 – Overview of CAN and Hioki Measurement Locations Used for Rationality Check Figure 32. The motor current values are reported from the Ballard motor inverters. Hioki current clamps were used to measure the fuel cell DC/DC output current, battery current, 12V DC/DC input current, 24V DC/DC input current, and fuel cell blower input current. Performing a current balance on the high voltage bus allows for a rationality check between the Hioki and CAN based measurements.

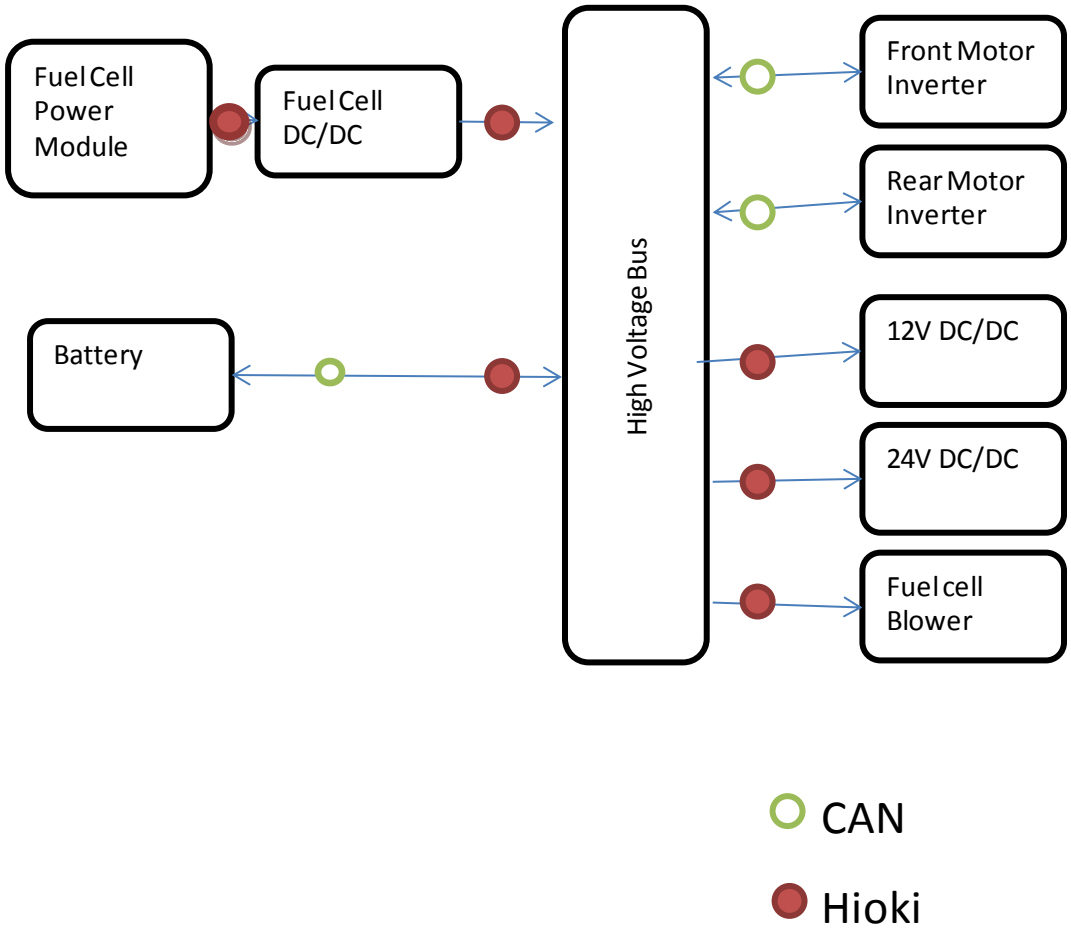

Figure 32 – Overview of CAN and Hioki Measurement Locations Used for Rationality Check

The values are plotted for a 35 second portion of a UDDS drive cycle in Figure 33. Clearly the rationality check demonstrates a high level of correlation between the Hioki calculated motor

current and the CAN calculated motor currents, with small variation during highly transient measurements. Therefore the CAN measurements are deemed to be accurate.

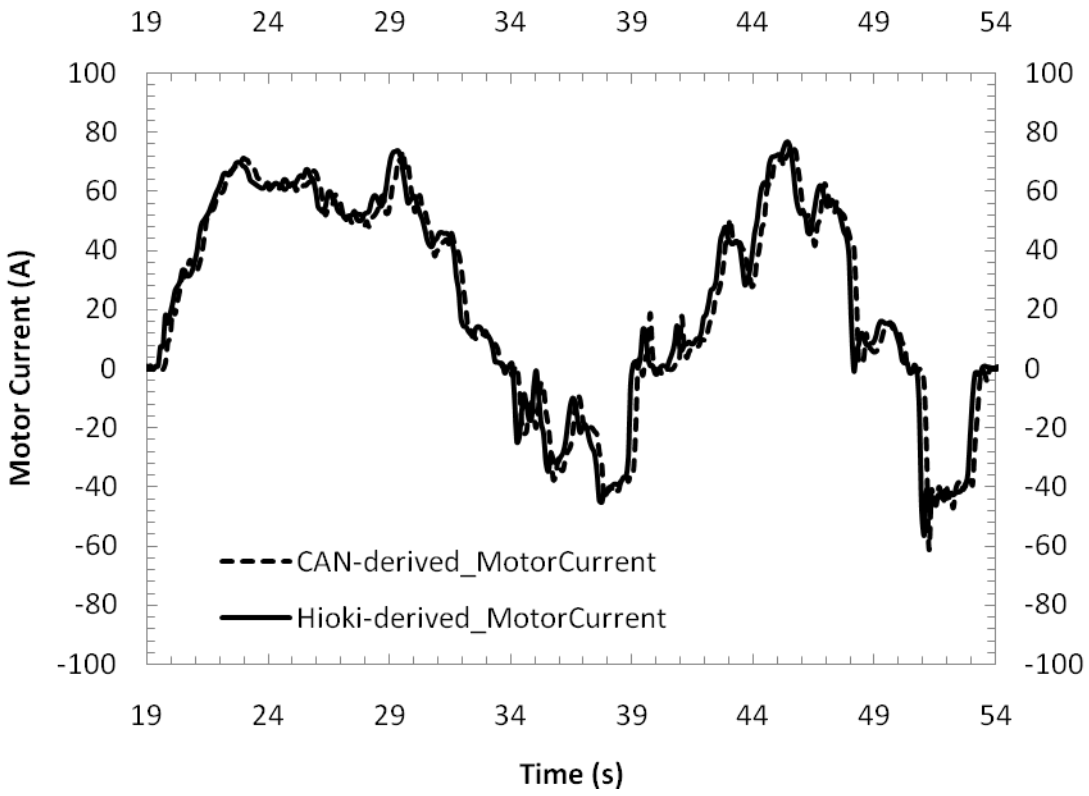

Figure 33 – CAN-derived and Hioki-derived total motor current for a 35s segment of a UDDS test cycle

In practice it was observed that the voltages reported by the Ballard motor inverters over CAN were less than those measured at the terminals. During the dynamometer testing a Hioki probe was placed on the high-voltage battery terminals. The Hioki measurements were compared with the CAN reported voltages from the Ballard motor inverters. There would be voltage losses along the OO high-voltage power lines during high current draws. The same 35 second data set was plotted with the voltage levels. To ensure there was not power transmission losses, the average offset between the Hioki and CAN reported voltages where evaluated when the respective motor current draw was less than 2 Amps. The average offsets for MCU1 and MCU2 were 7.70V and 5.31V respectively. As the Hioki measurement is believed to be the accurate value, the MCU1 and MCU2 CAN reported values are adjusted by these offsets.

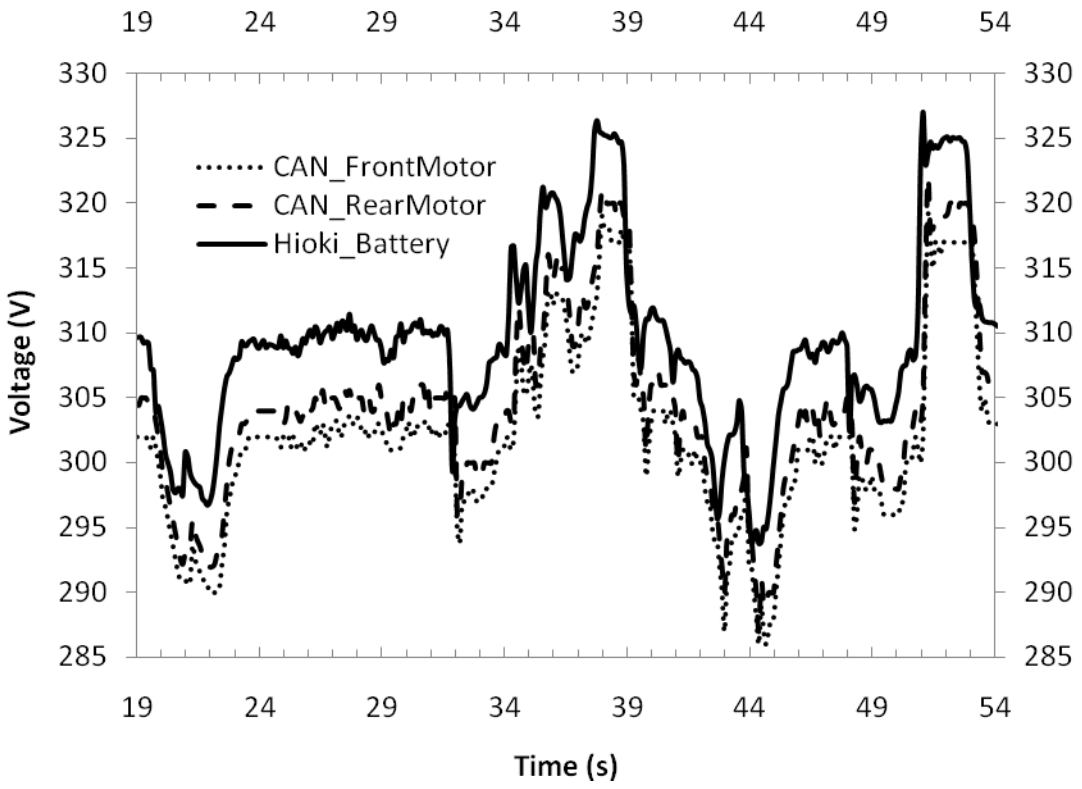

Figure 34 – CAN-based and Hioki-based voltages for a 35s segment of a UDDS test cycle

A major component model requiring validation is the fuel cell power module. An efficiency model requires three measurements: fuel cell voltage, fuel cell current, and hydrogen flow. The system purges hydrogen from the stack and uses some of the stack current to run electronics and some parasitic loads (e.g. recirculation pumps, valves) – this eliminates the ability to calculate the hydrogen consumed from fuel cell current using Faraday's constant. In addition, to accurately develop the efficiency map the fuel cell blower power draw from the high voltage bus must also be identified.

The fuel cell current and voltage measurements are measured by both the Hioki system and Fuel Cell Power Module (FCPM) controller and broadcast on the CAN bus. The current measurements for the fuel cell are shown in Figure 35. Two main differences are evident between the two measurements channels. The CAN based fuel cell measurement is smoother and slightly delayed as compared to the Hioki based measurements. The smoothing of the current measurement is due to the capacitor in the current measurement circuit within the FCPM. The delay is due to the fact that the FCPM controller measures the current, stores the

value, and transmits the value at a fixed time interval over CAN, which is then captured by the DAS. For the purposes of the model the Hioki measurements will be utilized.

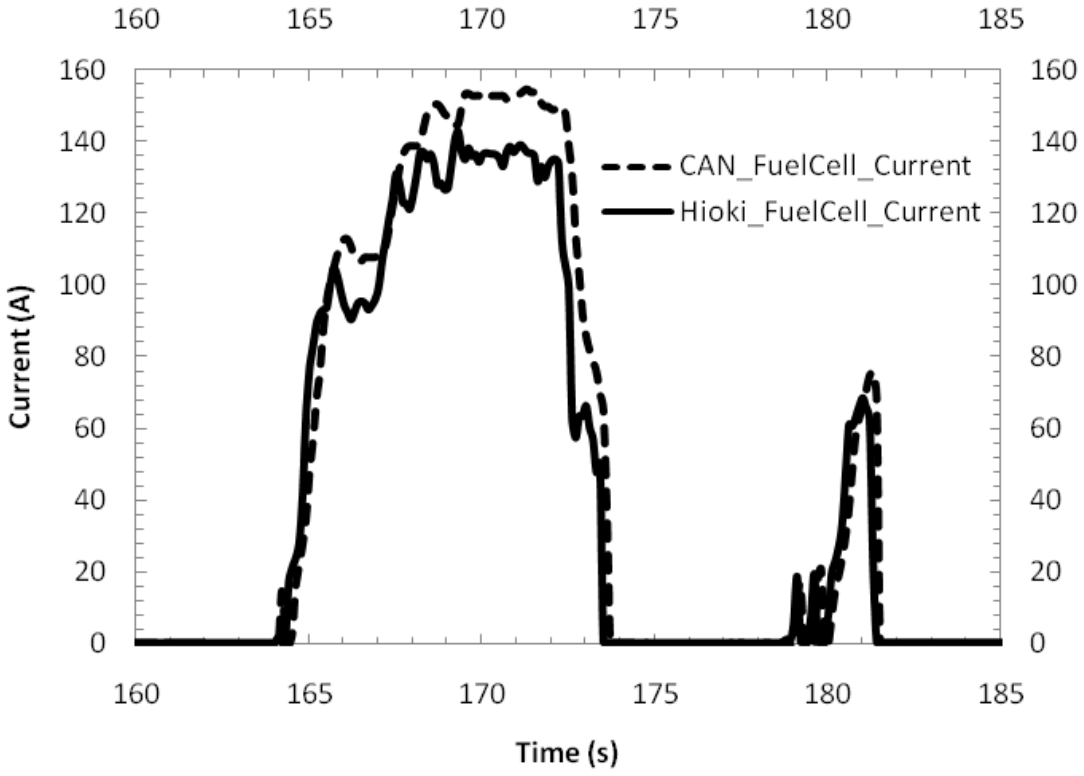

Figure 35 – Fuel cell CAN-based and Hioki-based current measurements for a 25s segment of a UDDS test cycle

The CAN and Hioki fuel cell voltage measurements are shown in Figure 36. The measurement values are almost identical with the exception of a slight delay. The delay is again due to the fact that the FCPM controller senses the voltage, stores and transmits the values at a fixed interval over CAN, which is then captured by the DAS (data acquisition system). Similar to the fuel cell current the Hioki measurements will be used for model development.

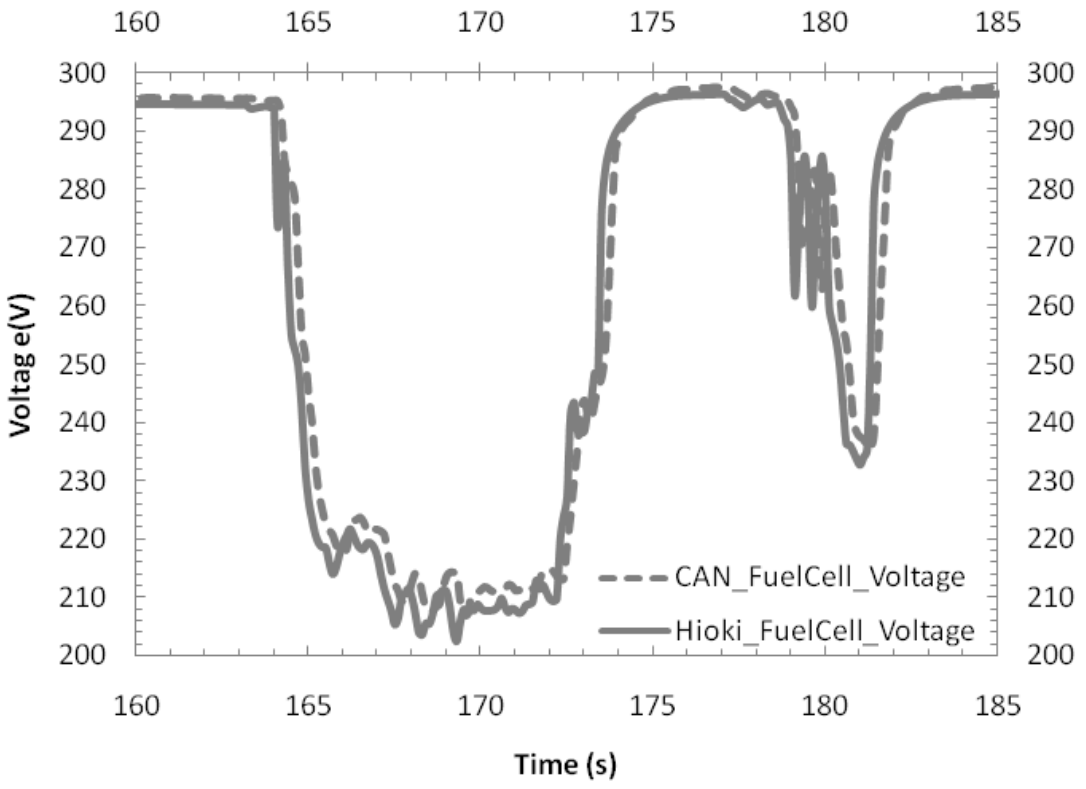

Figure 36 – Fuel cell CAN-based and Hioki-based voltage measurements for a 25s segment of a UDDS test cycle

The DAS incorporates hydrogen flow measurements taken at the hydrogen supply system from the dyanometer (there is no onboard system for measurement of hydrogen flow). There is a significant amount of high pressure tubing between the point of measurement and the vehicle fill port. The length is then extended from the fill port to the fuel cell intake. The result is a significant hydrogen residence volume causing transport delay and smoothing of the demand transients. This transport delay and demand smoothing is clearly illustrated in Figure 37. To develop an accurate fuel cell efficiency model the fuel cell and hydrogen variables must be aligned. To achieve alignment the hydrogen flow values will be advanced by the value of the transport delay from the point or measurement to the fuel cell and the fuel cell current values will be smoothed to compensate for the demand smoothing.

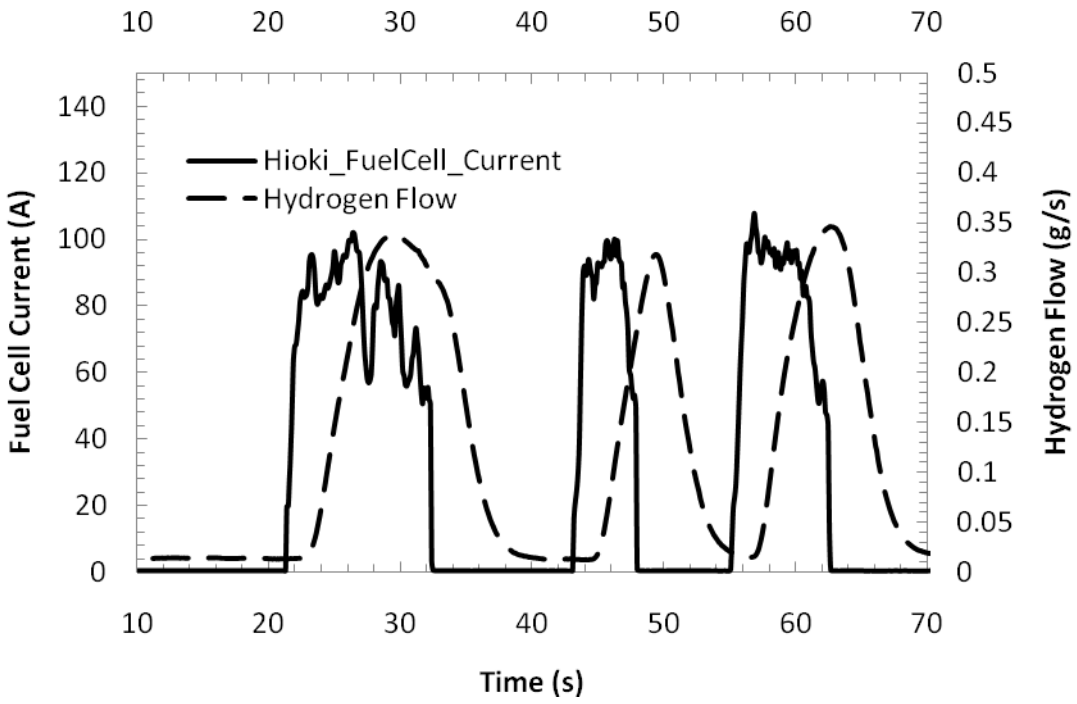

Figure 37 – Raw measurements of fuel cell current and hydrogen flow for a 60s portion of the UDDS test cycle

Advancing the hydrogen flow measurements by 1.5 seconds resulted in fuel cell current coinciding with increases in hydrogen flow. The time corrected results are shown in Figure 38. There remains a significant variation between the datasets due to the large hydrogen residence volume in the tubing causing a buffering of hydrogen flow. To permit the development of the efficiency model the fuel cell current value is averaged using a 4 second moving window average. The result of the average fuel cell current and time-advanced hydrogen flow is plotted in Figure 39. The combination of delaying the hydrogen flow measurement and average the fuel cell current permits for the elimination of residence volume effects in the fueling line. The implication of averaging the fuel cell power module to coincide with the capacitance effect of the residence volume of the fueling line introduces inaccuracy in the efficiency model under highly transient loads. Operational points for reasonably steady-state fuel cell power outputs will generate superior efficiency values.

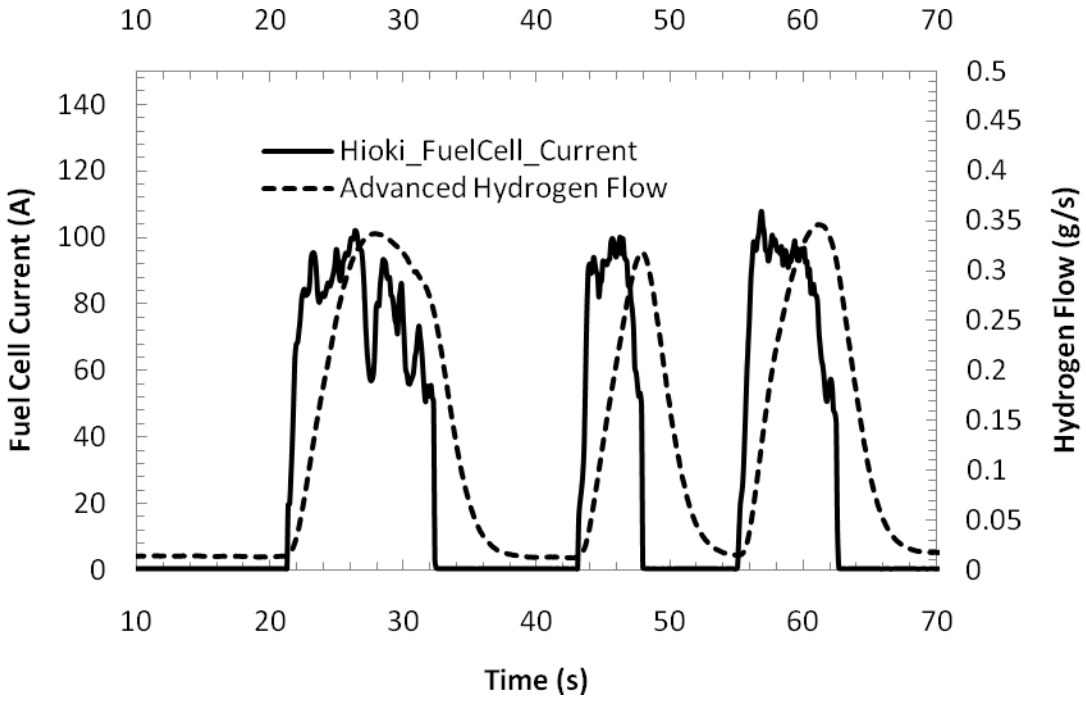

Figure 38 – Fuel cell current and time-corrected hydrogen flow for a 60s portion of the UDDS test cycle

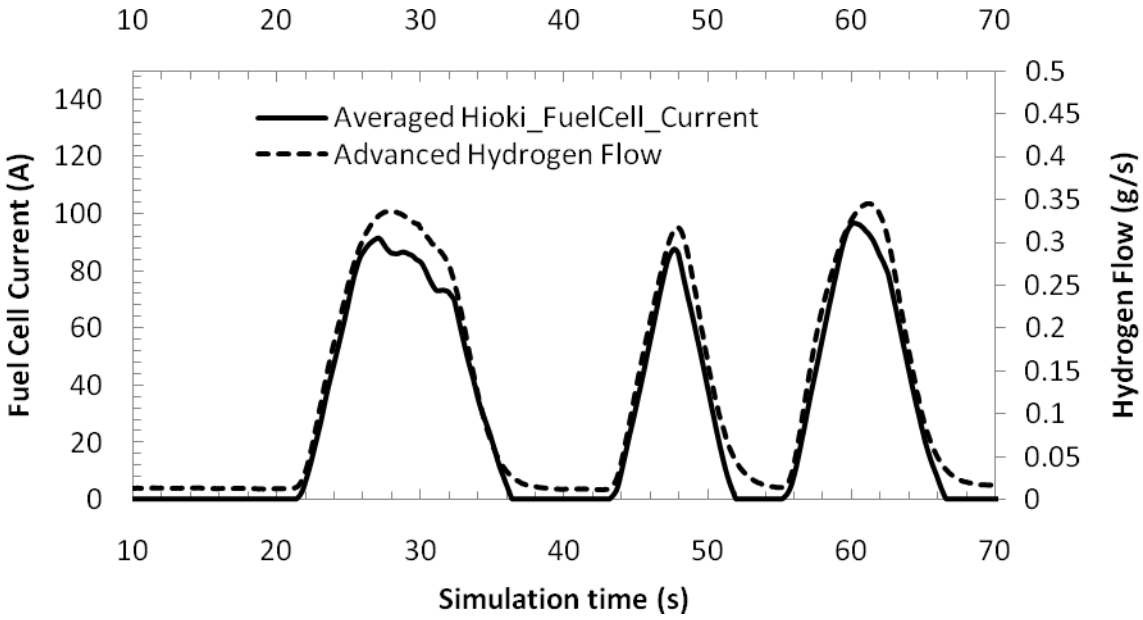

Figure 39 – Averaged fuel cell current and time-corrected hydrogen flow for a 60s portion of the UDDS test cycle

Given the successful rationality checks and calibrations discussed in this section, the results from dynamometer testing are utilized to improve the initial hybrid fuel cell vehicle model. All values presented beyond this point are adjusted based upon the calibrations discussed above. The processes of model improvement and validation are described in detail in the next two sections.

3.3.2 Model Development and Refinement

The initial vehicle model presented in section 3.1 included a number of required assumptions and incorporated a number of generic component models. To improve the accuracy of the component models, and subsequently the overall vehicle model, five major refinements are sought:

1. Fuel cell blower power consumption model based upon dynamometer results,
2. Fuel cell efficiency model based upon dynamometer results,
3. Quantification of 12V and 24V auxiliary loads,
4. DC/DC efficiency model as a function of voltage boost, and
5. Addition of voltage-following case for fuel cell power delivery to depict the correct causality during dips in bus voltage.

The fuel cell blower represents a significant auxiliary load. The initial design of the Hydrogenics Fuel Cell Power Module powered the blower off the fuel cell rail. The result was that the fuel cell output current was decreased by the blower load. In the third year of vehicle development the blower was connected to the battery rail instead to allow for faster spool during start-up. Previously the blower was powered of the 24V rail using DC/DC boost converters until the fuel cell was at a sufficiently high voltage. This modification caused the blower power draw to be of interest as it represented an auxiliary load apparent to the high voltage bus, and therefore must be considered in the hybrid control strategy algorithm.

To understand the behavior of the blower it is important to define the open-loop and closed-loop modes of FCPM operation. In both cases the vehicle's supervisory controller affects the blower, by determining the target fuel cell current that is to be requested. The final actuation of the control of the blower remains under the supervision of the FCPM controller. In closed-loop, the supervisory controller's fuel cell current request is broadcast over CAN to the FCPM. The FCPM utilizes the request value to spool the auxiliaries, including the blower, to prepare to deliver the requested current. The supervisory controller simultaneously uses the current

request as the set-point in the DC/DC current control loop with its associated slew rate limits. The result is feed-forward control of the fuel cell auxiliaries based upon the current request. The FCPM monitors the actual output current and adjusts the auxiliary control in the event significant deviations between fuel cell current request and actual fuel cell current. In open-loop the FCPM utilizes the measured output current to spool the auxiliaries, resulting in feed-back control. Closed-loop operation is preferred as it permits faster power draws and reduces the amount of starvation of the fuel cell stack (which is a degradation/failure cause of PEM fuel cell stack failure).

The values of fuel cell blower power draw as a function of fuel cell stack power output are provided in Figure 40. A significant amount of variation is present in Figure 40; however, there exists a clear trend between the blower auxiliary load and the stack output power. The variation can be partially explained by the closed-loop operation described earlier. Since the blower set-point is established based upon the fuel cell current request, rather than the actual fuel cell current, a plot of blower power versus fuel cell stack requested current would contain less variation. The fuel cell requested power was not captured during data acquisition; therefore the relationship is developed based upon the actual stack power.

The fuel cell blower power draw as a function of fuel cell stack power is defined by:

$$P_{Blower} = 3.46x10^{-11} * {P_{FC}}^3 - 1.66x10^{-6} * {P_{FC}}^2 + 5.01x10^{-2} * P_{FC} + 156 \quad (35)$$

Where P_{FC} is the fuel cell stack output power in Watts and P_{Blower} is the blower load in Watts, with an R^2 value of 0.915. In observing the figure the R^2 value was perceived to be unreasonably high; however, further investigation of the >50,000 data points plotted illustrated that a high density of data points are within the center portion of the distribution.

PSAT does not have a separate block for the fuel cell blower auxiliary load. The load is generally included in the fuel cell component model. To allow for accurately correlation of fuel cell power outputs the blower power load was included in the fuel cell power converter component model, allowing for the power draw to occur on the high voltage bus rather than on the fuel cell rail.

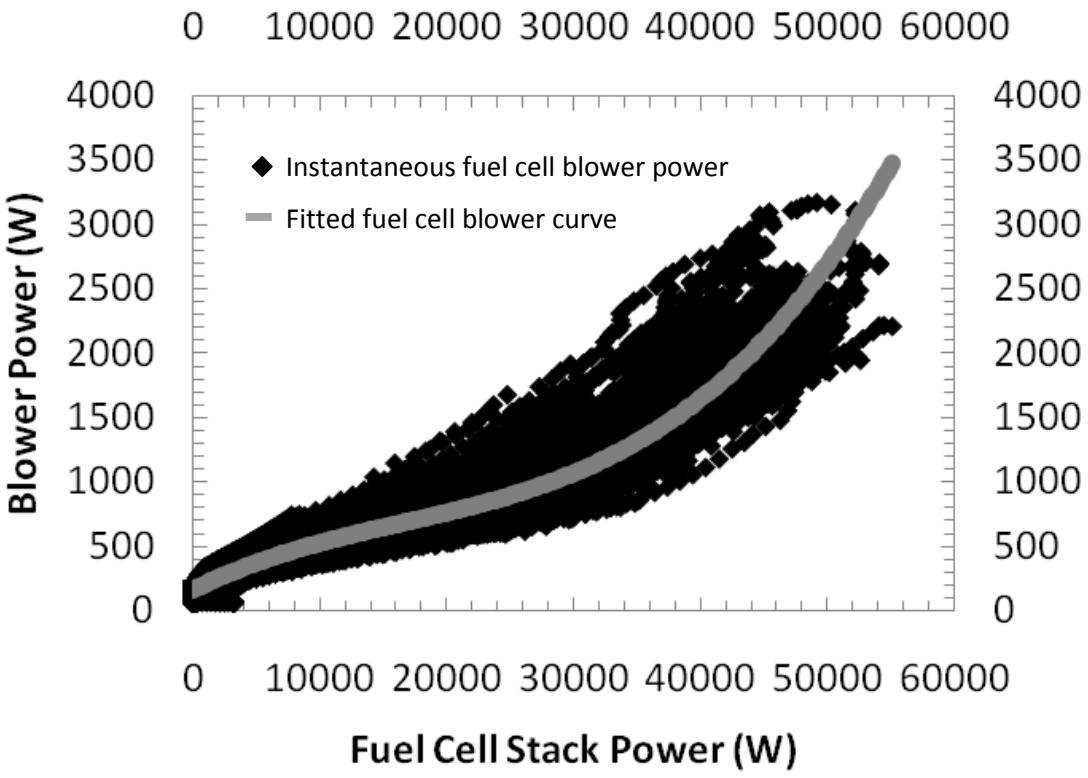

Figure 40 – Instantaneous fuel cell blower power draw sampled at 10Hz as a function of fuel cell stack output power for three UDDS test cycles (over 50,000 data points are plotted with a high density in the center of the distribution)

Data points from three UDDS test cycles were combined to develop a model for stack output voltage as a function of fuel cell current and temperature. The model was fit to the GSSEM (i.e. a semi-empirical fuel cell model introduced in Chapter 2) in the form of:

$$V = E_0 - \frac{RT}{nF} ln\left[p^*_{H_2}\left(p^*_{O_2}\right)^{0.5}\right] - \left[\xi_1 + \xi_2 T + \xi_3\left[ln\left(c^*_{O_2}\right)\right] + \xi_4 T\left[ln\left(\frac{i}{i_{ref}}\right)\right]\right] \quad (36)$$

which as a function of temperature and current simplifies to:

$$V = \alpha + \beta T + \gamma i + \delta T ln\left(\frac{i}{i_{ref}}\right) \quad (37)$$

The values of $\alpha, \beta, \gamma, \delta$ are provided Table 11. The R^2 value for the correlation is 0.928. The voltage map is provided as Figure 41. Combining the fuel cell voltage map with the blower power module correlation developed earlier enables the creation of a fuel cell efficiency map.

The resulting efficiency map is provided as Figure 42 and an associated contour map is provided as Figure 43. The efficiency is defined as the net power module output divided by the chemical energy flux derived from the hydrogen flow rate. As anticipated, and as presented in Chapter 2, the fuel cell power module exhibits low efficiencies at very low output powers and mildly decaying efficiencies at higher output powers. There is an unexpected increase in efficiency at higher powers and temperatures, this is believed to be a result of the averaging performed to correct for the residence time of the hydrogen fueling line. High powers and temperatures were only obtained for short periods under highly transient power demands. As a result of the averaging the efficiencies would be overestimated at the high powers and temperatures. Disregarding this anomaly caused by the fuel cell power averaging, the increased temperature reduces the amount of efficiency decay at higher output powers, caused by lower voltage drops at higher temperatures due to improved mass transfer.

PSAT initialization files were made using these efficiency and polarization maps. It should be noted that the efficiency map developed does not include the associated 12V and 24V loads.

Table 11 – Fuel cell stack voltage parameters for GSSEM structure in coded form

	Coding – Minimum (equal to -1)	**Coding –Maximum (equal to +1)**	**Coefficient**
Constant	--	--	255.788
Temperature, K	303	328	11.648
Current, A	1	230	-12.312
Temp*Ln(Current/Current$_{ref}$), K	0	1784	-41.541

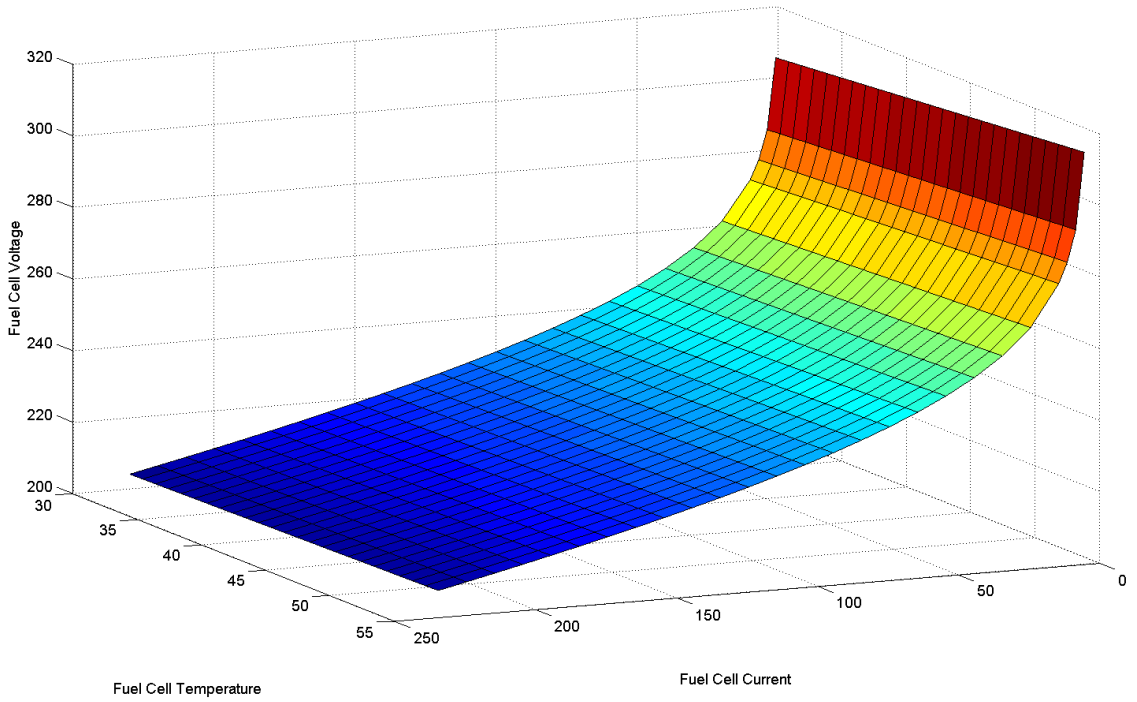

Figure 41 – Fuel cell stack voltage map as a function of fuel cell current and fuel cell temperature

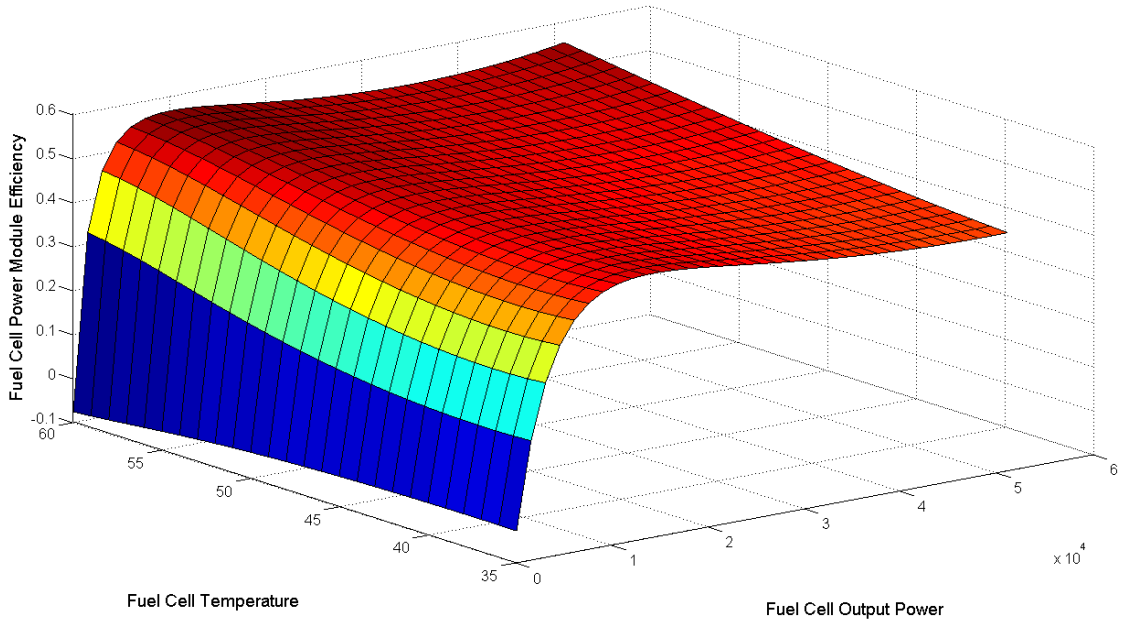

Figure 42 – Fuel cell power module efficiency map as a function of fuel cell current and fuel cell temperature

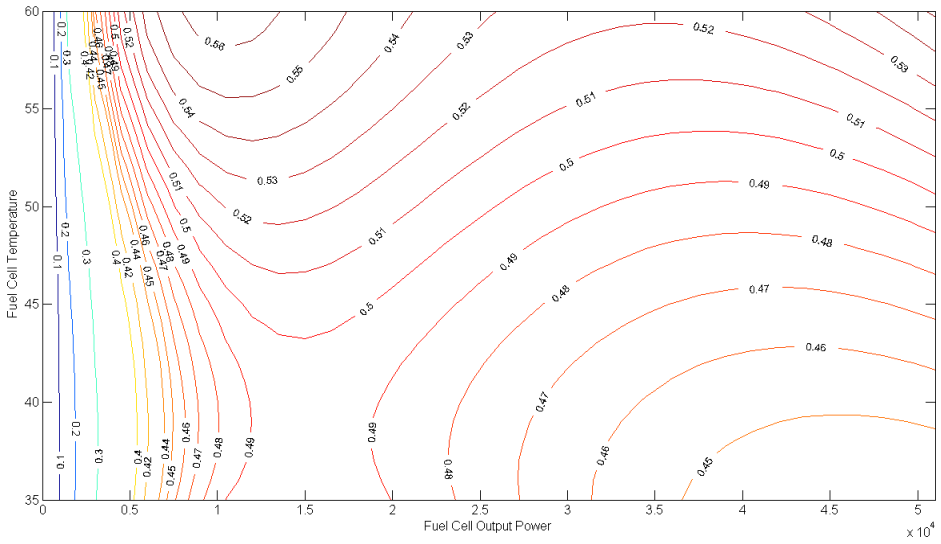

Figure 43 – Contour map for fuel cell power module efficiency as a function of output power and temperature

The third objective in the model refinement process was to improve the approximation of the 12V and 24V auxiliary loads. Note that PSAT does not permit the use of varying auxiliary loads for hybrid fuel cell vehicles, as all auxiliary loads must be constant or programmed "a priori". Despite the limitation of PSAT to consider variable auxiliary loads, correlations between operating parameters and the auxiliary loads were sought. Auxiliary loads for the 12V and 24V systems are provided as Figure 44 and Figure 45 respectively. The 12V load demonstrated a correlation with vehicle speed as high vehicle speeds corresponded to steady parasitic loads of 1230W. As the 12V bus includes a starter battery, the power surges exceeding 2000W correspond to significant draws on the 12V bus as the battery will buffer the demand. It was initially considered that the surges were the result of the electric power steering; however, this is not the case as this data was captured during dynamometer testing. The source of these 12V load surges is unknown. The standard deviation of the 12V auxiliary load is 141W, with an average load of 1231W.

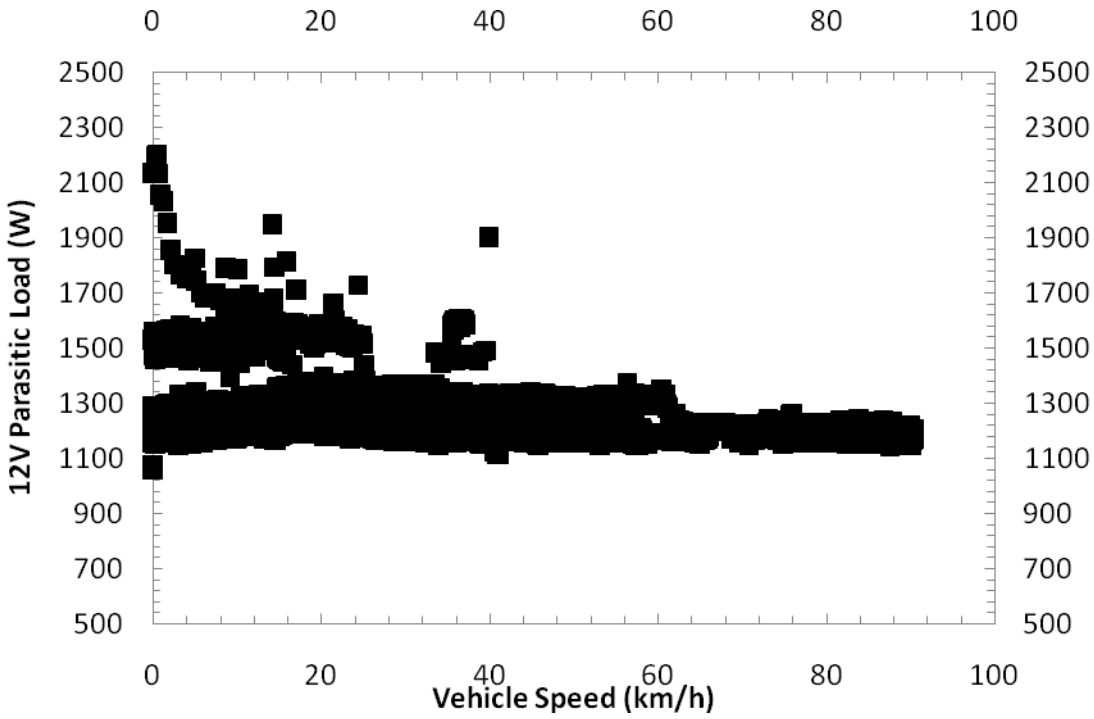

Figure 44 – Instantaneous 12V auxiliary load sampled at 10Hz as a function of vehicle speed for a UDDS test cycle

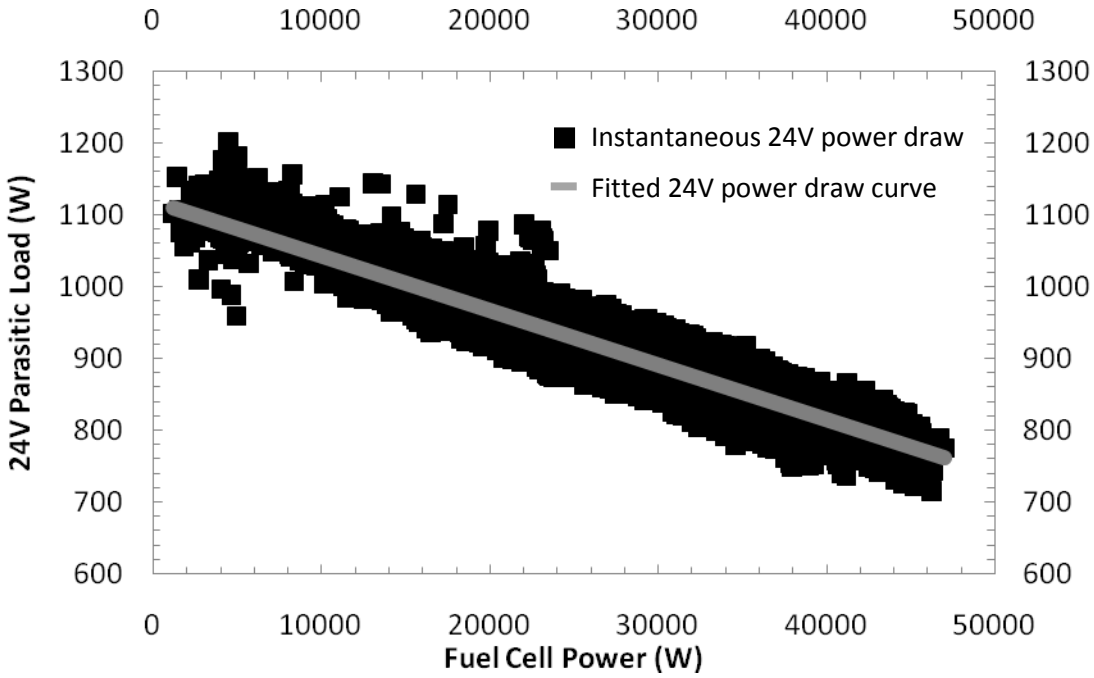

Figure 45 – Instantaneous 24V auxiliary load sampled at 10Hz as a function of fuel cell power for a UDDS test cycle

With no fuel cell load the 24V bus auxiliary draw is 1100W with a standard deviation of 170W. Under load the 24V bus parasitic load exhibits a negative linear trend of 0.0076W/W as a function of fuel cell output power. The R_2 value of the linear relationship is 0.85. While fuel cell auxiliaries such as the recirculation pump are powered off the 24V rail, it is unknown why an inverse relationship exists.

As previously mentioned, PSAT only allows for constant auxiliary loads in hybrid fuel cell vehicles. While this thesis develops a number of improved models for integration into PSAT the component models are limited by the information that is passed to them during simulation. The only variable passed to the auxiliary load component block is the battery voltage. Therefore, the combined average load of 2020W observed during the initial UDDS cycles is implemented in PSAT as the 12V and 24V combined load.

The fuel cell power converter model employed in the initial hybrid fuel cell vehicle modeling utilized a constant efficiency of 95%. A high-efficiency DC/DC converter was designed and built by a graduate student on vehicle team. The conversion efficiency as a function of voltage boost is provided as Figure 46. The DC/DC converter is not operated at boost percentages less than 10% due to operational issues related to the duty cycle provided to the Insulated-gate Bipolar Transistor (IGBT). The maximum boost ratio observed was just below 100%. The efficiency trend exhibits a logarithmic behavior at low boost followed by a slight linear efficiency decay. A variable efficiency power converter model was developed and integrated into PSAT that determines the efficiency as a function of the voltage boost. An accompanying initialization file was developed to represent the efficiency trend observed below.

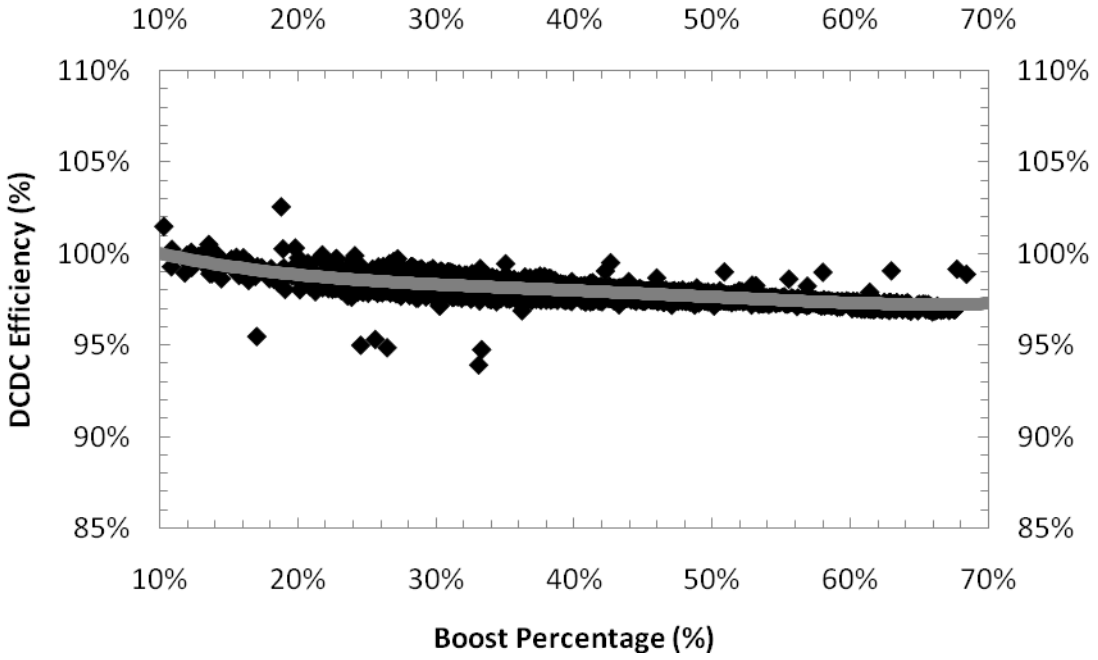

Figure 46 – DC/DC efficiency as a function of voltage boost

The final objective of the model refinement was to integrate voltage-following operation of the powertrain. This mode of operation must be integrated to accurately simulate the vehicle performance when the battery voltage drops below the fuel cell output voltage, resulting in loss of DC/DC control with fuel cell output power controlled by fuel cell voltage characteristics. Given that the hybrid topology utilizes is a boost converter, the fuel cell voltage must remain at or below the bus voltage. The implication of this requirement is that if during significant battery power draws the bus voltage drops below fuel cell open-circuit voltage then the fuel cell will begin to provide power in accordance with the voltage of the bus. This phenomenon is shown in Figure 47. At approximately 937.7 seconds the battery voltage nears the fuel cell open-circuit voltage. As a result the fuel cell begins to provide a small amount of power. At approximately 938.4 seconds the battery voltage begins to drop almost a full volt below the fuel cell open circuit voltage resulting in a surge of current from the fuel cell. As this event was not intentional and the FCPM controller was not requested for current an insufficient amount of reactant was available, resulting in cell starvation exhibited by a significant drop in fuel cell voltage. While the modeling of cell starvation was not stated for the objective of this work, incorporation of the voltage-following behavior into PSAT is important due to the real-world implications of this mode of operation.

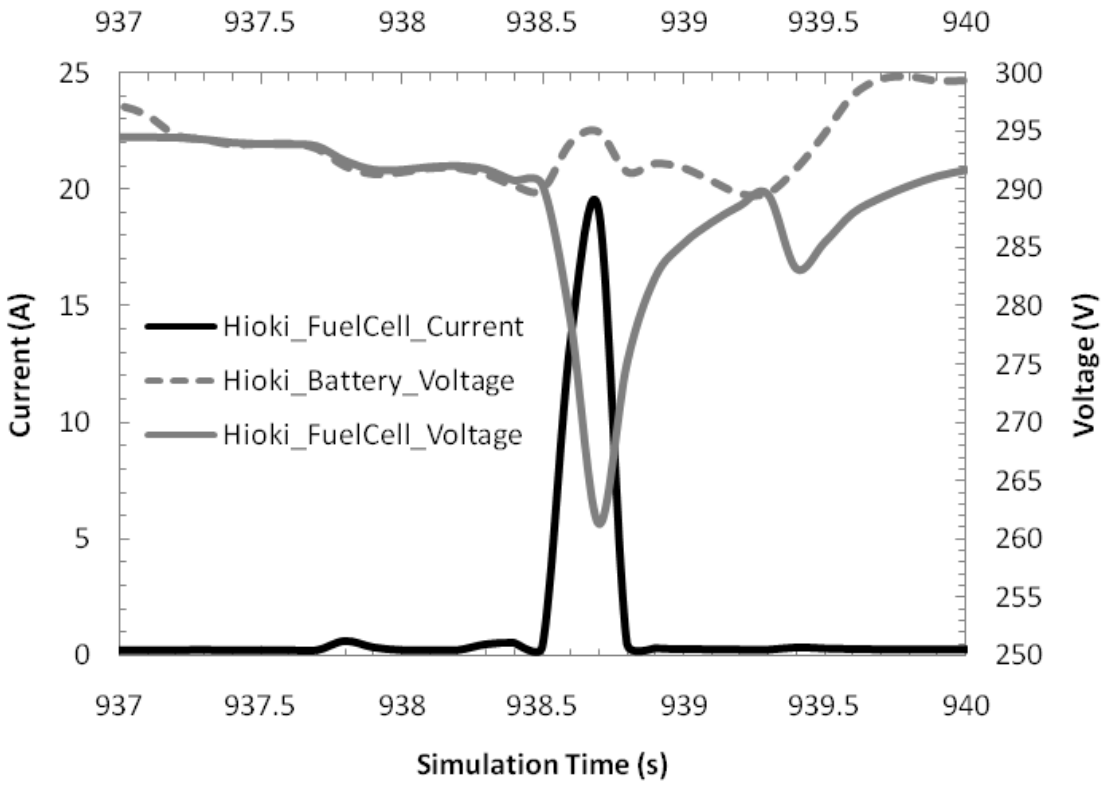

Figure 47 – Fuel cell voltage-following operation during a UDDS test cycle

As mentioned, the voltage-following operation is not captured natively in PSAT. The native PSAT format is non-causal with respect to bus voltage, assuming the actual fuel cell current is determined by the current request and the dynamics of the fuel cell model alone. To resolve this omission the following case structure is added where the outputs are coupled by the internal resistance of the components when the battery voltage falls below the fuel cell output voltage:

$$I_{fc}^{act}\left(V_{batt}, V_{fc}, I_{fc}^{req}\right) = \begin{cases} f(V_{batt}), & V_{batt} < V_{fc} \\ f(I_{fc}^{req}), & V_{batt} \geq V_{fc} \end{cases} \tag{38}$$

The second case listed is the normal mode of operation in PSAT. The first mode is added. If the bus voltage is detected to be below that of the fuel cell for the given current request, the current delivered is calculated from the modified polarization curve model that determines the output current for a given bus voltage.

With the creation of a separate fuel cell blower load model, refined fuel cell efficiency map, improved 12V/24V auxiliary load approximation, variable DC/DC efficiency model, and voltage-following fuel cell causality the model is prepared for validation. The next section evaluates the refined hybrid fuel cell PSAT model using a data set not used for the model development.

3.3.3 Model Validation

Thirteen UDDS test cycles were captured during the testing at Argonne. As a result of the previously mentioned motor fall-out issues, the thirteen data sets ranged in their ability to achieve the UDDS target speed profile. Four test cycles that exhibited acceptable achievement, as defined by no variations >2mph for longer than 10 seconds, were utilized in the model refinements described in the last section. A fifth test cycle that exhibited close speed performance to the target speed profile is used for validation of the vehicle model. The entire test cycle is 1361 seconds; however, only the first 505 seconds are shown to allow for clarity in the figures; the entire test cycle was used in model validation. The speed profiles of the actual and simulated vehicles are provided as Figure 48. The trace exhibits almost identical speed profiles for both the actual and simulated vehicles. The result demonstrates that both the real and virtual drivers were capable of following the target trace and that there was sufficient vehicle power and braking force.

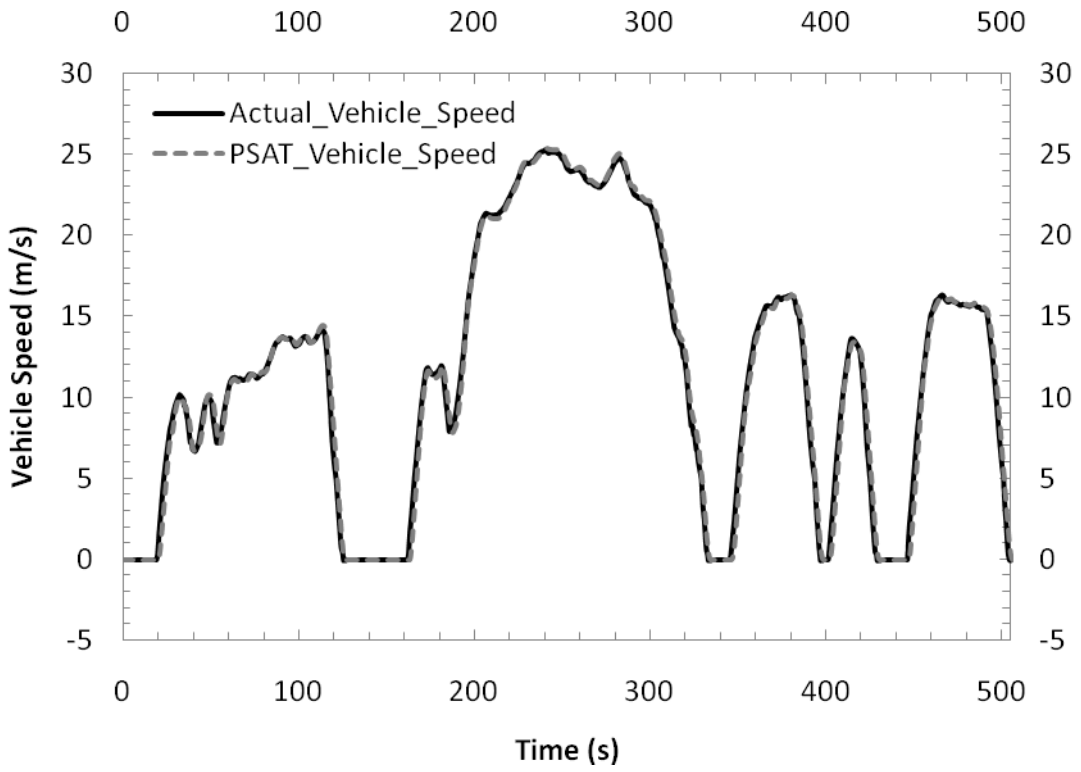

Figure 48 – Actual and simulated vehicle speeds for the first 505 seconds of a UDDS test cycle

The combined power output of the real and simulated motors is provided as Figure 49. The actual output motor powers are obtained as the sum of the product of torque and speed for both motors as broadcasted from the Ballard motor inverter on CAN. While the actual and simulated motor power output powers exhibit similar trends, they are not as similar as the speed profiles. Small variations are to be expected as the actual and virtual drivers are unlikely to follow identical torque requests to achieve the same overall vehicle speed. The one variation of interest is the additional peaks exhibited in the PSAT model. Given that these are occurring at peak power levels representing hard accelerations and decelerations this implies there may be an offset in the vehicle mass. The vehicle mass recorded on the dynamometer results is 5050lbs, and the simulation was performed at that mass. It is possible that the dynamometer measurement did not account for the second vehicle occupant that was in the vehicle during testing. Regardless, these profiles are well within a reasonable level of compliance.

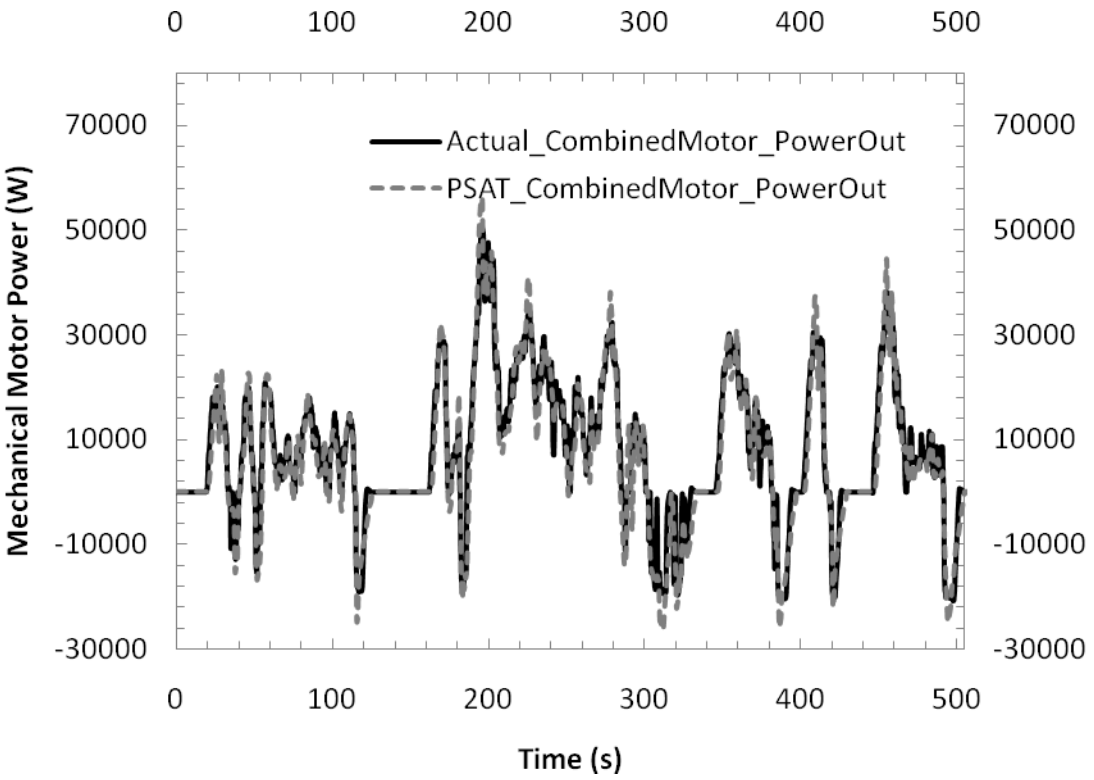

Figure 49 – Actual and simulated combined output motor power for the first 505 seconds of a UDDS test cycle

The combined motor input powers are plotted in Figure 50. As described in section 3.3.1, individual sensors were not placed upon the motors. Therefore, the combined motor current was determined using an energy balance on the high voltage bus. That value was multiplied by the battery voltage to determine the motor input power. Similar to Figure 49 the trends of both the actual and simulated vehicles are similar, suggested accurate motor efficiency models. The motor efficiency models were generated from performance data provided by Ballard and is provided in Appendix D. The additional peaks during power extremes are further amplified by the motor efficiency; however, again the variations between the profiles remain within a reasonable level of compliance.

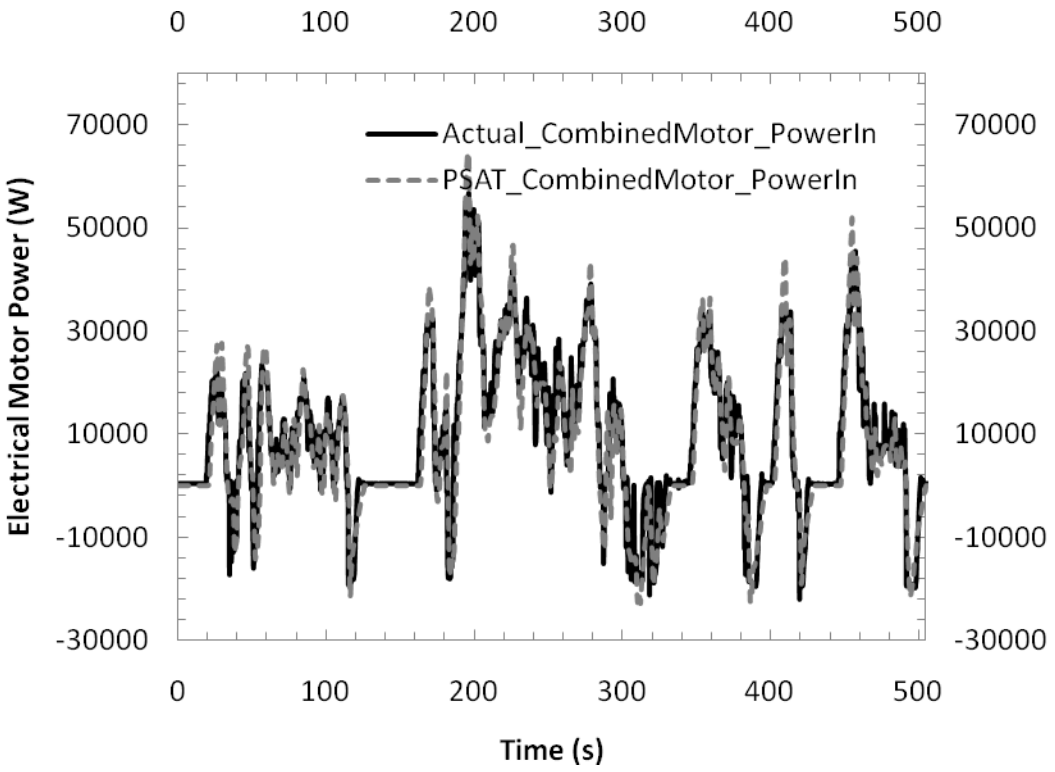

Figure 50 – Actual and simulated combined input motor power for the first 505 seconds of a UDDS test cycle

The actual and simulated combined 12V and 24V loads are provided in Figure 51. As discussed earlier, PSAT only allows for constant auxiliary loads or a priori defined auxiliary loads for hybrid fuel cell architectures. As expected the figure shows significant variations between the actual and simulated auxiliary loads. For the 505 seconds shown the actual loads are generally less than the simulated loads.

Over the remaining period of the UDDS test cycle the actual load is generally more than the simulated load. The variation can be correlated to vehicle speed as the first 505 second of the UDDS cycle represent the majority of the high speed portion and as presented in the last section the 12V load decreases as a function of vehicle speed and the 24V load decreases as a function of fuel cell power – both of which will be present in the first 505 seconds of the UDDS cycle. Improving this model will require changes to the PSAT framework to allow for additional information to be passed to the auxiliary load, thereby allowing for a variable auxiliary load model. The 12V auxiliary load model could be integrated into the fuel cell component model block in PSAT to allow for the load to vary as a function of fuel cell power; however, this

approach was not taken as it would not allow for a comparison of PSAT fuel cell output power with the measurements obtained during dynamometer testing.

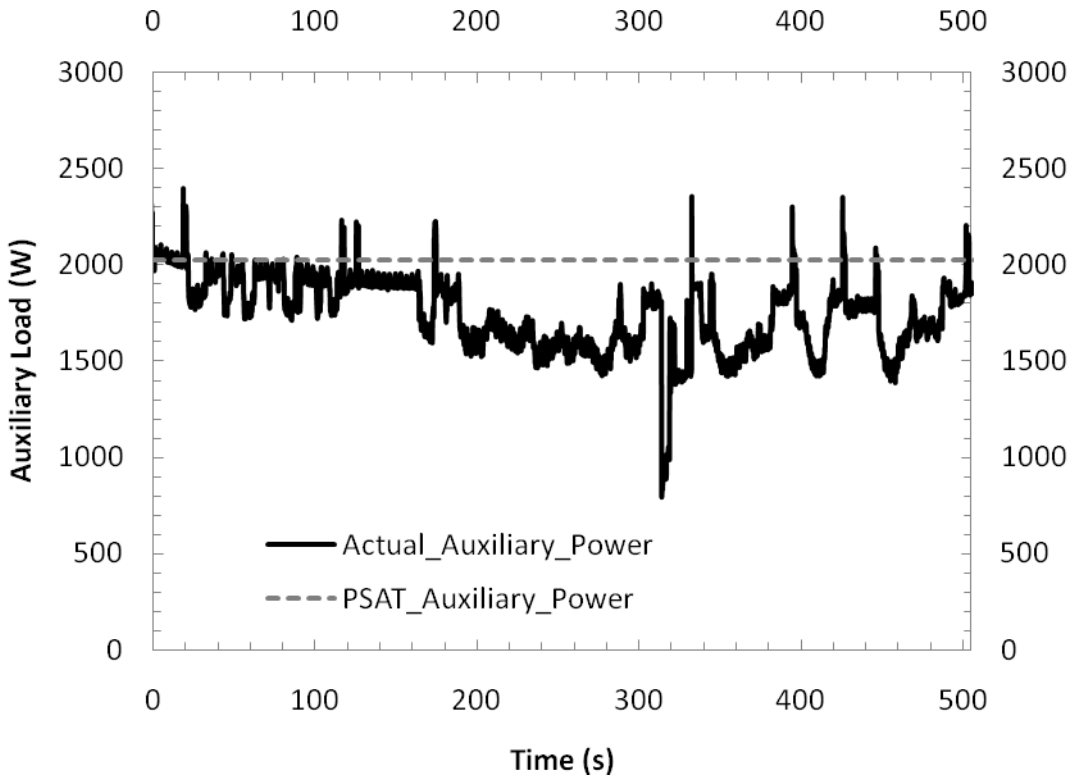

Figure 51 – Actual and simulated combined 12V and 24V auxiliary load for the first 505 seconds of a UDDS test cycle

The battery output powers measured using the Hioki probes and the SOC values reported by the Cobasys battery controller over CAN are compared to the simulated values in Figure 52 and Figure 53 respectively. Both curves demonstrate a relatively similar behavior, suggesting that the hybrid control and battery models are accurate. The battery model had been developed based upon operational data from on-road vehicle testing. The PSAT initialization file for the battery model is provided as Appendix D. The accuracy of the hybrid control model is to be expected as both the control logic for the onboard controller and for the PSAT model consist of the same Simulink code.

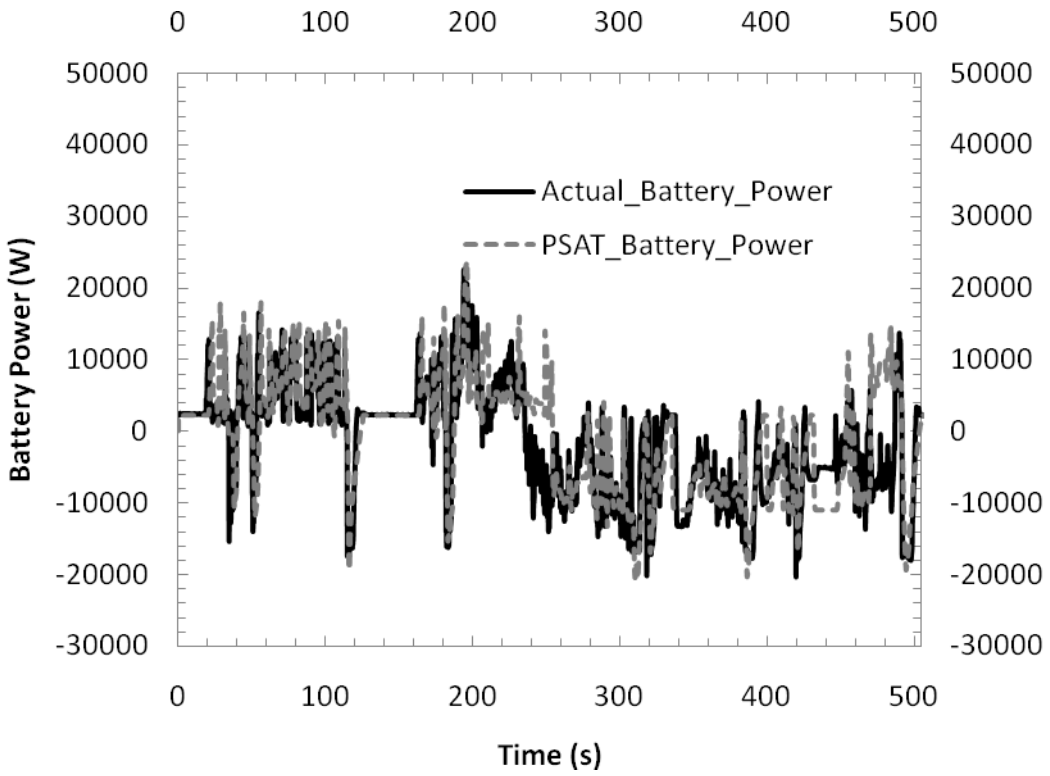

Figure 52 – Actual and simulated output battery power for the first 505 seconds of a UDDS test cycle

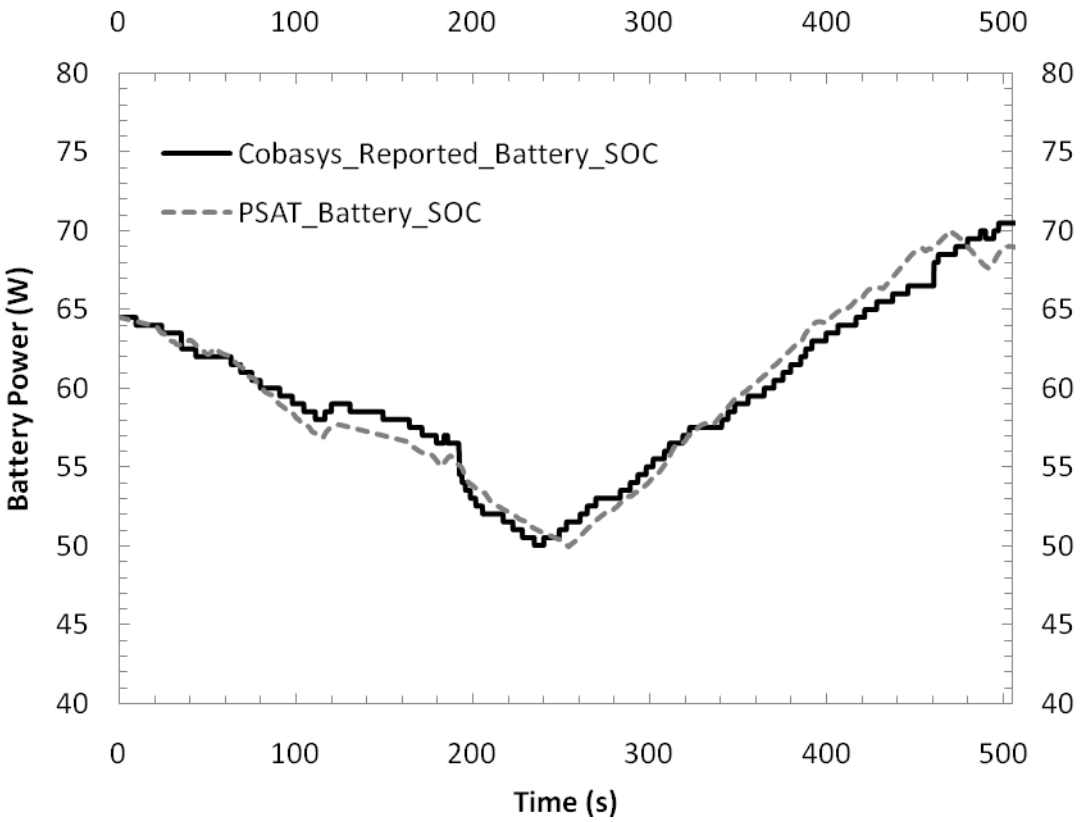

Figure 53 – Actual and simulated battery state-of-charge for the first 505 seconds of a UDDS test cycle

DC/DC output, fuel cell output, and hydrogen consumption rates are provided as Figures 53, 54, and 55 respectively. These curves also show a strong correlation between the actual and simulated vehicles, thereby further validating the hybrid control model and also validating the DC/DC and fuel cell models. The one notable consideration is that drop in DC/DC power, fuel cell, and hydrogen consumption rates during braking events in the PSAT result. This is a result of the simulated vehicle model transitioning from propulsion to a braking strategy with different fuel cell power algorithms. This is resolved in future simulations as the hybrid control propulsion algorithm is replicated in the braking algorithm.

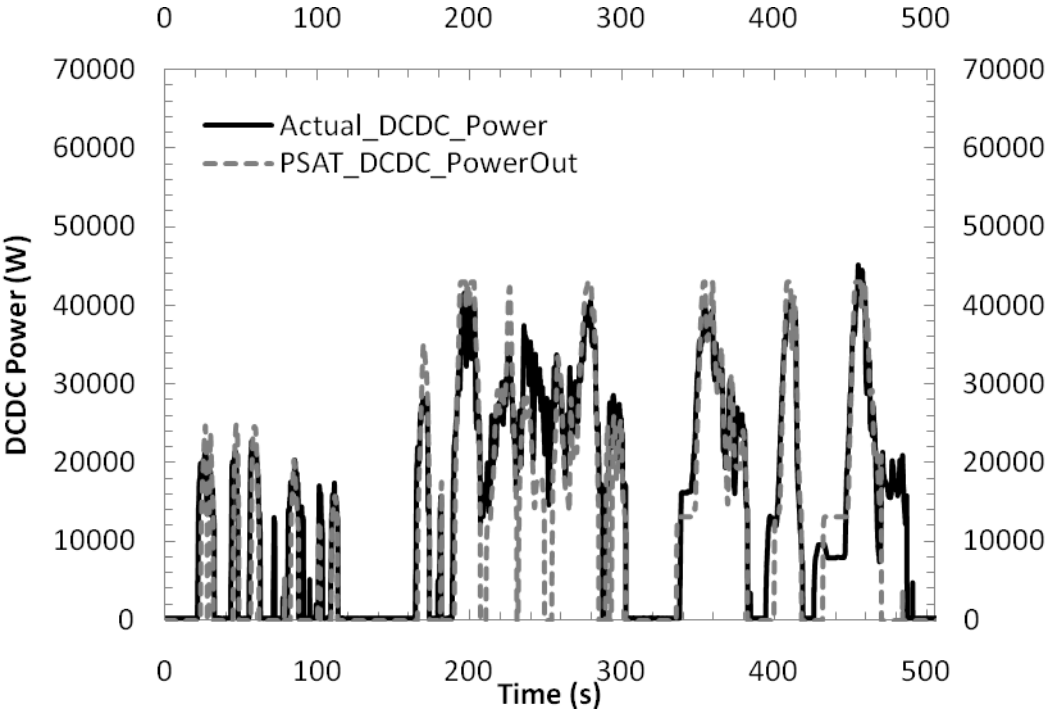

Figure 54 – Actual and simulated DC/DC output power for the first 505 seconds of a UDDS test cycle

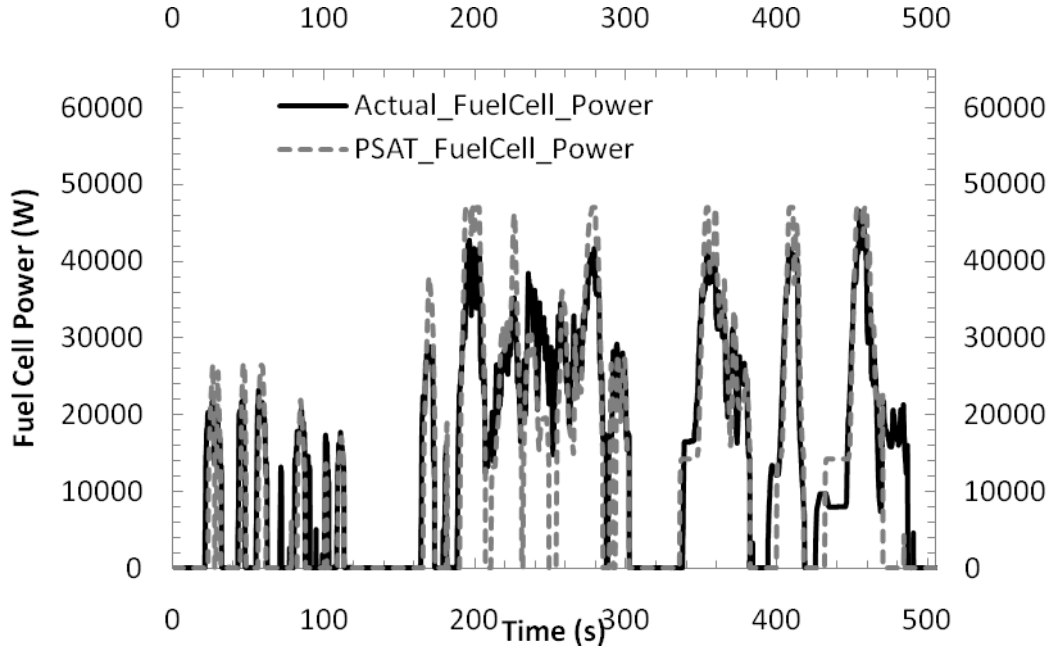

Figure 55 – Actual and simulated fuel cell output power for the first 505 seconds of a UDDS test cycle

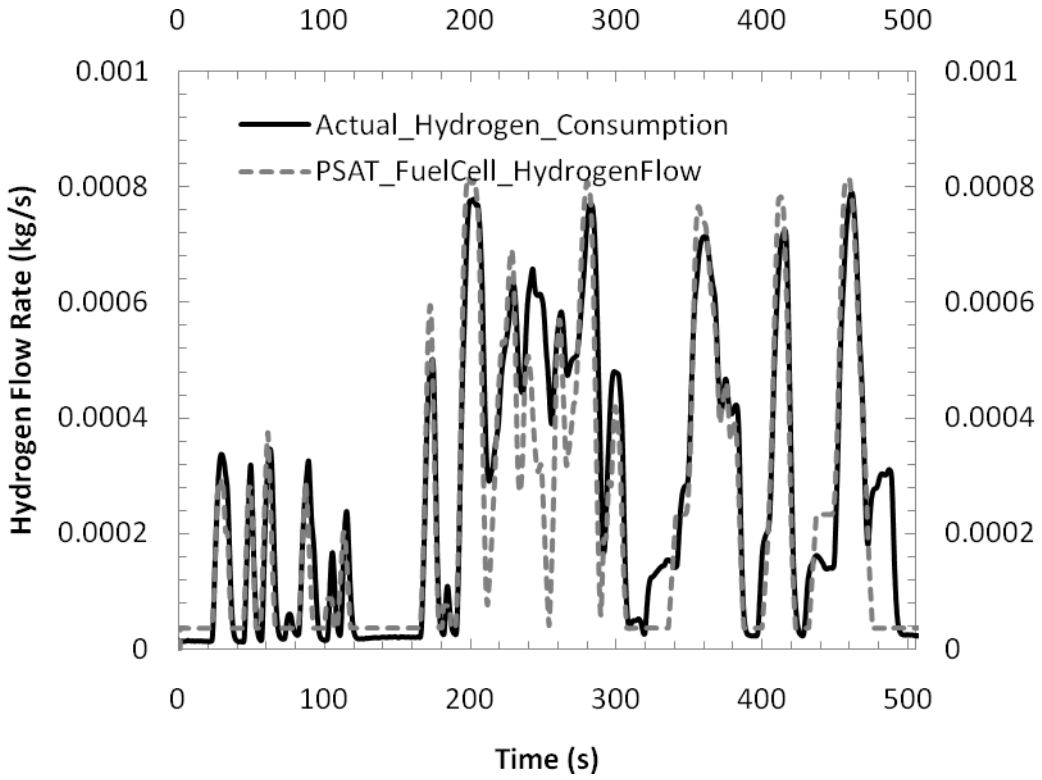

Figure 56 – Actual and simulated hydrogen consumption rate for the first 505 seconds of a UDDS test cycle

A summary of the energy consumed and component efficiency is provided as Table 12. The table demonstrates that the component models are approximating real-world performance very closely during propulsion; however, there are two significant differences during regenerative braking and battery charging. Specifically, the motor model overestimates the energy lost in the motor during regenerative braking. Additionally, the battery model underestimates the energy lost in the battery during charging. As discussed earlier, the regenerative braking is severely limited due to voltage limits on the motor. In addition, most of the energy does not cycle through the battery. The actual error in energy consumption for the first 505 seconds of the UDDS drive cycle is 3.7%. Therefore, although these variations are significant in relative terms, they not significantly in absolute terms.

Table 12 - Summary of component energy loss and efficiency for the first 505s of the UDDS drive cycle

Component	Actual		Simulation	
	Energy Loss (Wh)	Efficiency (%)	Energy Loss (Wh)	Efficiency (%)
Motor -Traction	232	85.2%	230	84.3%
Motor -Generator	13	95.1%	52	84.2%
Battery Discharge	15	95.9%	17	96.1%
Battery Charge	45	92.3%	25	95.5%
Fuel Cell	2522	43.4%	2338	42.9%
DCDC and Blower	137	93.3%	148	91.6%
Auxiliary	250		284	

The overall results of the entire UDDS validation are summarized in Table 13. The results clearly demonstrate the accuracy of the developed hybrid fuel cell vehicle model. The model is evidently suitable for use as a baseline vehicle model for testing alternative design scenarios and for incorporating component degradation models. The unadjusted energy values are calculated directly from the hydrogen consumed. The adjusted energy values combine the hydrogen consumption with a correction to account for differences in starting and ending battery SOC. To accurately account for the change in battery SOC, the change in capacity is divided by the average fuel cell and DC/DC efficiencies to determine the approximate amount of hydrogen required to correct for the SOC changes.

Table 13 - Summary of UDDS Model Validation

Parameter	Actual	Simulation
SOC change	-4.50%	-4.50%
Hydrogen (kg)	0.2396	0.2357
Distance (miles)	7.45	7.45
Unadjusted Fuel Consumption (L/100km equivalent	7.51	7.39
Adjusted Fuel Consumption (L/100km equivalent)	7.72	7.60
Unadjusted Fuel Economy (mpge)	31.3	31.8
Adjusted Fuel Economy (mpge)	30.5	31.0
Error	**1.62%**	

Simulation results for of the hybrid fuel cell vehicle model for HWFET and US06 test cycles are provided as Table 14. Due to the voltage limits imposed by the Ballard motor inverters, a limited amount of regenerative braking is recaptured. As a significant portion of braking energy is lost through mechanical braking a significant gain in fuel economy on the highway cycle is expected. Correspondingly, the aggressive driving nature of the US06 results in lower fuel economy but of the loss of some energy from braking.

Table 14 – Equivalent fuel consumption and fuel economy of the hybrid fuel cell vehicle model for UDDS, HWFET, and US06 drive cycles

Drive Cycle	**Adjusted Fuel Consumption (L/100km equiv)**	**Adjusted Fuel Economy (mpge)**
UDDS	7.60	31.0
HWFET	5.69	41.4
US06	8.65	27.2

The next chapter introduces component degradation and develops models for battery degradation. These causal component degradation models are then incorporated into this baseline vehicle in Chapter 5.

Chapter 4

Causal Component Degradation

The validated baseline hybrid fuel cell vehicle model developed in Chapter 3 is a Beginning-Of-Life model. As discussed in Chapter 2, fuel cells and batteries exhibit significant degradation over time (calendar-life) and use (cycle-life). The cycle-life of the components has been shown to be heavily dependent on the component's duty cycle. This chapter describes accelerated battery testing and develops a causal battery degradation model. A causal fuel cell degradation model is also developed based upon literature. In Chapter 5 these causal degradation models will be integrated into the baseline hybrid fuel cell vehicle model to enable evaluation of sizing and control decisions on lifetime vehicle performance.

4.1 Battery Degradation Mechanisms and Measurement

As described in Chapter 2, lithium ion battery chemistries are the most likely technology for advanced hybrid powertrains in the future due to superior power and energy densities, both gravimetric and volumetric, as well as anticipated lifetime performance. The lithium iron phosphate chemistry is a chemistry currently targeted for automotive application. In order to develop an accurate causal degradation model the degradation mechanisms and measurement methods must be understood.

A representative schematic of a lithium ion battery is provided as Figure 57. Copper and aluminum foils are used as the current collectors for the anode and cathode respectively. Progressing inwards, the anode is primarily carbon in the form of Meso Carbon Micro Beads (MCMB) and synthetic graphite (SFG) in a PolyVinylidine Binder (PVdF). With the exception of titanate-based anodes, most anodes in the current literature incorporate various carbon-based

structures. There are numerous electrode materials currently under evaluation, most consisting of >80 wt% of active material with <20 wt% blend of graphite, acetylene or carbon black, and PVdF binder. The specific cathode composition presented in Figure 57 is a nickel-cobalt based electrode used by Abraham in power fade studies [91]. The separator and electrolyte must have high lithium conductivity, electrically insulating, and form stable, ionically-conductive passivation layers on the cathode and anode. While variations have been investigated, the most common electrolyte consists of lithium hexaphosphoflourate ($LiPF_6$) in a solvent that contains a cyclic alkyl carbonate such as Ethylene Carbonate (EC) and a linear alkyl carbonate such as Ethyl Methyl Carbonate (EMC). The cyclic carbonate assists in the dissolution of salts while the linear carbonate lowered the viscosity to promote rapid ion transport [121]. Celgard is a common separator material used in many lithium batteries, and is primarily a polypropylene and/or polyethylene membrane structure.

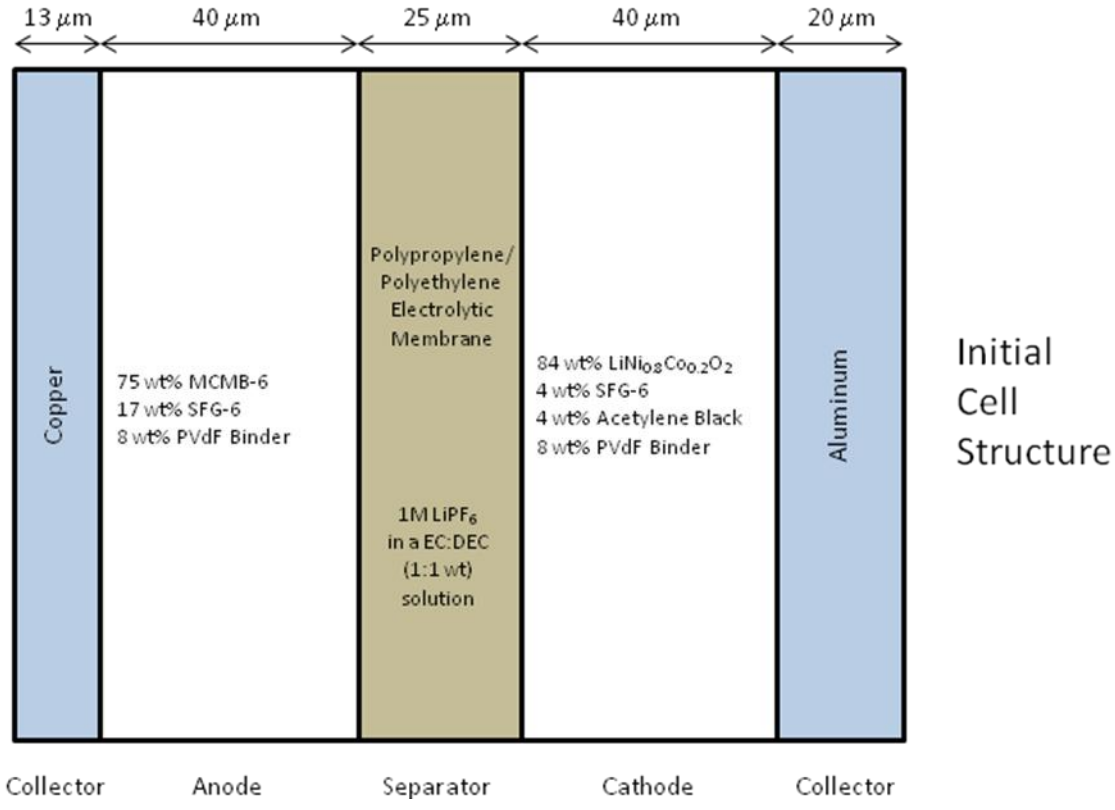

Figure 57 - Representative schematic of the initial structure for a lithium ion secondary battery chemistry

A characteristic phenomenon common to almost all of lithium ion chemistries is the formation of a substantial passivation layer at the anode-electrolyte interface known as the Solid Electrolyte Interface (SEI)[122]. This passivation layer of primarily lithiated alkyl carbonates is created during the first charging cycle of the battery and represents a significant loss of cyclable lithium within the cell [91]. To compensate for the initial loss of lithium, the cathode is first assembled with an excess of lithium. The amount of cyclable lithium lost in the first cycle, and therefore the excess initial loading of the cathode, ranges between 8% for graphitic anodes such as MCMB up to 50% for hard carbon anodes [122]. A small surface film is also formed at the electrolyte-cathode interface; however, this film is not a major source of cyclable lithium loss.

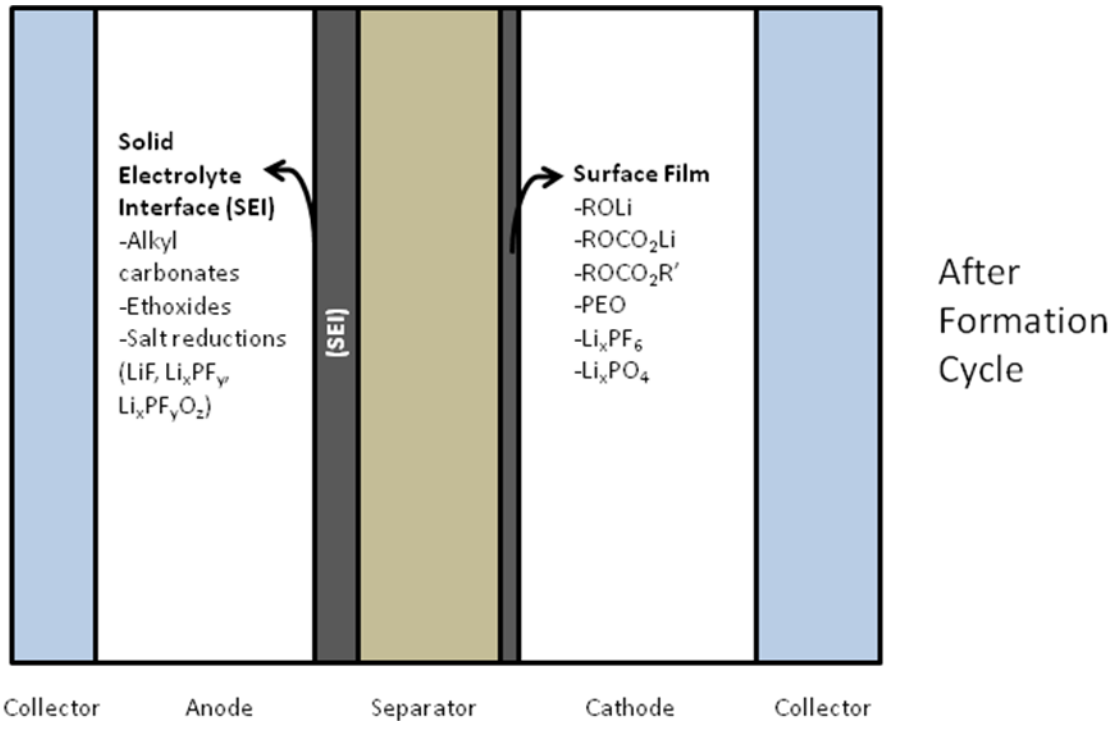

Figure 58 - Representative schematic of a lithium ion secondary battery chemistry after a formation cycle

As previously mentioned, batteries exhibit both power and capacity fade. These phenomenon are manifested through multiple mechanisms; however, a few key degradation mechanisms have been identified to be common factors among most lithium chemistries. The primary mechanisms are illustrated in Figure 59. Specifically, these include:

- SEI growth due to fracturing of the passivation layer resulting in further loss of cyclable lithium (capacity fade),

- Increase in electrolyte-cathode surface film growth increasing resistance to ion transport during the intercalation/deintercalation processes at the cathode (power fade), and
- Loss of electrode active material, more predominately at the anode. Causes include fracture of the graphite plane due to excessive mechanical stresses on the lattice during intercalation (charging to high SOC) causing electrical isolation, and blocking of the intercalation site by undesired species intercalation (capacity and power fade).

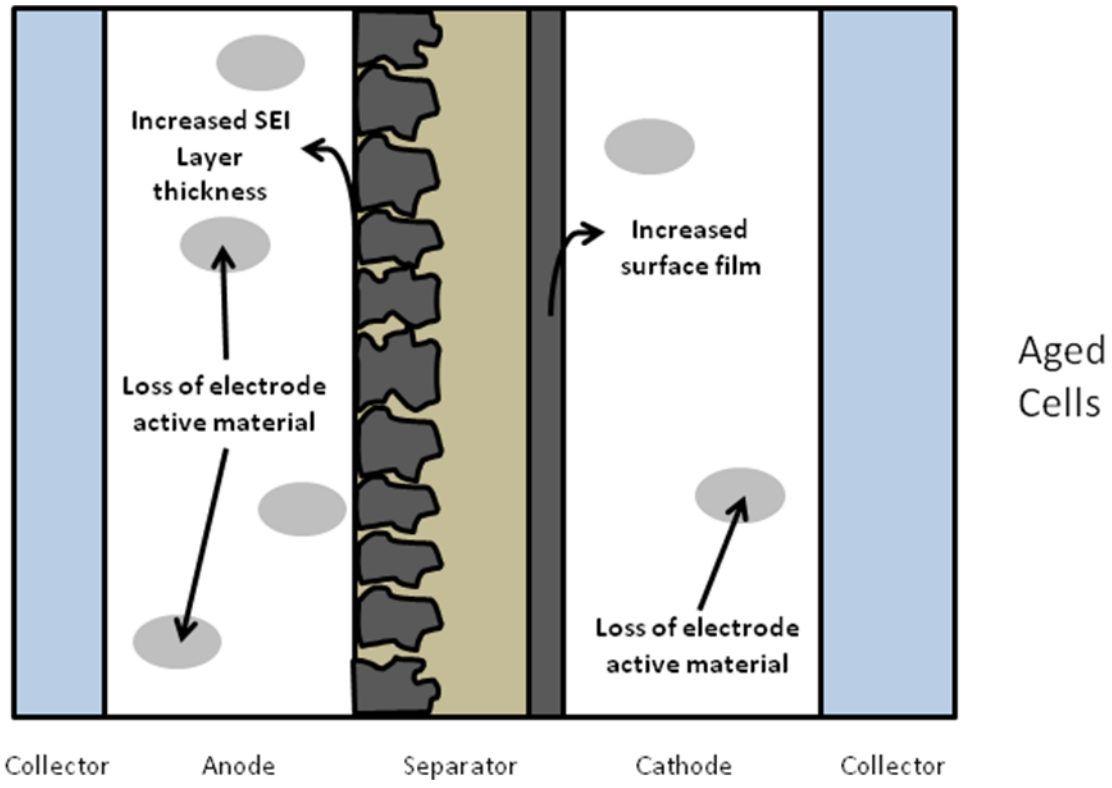

Figure 59 - Representative schematic of an aged lithium ion secondary battery chemistry

To properly identify and quantify the degradation mechanisms, robust and reliable diagnostic methods are required. A significant number of analytical methods have been employed to understand fundamental behavior and material science of lithium ion batteries. Methods have included XPS, Scanning Electron Microscopy (SEM), Electrochemical Impedance Spectroscopy (EIS), Cyclic Voltametry (CV), and Differential Capacity Analysis (DCA). The electrochemical characterization methods have been employed on both half cells and full cells. Half cell

measurements are obtained by the inclusion of a reference electrode into the cell, which permits the discrimination of the effects of individual electrodes. The method using a lithium-tin reference electrode is described in detail by Abraham [123]. The two methods that been employed extensively in durability studies have been EIS and DCA. Therefore, methods for interpreting the results of the experiments will first be introduced, followed by the key results of the durability studies to date.

A schematic representing a standard Electrochemical Impedance Spectra (EIS) for a secondary lithium ion chemistry is shown in Figure 60. The figure is labeled with the generally accepted interpretation of the spectra to physical phenomena [123]. The explanation of the genesis of the interpretations of spectra to physical phenomena is outside the scope of this thesis but is developed thoroughly by Dees et al [124]. There exist five parameters of interest in an EIS for a secondary lithium battery:

- F_{high}: the frequency at the high frequency minimum point. This value is generally on the order of 1kHz and is inversely proportional to the time constant (~1ms) of the corresponding physical phenomena; and
- Z'_{high}: the real component of the impedance spectra at the high frequency minimum point. Corresponds to electrical conductivity of the electrodes, ionic conductivity, and the contact resistance,
- F_{low}: the frequency at the low frequency minimum point. This value is generally on the order of 1Hz and is inversely proportional to the time constant (~1s) of the corresponding physical phenomena,
- Z'_{low}: the real component of the impedance spectra at the low frequency minimum point and corresponds to the sum of interfacial phenomena, electrical conductivity of the electrodes, ionic conductivity, and the contact resistance,
- F_{mid}: the frequency at the maximum imaginary impedance for the semi-circular arc of the spectra. The value has proven to correspond to the chemical nature of the SEI by the following equation:

$$f_{mid} = \frac{1}{2\pi\rho\epsilon} \quad (39)$$

Where ρ corresponds to the resistivity and ε corresponds to the permittivity of the SEI.

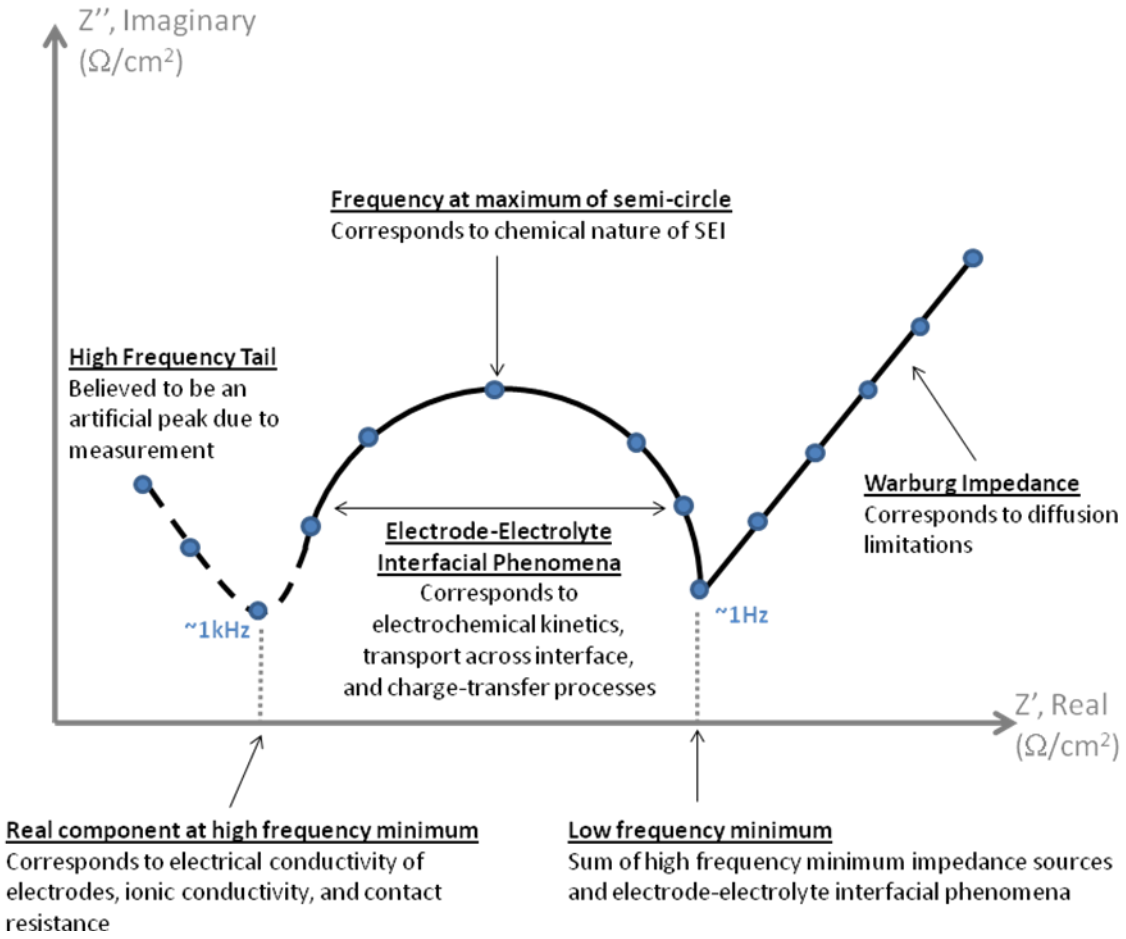

Figure 60 - Representative Electrochemical Impedance Spectrum for a standard secondary lithium ion battery (adapted from [125,123,124])

Considering the key variable of an EIS, an increase in either Z' value represents an increase in the real component of the internal resistance of the battery. A decrease in F_{low} or F_{high} corresponds to a subsequent increase in the time constant of the determining phenomena, resulting in a slower system response. A decrease in F_{mid} corresponds to an increase in the resistivity of the SEI.

Abraham et al. have utilized EIS on lithium batteries extensively, researching the validation of using a lithium-tin reference electrode as opposed to the highly reactive incumbent solid lithium reference electrode [123], the role of SEI in causing the surface film at the electrolyte-cathode interface [92], to quantify the effect of the temperature at which the EIS is captured [94], and the impedance of various electrolytic salts and additives [121]. In these studies Abraham concluded that:

- the lithium-tin reference electrode is a suitable replacement as the half-cell spectra reliably sum to the full-cell spectra once cell balancing is accounted for,
- diffusion of SEI components across the cell is not the cause of the electrolyte-cathode surface film. This was demonstrated by the existence of a surface film in a battery with a titanate anode that does not form an SEI,
- temperature has a major impact on the EIS obtained, in particular on the aged cells. To capture the appropriate state of the battery, if possible, the test method should be performed at the same temperature as the average temperature of the battery during operation, and
- Lithium hexaflourophosphate (LiPF6) exhibited the lowest impedance when compared to borate and flouroborate based electrolytes.

Utilizing a reference electrode, the contribution of the electrodes can be differentiated as the battery ages. A series of studies have utilized EIS to evaluate the impact of operating conditions on the power fade degradation mechanisms previously described [94,123,92,121]. Representative EIS spectra are provided as Figure 61. The cathode is clearly the dominant contributor to overall cell degradation and the specific degradation mechanism is increased resistance related to electrode-electrolyte interfacial interference, caused by surface film growth. Frequency minimums also increased implying slower time constants for the governing phenomena.

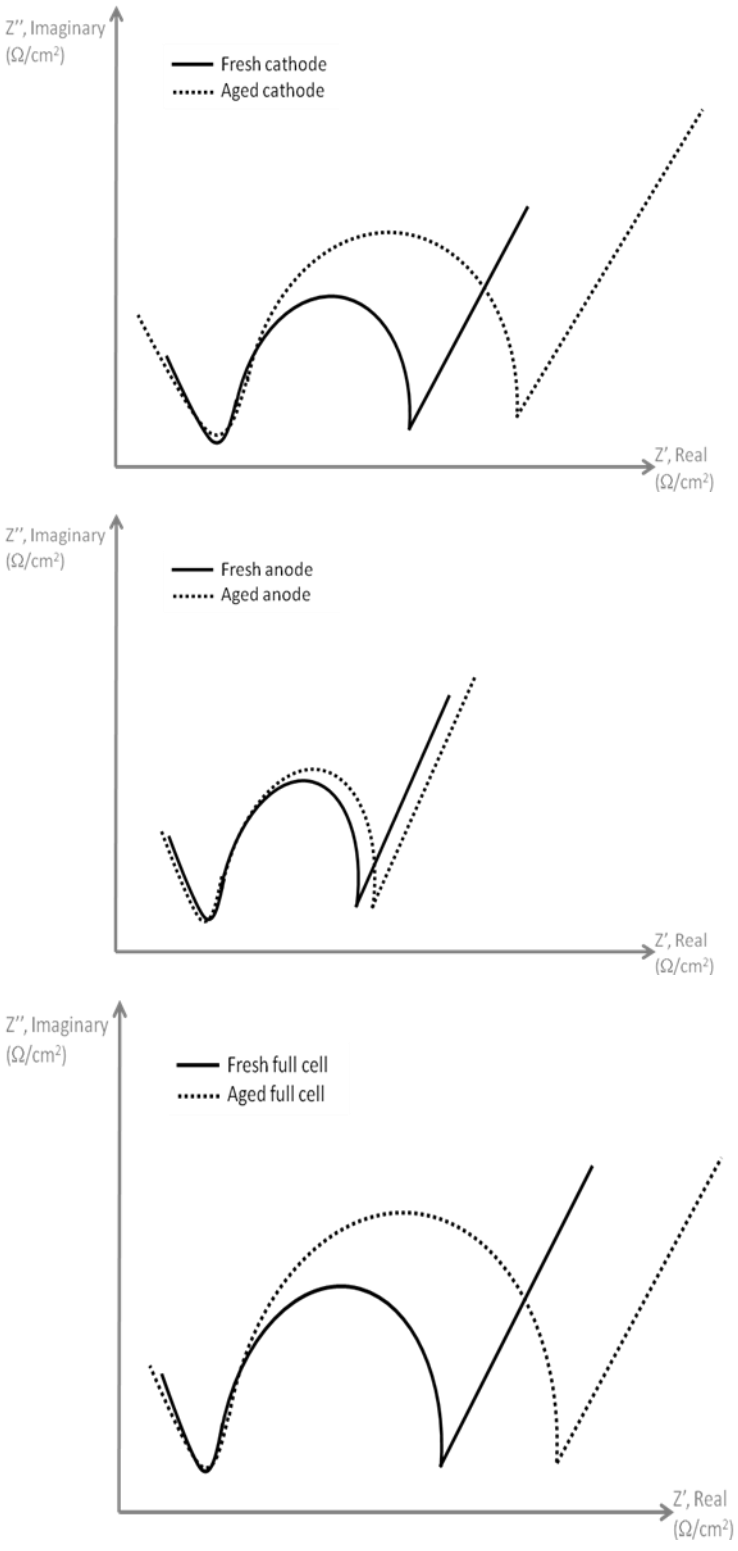

Figure 61 - Representative Electrochemical Impedance Spectrum for a standard secondary lithium ion battery (adapted from [125,123,124])

For lithium ion battery degradation literature the following has been discussed:

- degradation is in the form of both capacity and power fade,
- time (calendar life) and operation (cycle life) impact battery degradation,
- key factors that impact the degradation rate have been identified, and
- major degradation mechanisms for lithium batteries is understood.

Significant work has been performed by the US National Labs on the testing methods for batteries intended for hybrid vehicle applications. As introduced in Chapter 2, Idaho National Laboratory (INL) has published battery testing manuals for both charge-sustaining and charge-depleting batteries in addition to a publication developing a method to develop lifetime performance projections based upon 1 to 2 years of accelerated testing. These publications are of significant value; however, the results of batteries evaluated under the prescribed test methods will have limited ability to support causal degradation modeling. The test methods utilize standardized test profiles and thereby do not allow for the development of a degradation model based upon varied component duty cycles. To generate a data set for a causal battery degradation model based on vehicle operation parameters a hybrid test stand was fabricated and is described in the next section.

4.2 Hybrid Powertrain Degradation Test Stand

As part of this thesis project a hybrid fuel cell powertrain test stand was designed and built to perform component degradation studies and to enable scaled Component-In-The-Loop (CIL) testing. Due to cost and safety implications the system was designed at $1/50^{th}$ scale of the full powertrain to allow for the testing of smaller fuel cells and single cell batteries. The test stand was designed to approximate the actual vehicles as closely as possible, including the use of the same high-power contactors and controller. A schematic representation of the system is provided as Figure 62 and a picture of the actual test stand is provided as Figure 63. To allow for significant flexibility, high and low voltage supplies and loads were integrated. The low-voltage supply and load were a Lambda ZUP20-40-800 and TDI Dynaload RBL232 50-150-800 respectively. The high-voltage supply and load were the Lambda JFS1500-58 and Sorensen SLH300-18-1800 respectively. The system was designed to allow for fuel cell only, battery only, and hybrid testing. The test stand computer manages the supply and load to simulate the motor, fuel cell (during battery only testing), and the battery (during fuel cell only testing).

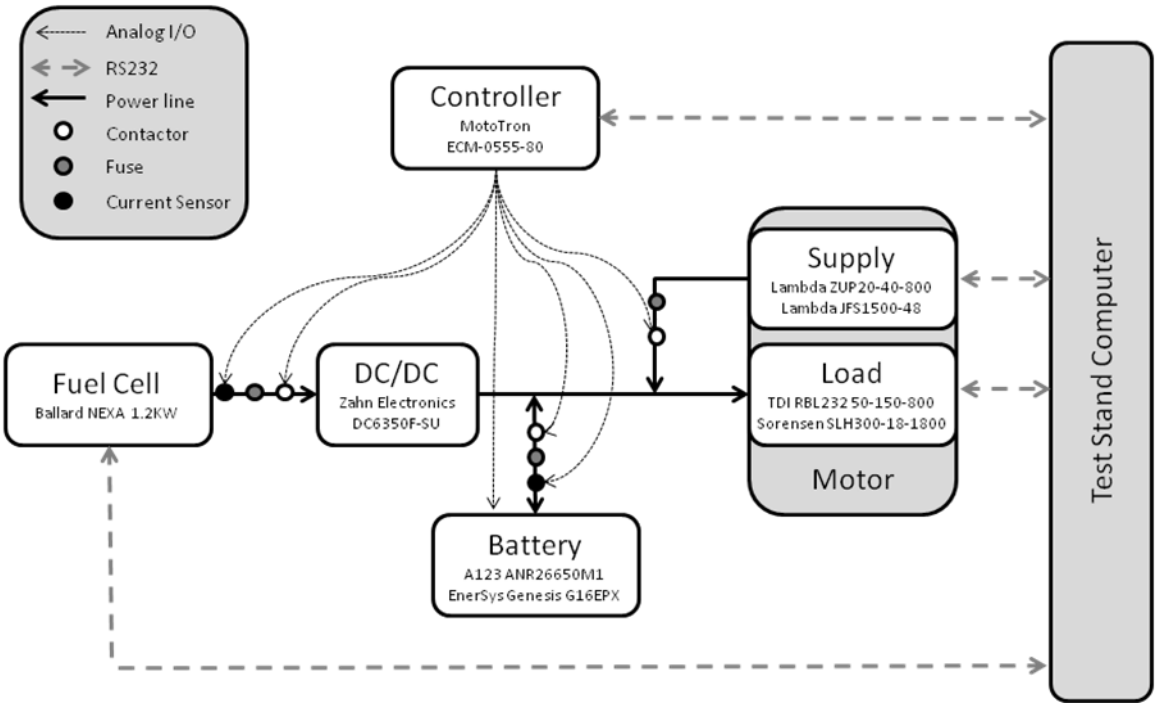

Figure 62 – Schematic representation of hybrid fuel cell powertrain test stand (E-stop circuit is not shown)

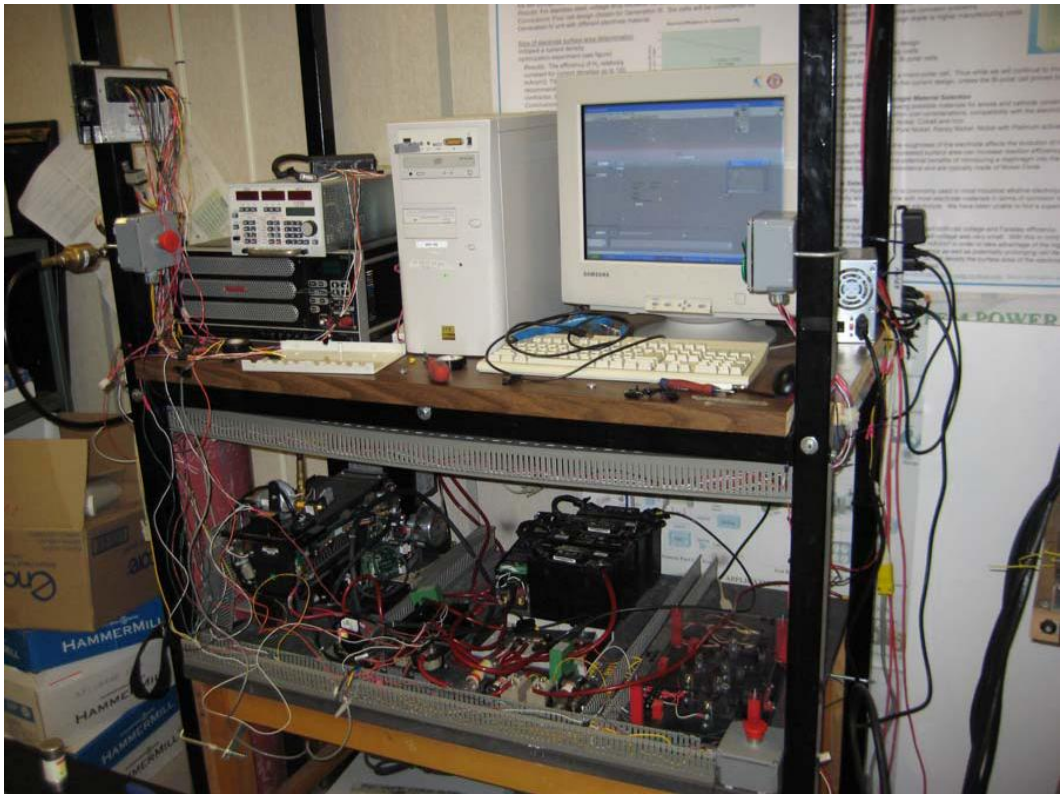

Figure 63 – Picture of hybrid fuel cell powertrain test stand

The MotoTron controller monitors the temperature, voltage, and current of the batteries. The controller also monitors the fuel cell current, senses the state of toggle switches that are used to determine the mode of operation and "start" request, monitors the state of the E-Stop (i.e. emergency shut-down) circuit, and controls the contactors. The controller interfaces to the test stand computer via RS232 communication. The test stand computer determines the set points for the supply and load and communicates the request over RS232. During fuel cell operation the test stand computer also runs the Ballard NEXA software that interfaces to the fuel cell power module via RS232. The Simulink control code written for the MotoTron controller and the LabView VI written for the Test Stand is provided in the Appendix B (due to the size of the code the screenshots are truncated, full code is available upon request).

General data acquisition is performed by the test stand computer except during testing that requires a high logging rate (1ms logging) when a Kvaser data-logger is attached to the MotoTron controller via CAN to enable required logging rate. An E-stop circuit was integrated that caused the immediate opening of the contactors on the power lines in the event that one of two E-stop buttons was hit – the E-stop circuit controls the 12V supply to the normally-open contactors, thereby acting in series with the MotoTron control circuit that controls the ground path of the contractor control circuit.

The lithium battery stand was built to hold three A123 lithium batteries in series. The initial revision of the battery holder did not include active cooling; however, initial commissioning of the stand found that that the batteries would reach the maximum recommended temperature within 10 seconds at 60A. The second iteration of the battery holder included voltage probes and active convection cooling by three 3.5" fans.

During initial commissioning thermistors were placed on both the top and side of the battery. The thermistors circuits were initially calibrated using a hot water bath. The top of the battery was directly exposed to the cathode current collector while the side of the battery was wrapped in a covering paper. For safety reasons the side of the battery was preferred as there was a concern that during extended testing the ground line of the thermistors would have come in contact with the battery, which would have caused a short through the sensing circuit. The initial tests demonstrated that the top-mounted and side-mounted thermistors measurements were within 1.0°C. The side mount location was used for all subsequent tests. The thermistor was attached using thermal paste to ensure good thermal contact.

The Zahn DC/DC converter is limited to a minimum 24V output; therefore an alternative battery was required during hybrid testing as the nominal output voltage of three A123 cells in series is approximately 11V. Four EnerSys Hawker Genesis 12V lead-acid batteries were strung in series for the hybrid testing. During commissioning the Zahn DC/DC converter was set to a constant voltage output of 49V. A result from two step tests in hybrid operation is provided as Figure 64. Upon the step in load current the battery provides instantaneous power that decays to 2A as the DC/DC converter increases the amount of fuel cell power.

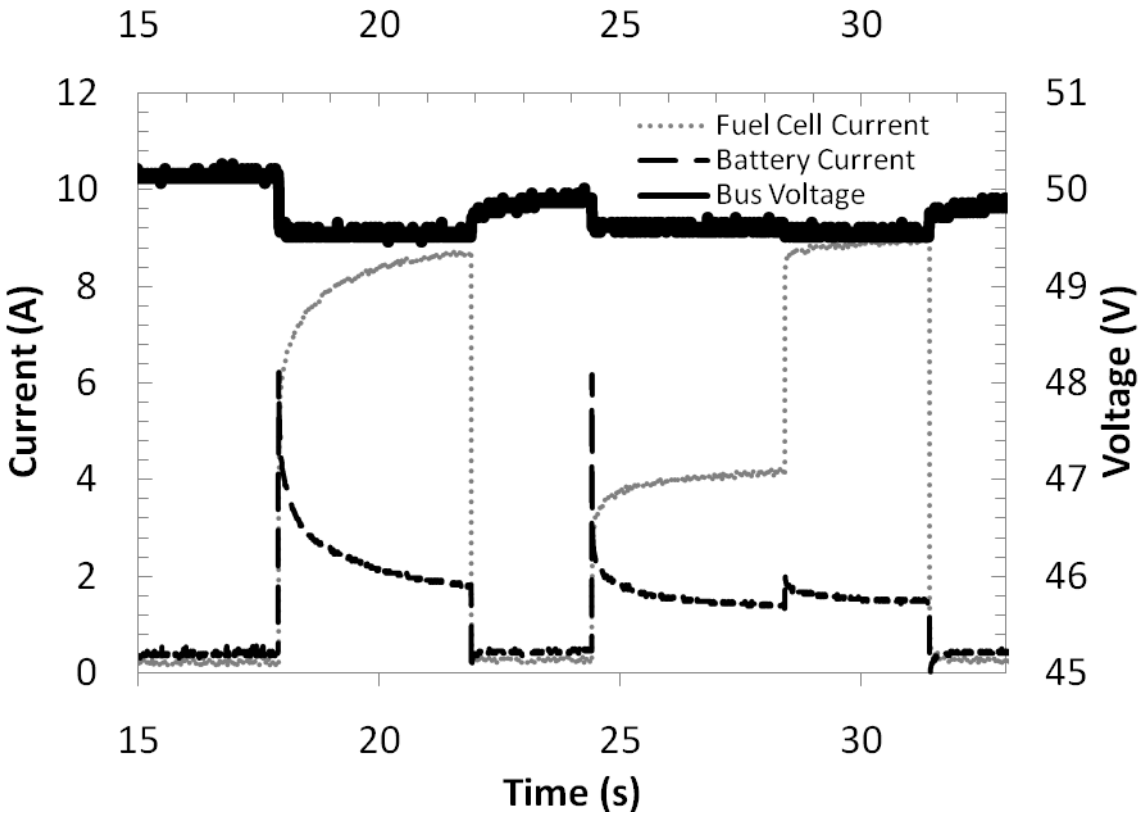

Figure 64 – Fuel cell and battery currents during a 10A load step and a 5A/10A two stage load step on hybrid test stand. DC/DC is set to a constant output voltage of 49V.

Load currents and voltages were reported by the TDI Dynaload. The Dynaload was operated in the 150A/10V mode of operation, which is specified to have 0.25% accuracy corresponding to 375mA and 25mV. The bus voltage was measured using a voltage divider circuit feeding a 10-bit analog to digital input on the MotoTron controller and was found to be within 150mV of values obtained from a Scope Digital Multimeter. The fuel cell current read from a hall-effect sensor

into a 10-bit analog to digital input on the MotoTron controller. The hall-effect sensor utilized had an accuracy of 0.5% the full scale corresponding to 250mA.

To properly perform a CIL emulation of the hybrid fuel cell vehicle described in Chapter 3 the DC/DC would have to be operated in current-control rather than voltage-control. To perform the battery degradation studies; however, this is not required as the fuel cell and DC/DC operation will be simulated by the power supply.

4.3 Battery Degradation Studies

A simplified schematic of the test stand operation during battery degradation studies is provided as Figure 65. The DC/DC and fuel cell are removed from the main bus. During initial testing balancing issues between the three A123 batteries in series was observed causing uneven SOC swings among the batteries. Given that SOC is a major driver of battery degradation the studies were modified to test cells individually.

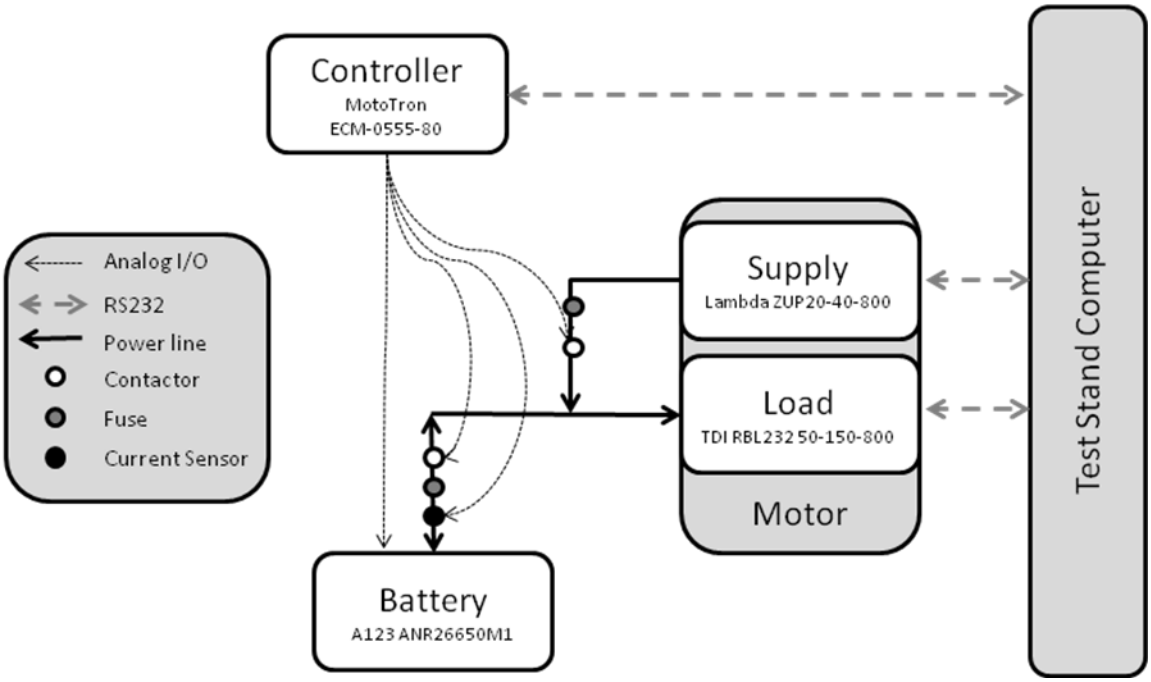

Figure 65 – Schematic representation of hybrid fuel cell test stand during battery degradation studies

The test procedure included the following nine components:

1. Nominal 1C Discharge (2.0V cut-off).
2. Nominal 1C CC/CV Charge (2.3A/3.8V with 50mA cut-off).
3. Nominal 10C Discharge (2.0V cut-off).
4. Nominal 3C CC/CV Charge (7.2A/3.8V with 50m2A cut-off).
5. Nominal 0.5C Discharge (2.0V cut-off).
6. Nominal 0.5C CC/CV Charge (1.15A/3.8V with 50mA cut-off).
7. Polarization curve (0/10/20/30/40/50/60/50/40/30/20/10/0 A repeated).
8. Nominal 4.3C CC/CV Charge (9.9A/3.8V with 50mA cut-off).
9. Test cycle repeated 100 times.

The initial eight tests were used for establishing the reference battery performance at given cycle intervals. The reference performance tests were repeated after every 100 cycles of the test cycle (test procedure #9). The test was run continuously until for 1000 charge/discharge (test procedure #9) test cycles.

Three tests were performed with a constant 60A discharge (26C) and 10A charge (4.3C), operating over the entire useable SOC range. The discharge/charge curve is provided as Figure 66. The first section includes a 60A discharge curve until 77 seconds. At 77 seconds the 10A constant current charge continues until 482 seconds where the charge protocol transitions to constant voltage until a the current decays to under 50mA. The intent of these studies was not to replicate duty cycles representative of hybrid vehicle performance. The intent was to:

1. identify the maximum degradation rate expected under continuous power operation,
2. evaluate the variability between batteries, and
3. identify the trend of capacity and power fade over the life of a battery.

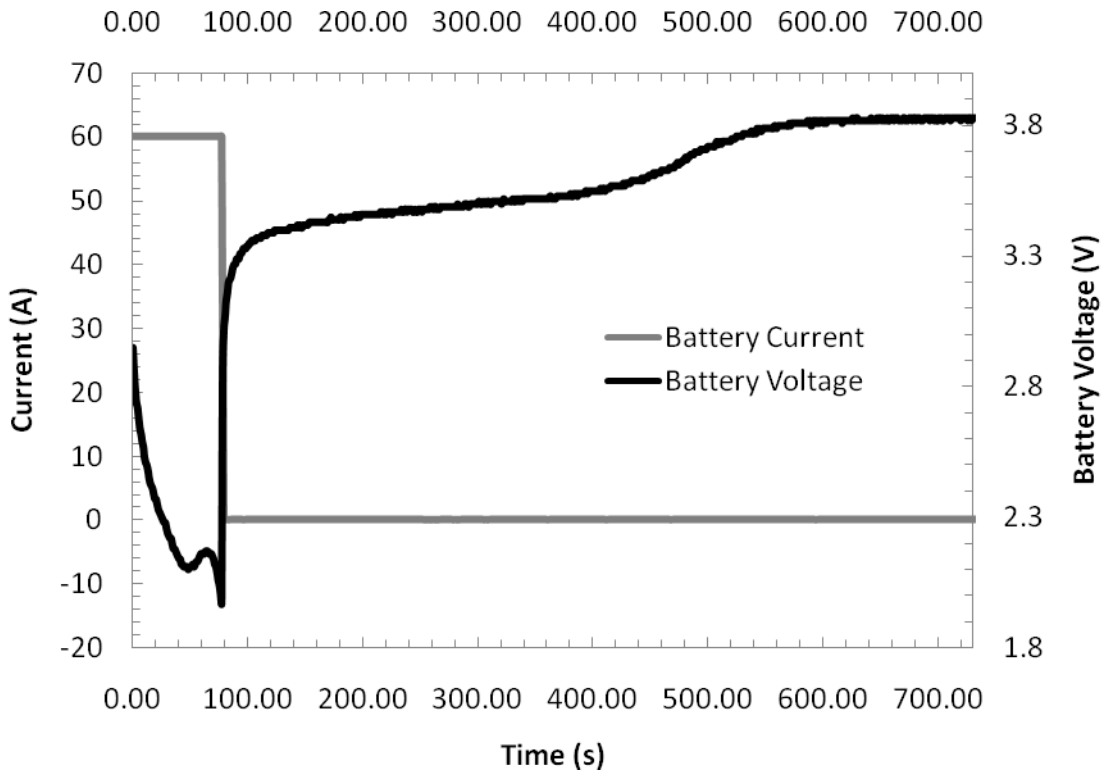

Figure 66 – 60A Discharge curve followed by a 10C charge CC/CV for the full SOC range. Temperature varies from 28ºC to 49ºC during the experiment.

The motivation for identifying the maximum degradation rate under continuous power operation was to validate the value of focusing on battery degradation. Should the battery exceed the lifetime performance requirements under high power, wide SOC range duty cycles the implication would be that the value of the research herein would be minimal. The averaged capacity fade results are given in Figure 67. The result clearly demonstrates that the capacity loss is significant over the first 1000 cycles. A more relevant representation of the battery capacity loss is as a function of energy delivered. The same capacity fade results are presented as a function of energy delivered in Figure 68. The standard deviation of the measurements across the three degradation studies are provided as error bars in both figures. The standard deviation across the three samples was found to be minimal. The results show a rapid capacity fade during initial operation followed by a slower capacity fade as the battery ages. As the battery has less capacity the later cycles deliver less energy. The phenomenon can be seen in Figure 68 in the spacing between subsequent data points. As each data point represents 100 test cycles the energy delivered between each successive data point decreases.

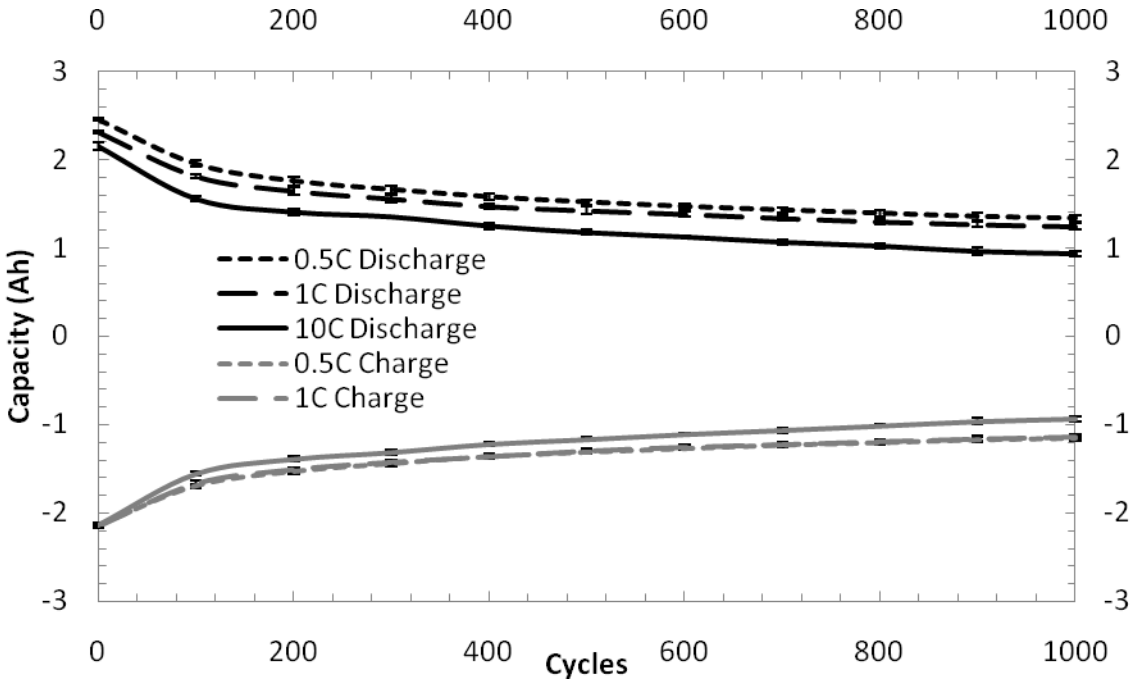

Figure 67 – Capacity fade of lithium batteries under 60A discharge, 10A charge, full SOC range, as a function of test cycle

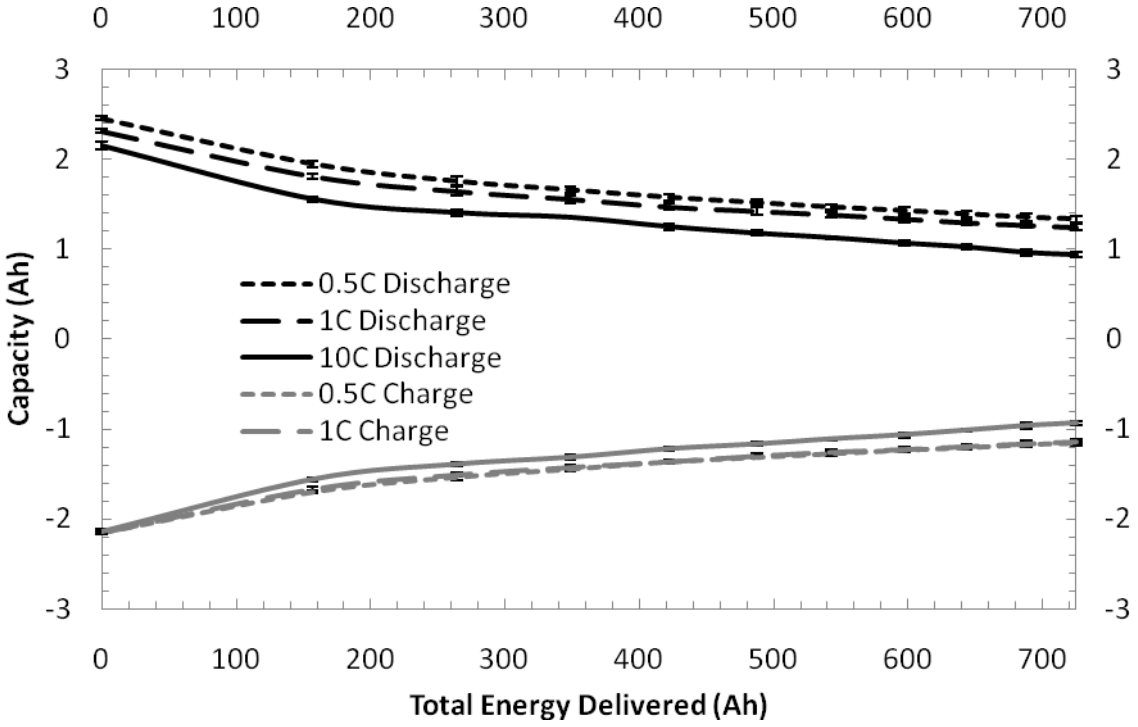

Figure 68 – Capacity fade of lithium batteries under 60A discharge, 10A charge, full SOC range, as a function of total energy delivered

The 60A results achieved the three objectives listed above. The capacity loss was significant and consistent across the batteries. The capacity loss was rapid during initial testing, slowing in rate as the battery continued to age. Observing the individual cycle results the length of time of the 60A discharge is significantly reduced after 200 cycles, thereby reducing the heat generated and subsequent battery temperature during the discharge process.

To evaluate the impact of the discharge rate and lower SOC limit three additional tests were performed with a constant 30A discharge (13C) and 10A charge (4.3C), over the entire useable SOC range. The lower SOC limit is achieved as a result of both the 60A and 30A tests discharging until a cut-off voltage of 2.0V is reached. Since the 30A testing will incur lower polarization losses the 30A tests will, in effect, discharge to a lower SOC. The average discharge and charge capacities for low current rates (0.5C) for both the 30A and 60A discharge tests are provided as Figure 69.

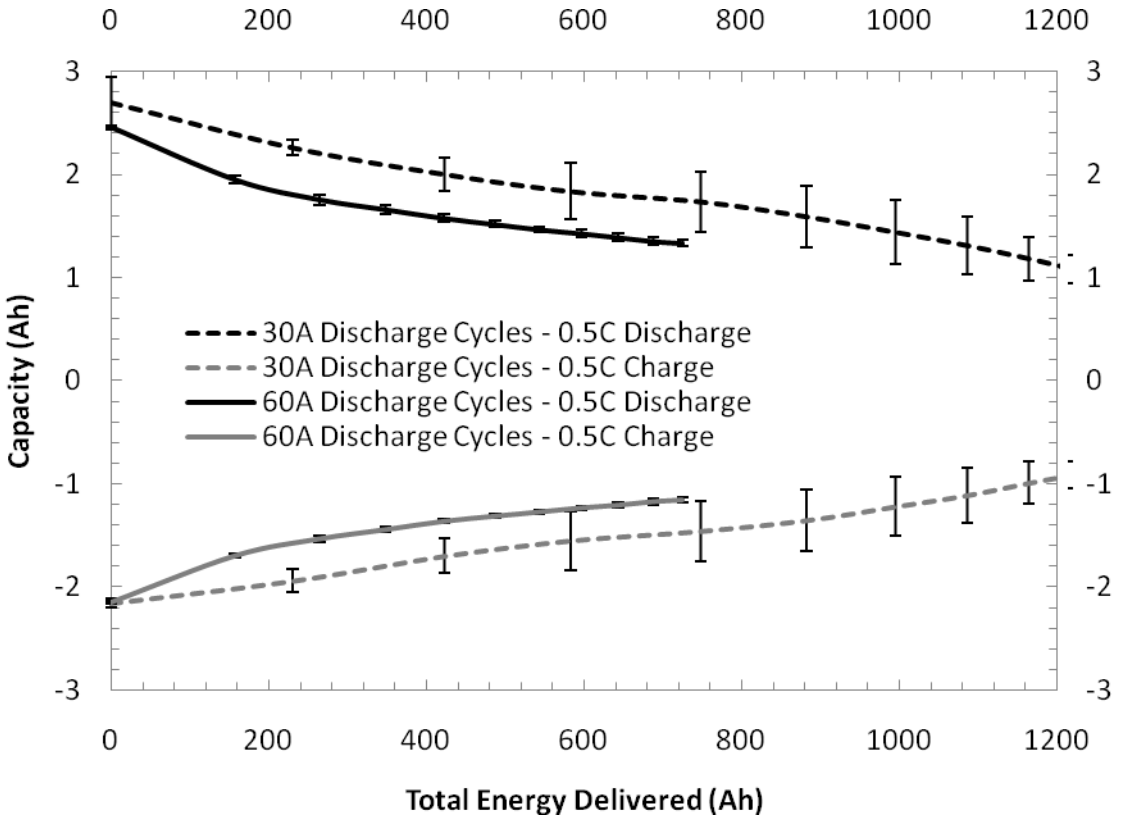

Figure 69 – Capacity of lithium batteries for 30A and 60A discharge tests, 10A charge, full SOC range, as a function of total energy delivered for 0.5C rates

In reviewing the differences between the 30A and 60A results key observations include:

- A variation between the 30A and 60A discharge capacities was observed at 0 Ah delivered (beginning-of-life). This result is unexpected. All batteries were purchased at the same time, from the same lot, and the variation highlights the variability in the fresh batteries in the as delivered state. Note that the charge capacities are the same for both test sets. The charge process follows a constant current/constant voltage protocol whereas the discharge process utilizes a cut-off voltage. As a result the discharge process is impacted by cell impedance to a greater degree than charge measurements, thereby suggesting the variation between the 30A and 60A test sets is related to impedance rather than cyclable lithium content.
- Significantly more variability between 30A test results than the variability for 60A test results was observed. Reviewing the individual test results there was a significant variation in BOL capacities compared to the individual BOL of the 60A tests. Again, this is potentially a demonstration of the variability in the manufacturing process.
- Despite the increased variability of the 30A test set there was significantly higher initial degradation rates exhibited by the 60A test results than the 30A test results. After an initial accelerated degradation rate of the 60A tests, both the 60A and 30A demonstrated similar linear degradation rates.

In relative terms, the capacity fade reported in %-loss terms are provided in

Figure 70 for 60A tests. The capacity fade in %-loss terms for 30A tests are provided in Figure 71. The 60A results highlight the logarithmic initial capacity loss rate followed by subsequent linear capacity degradation. The 30A results demonstrate a high amount of variability and demonstrate a relatively continuous linear trend.

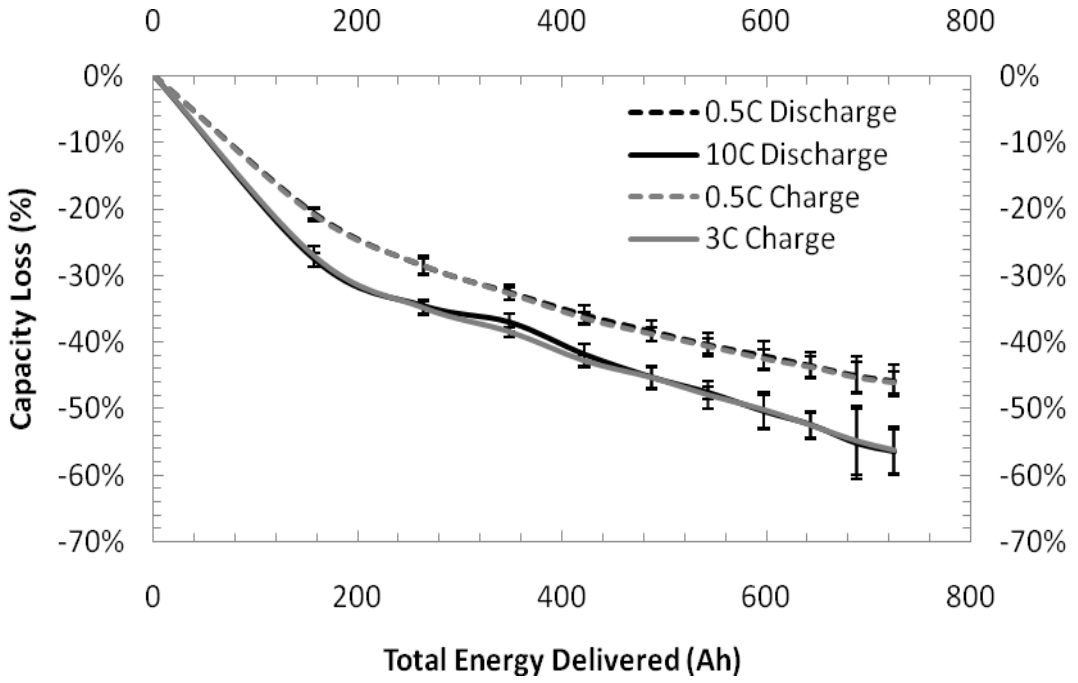

Figure 70 – Percent of capacity fade of lithium batteries for 60A discharge, 10A charge, full SOC range, as a function of total energy delivered

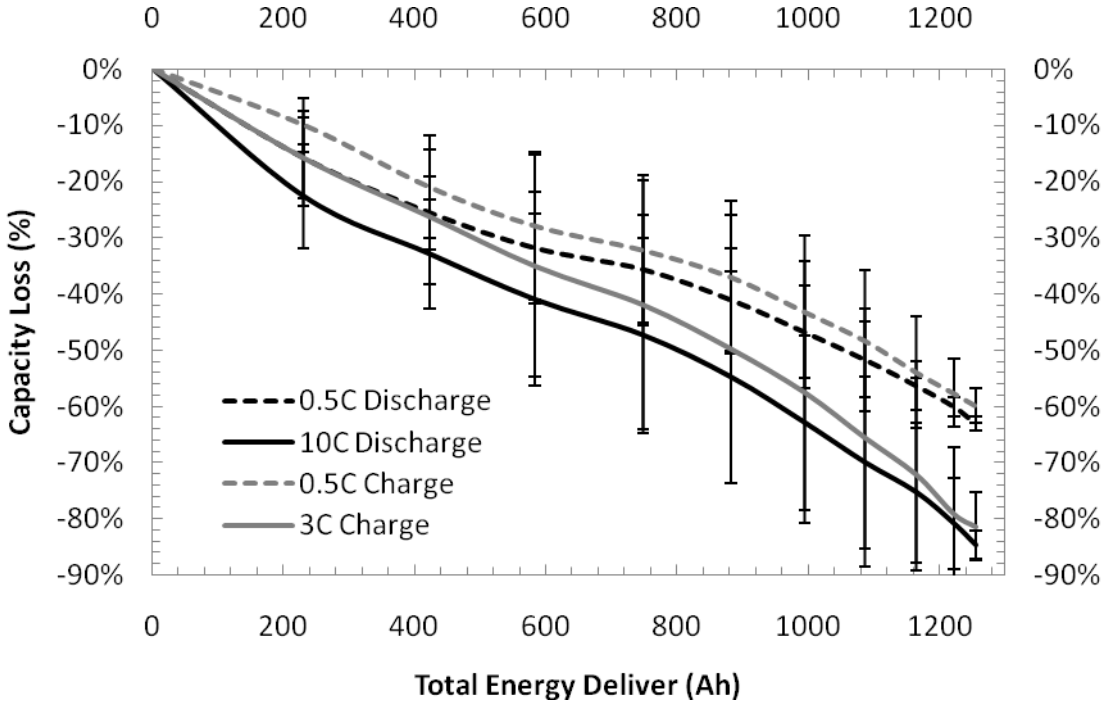

Figure 71 – Percent of capacity fade of lithium batteries for 30A discharge, 10A charge, full SOC range, as a function of total energy delivered

Two factors accelerating degradation are competing in comparing the 30A and 60A results. The 30A testing extends the discharge process to a lower SOC. The 60A tests generate more heat resulting in higher battery temperatures. The temperature profiles for the 60A and 30A discharge cycling is provided as Figure 71 and Figure 73 respectively. The increased degradation of the 60A testing suggests that the temperature effects are more significant than the lower SOC operation. The average battery temperature for a 30A test was 31.5°C compared to 33.2°C for a 60A test. During discharge cycles the average temperatures were 29.4°C and 32.6°C for the 30A and 60A tests respectively. Due to the thermal inertia and heat transfer from the battery core the surface temperature rise is not completely realized until the subsequent charge cycle. The average temperatures for the charge cycles were 33.0°C and 34.8°C for the 30A and 60A cycles respectively. During the initial 100 cycles when the highest capacity degradation rate is observed for the 60A tests the average temperatures for the discharge and charge processes are 35.8°C and 36.9°C respectively.

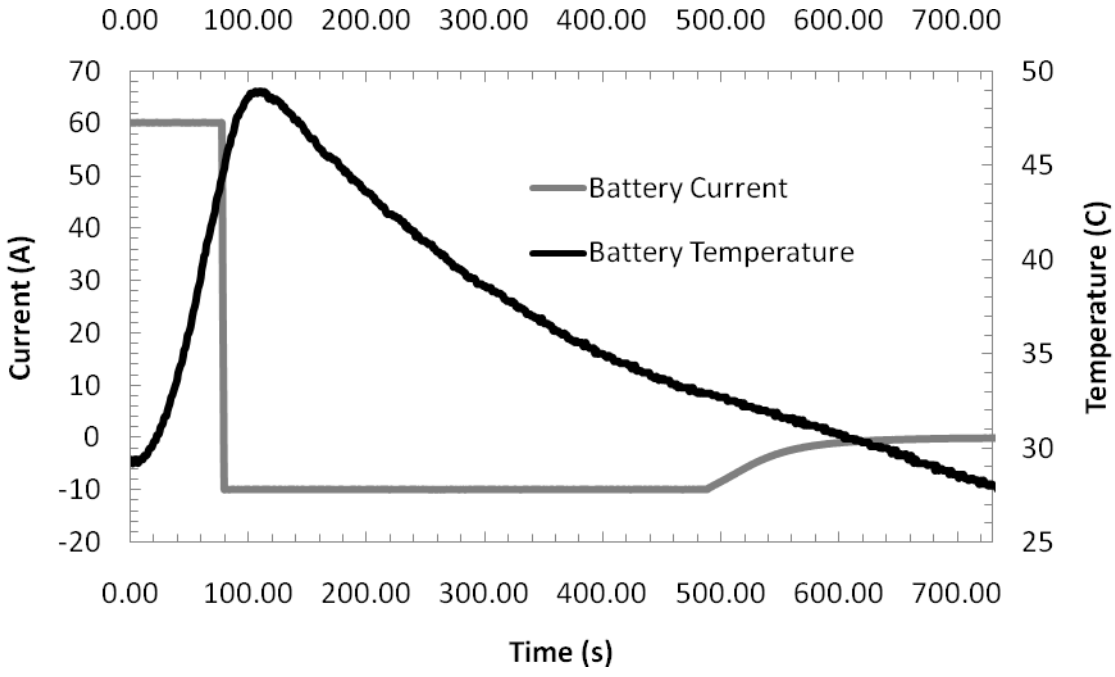

Figure 72 – Battery temperature during a discharge/charge cycle with 60A discharge, 10A charge, and full SOC swing

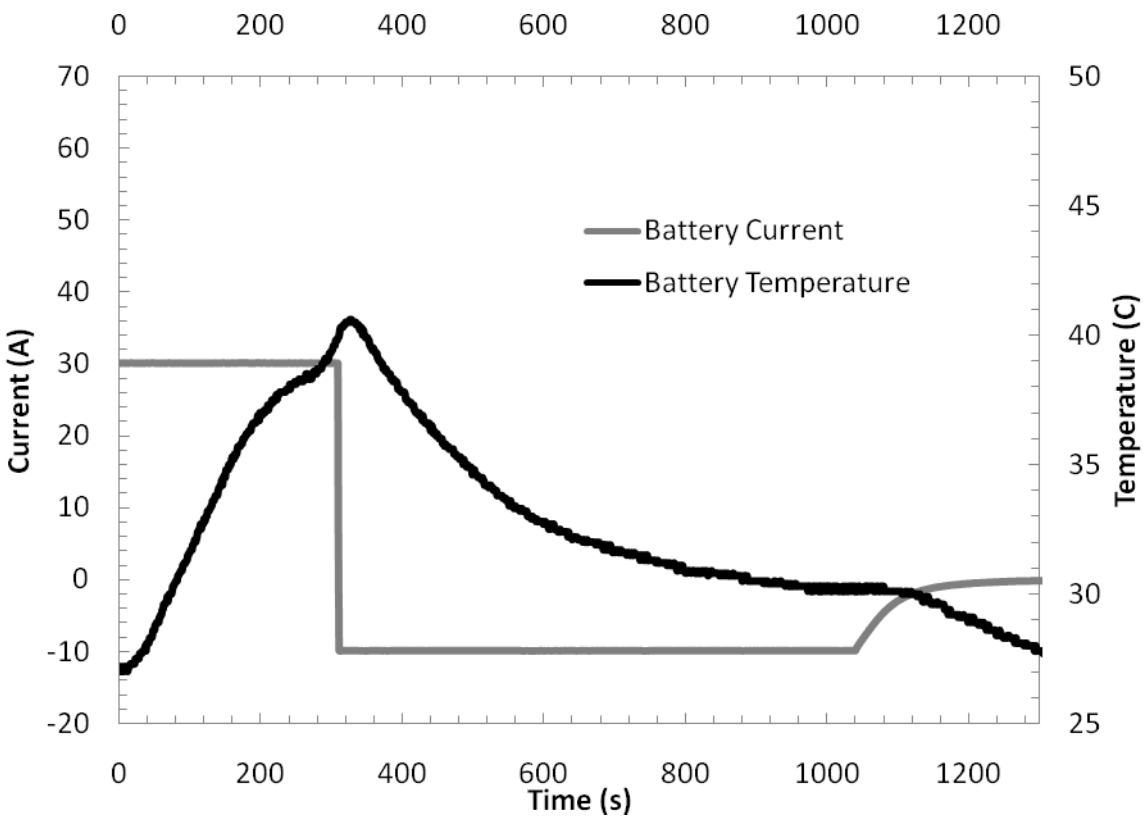

Figure 73 – Battery temperature during a discharge/charge cycle with 30A discharge, 10A charge, and full SOC swing

As previously discussed, the power fade that is manifested as an increase in impedance is also of interest when considering the lifetime performance in hybrid powertrains. Given that powertrain components must operate within a specific voltage range, increased impedance results in lower useable battery power levels available for acceleration and regenerative braking events. In addition, the increase in impedance results in more current required to deliver a given power request, further increasing the effective capacity fade (in Wh) of the battery. Polarization curves for 0, 100, 500, and 1000 cycles for a 60A degradation test are provided in Figure 74. The polarization curves clearly demonstrate the increased ohmic resistance and mass transfer limitations as the battery degrades.

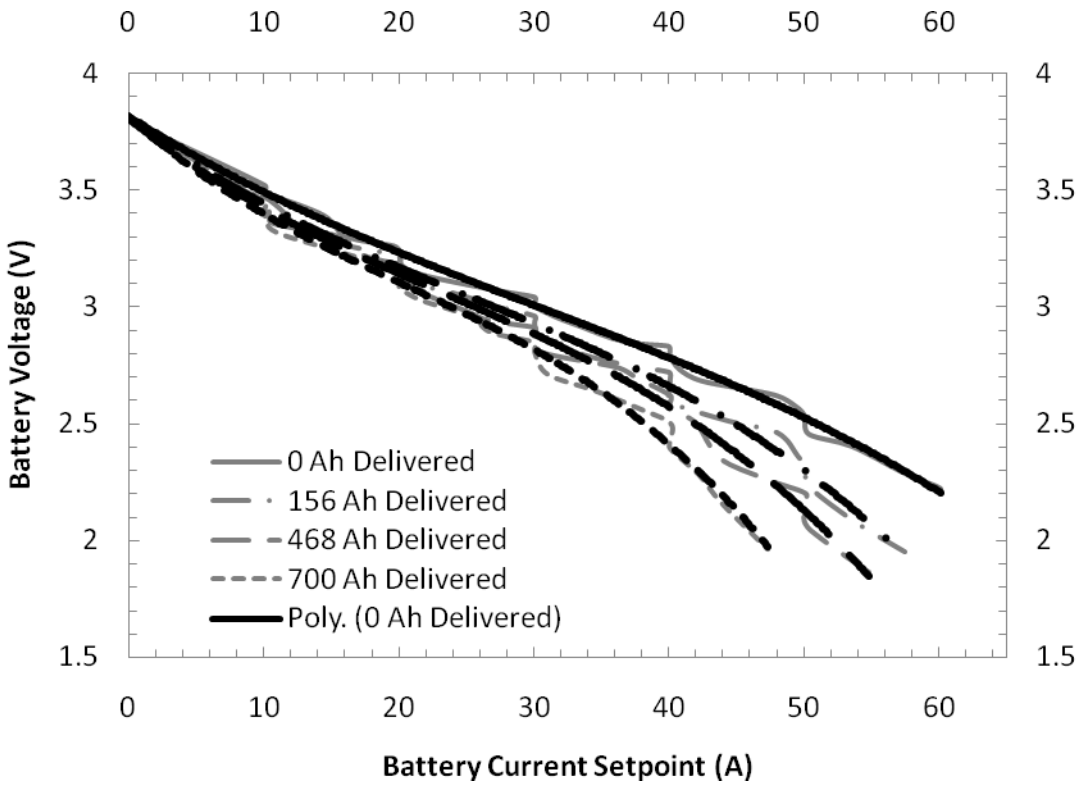

Figure 74 – Battery polarization curves at 0, 100, 500, and 1000 cycles for 60A discharge, 10A charge, full SOC range, as a function of total energy delivered

The polarization curves for a battery degraded under the 30A discharge regime is compared with the polarization curve for a battery degraded under the 60A discharge regime in Figure 75. Both batteries have delivered approximately 700 Ah of energy. The result clearly demonstrates that the 60A battery exhibits higher impedance. These results support the SEI growth phenomenon as the primary degradation mechanism to the capacity degradation. SEI growth reduces the cyclable lithium causing capacity loss while increasing the surface film resistance, corresponding to the observed result of the higher capacity fade of the 60A batteries corresponding to higher power fade as a result of higher resistance.

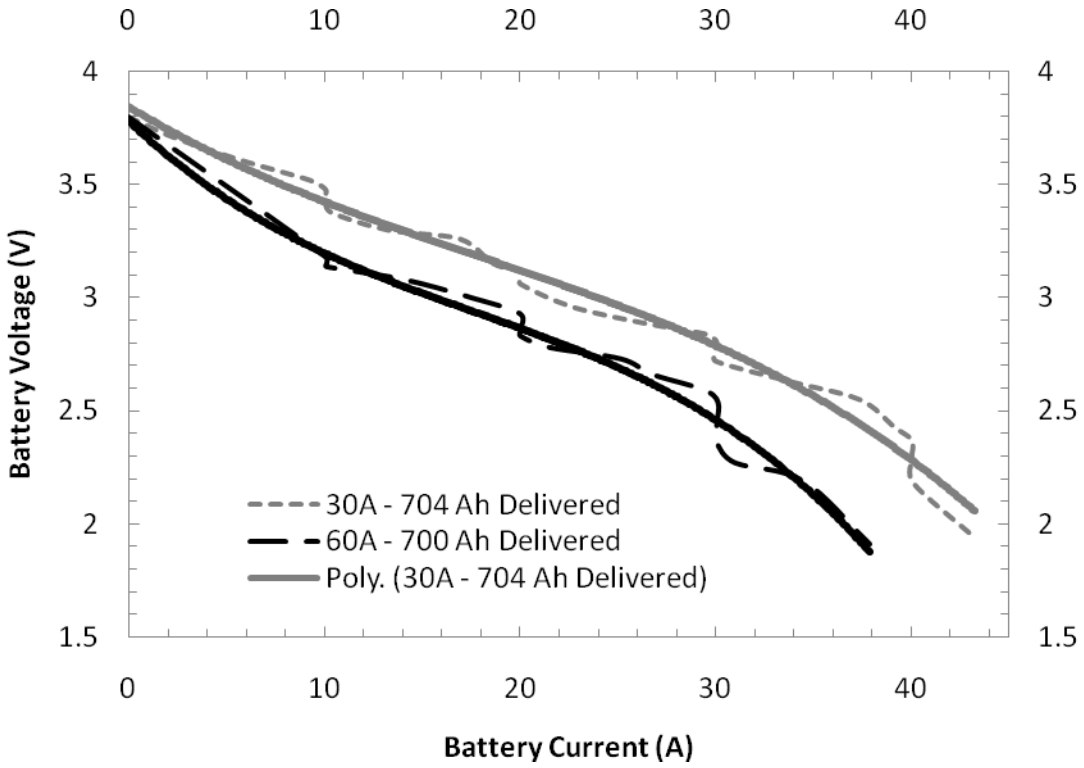

Figure 75 – Battery polarization curves for aged batteries discharged at 30A and 60A discharge, 10A charge, full SOC range, as a function of total energy delivered

The power fade as a function of total energy delivered at multiple current levels for degradation at 60A discharge, 10A charge, with full SOC range is provided as Figure 76. The power fade for low discharge rates is negligible; however, the power fade for high discharge rates demonstrates three characteristic portions:

1. An initial section of rapid power fade,
2. A mid-range section of linear power fade, and
3. A final section of accelerated power fade.

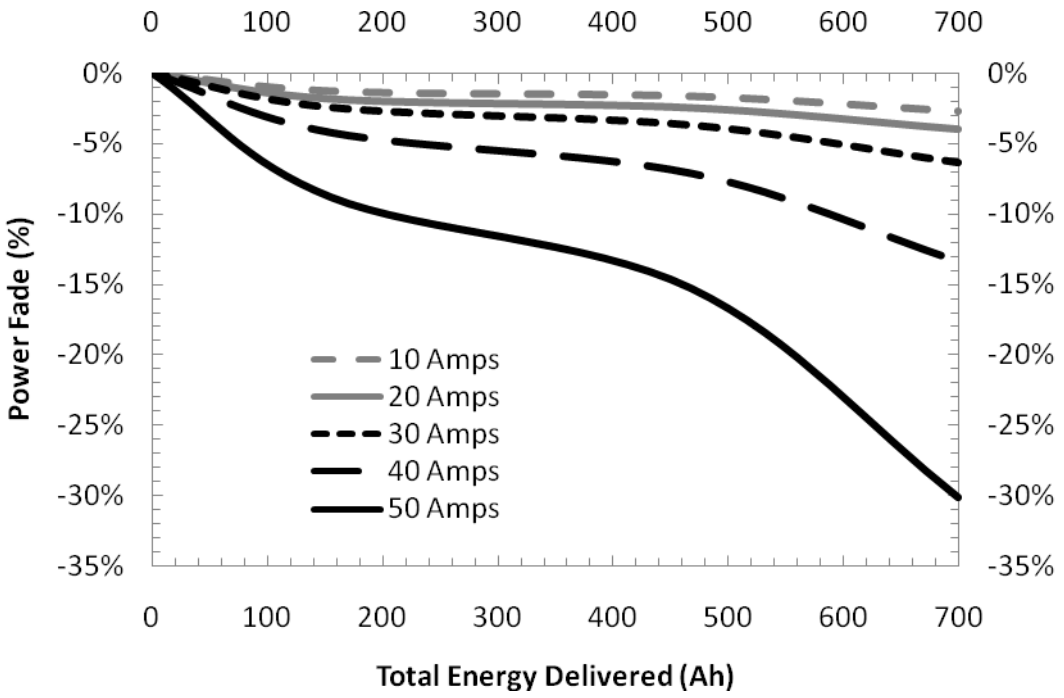

Figure 76 – Percentage of power fade for aged batteries discharged at 60A discharge, 10A charge, full SOC range, as a function of total energy delivered

Capacity tests and polarization curves provide valuable performance benchmarks for evaluating battery degradation. These tests; however, provide limited information on the specific phenomena that are causing the capacity loss and increased impedance. As previously introduced, AC impedance is a valuable analytic tool to assist in the characterization of the key degradation mechanisms. AC impedance is investigated further in the next section.

4.3.1 AC Impedance Measurements

AC Impedance spectra were obtained for fresh and aged batteries. A Princeton Applied Research 273A Potentiostat/Galvanostat was used in combination with 1260A Impedance/Gain-Phase Analyzer. Zplot software was used to operate the equipment. The battery was connected using the 4-point connection method, with the twisted working and twisted sensing to reduce signal noise. The test was performed galvanostatically with an excitation current of 700mA and an integration time of 30s per test point. The spectra were acquired across a frequency range of 100 kHz to 0.1 Hz with 7 test points per decade. Lower integration times, excitation currents, or potentiostatic operation resulted in poor signal-to-noise ratios. Repeat measurements were taken demonstrating less than 1% variance between spectral analyses. Due to the significant

impact of SOC on cell impedance, the batteries were charged to 98% SOC. Spectra were taken for the batteries at specific mAh increments and the spectra was repeated until a 0% SOC was reached. The spectra for a fresh battery over a complete SOC range are provided as Figure 77.

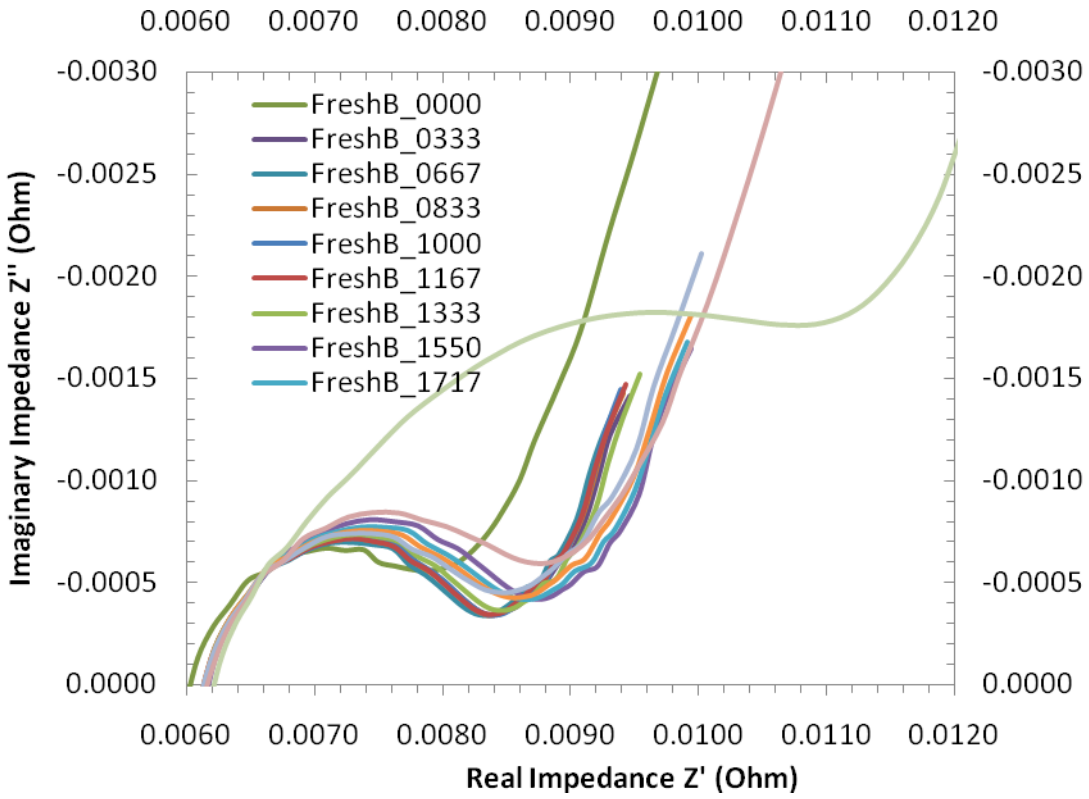

Figure 77 – AC Impedance Spectra for a fresh lithium battery at various SOC values (the values represented in the legend correspond to mAh discharged)

The spectra taken across a complete SOC range demonstrate that:

- All spectra exhibited the semi-circular profile with Warburg impedance as reported in literature,
- the real impedance is lowest at very high SOC values,
- the low frequency minima has a high imaginary impedance at very high SOC,
- with the exception of SOC extremes, the spectra are consistent across wide range of SOC values (10%-90%), and
- the real and imaginary impedance increases significantly at very low SOC values.

Similar behavior was observed for spectra of degraded batteries. Detailed spectral data is provided in the Appendix C. Due to the consistency of the spectra for mid-range SOC values the spectra for fresh, 30A discharged, and 60A discharged batteries are compared in Figure 78. The differences in spectra combined with the literature results above provide a significant amount of interpretation of the degradation mechanisms. Both degraded batteries demonstrate a significant rightward translation of the entire spectra, corresponding to an increase in contact resistance and decrease in ionic conductivity in the bulk solution. The amount of translation between the two discharge rates is identical, thereby suggesting that the increase in contact resistance and/or decrease in ionic conductivity in the bulk solution is not dependent on dependent on discharge rate. The width of the semi-circular arc is increased for both degraded batteries, with a greater increase exhibited by the battery degraded at 60A. The width of the semi-circular arc corresponds to electrochemical kinetics, transport across the SEI, and the charge-transfer process. The increased width of the semi-circular arc of the 60A degraded battery suggests that a thicker SEI layer has developed causing an increase in transport losses across the layer as compared to the battery degraded at a 30A discharge rate. The frequency of the maximum imaginary impedance of the semi-circular arc is 138 Hz for the three spectra, suggesting that ageing did not cause any significant change in the porosity of the SEI layer.

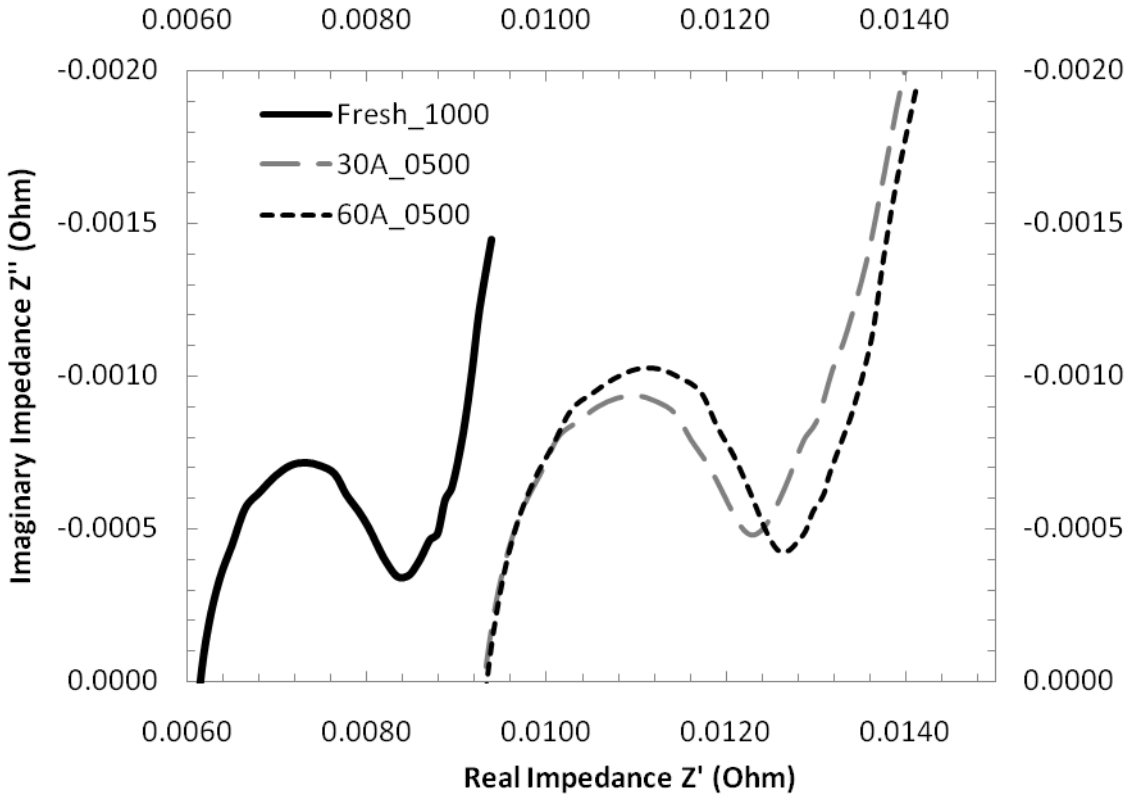

Figure 78 – AC Impedance Spectra for fresh, 30A discharged, and 60A discharged lithium batteries at approximately 50% SOC

The results of the capacity tests, polarization curves, and AC impedance measurements have demonstrated significant capacity and power fade of the batteries due to cycling. The results of the three test methods support the hypothesis that the SEI layer thickness is increasing as a function of age, further accelerated by the 60A discharge rate as compared to the 30A discharge rate. The AC impedance results also suggest that there is a demonstrable increase in contact resistance and/or reduction in ionic conductivity.

It is important to reiterate that these results are not intended to directly translate into battery lifetimes in hybrid powertrains. As introduced in Chapter 2, the significant majority of published lithium battery degradation studies utilized low charge and discharge rates (<1C) or minimal SOC ranges. These results are intended to complement the existing knowledge of battery degradation with high current rate, high SOC range battery degradation results. In the next section these results are combined with previously published battery degradation model to

develop a causal degradation model suitable for model-based design based on vehicle powertrain performance.

4.4 Battery Degradation Model

Ning has developed degradation models that incorporate higher currents present in hybrid powertrain operation and incorporates the degradation considerations for constant voltage (max voltage) charging operation [126]. Ning's most recent model incorporates porous electrode theory, concentrated solution theory, Ohm's law, intercalation/deintercalation kinetics and transport in solid phase and electrolyte phase. No rest time is included in the model development. The primarily mechanism of cyclable lithium ion loss is considered to be a parasitic reaction between ethylene carbonate (EC) and lithium at the SEI layer following the structure of:

$$CH_2CH_2OCO_2 + 2e^- + 2e^- = LiCH_2CH_2OCO_2Li \quad (40)$$

Within the Ning model the lithium concentration at the anode is updated for each discharge cycle give the following equation:

$$c_s^0|_{N+1} = c_s^0|_N + \frac{Q_s}{F\epsilon_s} \quad (41)$$

Where Q_s represents the volume-average loss of lithium. In addition to changing the lithium concentration, the SEI layer thickness increases the SEI film resistance according to the equation:

$$R_f\big|_{N+1} = R_f\big|_N + R_f\big|_{para,N} \quad (42)$$

The resistance is derived from the SEI thickness by the equation:

$$R_f\big|_N = \frac{\delta_f|_N}{\kappa} \quad (43)$$

Where the thickness of the SEI is derived from:

$$\frac{\partial \delta_f|}{\partial t} = -\frac{j_{para}|\,X\,M}{\rho\,X\,F} \quad (44)$$

The wall flux of the parasitic reaction is related to the total wall flux by the equation:

$$j = j_{int} + j_{para} \tag{45}$$

Where the parasitic flux is derived following a simple Tafel relation of:

$$j_{para} = j_{para}^{0} exp\left(\frac{\alpha_c F}{RT}\eta\right) \tag{46}$$

Where:

$$\eta = \phi_s - \phi_e - U_{para} - jR_f \tag{47}$$

The wall flux of the intentional reaction is given by the Butler-Volmer equation:

$$j_{int} = Fk(c_e)^{\alpha_a}\left(c_{s,max}\right)^{\alpha_a}\left(c_{s/e}\right)^{\alpha_a}\left(exp\left(\frac{\alpha_a F}{RT}\eta\right) - exp\left(\frac{\alpha_c F}{RT}\eta\right)\right) \tag{48}$$

$$\eta = \phi_s - \phi_e - U_{ref} - jR_f \tag{49}$$

$$R_f = 0 \text{ for cathode} \tag{50}$$

$$R_f\big|_{N+1} = R_f\big|_N + R_f\big|_{para,N} \text{ for anode} \tag{51}$$

To solve these equations the bulk and surface lithium concentrations and potentials must be solved. The bulk concentration, surface concentration, electrolyte potential, and anode potential are found by simultaneously solving five equations based upon Ohm's law and material balances. The solution is function of X and t; X defined by an axis that extends from the cathode to the anode. Ning compared the model results to experimental results, showing good correlation between the model and actual values. The simulation of 2000 cycles took 15 hours.

As mentioned, the Ning model assumes that the SEI layer growth occurs as a result of the overvoltage present between the anode and the electrolyte during charging, with a parasitic reaction reference voltage of 0.38V. While the paper discusses the of End of Charge Voltage (EOCV), Depth of Discharge (DOD), Charge Rate (CR), and Discharge Rate (DR) as factors affecting battery cycle-life, the model developed is driven almost exclusively by CR and EOCV. Although the Ning model is an excellent base model, the following limitations make it unsuitable for the causal degradation modeling required for this thesis:

1. The model requires extensive time to run. 15 hours for modeling 2000 battery cycles is prohibitively long considering that the battery degradation model is only a subsection of the overall vehicle model. The most computationally expensive step in the Ning model is solving the set of partial differential equations (derivations of Ohm's law and materials balance) that generate the lithium concentration and potential profiles.
2. The model does not specifically incorporate the effects of depth of discharge (DOD), which is 1-SOC. The degradation rate is a function of the overvoltage with no specific acceleration of the degradation rate due to operation at high DOD. The additional Ohmic losses causing increased over-voltages at DOD extremes causes a slight increase in the overvoltage for a given reaction current; however, this is poorly captured in the Ning model.
3. The model makes no consideration for discharge rate (DR). In subsequent papers by Zhang and Boovaragavan revising the Ning model, the effect of DR and DOD are discussed [101,127-129]. The proposed degradation mechanism is based upon volume changes in the anode due to heating and deintercalation/intercalation at high and low DOD (low and high SOC). The volume changes in the ductile graphitic anode cause the stiff SEI layer to crack exposing portions of the electrode surface to the electrolyte enable increased SEI formation.

Despite these limitations, the Ning model is used as a reference model due to its considerations of the effects of high discharge rates as well as constant voltage charging. In the work described herein a 0-D empirical model is developed based upon the general premises and mechanisms discussed in Ning's 1-D analytical model. Ning demonstrated that under 1C charge and 0.5C discharge conditions the electrolyte concentration can vary up to 275 mol/m^3 (1150 mol/m^3 at the cathode collector plate to 875 mol/m^3 at the anode collector plate). In the 0-D empirical model developed in this work, the variation in electrolyte concentration is assumed to be negligible as compared to the significant applied and observed over-voltages present at 23C discharge and 4C charge conditions.

The model is extended to include considerations for DOD and DR and is calibrated using the results of the very high discharge/charge (>4C) testing performed in the previous section.

4.4.1 Model Development Based Upon Experimental Results

The Ning model has been validated to actual results based at low discharge (0.5C) and low charge rates (1C). The battery pack in the baseline hybrid fuel cell vehicle is 8Ah, meanwhile discharge currents of up to 200 amps are observed in operation. Correspondingly the degradation model must be capable of considering high charge and discharge rates. As a result, the Ning model is modified based upon the results of the high current testing performed in the previous section. Prior to calibrating the model to the high current operation, the structure of the model is modified to include DR and DOD effects and to simplify the model to permit integration into the baseline hybrid fuel cell vehicle model. The specific differences between the 60A and 30A battery operating conditions and subsequent degradation rates are first reviewed. Discharge voltage and temperature profiles for 60A and 30A tests are provided as Figure 79 and Figure 80 respectively – curves are provided for the 9^{th}, 371^{st}, and the 875^{th} cycles. As expected, the 9^{th} cycle 60A discharge continues for approximately half the duration of the 30A discharge. Of significant interest is the difference in temperature in the BOL 60A test resulting in an increase in the battery voltage during the discharge. The increased battery voltage is believed to be a result a reduction in the mass transfer losses as a result of the increasing battery temperature. The increasing voltage is not apparent in the 30A testing.

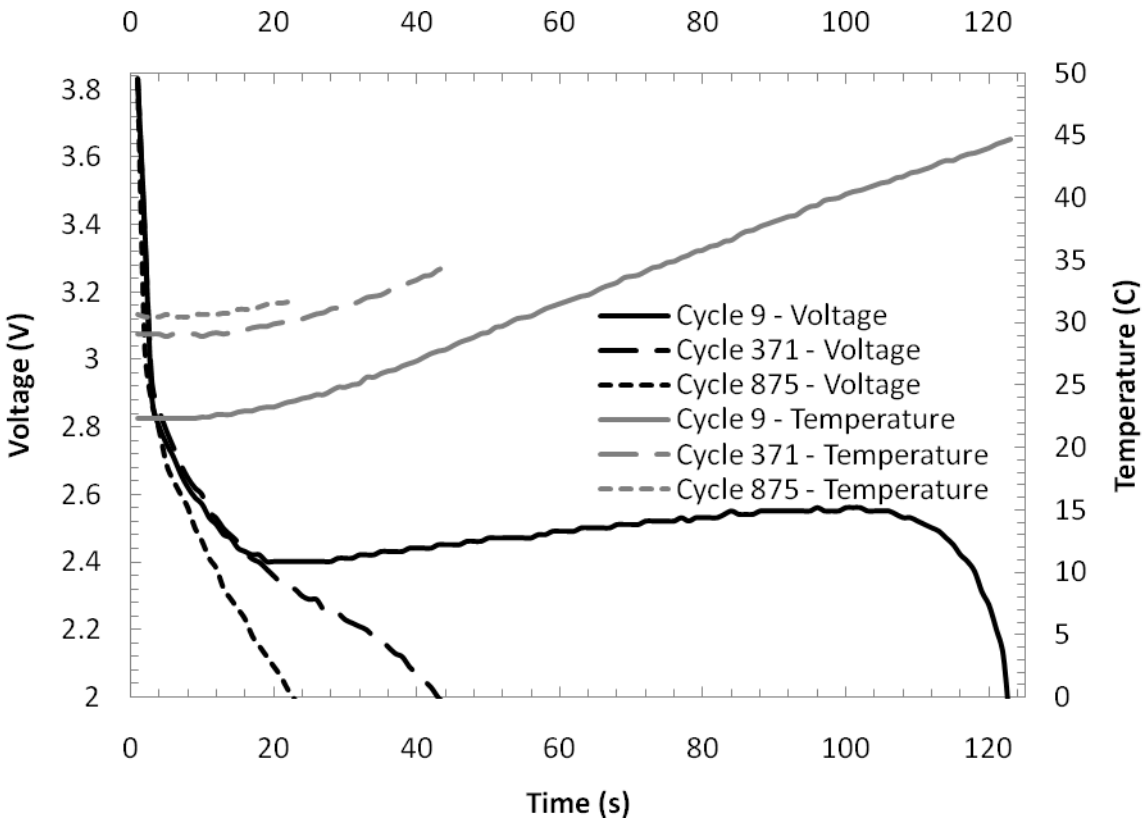

Figure 79 – 60A Discharge voltage and temperature profiles at 9, 371, and 875 cycles

As the capacity fade results would suggest, the discharge curve is drastically different for the 9th and 371st cycles in the 60A test whereas the difference is significantly less for the corresponding 30A curves. The degradation rate associated with the early cycling during the 60A tests demonstrated logarithmic capacity loss while the other five (5) curves provided in Figure 79 and Figure 80 demonstrated smaller, relatively linear, degradation rates. The significant differentiator between the 9th cycle curve for the 60A tests and all other curves is the rate of battery temperature increase and the maximum temperature achieved. The corresponding curves for the charge profiles are provided as Figure 81 and Figure 82. Despite all tests being charged at 10A, the heat generated during the 60A discharge resulted in a significant difference for the profile of the 9th cycle 60A test. Given that the degradation rate is significantly higher for the first 200 cycles of the 60A test any other test section, it is critical that temperature must be integrated as an accelerating factor in the degradation model.

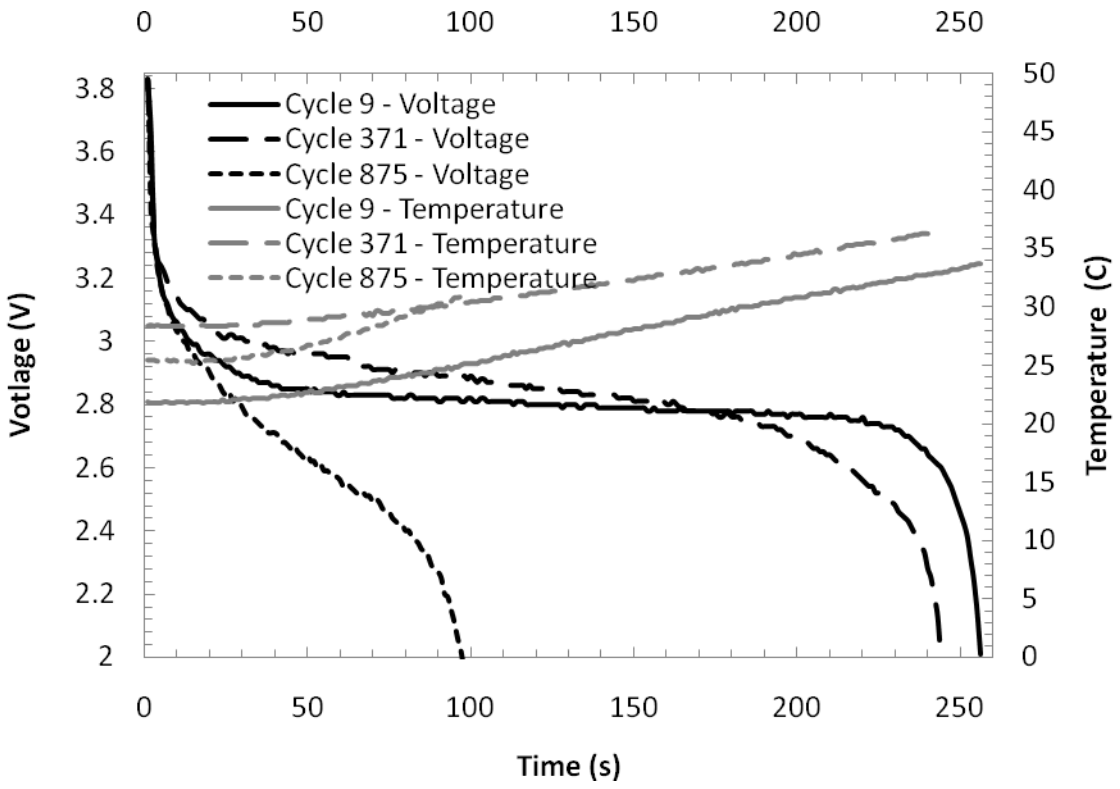

Figure 80 – 30A Discharge voltage and temperature profiles at 9, 371, and 875 cycles

Both the 30A and the 60A tests used a CC/CV charge profile with a maximum current of 10A to a maximum voltage of 3.8V, continuing charge until a cut-off current of 50mA. As a result, all tests included a similar upper SOC limit. Discharge was continued until a cut-off voltage of 2.0V was reached. As a result of ohmic losses a slightly lower SOC was achieved during the 30A test. As previously mentioned, a number of papers have discussed the significant impact of SOC swing on battery degradation. For instance, Bloom found a significant increase in degradation rate using an SOC swing of 6% as compared to 3% [130]. As the 60A test results demonstrated higher degradation rates, it can be concluded that any marginal increases in degradation rate as a result of the slightly increased SOC swing has significantly less impact than that impact of higher temperatures.

Degradation tests were attempted on the hybrid powertrain test stand using profiles with smaller SOC swing. These tests were unsuccessful as the coulomb-counting method employed was found to be significantly inaccurate during high current testing. Improved SOC approximation is required for the test stand to be capable of employing SOC-based test cycles.

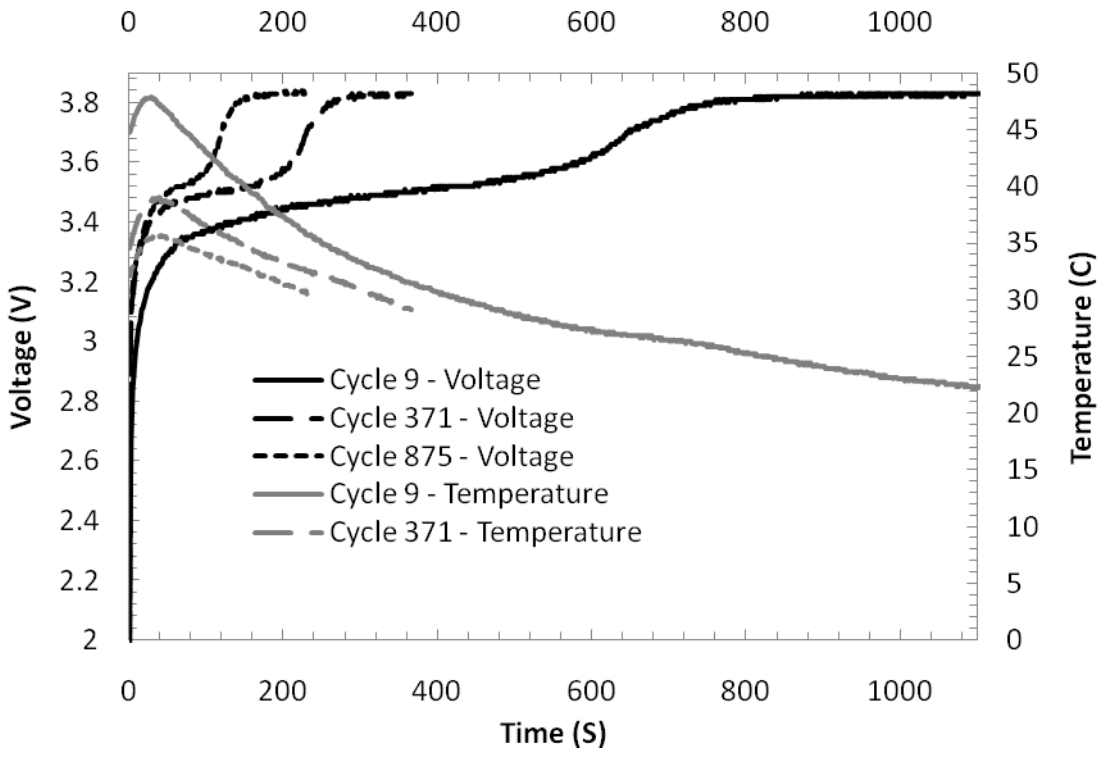

Figure 81 – 10A charge voltage and temperature profiles after a 60A discharge

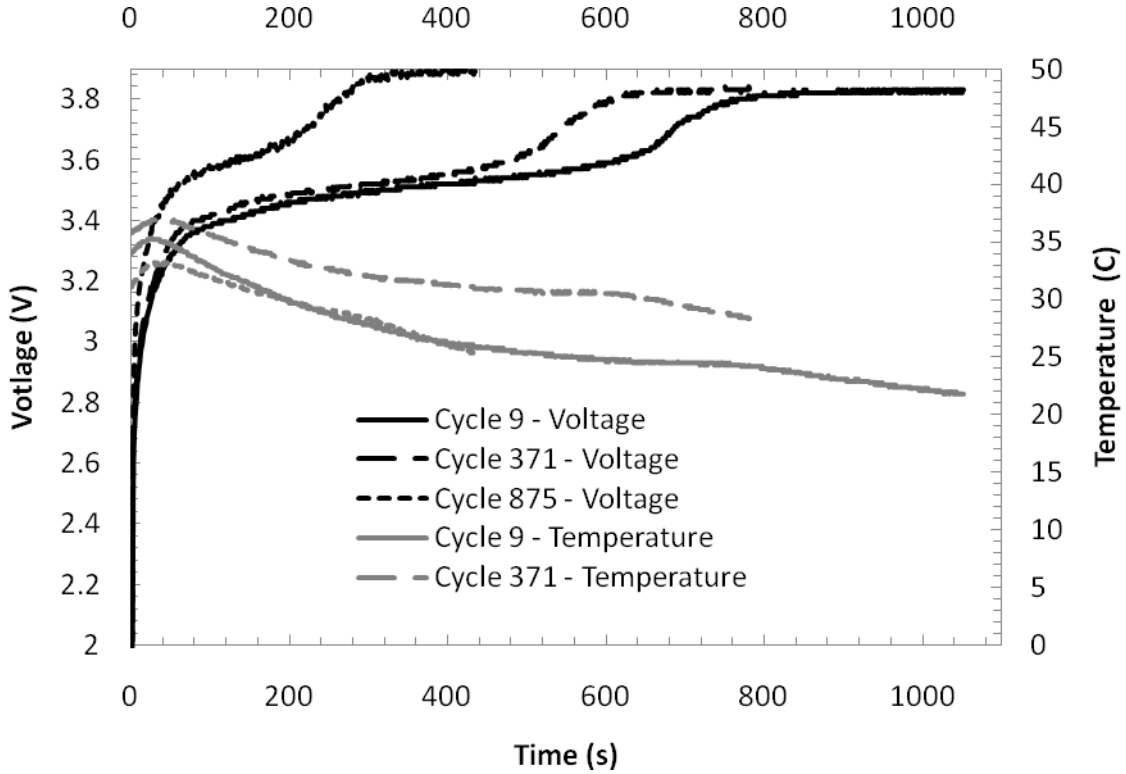

Figure 82 – 10A Charge voltage and temperature profiles after a 30A discharge

Based upon the degradation factors observed during the high current testing and discussed in literature, degradation accelerating factors are added to the Ning model adapting equation 46 to:

$$j_{para} = \propto_{Temp}^{n,ave} \propto_{SOC}^{n,ave} j_{para}^{0} exp\left(\frac{\alpha_c F}{RT}\eta\right) \quad (52)$$

Where the α terms correspond to accelerating factors due to temperature and SOC. The equation for the temperature acceleration factor is adapted from previous papers that have found the effect of temperature follows an Arrhenius behavior in the form:

$$\propto_{Temp}^{n} = exp\left(\frac{-40498}{RT}\left(\frac{1}{T} - \frac{1}{T^o}\right)\right) \quad (53)$$

The temperature acceleration factor is averaged using the form:

$$\propto_{Temp}^{n,ave} = 0.01 * \left(\propto_{Temp}^{n}\right)^{z_1} + 0.99 * \propto_{Temp}^{n-1,ave} \quad (54)$$

Similarly, the SOC accelerating factor is calculated by the equation:

$$\propto_{SOC}^{n} = exp\left(\frac{-100}{abs(60-SOC)}\right) \quad (55)$$

And is averaged using:

$$\propto_{SOC}^{n,ave} = 0.01 * (1 + \beta_1 * \propto_{SOC}^{n})^{z_2} + 0.99 * \propto_{SOC}^{n-1,ave} \quad (56)$$

To accelerate the simulation the empirical model assumes the variation in electrolyte concentration across the cell is negligible under 23C discharge and 4C charge rates as compared to the over=voltages present. As a result, the empirical model is a 0-D model as the X-axis is not considered and the overvoltage required in equation 52 is obtained directly from the overvoltage applied to the cell. The parasitic reaction current density is used to generate the capacity and power fade estimated using equations 41-44. The parameters that fit the degradation rates observed during the high current degradation testing described above are provided in Table 15.

Table 15 - Battery degradation model fitting parameters

Parameter	Value
β_1	2
Z_1	0.25
Z_2	4
J^o_{para}	0.00000008
α_c	0.5

It is important to note that equation 52 is driven by the overvoltage applied during the charging process. The overvoltage is derived from the applied voltage and Open-Circuit Voltage (OCV). As a result, care must be taken to ensure that the OCV estimation is accurate. The voltage profile for a fresh battery during 0.5C charge and discharge curves is provided as Figure 83. The OCV profile is derived as the middle curve between the charge and discharge profiles. The voltage profile of an aged battery is added in Figure 84. The SOC values are quoted in relative SOC rather than absolute SOC or Ah. The figures demonstrate clearly that the OCV curves remain relatively constant as the battery ages with respect to the relative SOC. As a result, the OCV values are determined based upon the fresh battery profile and are kept constant in the battery model developed in Simulink for PSAT.

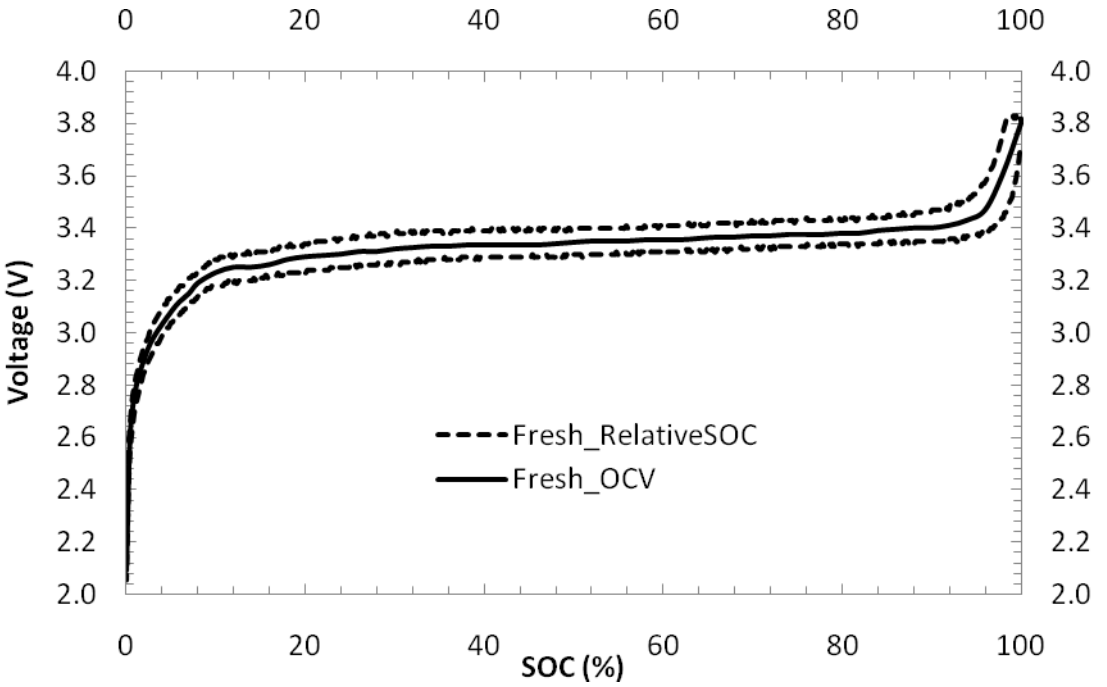

Figure 83 –Open-circuit voltage for a fresh battery as a function of state-of-charge. Dotted lines represent voltages under 0.5C charge and discharge conditions.

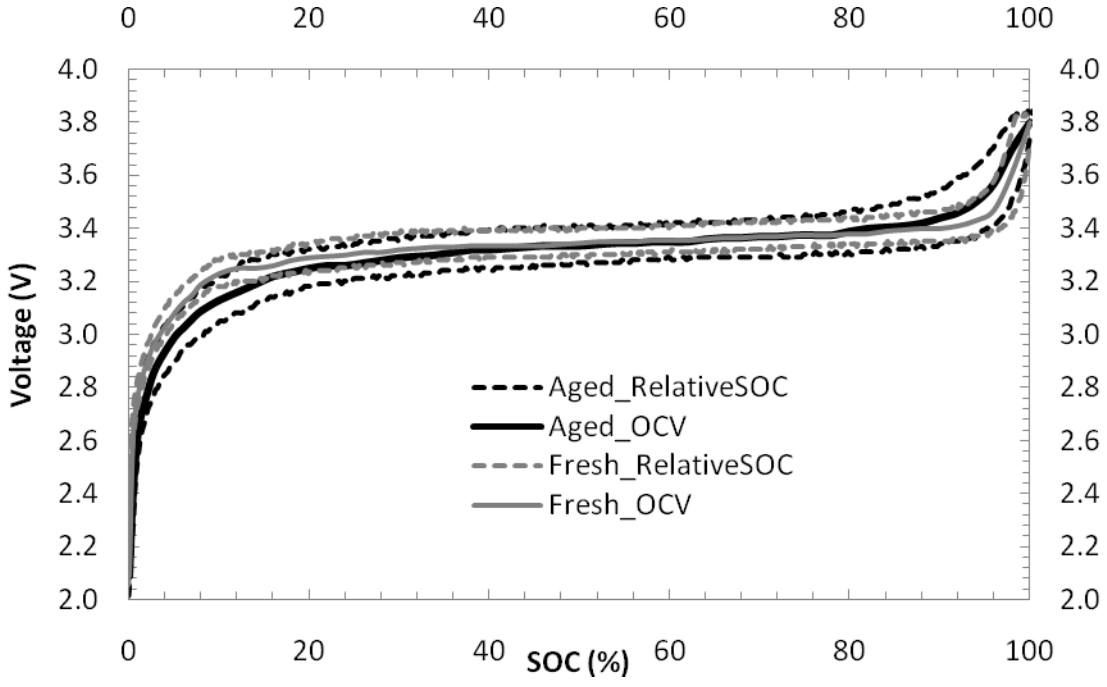

Figure 84 –Open-circuit voltage for fresh and aged batteries as a function of state-of-charge. Dotted lines represent voltages under 0.5C charge and discharge conditions.

The output of the causal degradation model for a 60A degradation test is provided as Figure 85. The simulation outputs of the base Ning model (with the 0-D simplification) and with only the SOC or the temperature accelerating factors are also provided. The figure clearly demonstrates a high level of accuracy in the ability of the causal degradation model to elucidate real-world behavior. The large oscillation in the actual battery capacity between 40 and 200 cycles is related to the heating effect described earlier. In initial cycles the battery heats sufficiently, causing a rise in the output voltage, extending the duration of the test. In subsequent cycles the increase in ohmic resistance results in the cut-off voltage being reached before sufficient heat has been generated to increase the output voltage. Despite the period of oscillation the correlation between the simulated and actual degradation curves is evident.

The resulting causal empirical model has been based upon degradation mechanisms previously introduced and validated in Ning's 1-D model. The empirical model with temperature and SOC accelerating factors has been shown to correlate well with high current degradation results. The development of a causal fuel cell degradation model is discussed next.

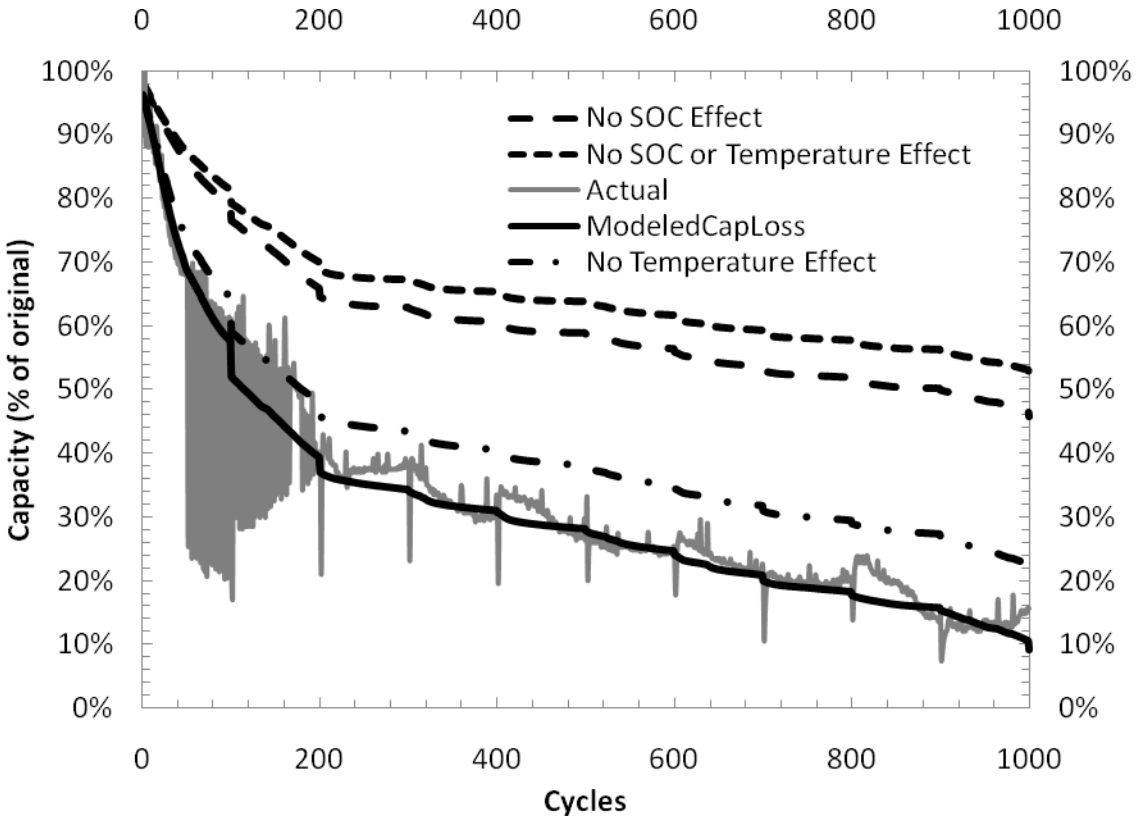

Figure 85 – Actual and simulated capacity fade for a battery tested at 60A discharge

4.5 Fuel Cell Degradation Model

A simplified empirical causal degradation model is developed based upon the fuel cell degradation studies summarized in Table 3 in Chapter 2. The studies exhibited significantly different degradation rates as a result of membrane construction, operating temperature, and load profile (constant current versus cycled current). Membrane construction is not a function of in-vehicle operation and is therefore not considered in the causal degradation model. The fuel cell temperatures observed during fuel cell operation were significantly lower than those present during most of the degradation studies described. In addition, the Hydrogenics stack is a lower pressure system and is therefore operated at lower temperatures. As a result, the effect of temperature is not considered and the lower temperature (75°C) tests are weighted higher in the formulation of the degradation equation. The degradation rate for steady state operation was approximately 10 μV/hr, whereas cyclic operation exhibited approximately 90 μV/hr. In considering this trend and given the desire to have a simple model for rapid vehicle modeling efforts the degradation rate is manifested as a decrease in open circuit voltage according to the following equation:

$$\frac{\partial V_{decay}}{\partial t} = -\frac{0.000225}{3600} * stdev\left(P_{FC}^{N}, P_{FC}^{N-1} P_{FC}^{N-2} P_{FC}^{N-3} P_{FC}^{N-4}\right) - \frac{0.0000010}{3600} \quad (57)$$

Where the degradation rate is driven by the standard deviation of the power outputs for the five previous seconds. While this model is solely empirical in nature, the integration of the standard deviation term is included as an aggregate of the impacts of cyclic operation causing:

- mechanical wear of the membrane due to thermal and humidity cycling,
- platinum particle dissolution in the cathode due to potential cycling,
- chemical degradation via radical attack due to time at open circuit voltage, and
- carbon corrosion as a result of start-stop cycles.

Considering the GSSEM and that equations 18-20 are a function of voltage and current, which in application are a function of time, taking the partial derivative of the membrane resistance as a function of time yields:

$$\frac{\partial r_M^N}{\partial t} = -\frac{A}{li}\frac{\partial V_{decay}}{\partial t} + \frac{A}{li^2}\frac{\partial i_{decay}}{\partial t} \quad (58)$$

Assuming that the degradation is manifested as solely as voltage decay, the second term in equation 58 becomes zero. As a result, combining equations 57 and 58 yields:

$$\frac{\partial r_M^N}{\partial t} = \frac{A}{li}\left(\frac{0.000225}{3600} * stdev\left(P_{FC}^N, P_{FC}^{N-1}P_{FC}^{N-2}P_{FC}^{N-3}P_{FC}^{N-4}\right) + \frac{0.0000010}{3600}\right) \quad (59)$$

Taking a partial derivative of λ with respect to r_m and considering the current and temperature decay differentials to be negligible yields:

$$\frac{\partial \lambda}{\partial t} = \frac{-181.6\left(1 + 0.03\left(\frac{i}{A}\right) + 0.062\left(\frac{T}{303}\right)^2\left(\frac{i}{A}\right)^{2.5}\right)}{(r_M^N)^2 * exp\left(4.18\left[\frac{T-303}{T}\right]\right)} \dots$$

$$\dots\left[\frac{A}{li}\left(\frac{0.000225}{3600} * stdev\left(P_{FC}^N, P_{FC}^{N-1}P_{FC}^{N-2}P_{FC}^{N-3}P_{FC}^{N-4}\right) + \frac{0.0000010}{3600}\right)\right] \quad (60)$$

Equation 60 provides a degradation function for the decrease in λ as the fuel cell ages and can be compared to the GSSEDM developed by Fowler [77]. The PSAT fuel cell model determines the hydrogen fuel rate given the output power. Given that a percentage point in voltage decay results in a percentage point increase in fuel cell current to maintain the output power and that the current directly correlates to fuel consumption, the percentage point in voltage decay is manifested as a percentage point increase in fuel consumption. Therefore, the fuel cell State Of Health (SOH) is calculated as:

$$SOH_{FC}(t) = \frac{V_{BOL} - V_{decay}(t)}{V_{BOL}} \quad (61)$$

Which in turn determines the hydrogen consumption as:

$$H2(t) = \frac{H2_{BOL}}{SOH_{FC}(t)} \quad (62)$$

This chapter described the design and construction of a hybrid powertrain test stand intended for component model development and degradation studies. High current testing was performed on lithium ion batteries and a causal degradation model was developed by adapting Ning's battery degradation model with the high current results. The battery degradation model is semi-empirical, accelerating the degradation at higher temperatures, SOC extremes, and higher charge rates. A corresponding causal degradation model was developed for the fuel cell

based upon previous fuel cell degradation studies. Within the model the fuel cell degradation rate is accelerated during highly transient operation.

Chapter 4 developed these causal models, which are derived from real-world degradation rates. Chapter 3 developed and validated a baseline hybrid fuel cell vehicle model. Chapter 5 integrates the causal degradation models of Chapter 4 into the baseline vehicle model from Chapter 3.

Chapter 5

Lifetime Hybrid Fuel Cell Vehicle Modeling

Model-based design strives to improve system design by quantifying the impact of sizing and control strategy decisions. The objective of model-based design is to accelerate and reduce the cost of the design process as compared to the full-scale prototype method. Given the high cost, complexity, and time associated with degradation testing this design problem is ideally suited for the application of model-based design principles.

A baseline vehicle model validated to within 2% of actual performance was developed in Chapter 3. Causal degradation models were developed in Chapter 4 for the battery and fuel cell components based upon additional degradation studies and previously published degradation studies. The causal degradation models have been developed in accordance with the PSAT structure within the Simulink software environment. Since the battery degradation model is based upon lithium iron phosphate chemistry, the nickel-metal hydride battery pack utilized in the baseline vehicle model is replaced with a corresponding lithium iron phosphate with similar nominal voltage and capacity within this future powertrain modeling efforts.

The A123 batteries degraded in Chapter 4 had a nominal voltage of 3.3V with a rated capacity of 2.3Ah. The observed BOL capacity for reasonable discharge rates was closer to 2.1Ah. As a result, the PSAT lithium battery pack consisted of 90 cells in series and 4 strings in parallel. The result was a pack with a nominal voltage of 297V and capacity of 8.4Ah compared to a 312V nominal (288V rated) NiMH battery pack with an 8.5Ah nominal capacity. The UDDS cycle was

repeated with the lithium-ion battery pack resulting in a 3% reduction in fuel consumption due to the higher efficiencies of the lithium ion pack. The Simulink model files and .m initialization files are provided in Appendix D.

Two considerations in performing lifetime modeling are computation time and file size. Using an Intel Core 2 Duo at 1.73 GHz with 2GB of RAM the time required to complete a drive cycle simulation ranged from approximately 4 minutes for an HWFET cycle to 25 minutes for a 3x repeat of the tripEPA combined. The tripEPA combined represents a UDDS cycle followed by an HWFET cycle. The computation time equated to roughly 0.1-0.3 minutes for every kilometer travelled. Therefore, to model a 200,000km lifespan of a vehicle would require 14-42 days. While this computation time is slightly prohibitive, the main challenge is the file size. The data file for a UDDS cycle is approximately 15MB, or roughly 1.1MB/km. Therefore, the associated data file for a 200,000km vehicle lifespan would be approximately 220GB. The computation time and file size varies depending on the characteristic of the drive cycle; however, even at the favourable end of the range the time and sizes are prohibitive. To resolve this issue a Matlab script was written that simulates the vehicle at every 10000 km. In PSAT the "Manu Simu Stop" option is activated, and after the Simulink model is created the ACAD_Stevens_Lifetime function is called. The script is provided in Appendix E.

The script simulates the vehicle over the drive cycle specified. At the completion of the drive cycle the "per km" rate of degradation is determined for the fuel cell SOH, battery capacity SOH, and battery power SOH. The "per km" rates are assumed to be sufficiently linear for the 10000 km window and new initial SOH values are calculated for the next simulation interval. The file re-initializes the component files with the aged SOH values and repeats the simulation. The process repeats until a 200,000km lifetime is modeled. The resulting simulations require between 80 minutes and 9 hours to complete.

Combining the hybrid fuel cell vehicle model that includes causal degradation models for the fuel cell and battery with the lifetime modeling script the impact of hybrid control strategy algorithms and component sizing decisions on lifetime vehicle performance can be quantified. The analysis herein comprises of three evaluations, being:

1. Comparison of the lifetime performance of the hybrid control strategies introduced in Chapter 3,

2. Comparison of the lifetime performance for all-electric and blended operation for a plug-in hybrid variation, and
3. Quantification of the impact of battery over-sizing in the plug-in hybrid variation.

5.1 Effect of hybrid control strategy

Rule-based, load-follow, load-level, and cost function-based hybrid control algorithms were presented and evaluated for BOL performance of the initial vehicle model in Chapter 3. The gasoline fuel economy consumption equivalent for the four different control strategies over the lifetime of the vehicle are provided in Figure 86. The fuel economy values included a correction for the SOC variation between the start and end of the simulation cycle. While all scenarios exhibit an increase in fuel consumption as the vehicle ages, the importance of considering lifetime performance is highlighted in the case of rule-based versus cost function control strategies. In evaluating BOL performance, the cost function would be preferred as it achieves lower initial fuel consumption. In reviewing the anticipated lifetime performance; however, it is evident that the rule-based control strategy would be preferred as the cost function exhibits a higher rate of fuel economy over the age of the vehicle.

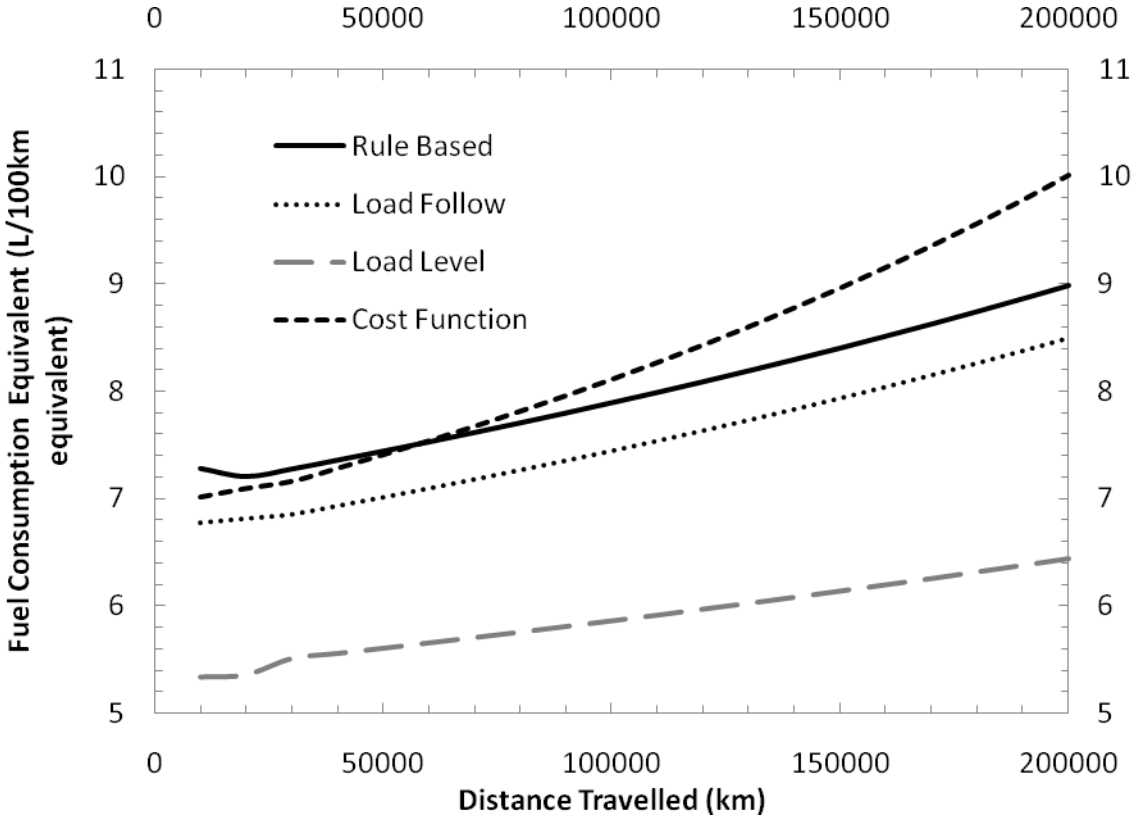

Figure 86 – Fuel consumption equivalent over the vehicle lifetime for different hybrid control strategies

The vehicle architecture ultimately derives all of the energy from the fuel cell (the SOC correction considers the SOC to be replenished/depleted by fuel cell energy) and only a fraction of energy cycles through the battery. As a result, the increase in fuel economy is expected to be impacted greater by the fuel cell degradation that the battery degradation. The fuel cell SOH over the lifetime of the vehicle is provided as Figure 87, revealing that the rate of fuel consumption increase corresponds to the rate of decrease in fuel cell SOH. Despite the fact that the cost function was initially designed to improve lifetime performance, the algorithm used represents an initial attempt at integrated real-time consideration of component degradation.

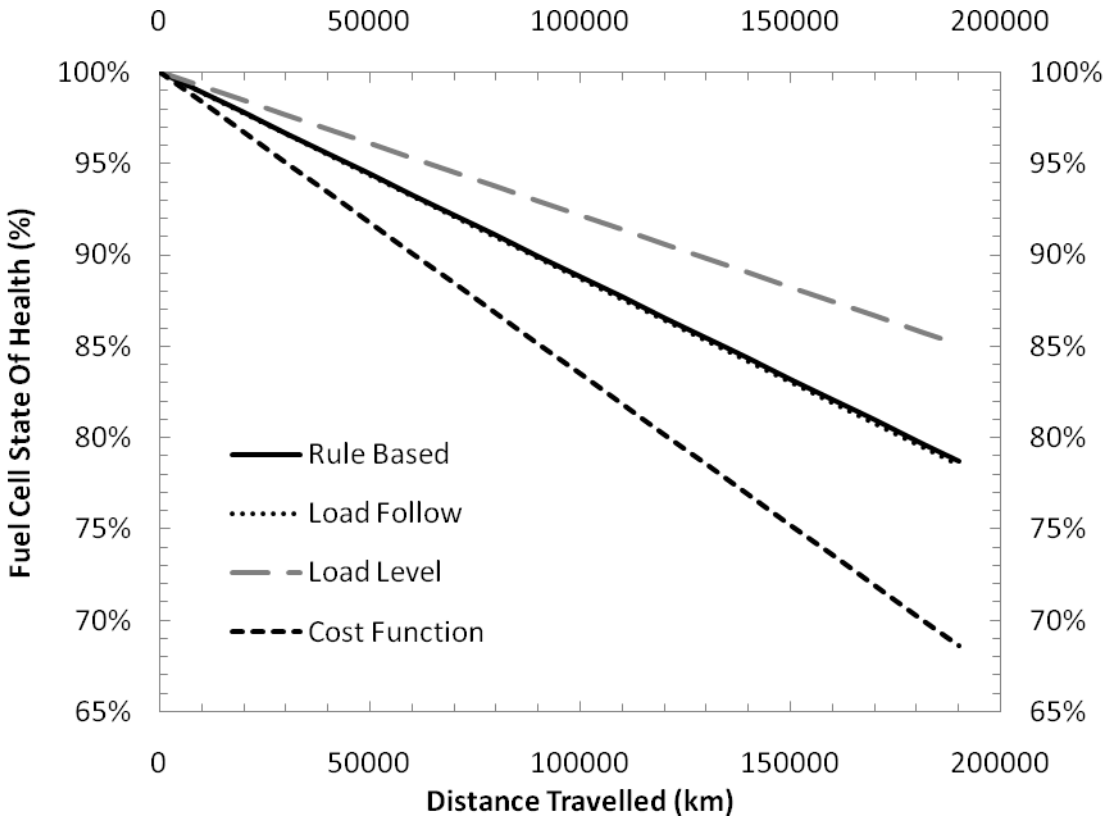

Figure 87 – Fuel cell State of Health (SOH) over the lifetime of the vehicle

The main driver of the accelerated degradation of fuel cell SOH is high transient power demands of the fuel cell power module, which thereby increase the degradation rate.

These results assume that the drive cycle is the UDDS cycle repeated throughout the vehicle life. The analysis was repeated with the HWFET drive cycle yielding similar trends; however, the fuel

advantage of the load level control strategy was reduced as all BOL fuel consumption equivalent values ranged from 5.2-5.8 L/100km equivalent.

5.2 Plug-In Vehicle: Blended vs. All-Electric Range

The battery pack from the vehicle model described above had a nominal capacity of ~2.5 kWh. In order to facilitate the integration of a charge-depleting mode of operation a model scenario was developed with the battery increased to ~10kWh by increasing the number of parallel strings from 4 to 16. The resulting pack mass was scaled accordingly, with an assumed packaging factor of 1.1. The packaging factor is multiplied by the additional cell mass to account for additional packaging, controls, and cooling mass. All other powertrain components were maintained. Given the significant increase in the power capability of the battery pack the fuel cell could have been downsized; however, that type of analysis is outside the scope of this thesis. The two common variations of the charge-depleting control strategies introduced in Chapter 2 are considered. The blended control strategy is a variation of the rule-based control strategy discussed earlier, with the modifications that the charge-depleting mode of operation continues until the SOC reaches 5% and fuel cell power threshold was increased to 22,000W. As a result the battery is used at any point the total electrical load is less than 22,000W and the fuel cell operates during power draws exceeding the threshold. For the all-electric control strategy the battery provides all power until the 5% limit is reached. In both cases the control strategy follows the rule-based control strategy operating between 5% and 25% SOC in the charge-sustaining mode of operation. The drive cycle considered was three completions of the trip EPA combined cycle, ensuring that the operation would include both charge-depleting and charge-sustaining portions.

It is important to note that the 20% SOC range (5% to 25%) during charge-sustaining mode of operation represents a significantly more energy than a corresponding 20% SOC range on the baseline vehicle. As a result, it is suggested that future simulations narrow the charge-sustaining SOC range to reflect a similar amount of energy as used in the baseline vehicle.

As the rapid degradation results of Chapter 4 would suggest, the battery degradation is significant and does not last the life of the vehicle. The battery capacity and power state of health over the first 30,000km of operation are provided as Figures 87 and 88 respectively. The results demonstrate that the capacity degradation is more significant than the power

degradation. The degradation rate of the all-electric charge-depleting strategy was significantly higher than the blended operation – demonstrating approximately 20% faster degradation in terms of both capacity and power degradation.

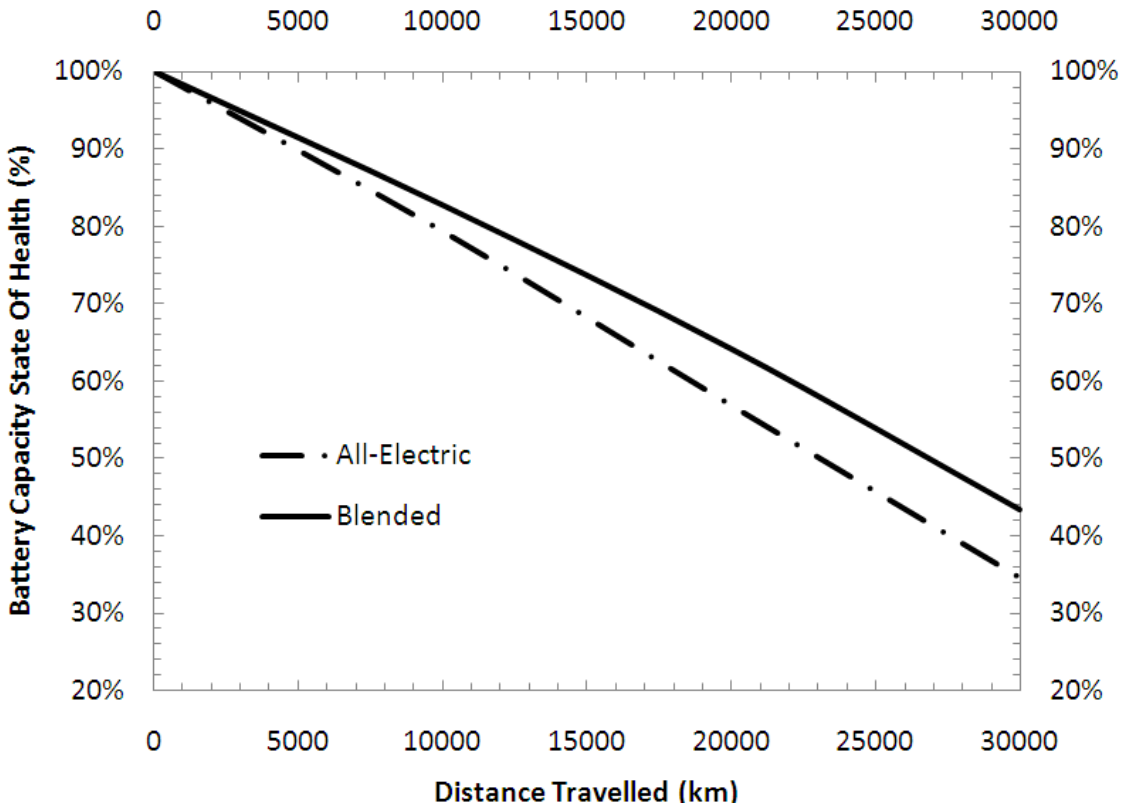

Figure 88 – Battery capacity state of health for blended and all-electric charge depleting control strategies

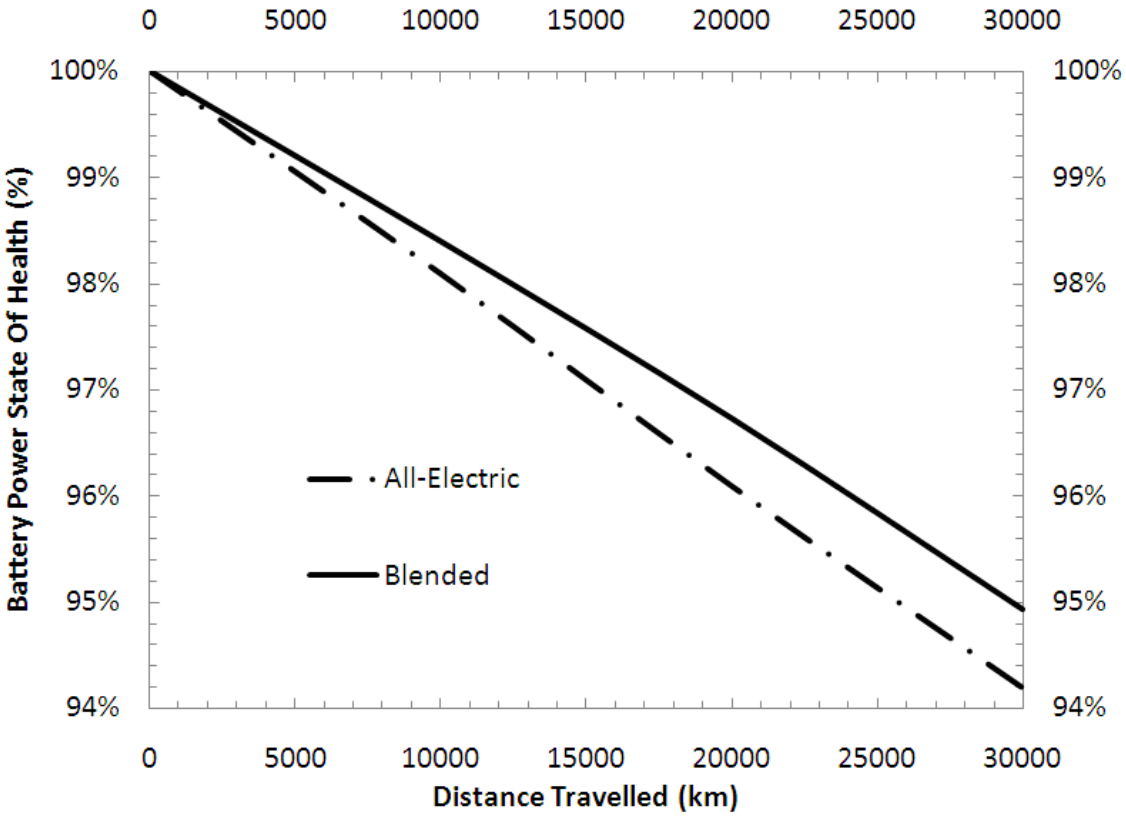

Figure 89 – Battery power state of health for blended and all-electric charge depleting control strategies

The fuel consumption and battery energy output for the two control strategies are provided in Figure 90. The fuel consumption trend (solid lines) demonstrates an initial advantage of the all-electric control strategy, follow by a slight advantage of the blended control strategy at 10,000km, which is negated and both control strategies exhibit similar fuel consumption values after 20,000km. The reason for the convergence of the curves is that the charge-sustaining portion of the drive cycle becomes increasingly weighted as the battery capacity degrades and the subsequent charge-depleting distance decreases.

The results clearly indicate the impact of the charge-depleting control strategy on fuel consumption and battery degradation. The impact of the charge-depleting control strategy on fuel consumption decreases as the battery ages as a result of the decrease fraction of travel in the charge-depleting mode of operation. The all-electric charge-depleting operation increases the degradation rate of the battery as compared to the blended charge-depleting operation.

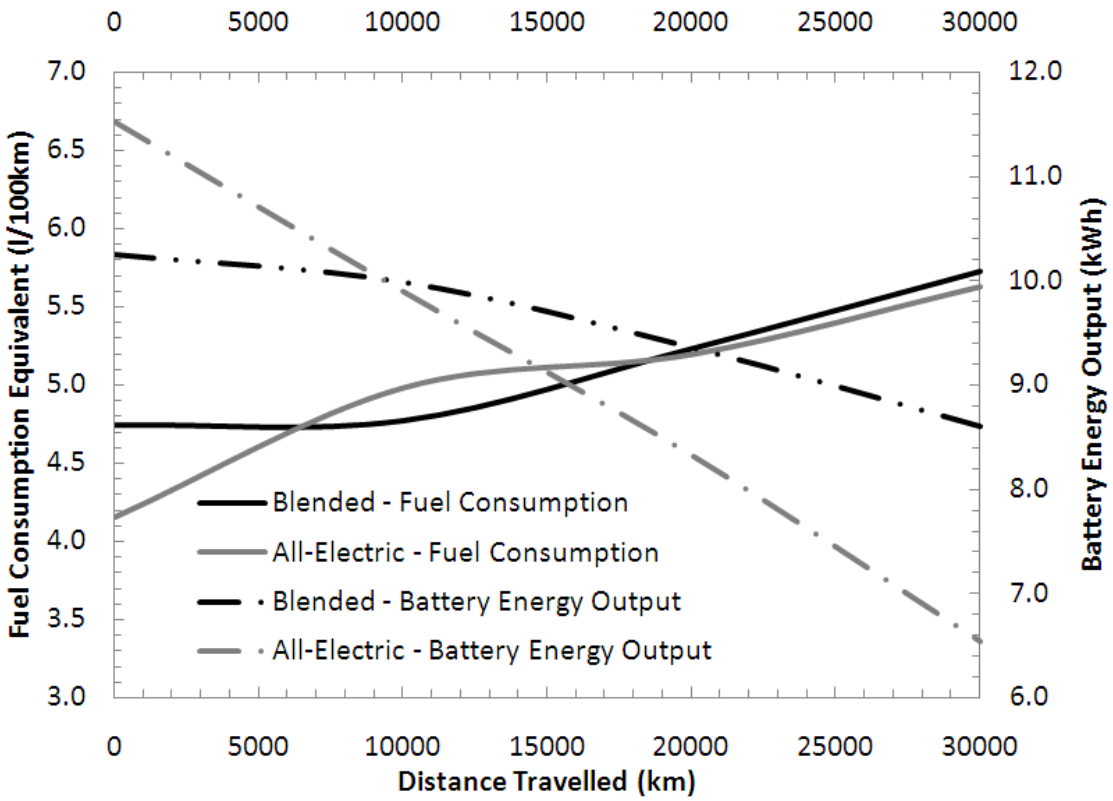

Figure 90 – Fuel consumption and battery energy output for blended and all-electric charge depleting control strategies

5.3 Plug-In Vehicle: Increasing Rated Battery Capacity

As discussed in the Introduction, a common practice is to oversize the battery. The practice of oversizing has two impacts. The first is that additional capacity provides additional margin for maintaining a minimum performance value – meaning that additional degradation can occur before a minimum performance metric is no longer met. The second is that the operating conditions represent a smaller fraction of the overall operating window (i.e. a smaller state of charge swing), thereby reducing the rate of degradation. These concepts are evaluated by performing a lifetime simulation of a plug-in hybrid vehicle incorporating a larger battery pack. As discussed in the last section, a nominal 10kWh battery pack consisting of 16 strings in parallel was implemented. In this section that battery pack is increased to 15 KWh by increasing the number of strings in parallel to 24 strings. As the intent was to reduce the useable window of the battery pack the initial SOC was reduced from 97% to 85% and the end of charge-depleting SOC limit was increased from 5% to 25%. The result is that the same amount of nominal energy

is available from the battery pack; however, this energy represents a smaller fraction of the total energy available from the battery pack and avoids operation at SOC extremes. The subsequent battery capacity SOH is plotted in Figure 91. Over the first 30,000km the degradation of the larger battery pack is significantly less – both in percentage terms and absolute terms. As a result, the reduction in degradation rate and increase in operating margin was demonstrated.

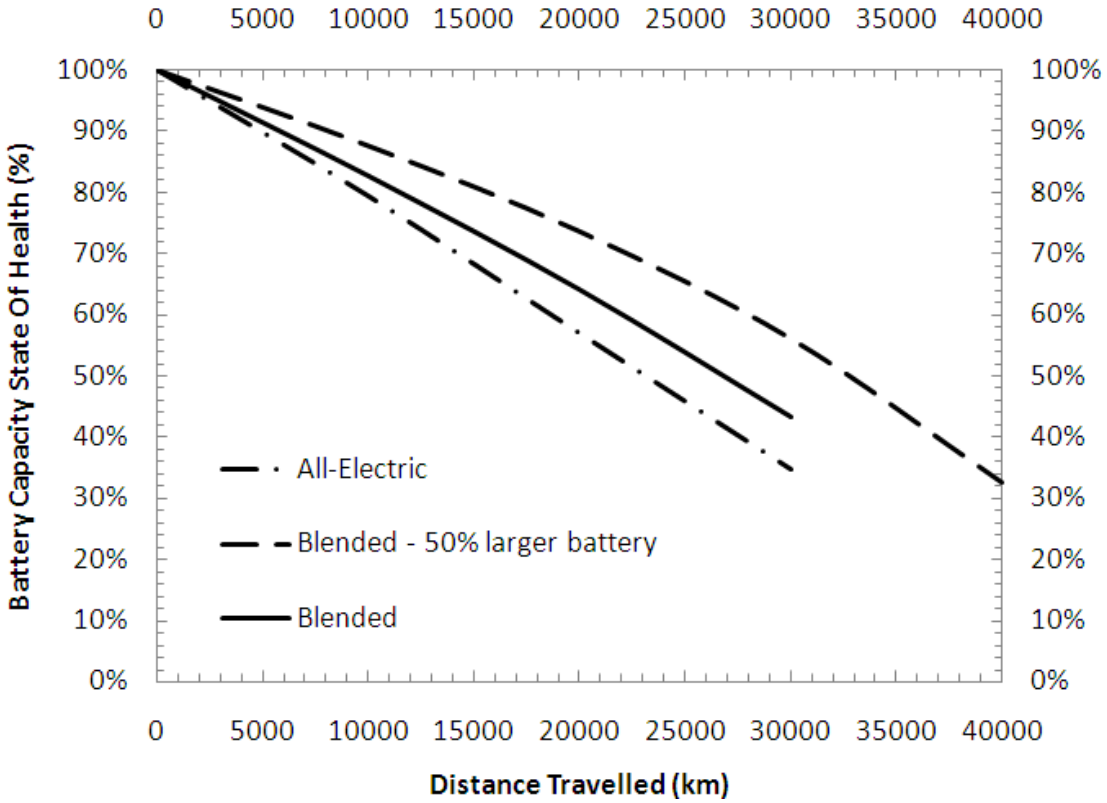

Figure 91 – Battery capacity state of health for blended and all-electric charge depleting control strategies with a larger battery

In this chapter, the impact of charge-sustaining hybrid control strategy, drive cycle, charge-depleting control strategy, and component sizing on lifetime vehicle performance has been evaluated. It is important to reiterate that the battery causal degradation model was developed based upon high discharge rates and large SOC swing and additional work is required to ensure the model is equally valid for all operation modes. Despite the additional development required on the component degradation models, the accelerating degradation factors (temperature, SOC, overvoltage) and the general relationship of the degradation acceleration are expected to remain consistent. As a result, the current models may overestimate the degradation rate of

the battery; however, the models provide valuable information for comparison purposes between control strategies and sizing.

The results herein demonstrate the significant potential of integrating causal degradation models into a model-based design process. The simulation that requires less than a day of computational time can provide valuable insight into the impact of control and sizing decisions on lifetime vehicle performance. Increasing battery capacity increases the battery lifetime; however, it comes at additional cost and mass. The approach described herein allows for quantifying the relationship for a given application and vehicle, thereby allowing for an informed tradeoff of component life with cost and mass.

Chapter 6

Conclusions, Contributions, and Recommendations

For the development of a model-based design approach for hybrid fuel cell powertrains, research in three specific areas was required. The first area of research included the development of a validated hybrid fuel cell vehicle model. Given the lack of data available, a hybrid fuel cell passenger vehicle was designed, built, refined, and tested. The resulting data allowed for the development of a validated hybrid fuel cell vehicle model that could be used reliably for the prediction of energy consumption. The second area of research included the development of a causal battery and fuel cell degradation models. Given the lack of high current battery degradation data, a hybrid powertrain test stand was designed, built, and operated. The resulting data allowed for the adaption of a previously published battery degradation data and models to include causal degradation at high charge and discharge currents. Additionally, a causal fuel cell degradation model was developed based upon degradation rates published in various studies. The third area of research consisted of bridging the causal degradation models with the baseline hybrid fuel cell vehicle model, including lifetime simulations that were feasible in terms of computation time and file size. Finally, the capability of the developed hybrid fuel cell vehicle model to evaluate component sizing and control decisions was demonstrated. The demonstration was extended to consider the component degradation in a plug-in hybrid variation of the powertrain.

6.1 Conclusions

The following results were achieved:

- a hybrid hydrogen fuel cell vehicle was designed and built at the University of Waterloo. This is one of first successfully student built fuel cell passage vehicles. During dynamometer testing at Argonne National Laboratory the vehicle achieved an equivalent gasoline fuel consumption of 7.72L/100km (31 mpg_e) on the UDDS drive cycle, and the vehicle was able to successfully complete a road trial from New York to Washington.
- A baseline vehicle model is developed and validated to dynamometer performance of the hybrid fuel cell vehicle. The results demonstrate accuracy of the model to be within 2% of the actual energy consumption. Additionally, a high level of accuracy was observed for the individual component models. The validated hybrid fuel cell model predicted equivalent fuel consumptions of 5.69L/100km and 8.65L/100km for the HWFET and US06 cycles respectively.
- a scaled hybrid fuel cell powertrain test stand was successfully built to allow for accelerated testing for lithium ion batteries. Battery degradation studies were successfully performed consisting of 1000 cycles of 60A discharge, 10A charge rates, over the entire useable SOC window at that current. Given that a 2V cut-off voltage was used to denote end-of-discharge, the corresponding SOC range was approximately 95% to 10%. Additional studies were successfully performed for 30A discharge rates. All studies demonstrated over 50% capacity degradation during the 1000 cycles. Power degradation was also found to be significant.
- a causal battery degradation model was developed for a lithium ion ($LiFePO_4$ cathode) chemistry and was validated to data from the scaled hybrid powertrain test stand. The causal degradation model added temperature and state of charge (SOC) accelerating factors to a previously developed battery degradation model. The 0-D model was empirically derived from degradation results that represents the main degradation mechanisms that were introduced and validated in a 1-D first principles model previously developed by Ning.

- a causal fuel cell degradation model was developed based upon literature results. The degradation rate was accelerated by transient operation, aggregating the effects of humidity cycling, potential cycling, time at OCV, and start/stop cycles.
- the causal component degradation models was integrated into the baseline vehicle model to create a hybrid fuel cell vehicle model that degrades based on design parameters and operating conditions.
- various control strategies were compared to evaluate lifetime performance. The initial form of the cost function demonstrated the most significant increase in fuel consumption as the vehicle ages. This was a novel application of cost function to the reliability of hydrogen vehicle powertrains.
- a variation of the baseline model consisting of a larger battery pack permitting the integration of charge-depleting operation was developed. The capacity degradation was found to be an order of magnitude more significant than the power degradation. The impact of blended and all-electric hybrid control strategies during charge-depleting operation was evaluated. The all-electric control strategy was found to increase the battery degradation by ~20% as compared to the blended control strategy.
- For a specific powertrain design, the battery pack capacity was increased by 50% while the useable energy was maintained. The result of the battery pack oversizing was compared to the previous result. The oversized battery pack demonstrated lower degradation rates in both percentage and absolute terms.

The work represents the foundational research required for the development of electrochemical component degradation into the model based design process for fuel cell vehicles. The causal component degradation requires additional refinement; however, an initial hybrid fuel cell vehicle model incorporating component degradation was developed and the ability to quantify the impact of sizing and control design decisions was clearly demonstrated.

6.2 Contributions

This research contains a number of novel contributions to the scientific community and the publically available body of knowledge. Specifically,

- A student-built hybrid fuel cell passenger vehicle was build and made available for research. The vehicle was used for both Public Outreach and research programs. The

dynamometer testing has provided validated component performance data that can be used for overall vehicle performance. Prior to the start of this project very limited information was available on the real-world performance of hybrid fuel cell passenger vehicles (and much of the data was closely protected by OEM vehicle manufacturing companies).

- A validated charge-sustaining hybrid fuel cell vehicle model was developed. Similar to the previous point, almost no models were available that had been validated to real-world performance, with components sizings of the order of magnitude required for a passenger vehicle, and relatively contemporary technology. Through this research a validated hybrid fuel cell vehicle model has been made available to the scientific community. This research also advanced the practice of model based design processes by applying this process to a fuel cell vehicle.
- High current and full SOC degradation data of commercial lithium ion batteries were developed in the lab. Previously published results consisted of low currents or low SOC swings. The results presented herein present degradation for simultaneous operation of both wide SOC ranges and high discharge and charge rates. This data is required for consideration of plug-in hybrid vehicles.
- Causal component degradation model of a lithium battery for high current and large SOC swings. The previous point describes the lack of degradation data available. This point highlights the contribution of a causal degradation model based upon the data captured.
- The development of a hybrid fuel cell vehicle model that incorporates causal component degradation. As of both the initiation and completion of this research, no known equivalent has been presented or published. The degrading component model is believed to be the first hybrid fuel cell powertrain model developed that permits the simulation of lifetime vehicle performance. As presented in the thesis, the value of the model is significant for the quantification of sizing and control design decisions.

6.3 Recommendations

As previously mentioned, the work performed as part of this research is foundational in nature. The work presented develops a validated baseline vehicle model and framework for the integration of component degradation into model-based design. While there are a number of

potential extensions and applications of this body of work, the three that are of immediate interest and importance are:

1. Evaluation of the effect of electrolyte concentration gradients under various charge and discharge rates. The empirical model that was developed assumes that the variation in electrolyte concentration across the cell is negligible as compared to the high charge and discharge rates collected herein. It is recommended that this assumption be investigated in detail and it be determined that the charge and discharge currents at which the electrolyte concentration gradients becomes significant be identified. This would allow for the selection of the appropriate 0-D empirical or 1-D first principles degradation models based upon the charge or discharge rate.

2. Refinement of the causal component degradation models. The battery model was developed based upon high discharge and charge currents and large SOC swings. Subsequently the degradation model may overestimate the degradation rate at lower currents and/or narrower SOC ranges. The ability of the model to accurately predict lifetime performance depends on the accuracy of the degradation model. Due to the varying nature of the duty cycle during operation the causal model must demonstrate sufficient accuracy for all anticipated levels of operating conditions. The amount of data required for such a model is likely beyond the capabilities of an academic program, but could be developed in partnership with a battery pack developer.

3. Development of optimal design criteria for sizing and control decisions. The integration of optimization loops to the design process was discussed in Chapter 2. The integration of a Simulated Annealing (SA) loop into the causal degradation vehicle model was initiated but not completed. The optimization must include simultaneous optimization of sizing and control parameters. The accelerated 'build' timetable for the vehicle, and limited component availability were impediments to more detailed used of the model based design process, but this work a has clearly demonstrated the value of such work.

4. Development of a real-time control strategy that minimizes the effect of drive cycle on component degradation. The optimal design described above is anticipated to be heavily dependent on the drive cycle. The development of a real-time control strategy that considers component degradation would be of significant value. While the power demand for the traction motor is fixed by the driver, the control strategy would control

the battery and fuel cell duty cycles to minimize the overall degradation rate. As previously described, the OEM must design the vehicle in anticipation of the highest expected degradation rate. If a control strategy is developed that reduces the variation in degradation rate the highest expected degradation rate will decrease, thereby permitting a downsizing of the component sizing. This was the intent of the cost function control strategy – the results presented in Chapter 5 demonstrate that significant work remains on this front. This work could also be extended into the business modeling field with the development of warranty programs for future vehicles.

This list is not exhaustive by any measure. These three items; however, are suggested as the three obvious extensions that are believed to have the largest potential benefits to this body of research.

References

[1] J. Heywood, “Fueling our transportation future,” *SCIENTIFIC AMERICAN*, vol. 295, Sep. 2006, pp. 60-63.

[2] M. Kromer and J. Heywood, “A Comparative Assessment of Electric Propulsion Systems in the 2030 US Light-Duty Vehicle Fleet,” *2008-01-0459*, Detroit, Michigan: SAE Digital Library , 2008.

[3] K. Jeong and B. Oh, “Fuel economy and life-cycle cost analysis of a fuel cell hybrid vehicle,” *JOURNAL OF POWER SOURCES*, vol. 105, Mar. 2002, pp. 58-65.

[4] A. Schafer, J. Heywood, and M. Weiss, “Future fuel cell and internal combustion engine automobile technologies: A 25-year life cycle and fleet impact assessment,” *ENERGY*, vol. 31, Sep. 2006, pp. 2064-2087.

[5] B. Williams and K. Kurani, “Commercializing light-duty plug-in/plug-out hydrogen-fuel-cell vehicles: "Mobile Electricity" technologies and opportunities,” *JOURNAL OF POWER SOURCES*, vol. 166, Apr. 2007, pp. 549-566.

[6] J. Van Mierlo and G. Maggetto, “Fuel cell or battery: Electric cars are the future,” *FUEL CELLS*, vol. 7, Apr. 2007, pp. 165-173.

[7] J.M. Miller, *Propulsion Systems for Hybird Vehicles*, Peter Peregrinus Ltd, 2003.

[8] L. Guzzella and A. Sciarretta, *Vehicle Propulsion Systems: Introduction to Modeling and Optimization, 2nd edition*, Springer, 2007.

[9] I. Buchmann, “Are the Hybrid Cars here to stay?,” *Battery University*. http://www.batteryuniversity.com/parttwo-40a.htm

[10] M. Dubarry and B. Liaw, “Development of a universal modeling tool for rechargeable lithium batteries,” *JOURNAL OF POWER SOURCES*, vol. 174, Dec. 2007, pp. 856-860.

[11] M. Dubarry, V. Svoboda, R. Hwu, and B. Liaw, “A roadmap to understand battery performance in electric and hybrid vehicle operation,” *JOURNAL OF POWER SOURCES*, vol. 174, Dec. 2007, pp. 366-372.

[12] T. Markel and A. Simpson, “Plug-In Hybrid Electric Vehicle Energy Storage System Design,” *NREL/CP-540-39614*, Baltimore, Maryland: 2006.

[13] M. Dennis, “GM-VOLT : Chevy Volt Electric Car Site » Blog Archive » Latest Chevy Volt Battery Pack and Generator Details and Clarifications.”

[14] R. Ahluwalia and X. Wang, “Fuel cell systems for transportation: Status and trends,” *JOURNAL OF POWER SOURCES*, vol. 177, Feb. 2008, pp. 167-176.

[15] M. Herniter, Z. Chambers, S. Prabhu, M. Stevens, M. Fowler, and R. Fraser, “Model-Based Design for Hybrid Electric Vehicle Development,” *EVS-22*, Yokohoma, Japan: 2006.

[16] L. Slezak, *Advanced Vehicle Technology Analysis and Evaluation Activities - FY2006 Annual Report*, U.S. Department of Energy's FreedomCAR and Vehicle Technologies (FCVT) Program, 2007.

[17] T. McGuire, T. Roche, A. Weinberger, P. Friebe, and J. Friedrich, “Utilizing Automated Report Generation and Data Acquisition Tools to Guide Fue lCell Vehicle Fleet Operations,” *2008-01-0462*, Detroit, Michigan: SAE Digital Library, 2008.

[18] D. Gao, C. Mi, and A. Emadi, “Modeling and simulation of electric and hybrid vehicles,” *PROCEEDINGS OF THE IEEE*, vol. 95, Apr. 2007, pp. 729-745.

[19] C. Samaras and K. Meisterling, “Life cycle assessment of greenhouse gas emissions from plug-in hybrid vehicles: Implications for policy,” *ENVIRONMENTAL SCIENCE & TECHNOLOGY*, vol. 42, May. 2008, pp. 3170-3176.

[20] A. Burke, “Batteries and ultracapacitors for electric, hybrid, and fuel cell vehicles,” *PROCEEDINGS OF THE IEEE*, vol. 95, Apr. 2007, pp. 806-820.

[21] K. Jonasson, “Analysing Hybrid Drive System Topologies,” PhD Thesis, Lund University. http://www.iea.lth.se/publications/Theses/LTH-IEA-1031.pdf

[22] W. Gao, “Performance comparison of a fuel cell-battery hybrid powertrain and a fuel cell-ultracapacitor hybrid powertrain,” *IEEE TRANSACTIONS ON VEHICULAR TECHNOLOGY*, vol. 54, May. 2005, pp. 846-855.

[23] J. Wishart, “Modelling, Simulation, Testing, and Optimization of Advanced Hybrid Vehicle Powertrains,” PhD, University of Victoria, 2008.

[24] S. Kim and S. Choi, “Development of Fuel Cell Hybrid Vehicle by Using Ultra-Capacitors as a Secondary Power Source,” *SAE Digital Library*, Detroit, Michigan: 2005.

[25] J. Bauman and M. Kazerani, “A comparative study of fuel-cell-battery, fuel-cell-ultracapacitor, and fuel-cell-battery-ultracapacitor vehicles,” *IEEE TRANSACTIONS ON VEHICULAR TECHNOLOGY*, vol. 57, Mar. 2008, pp. 760-769.

[26] Z. Filipi, L. Louca, B. Daran, C. Lin, U. Yildir, B. Wu, M. Kokkolaras, D. Assanis, H. Peng, P. Papalambros, J. Stein, D. Szkubiel, and R. Chapp, “Combined optimisation of design and power management of the hydraulic hybrid propulsion system for the 6x6 medium truck,” *INTERNATIONAL JOURNAL OF HEAVY VEHICLE SYSTEMS*, vol. 11, 2004, pp. 372-402.

[27] B. Wu, C. Lin, Z. Filipi, H. Peng, and D. Assanis, “Optimal power management for a hydraulic hybrid delivery truck,” *VEHICLE SYSTEM DYNAMICS*, vol. 42, Aug. 2004, pp. 23-40.

[28] P. Moseley and D. Rand, “Changes in the demands on automotive batteries require changes in battery design,” *JOURNAL OF POWER SOURCES*, vol. 133, May. 2004, pp. 104-109.

[29] Y. Gao and M. Ehsani, “Parametric design of the traction motor and energy storage for series hybrid off-road and military vehicles,” *IEEE TRANSACTIONS ON POWER ELECTRONICS*, vol. 21, May. 2006, pp. 749-755.

[30] Y. Gao and M. Ehsani, “A torque and speed coupling hybrid drivetrain - Architecture, control, and simulation,” *IEEE TRANSACTIONS ON POWER ELECTRONICS*, vol. 21, May. 2006, pp. 741-748.

[31] T. Christen and M. Carlen, “Theory of Ragone plots,” *JOURNAL OF POWER SOURCES*, vol. 91, Dec. 2000, pp. 210-216.

[32] T. Christen and C. Ohler, “Optimizing energy storage devices using Ragone plots,” *JOURNAL OF POWER SOURCES*, vol. 110, Jul. 2002, pp. 107-116.

[33] J. Pukrushpan, H. Peng, and A. Stefanopoulou, “Control-oriented modeling and analysis for automotive fuel cell systems,” *JOURNAL OF DYNAMIC SYSTEMS MEASUREMENT AND CONTROL-TRANSACTIONS OF THE*, vol. 126, Mar. 2004, pp. 14-25.

[34] R. Ahluwalia, X. Wang, and A. Rousseau, “Fuel economy of hybrid fuel-cell vehicles,” *JOURNAL OF POWER SOURCES*, vol. 152, Dec. 2005, pp. 233-244.

[35] P. Corbo, F. Corcione, F. Mighardini, and O. Veneri, “Experimental study of a fuel cell power train for road transport application,” *JOURNAL OF POWER SOURCES*, vol. 145, Aug. 2005, pp. 610-619.

[36] P. Corbo, F. Corcione, F. Migliardini, and O. Veneri, “Experimental assessment of energy-management strategies in fuel-cell propulsion systems,” *JOURNAL OF POWER SOURCES*, vol. 157, Jul. 2006, pp. 799-808.

[37] P. Corbo, F. Corcione, F. Migliardini, and O. Veneri, “Energy management in fuel cell power trains,” *ENERGY CONVERSION AND MANAGEMENT*, vol. 47, Nov. 2006, pp. 3255-3271.

[38] Y. Guezennec, Ta-Young Choi, G. Paganelli, and G. Rizzoni, “Supervisory control of fuel cell vehicles and its link to overall system efficiency and low-level control requirements,” *American Control Conference, 2003. Proceedings of the 2003*, 2003, pp. 2055-2061 vol.3.

[39] S. Gurski, H. Lohse-Busch, G. Henshaw, and D. Nelson, “Design of a Zero Emission Sport Utility Vehicle for FutureTruck 2002,” *2003-01-1264*, Detroit, Michigan: SAE Digital Library, 2003.

[40] B. Jeanneret and T. Markel, “Adaptive energy management strategy for fuel cell hybrid vehicles,” *SAE Digital Library*, Detroit, Michigan: 2004.

[41] Z. Jiang, L. Gao, and R. Dougal, “Flexible multiobjective control of power converter in active hybrid fuel cell/battery power sources,” *Power Electronics, IEEE Transactions on*, vol. 20, 2005, pp. 244-253.

[42] M. Ouyang, L. Xu, J. Li, L. Lu, D. Gao, and Q. Me, “Performance comparison of two fuel cell hybrid buses with different powertrain and energy management strategies,” *JOURNAL OF POWER SOURCES*, vol. 163, Dec. 2006, pp. 467-479.

[43] V. Paladini, T. Donateo, A. de Risi, and D. Laforgia, “Super-capacitors fuel-cell hybrid electric vehicle optimization and control strategy development,” *ENERGY CONVERSION AND MANAGEMENT*, vol. 48, Nov. 2007, pp. 3001-3008.

[44] P. Rodatz, G. Paganelli, A. Sciarretta, and L. Guzzella, “Optimal power management of an experimental fuel cell/supercapacitor-powered hybrid vehicle,” *CONTROL ENGINEERING PRACTICE*, vol. 13, Jan. 2005, pp. 41-53.

[45] A. Schell, H. Peng, D. Tran, E. Stamos, C. Lin, and M. Kim, “Modelling and control strategy development for fuel cell electric vehicles,” *ANNUAL REVIEWS IN CONTROL*, vol. 29, 2005, pp. 159-168.

[46] M. Stevens, C. Mendes, M. Fowler, and R. Fraser, “Fuel Cell Hybrid Control Strategy Development,” *2006-01-0214*, Detroit, Michigan: SAE Digital Library, 2006.

[47] O. Sundstrom and A. Stefanopoulou, “Optimum battery size for fuel cell hybrid electric vehicle - Part I,” *JOURNAL OF FUEL CELL SCIENCE AND TECHNOLOGY*, vol. 4, May. 2007, pp. 167-175.

[48] R. Ahluwalia, X. Wang, A. Rousseau, and R. Kumar, “Fuel economy of hydrogen fuel cell vehicles,” *JOURNAL OF POWER SOURCES*, vol. 130, May. 2004, pp. 192-201.

[49] M. Gokasan, S. Bogosyan, and D. Goering, “Sliding mode based powertrain control for efficiency improvement in series hybrid-electric vehicles,” *IEEE TRANSACTIONS ON POWER ELECTRONICS*, vol. 21, May. 2006, pp. 779-790.

[50] V. Johnson, K. Wipke, and D. Rausen, “HEV control strategy for real-time optimization of fuel economy and emissions,” *2000-01-1543*, Arlington, Virginia: SOCIETY OF AUTOMOTIVE ENGINEERING, 2000.

[51] M. Duoba and R. Carlson, “Test Procedure Development for “Blended Type” Plug-In Hybrid Vehicles,” *2008-01-0457*, Detroit, Michigan: SAE Digital Library, 2008.

[52] V. Freyermuth, E. Fallas, and A. Rousseau, “Comparison of Powertrain Configuration for Plug-in HEVs from a Fuel Economy Perspective,” *SAE Digital Library*, Detroit, Michigan: 2008.

[53] P. Sharer, A. Rousseau, D. Karbowski, and S. Pagerit, “Plug-in Hybrid Electric Vehicle Control Strategy: Comparison between EV and Charge-Depleting Options,” *SAE Digital Library*, Detroit, Michigan: 2008.

[54] J. Larminie and A. Dicks, *Fuel Cell Systems Explained*, J. Wiley, 2003.

[55] B. Steele, “Material science and engineering: The enabling technology for the commercialisation of fuel cell systems,” *JOURNAL OF MATERIALS SCIENCE*, vol. 36, Mar. 2001, pp. 1053-1068.

[56] C. Maxoulis, D. Tsinoglou, and G. Koltsakis, “Modeling of automotive fuel cell operation in driving cycles,” *ENERGY CONVERSION AND MANAGEMENT*, vol. 45, Mar. 2004, pp. 559-573.

[57] V. Mehta and J. Cooper, “Review and analysis of PEM fuel cell design and manufacturing,” *JOURNAL OF POWER SOURCES*, vol. 114, Feb. 2003, pp. 32-53.

[58] “DuPont™ Nafion® Membranes and Dispersions for DuPont Fuel Cells.”

[59] K. Haraldsson and K. Wipke, “Evaluating PEM fuel cell system models,” *JOURNAL OF POWER SOURCES*, vol. 126, Feb. 2004, pp. 88-97.

[60] A. Biyikoglu, “Review of proton exchange membrane fuel cell models,” *INTERNATIONAL JOURNAL OF HYDROGEN ENERGY*, vol. 30, Sep. 2005, pp. 1181-1212.

[61] D. Cheddie and N. Munroe, “Review and comparison of approaches to proton exchange membrane fuel cell modeling,” *JOURNAL OF POWER SOURCES*, vol. 147, Sep. 2005, pp. 72-84.

[62] J. Amphlett, R. Baumert, R. Mann, B. Peppley, P. Roberge, and T. Harris, “Performance modeling of the Ballard Mark IV solid polymer electrolyte fuel cell - Mechanistic model development,” *JOURNAL OF THE ELECTROCHEMICAL SOCIETY*, vol. 142, Jan. 1995, pp. 1-8.

[63] J. Amphlett, R. Baumert, R. Mann, B. Peppley, P. Roberge, and T. Harris, “Performance modeling of the Ballard Mark IV solid polymer electrolyte fuel cell - Empirical model development,” *JOURNAL OF THE ELECTROCHEMICAL SOCIETY*, vol. 142, Jan. 1995, pp. 9-15.

[64] J. Kim, S. Lee, S. Srinivasan, and C. Chamberlin, “Modeling of proton-exchange membrane fuel-cell performance with an emperical-equation,” *JOURNAL OF THE ELECTROCHEMICAL SOCIETY*, vol. 142, Aug. 1995, pp. 2670-2674.

[65] R. Mann, J. Amphlett, M. Hooper, H. Jensen, B. Peppley, and P. Roberge, “Development and application of a generalised steady-state electrochemical model for a PEM fuel cell,” *JOURNAL OF POWER SOURCES*, vol. 86, Mar. 2000, pp. 173-180.

[66] T. Springer, T. Zawodzinski, and S. Gottesfeld, “Polymer electrolyte fuel cell model,” *JOURNAL OF THE ELECTROCHEMICAL SOCIETY*, vol. 138, Aug. 1991, pp. 2334-2342.

[67] L. Dumercy, R. Glises, H. Louahlia-Gualous, and J. Kauffmann, “Thermal management of a PEMFC stack by 3D nodal modeling,” *JOURNAL OF POWER SOURCES*, vol. 156, May. 2006, pp. 78-84.

[68] G. Karimi, J. Baschuk, and X. Li, “Performance analysis and optimization of PEM fuel cell stacks using flow network approach,” *JOURNAL OF POWER SOURCES*, vol. 147, Sep. 2005, pp. 162-177.

[69] D. Boettner and M. Moran, “Proton exchange membrane (PEM) fuel cell-powered vehicle performance using direct-hydrogen fueling and on-board methanol reforming,” *ENERGY*, vol. 29, Dec. 2004, pp. 2317-2330.

[70] D. Boettner, G. Paganelli, Y. Guezennec, G. Rizzoni, and M. Moran, “Proton Exchange Membrane Fuel Cell System Model for Automotive Vehicle Simulation and Control,” *JOURNAL OF ENERGY RESOURCES TECHNOLOGY*, vol. 124, Mar. 2002, pp. 20-27.

[71] D. Boettner, G. Paganelli, Y. Guezennec, G. Rizzoni, and M. Moran, “On-board reforming effects on the performance of proton exchange membrane (PEM) fuel cell vehicles,” *JOURNAL OF ENERGY RESOURCES TECHNOLOGY-TRANSACTIONS OF THE ASME*, vol. 124, Sep. 2002, pp. 191-196.

[72] M. Fowler, J. Amphlett, R. Mann, B. Peppley, and P. Roberge, “Issues associated with voltage degradation in a PEMFC,” *JOURNAL OF NEW MATERIALS FOR ELECTROCHEMICAL SYSTEMS*, vol. 5, Oct. 2002, pp. 255-262.

[73] “Review of the Research Program of the FreedomCAR and Fuel Partnership: First Report.” http://books.nap.edu/openbook.php?isbn=0309097304

[74] S. Cleghorn, D. Mayfield, D. Moore, J. Moore, G. Rusch, T. Sherman, N. Sisofo, and U. Beuscher, "A polymer electrolyte fuel cell life test: 3 years of continuous operation," *JOURNAL OF POWER SOURCES*, vol. 158, Jul. 2006, pp. 446-454.

[75] R. Baldwin, M. Pham, A. Leonida, J. McElroy, and T. Nalette, "Hydrogen oxygen proton-exchange membrane fuel-cells and electrolyzers," *JOURNAL OF POWER SOURCES*, vol. 29, Feb. 1990, pp. 399-412.

[76] S. Knights, K. Colbow, J. St-Pierre, and D. Wilkinson, "Aging mechanisms and lifetime of PEFC and DMFC," *JOURNAL OF POWER SOURCES*, vol. 127, Mar. 2004, pp. 127-134.

[77] M. Fowler, R. Mann, J. Amphlett, B. Peppley, and P. Roberge, "Incorporation of voltage degradation into a generalised steady state electrochemical model for a PEM fuel cell," *JOURNAL OF POWER SOURCES*, vol. 106, Apr. 2002, pp. 274-283.

[78] A. Kulikovsky, H. Scharmann, and K. Wippermann, "Dynamics of fuel cell performance degradation," *ELECTROCHEMISTRY COMMUNICATIONS*, vol. 6, Jan. 2004, pp. 75-82.

[79] F. Uribe and T. Zawodzinski, "A study of polymer electrolyte fuel cell performance at high voltages. Dependence on cathode catalyst layer composition and on voltage conditioning," *ELECTROCHIMICA ACTA*, vol. 47, Aug. 2002, pp. 3799-3806.

[80] F. de Bruijn, V. Dam, and G. Janssen, "Durability and degradation issues of PEM fuel cell components," *FUEL CELLS*, vol. 8, Feb. 2008, pp. 3-22.

[81] J. Christophersen, G. Hunt, C. Ho, and D. Howell, "Pulse resistance effects due to charging or discharging of high-power lithium-ion cells: A path dependence study," *JOURNAL OF POWER SOURCES*, vol. 173, Nov. 2007, pp. 998-1005.

[82] "Vehicle Technologies Program: Multi-Year Program Plan." Department of Energy http://www1.eere.energy.gov/vehiclesandfuels/resources/fcvt_mypp.html

[83] "Battery Test Manual for Plug-In Hybrid Electric Vehicles." Idaho National Laboratory. http://www.inl.gov/technicalpublications/Documents/3952791.pdf

[84] J. Nan, Y. Yang, J. You, and Z. Lin, "Influence of surface pretreatment and charge-discharge mode on cycle performance of metal hydride electrodes," *JOURNAL OF POWER SOURCES*, vol. 79, May. 1999, pp. 64-68.

[85] J. Yu, S. Lee, K. Cho, and J. Lee, "The cycle life of Ti0.8Zr0.2V0.5Mn0.5-xCrxNi0.8 (x=0 to 0.5) alloys to metal hydride electrodes of Ni-metal hydride rechargeable battery," *JOURNAL OF THE ELECTROCHEMICAL SOCIETY*, vol. 147, Jun. 2000, pp. 2013-2017.

[86] Y. Xu, C. Chen, X. Wang, and Q. Wang, "The relationship between the high-rate dischargeability and the diffusion coefficient and exchange current for Ti0.5Ni0.25Al0.25 metal hydride alloys," *JOURNAL OF ALLOYS AND COMPOUNDS*, vol. 335, Mar. 2002, pp. 262-265.

[87] A. Svensson, L. Valoen, and R. Tunold, "Modeling of the impedance response of porous metal hydride electrodes," *ELECTROCHIMICA ACTA*, vol. 50, Apr. 2005, pp. 2647-2653.

[88] A. Hammouche, E. Karden, and R. De Doncker, "Monitoring state-of-charge of Ni-MH and Ni-Cd batteries using impedance spectroscopy," *JOURNAL OF POWER SOURCES*, vol. 127, Mar. 2004, pp. 105-111.

[89] L. Zhang, “AC impedance studies on sealed nickel metal hydride batteries over cycle life in analog and digital operations,” *ELECTROCHIMICA ACTA*, vol. 43, 1998, pp. 3333-3342.

[90] L. Kanevskii and V. Dubasova, “Degradation of lithium-ion batteries and how to fight it: A review,” *RUSSIAN JOURNAL OF ELECTROCHEMISTRY*, vol. 41, Jan. 2005, pp. 1-16.

[91] D. Abraham, J. Liu, C. Chen, Y. Hyung, M. Stoll, N. Elsen, S. MacLaren, R. Twesten, R. Haasch, E. Sammann, I. Petrov, K. Amine, and G. Henriksen, “Diagnosis of power fade mechanisms in high-power lithium-ion cells,” *JOURNAL OF POWER SOURCES*, vol. 119, Jun. 2003, pp. 511-516.

[92] D. Abraham, E. Reynolds, E. Sammann, A. Jansen, and D. Dees, “Aging characteristics of high-power lithium-ion cells with LiNi0.8Co0.15Al0.05O2 and Li4/3Ti5/3O4 electrodes,” *ELECTROCHIMICA ACTA*, vol. 51, Oct. 2005, pp. 502-510.

[93] J.P. Christophersen, C.D. Ho, C.G. Motloch, D. Howell, and H.L. Hess, “Effects of Reference Performance Testing during Aging Using Commercial Lithium-Ion Cells,” *JOURNAL OF THE ELECTROCHEMICAL SOCIETY*, vol. 153, Jul. 2006, pp. A1406-A1416.

[94] D. Abraham, E. Reynolds, P. Schultz, A. Jansen, and D. Dees, “Temperature dependence of capacity and impedance data from fresh and aged high-power lithium-ion cells,” *JOURNAL OF THE ELECTROCHEMICAL SOCIETY*, vol. 153, 2006, pp. A1610-A1616.

[95] I. Bloom, A. Jansen, D. Abraham, J. Knuth, S. Jones, V. Battaglia, and G. Henriksen, “Differential voltage analyses of high-power, lithium-ion cells 1. Technique and application,” *JOURNAL OF POWER SOURCES*, vol. 139, Jan. 2005, pp. 295-303.

[96] R. Spotnitz, “Simulation of capacity fade in lithium-ion batteries,” *JOURNAL OF POWER SOURCES*, vol. 113, Jan. 2003, pp. 72-80.

[97] J.R. Belt, C.D. Ho, T.J. Miller, M.A. Habib, and T.Q. Duong, “The effect of temperature on capacity and power in cycled lithium ion batteries,” *JOURNAL OF POWER SOURCES*, vol. 142, Mar. 2005, pp. 354-360.

[98] G. Ning and B. Popov, “Cycle life modeling of lithium-ion batteries,” *JOURNAL OF THE ELECTROCHEMICAL SOCIETY*, vol. 151, 2004, pp. A1584-A1591.

[99] R.B. Wright, J.P. Christophersen, C.G. Motloch, J.R. Belt, C.D. Ho, V.S. Battaglia, J.A. Barnes, T.Q. Duong, and R.A. Sutula, “Power fade and capacity fade resulting from cycle-life testing of Advanced Technology Development Program lithium-ion batteries,” *JOURNAL OF POWER SOURCES*, vol. 119-121, Jun. 2003, pp. 865-869.

[100] G. Sikha, P. Ramadass, B. Haran, R. White, and B. Popov, “Comparison of the capacity fade of Sony US 18650 cells charged with different protocols,” *JOURNAL OF POWER SOURCES*, vol. 122, Jul. 2003, pp. 67-76.

[101] Q. Zhang and R. White, “Capacity fade analysis of a lithium ion cell,” *JOURNAL OF POWER SOURCES*, vol. 179, May. 2008, pp. 793-798.

[102] H. Haskins, V. Battaglia, J. Christophersen, I. Bloom, G. Hunt, and E. Thomas, *Battery Technology Life Verification*
Test Manual, Idaho Falls, ID: Idaho National Laboratory, .

[103] M. Dubarry, V. Svoboda, R. Hwu, and B. Liaw, “Capacity loss in rechargeable lithium cells during cycle life testing: The importance of determining state-of-charge,” *JOURNAL OF POWER SOURCES*, vol. 174, Dec. 2007, pp. 1121-1125.

[104] C. Mendes, S. Lambert, and R. Fraser, “The Application of Model-Based Design Techniques in Academic Design Projects,” *2006-01-1312*, Detroit, Michigan: SAE Digital Library, 2006.

[105] K. Hauer and R. Moore, “Fuel Cell Vehicle Simulation – Part 1: Benchmarking Available Fuel Cell Vehicle Simulation Tools,” *FUEL CELLS*, vol. 3, Nov. 2003, pp. 84-94.

[106] K. Hauer and R. Moore, “Fuel Cell Vehicle Simulation – Part 2: Methodology and Structure of a New Fuel Cell Simulation Tool,” *FUEL CELLS*, vol. 3, Nov. 2003, pp. 95-104.

[107] K. Hauer and R. Moore, “Fuel Cell Vehicle Simulation – Part 3: Modeling of Individual Components and Integration into the Overall Vehicle Model,” *FUEL CELLS*, vol. 3, Nov. 2003, pp. 105-121.

[108] “Argonne PSAT Model.” Argonne National Laboratory. http://www.transportation.anl.gov/software/PSAT/

[109] R. Moore, K. Hauer, D. Friedman, J. Cunningham, P. Badrinarayanan, S. Ramaswamy, and A. Eggert, “A dynamic simulation tool for hydrogen fuel cell vehicles,” *JOURNAL OF POWER SOURCES*, vol. 141, Mar. 2005, pp. 272-285.

[110] R. Moore, S. Ramaswany, J. Cunningham, and K. Hauer, “A Dynamic Simulation Tool for the Battery-Hybrid Hydrogen Fuel Cell Vehicle,” *FUEL CELLS*, vol. 6, Oct. 2006, pp. 387-402.

[111] R. Moore, K. Hauer, G. Randolf, and M. Virji, “Fuel cell hardware-in-loop,” *JOURNAL OF POWER SOURCES*, vol. 162, Nov. 2006, pp. 302-308.

[112] A. Rousseau, P. Sharer, and R. Ahluwalia, “Energy storage requirements for fuel cell vehicles,” *2004-01-1302*, Detroit, Michigan: SAE Digital Library, 2004.

[113] M. Ogburn, D. Nelson, K. Wipke, and T. Markel, “Modeling and Validation of a Fuel Cell Hybrid Vehicle,” *2000-01-1566*, Detroit, Michigan: SAE Digital Library, 2000.

[114] Y. Jia, H. Wang, and M. Ouyang, “Electric power system for a Chinese fuel cell city bus,” *JOURNAL OF POWER SOURCES*, vol. 155, Apr. 2006, pp. 319-324.

[115] D. Assanis, G. Delagrammatikas, R. Fellini, Z. Filipi, J. Liedtke, N. Michelena, P. Papalambros, D. Reyes, D. Rosenbaum, A. Sales, and M. Sasena, “Optimization Approach to Hybrid Electric Propulsion System Design,” *MECHANICS BASED DESIGN OF STRUCTURES AND MACHINES*, vol. 27, 1999, p. 393.

[116] R. Fellini, N. Michelena, P. Papalambros, and M. Sasena, “Optimal design of automotive hybrid powertrain systems,” *Environmentally Conscious Design and Inverse Manufacturing, 1999. Proceedings. EcoDesign '99: First International Symposium On*, 1999, pp. 400-405.

[117] K. Wipke, T. Markel, and D. Nelson, “Optimizing Energy Management Strategy and Degree of Hybridization for a Hydrogen Fuel Cell SUV,” *Electric Vehicle Symposium*, Berlin: 2001.

[118] W. Gao and S. Porandla, “Design optimization of a parallel hybrid electric powertrain,” *Vehicle Power and Propulsion, 2005 IEEE Conference*, 2005, p. 6 pp.

[119] J. Han, M. Kokkolaras, and P. Papalambros, “Optimal Design of Hybrid Fuel Cell Vehicles,” *FUEL CELL SCIENCE, ENGINEERING AND TECHNOLOGY*, Irvine, California: ASME, 2006.

[120] M. Gobbi, I. Haque, P. Papalambros, and G. Mastinu, “A Critical Review of Optimization Methods for Road Vehicles Design,” Portsmouth, Virginia: 2006.

[121] D. Abraham, M. Furczon, S. Kang, D. Dees, and A. Jansen, “Effect of electrolyte composition on initial cycling and impedance characteristics of lithium-ion cells,” *JOURNAL OF POWER SOURCES*, vol. 180, May. 2008, pp. 612-620.

[122] P. Arora, R. White, and M. Doyle, “Capacity fade mechanisms and side reactions in lithium-ion batteries,” *JOURNAL OF THE ELECTROCHEMICAL SOCIETY*, vol. 145, Oct. 1998, pp. 3647-3667.

[123] D. Abraham, S. Poppen, A. Jansen, J. Liu, and D. Dees, “Application of a lithium-tin reference electrode to determine electrode contributions to impedance rise in high-power lithium-ion cells,” *ELECTROCHIMICA ACTA*, vol. 49, Oct. 2004, pp. 4763-4775.

[124] D. Dees, E. Gunen, D. Abraham, A. Jansen, and J. Prakash, “Alternating current impedance electrochemical modeling of lithium-ion positive electrodes,” *JOURNAL OF THE ELECTROCHEMICAL SOCIETY*, vol. 152, 2005, pp. A1409-A1417.

[125] M. Dolle, F. Orsini, A. Gozdz, and J. Tarascon, “Development of reliable three-electrode impedance measurements in plastic Li-ion batteries,” *JOURNAL OF THE ELECTROCHEMICAL SOCIETY*, vol. 148, Aug. 2001, pp. A851-A857.

[126] G. Ning, R. White, and B. Popov, “A generalized cycle life model of rechargeable Li-ion batteries,” *ELECTROCHIMICA ACTA*, vol. 51, Feb. 2006, pp. 2012-2022.

[127] V. Boovaragavan and V.R. Subramanian, “A quick and efficient method for consistent initialization of battery models,” *ELECTROCHEMISTRY COMMUNICATIONS*, vol. 9, Jul. 2007, pp. 1772-1777.

[128] V. Boovaragavan, S. Harinipriya, and V.R. Subramanian, “Towards real-time (milliseconds) parameter estimation of lithium-ion batteries using reformulated physics-based models,” *JOURNAL OF POWER SOURCES*, vol. 183, Aug. 2008, pp. 361-365.

[129] Q. Zhang, Q. Guo, and R. White, “Semi-empirical modeling of charge and discharge profiles for a LiCoO2 electrode,” *JOURNAL OF POWER SOURCES*, vol. 165, Feb. 2007, pp. 427-435.

[130] I. Bloom, B. Cole, J. Sohn, S. Jones, E. Polzin, V. Battaglia, G. Henriksen, C. Motloch, R. Richardson, T. Unkelhaeuser, D. Ingersoll, and H. Case, “An accelerated calendar and cycle life study of Li-ion cells,” *JOURNAL OF POWER SOURCES*, vol. 101, Oct. 2001, pp. 238-247.

Appendix A

Controller Pinouts

Controller:	Mototron ECU565-128
Processor:	Motorola MPC565
Clock Frequency:	56 MHz
Internal Flash:	1M
External Flash:	NIL
EEPROM	8K serial/ optional 64K x 8 (parallel)
Internal SRAM:	36K
Supply Voltage:	6-32VDC
Document Revision #	0

UWAFT Signal Name	Type	Range	Description	Mototron Name	Mototron Pin	Wire Number	Wire Colour	Connected To
Inputs - Analog								
SC2_A1	Input - Analog - 10 bit	0-5V	Intended for potentiometers. Tau=1ms. 220K pull down.	AN1M	A14	14	Tan	12V sens
SC2_A2	Input - Analog - 10 bit	0-5V	Intended for potentiometers. Tau=1ms. 220K pull down.	AN2M	A18	18	White/Dark Blue	24V sens
SC2_A3	Input - Analog - 10 bit	0-5V	Intended for potentiometers. Tau=1ms. 220K pull down.	AN3M	A8	8	Brown/White	DCDC_FC Current
SC2_A4	Input - Analog - 10 bit	0-5V	Intended for pressure sensors. Tau=100µs. 51K pull down. Intended for Manifold Air Pressure Sensor.	AN4M	A29	29	White/Light Blue	24V_VicorE_Status
SC2_A5	Input - Analog - 10 bit	0-5V	Intended for pressure sensors. Tau=1ms. 51K pull down.	AN5M	A30	30	White/Black	24V_VicorF_Status
SC2_A6	Input - Analog - 10 bit	0-5V	Intended for pressure sensors. Tau=1ms. 51K pull down.	AN6M	A6	6	Light Blue/White	
SC2_A7	Input - Analog - 10 bit	0-5V	Intended for pressure sensors. Tau=1ms. 51K pull down.	AN7M	A21	21	Dark Blue	TPS_SensorA
SC2_A8	Input - Analog - 10 bit	0-5V	Intended for pressure sensors. Tau=1ms. 51K pull down.	AN8M	A17	17	Brown	TPS_SensorB
SC2_A9	Input - Analog - 10 bit	0-5V	Intended for pressure sensors. Tau=1ms. 51K pull down.	AN9M	A25	25	Light Blue/Black	12V Vicor Current Sensor
SC2_A10	Input - Analog - 10 bit	0-5V	Intended for pressure sensors. Tau=1ms. 51K pull down.	AN10M	A16	16	Green	24V Vicor Current Sensor
SC2_A11	Input - Analog - 10 bit	0-5V	Intended for pressure sensors. Tau=1ms. 51K pull down.	AN11M	A26	26	Pink/Black	12V_VicorB_Status
SC2_A12	Input - Analog - 10 bit	0-5V	Intended for pressure sensors. Tau=1ms. 51K pull down.	AN12M	A15	15	Tan/Green	12V_VicorC_Status
SC2_A13	Input - Analog - 10 bit	0-5V	Intended for variable resistance sensor (eg. Thermistos). Tau=1ms. 2.2K pull UP.	AN13M	A10	10	Red/Pink	brake cylinder pressure
SC2_A14	Input - Analog - 10 bit	0-5V	Intended for variable resistance sensors (eg. Themistors), Tau=1ms, 1K pull up.	AN14M	A28	28	Dark Blue/White	DCDC_MainInductorThermistor
SC2_A15	Input - Analog - 10 bit	0-5V	Intended for variable resistance sensors (eg. Themistors), Tau=1ms, 1K pull up.	AN15M	A5	5	White/Orange	FC_CoolantInThermistor
SC2_A16	Input - Analog - 10 bit	0-5V	Intended for variable resistance sensors (eg. Themistors), Tau=1ms, 1K pull up.	AN16M	A27	27	Orange/Pink	H2_CabinSensorA
SC2_A17	Input - Analog - 10 bit	0-5V	Intended for variable resistance sensors (eg. Themistors), Tau=1ms, 1K pull up.	AN17M	A7	7	White/Yellow	H2_CabinSensorB
SC2_A18	Input - Analog - 10 bit	0-5V	Intended for variable resistance sensors (eg. Themistors), Tau=1ms, 1K pull up.	AN18M	C10	66	Yellow/White	MCU1_CoolantInThemistor
SC2_A19	Input - Analog - 10 bit	0-5V	Intended for variable resistance sensors (eg. Themistors), Tau=1ms, 1K pull up.	AN19M	C11	67	Pink/Brown	MCU1_CoolantOutThermistor
SC2_A20	Input - Analog - 10 bit	0-5V	Intended for variable resistance sensors (eg. Themistors), Tau=1ms, 1K pull up.	AN20M	C9	65	Yellow/Red	DCDC_CapNeg_Thermistor
SC2_A21	Input - Analog - 10 bit	0-5V	Intended for variable resistance sensors (eg. Themistors), Tau=1ms, 1K pull up.	AN21M	C2	58	Brown/White	DCDC_CapPos_Thermistor
SC2_A22	Input - Analog - 10 bit	0-5V	Intended for variable resistance sensors (eg. Themistors), Tau=1ms, 1K pull up.	AN22M	C4	60	Brown/Yellow	DCDC_IGBTPos_Thermistor

SC2_SW1	Input - Digital - Switch	Not specified	Discrete switch, Frequency, IRQ, V_{IL} = 2.0V max, V_{IH}=2.5Vmin, Tau=5.1µs, 1K pull up. May be used for high speed MAF sensors.	DG1	B7	39	Light Blue/Black	DCDC_IGBT Okay
SC2_SW2	Input - Digital - Switch	Not specified	Discrete switch, Frequency, IRQ, VIL = 2.0V max, VIH=2.5Vmin, Tau=1ms, 1K pull up.	DG2	C16	72	Black	SAFE_EstopMonitor
Power								
SC2_ECU_KEY_SW	Input - Key Switch	Not specified	ECU WAKE - Wake up module	KEY_SW	B2	34	Green/Black	Connected
SC2_DVRP_1	Input - Main power	Not specified	Main power input from battery through the main power relay, power to module (H-Bridges) and loads	DRVP	A18	98	Pink/Brown	Connected
SC2_DVRP_2	Input - Main power	Not specified	Main power input from battery through the main power relay, power to module (H-Bridges) and loads	DRVP	A19	99	Orange	Connected
SC2_MPRD	Output - Main power relay driver		Main Power Relay Driver - holds the controller ON until released by application after ECUP is removed	MPRD	B18	50	Red/Blue	Connected
SC2_BATT	Output - Battery	Not specified	Battery Connection	BATT	B8	40	Yellow/Black	Connected
SC2_XDRG	Input - Transducer Ground	0V	Transducer Ground - Return for Transducers	XDRG	A24	24	Red/Purple	Connected
SC2_XDRG	Input - Transducer Ground	0V	Transducer Ground - Return for Transducers	XDRG	B24	56	Black/Yellow	Connected
SC2_DRVG_1	Input - System (battery) grounds	0V	System (battery) ground connections	DRVG	A15	95	Black/Yellow	Connected
SC2_DRVG_2	Input - System (battery) grounds	0V	System (battery) ground connections	DRVG	A16	96	Black/White	Connected
SC2_DRVG_3	Input - System (battery) grounds	0V	System (battery) ground connections	DRVG	B9	113	Gray/Red	Connected
SC2_DRVG_4	Input - System (battery) grounds	0V	System (battery) ground connections	DRVG	A24	104	Black/White	Connected
Output								
SC2_XDRP_1	Output - Powering sensor transducers	5V	Intended for powering sensor transducers, 300mA max	XDRP_A	B11	43	Orange	5V TPS Reference
SC2_XDRP_2	Output - Powering sensor transducers	5V	Intended for powering sensor transducers, 300mA max	XDRP_B	A11	11	White	DCDC_PowerforFaultDetection
SC2_LSUH1	Output - PWM/ LSU Heater	Not specified	Intended to drive heaters for the Lambda Sensing Units, 2.OA low side drivers, high current - 10A	LSO1	B20	52	Pink/Light Blue	MCU2_FuseBox_Power
SC2_LSUH2	Output - PWM/ LSU Heater	Not specified	Intended to drive heaters for the Lambda Sensing Units, 2.OA low side drivers, high current - 10A	LSO2	B19	51	Yellow/White	BCM_FuseBox_MicroPower
SC2_LSO3	Output - PWM with current feedback	Not specified	These are 2.0A low side drivers with current feedback, 10A max	LSO3	A23	23	Purple/Yellow	FCPM_EnableTrigger (KeyIn)
SC2_LSO4	Output - PWM with current feedback	Not specified	These are 2.0A low side drivers with current feedback, 10A max	LSO4	B21	125	Purple/Yellow	FCPM_PosContactor_Enable
SC2_LSO5	Output - PWM	Not specified	These are 2.0A low side drivers intended to drive resistive loads, 10A max	LSO5	B12	116	White/Orange	FCPM_Precharge_Enable
SC2_LSO6	Output - PWM	Not specified	These are 2.0A low side drivers intended to drive resistive loads, 10A max	LSO6	B15	119	Green/Yellow	DCDC_IGBTPWM
SC2_LSO7	Output - PWM	Not specified	These are 2.0A low side drivers intended to drive resistive loads, 10A max	LSO7	B17	121	Black/Green	AC comp
SC2_LSO8	Output - PWM	Not specified	These are 2.0A low side drivers intended to drive resistive loads, 10A max	LSO8	B19	123	Tan/Purple	BCM Coolant Pump
SC2_LSO9	Output - PWM	Not specified	These are 2.0A low side drivers intended to drive resistive loads, 10A max	LSO9	B18	122	Purple	BCM Contactor
SC2_LSO10	Output - PWM	Not specified	These are 2.0A low side drivers intended to drive resistive loads, 10A max	LSO10	B20	124	Light Blue/White	MCU1_FuseBox_Power
SC2_H1+	Output - H-Bridge	Not specified	These outputs are high current drivers intended for loads that may be operated in either polaroty such as DC motors, 5A max	H1+	A9	89	Tan/Light Blue	BCM_KeyIn
SC2_H2+	Output - H-Bridge	Not specified	These outputs are high current drivers intended for loads that may be operated in either polaroty such as DC motors, 10A max	H2+	B22	126	Tan/White	MCU1_KeyIn
SC2_H3+	Output - H-Bridge	Not specified	These outputs are high current drivers intended for loads that may be operated in either polaroty such as DC motors, 10A max	H3+	B16	120	Green/Red	MCU2_KeyIn
Communications								
SC2_CAN1+	Communications - CAN High	2.5-3.5V	CAN 2.0B, Standard or Extended ID, set to 250kbaud, can run at 500kbaud	CAN1+	B9	41	Green/Purple	Battery CANbus
SC2_CAN1-	Communications - CAN Low	1.5-2.5V	CAN 2.0B, Standard or Extended ID, set to 250kbaud, can run at 500kbaud	CAN1-	B10	42	Green/Brown	Battery CANbus
SC1_CAN2+	Communications - CAN High	2.5-3.5V	CAN 2.0B, Standard or Extended ID, set to 250kbaud, can run at 500kbaud	CAN2+	C17	73	Gray/White	Main CANbus
SC2_CAN2-	Communications - CAN Low	1.5-2.5V	CAN 2.0B, Standard or Extended ID, set to 250kbaud, can run at 500kbaud	CAN2-	C18	74	Gray/Red	Main CANbus

Controller:	Mototron ECU555-80
Processor:	Motorola MPC555
Clock Frequency:	40 MHz
Internal Flash:	448K
External Flash:	2M (optional)
EEPROM	8K serial/optional 128k (parallel)
Internal SRAM:	32K
Supply Voltage:	8-16V
Document Revision #	0

UWAFT Signal Name	Type	Range	Description	Mototron Name	Mototron Pin	Wire Number	Wire Colour	Connected To	Application
Inputs - Analog									
SC1_A1	Input - Analog - 10 bit	0-5V	Intended for pressure sensors. Tau=1ms. 51K pull down.	AN1	A3	3	Yellow	12V Current Sense	12V Bus Current Monitoring
SC1_A2	Input - Analog - 10 bit	0-5V	Intended for pressure sensors. Tau=1ms. 51K pull down.	AN2	A4	4	Blue/Black	24V Current Sense	24V Bus Current Monitoring
SC1_A4	Input - Analog - 10 bit	0-5V	Intended for potentiometers. Tau=1ms. 220K pull down.	AN4	A6	6	Light Blue/White	DC/DC fuel cell current sensor	Used for dc/dc control
SC1_A5	Input - Analog - 10 bit	0-5V	Intended for potentiometers. Tau=1ms. 220K pull down.	AN5	A7	7	White/Yellow	DC/DC main inductor thermistor	Used for dc/dc control
SC1_A6	Input - Analog - 10 bit	0-5V	Intended for potentiometers. Tau=1ms. 220K pull down.	AN6	A8	8	Brown/White	DC/DC IGBT thermistor	Used for dc/dc control
SC1_A7	Input - Analog - 10 bit	0-5V	Intended for potentiometers. Tau=1ms. 220K pull down.	AN7	A9	9	Yellow/Pink	DC/DC capacitor thermistor	Used for dc/dc control
SC1_A8	Input - Analog - 10 bit	0-5V	Intended for potentiometers. Tau=1ms. 220K pull down.	AN8	A10	10	Red/Pink	DC/DC cold plate thermistor	Used for dc/dc control
SC1_A9	Input - Analog - 10 bit	0-5V	Intended for variable resistance sensors (eg. Thermistors), Tau=1ms, 1K pull up.	AN9	A14	14	Tan	12V Voltage Monitor	12V Bus Voltage Monitoring
SC1_A10	Input - Analog - 10 bit	0-5V	Intended for variable resistance sensors (eg. Thermistors), Tau=1ms, 1K pull up.	AN10	A15	15	Tan/Green	24V Voltage Monitor	24V Bus Voltage Monitoring
Inputs - Digital									
SC1_SW1	Input - Digital - Switch	Not specified	Discrete switch, Frequency, IRQ, V_{IL} = 2.0V max, V_{IH}=2.5Vmin, Tau=1ms, 1K pull up.	DG1	B15	47	Black/Blue	IGBT okay signal	Used for status update for the dc/dc converter
Power									
SC1_ECUP	Input - ECUP Signal	9-16V	Power signal for starting controller and for initiating shutdown process	ECUP	A1	1	Purple/White	To fuse box	Provide power signal when key is in ON, ACCESS, & START positions
SC1_DVRP_1	Input - Main power	9-16V	Main power input from battery through the main power relay, power to module and loads	DRVP	B17	49	Red/Blue	From main power relay	
SC1_DVRP_2	Input - Main power	9-16V	Main power input from battery through the main power relay, power to module and loads	DRVP	B18	50	Red/Blue	From main power relay	
SC1_MPRD	Output - Main power relay driver		Main Power Relay Driver - holds the controller ON until released by application after ECUP is removed	MPRD	B4	36	Yellow/Purple	To main power relay coil	
SC1_DRVG_1	Input - System (battery) grounds	0V	System (battery) ground connections	DRVG	C15	71	Black	From battery	
SC1_DRVG_2	Input - System (battery) grounds	0V	System (battery) ground connections	DRVG	C16	72	Black	From battery	
SC1_DRVG_3	Input - System (battery) grounds	0V	System (battery) ground connections	DRVG	C24	80	Black	From battery	
Output									
Communications									
SC1_CAN1+	Communications - CAN High	2.5-3.5V	CAN 2.0B, Standard or Extended ID, set to 250kbaud, can run at 500kbaud	CAN1+	A11	11	White	To UWAFT CAN Network	
SC1_CAN1-	Communications - CAN Low	1.5-2.5V	CAN 2.0B, Standard or Extended ID, set to 250kbaud, can run at 500kbaud	CAN1-	A21	21	Dark Blue	To UWAFT CAN Network	
SC1_CAN2+	Communications - CAN High	2.5-3.5V	CAN 2.0B, Standard or Extended ID, set to 250kbaud, can run at 500kbaud	CAN2+	A31	31	Yellow	To GM CAN Network	
SC1_CAN2-	Communications - CAN Low	1.5-2.5V	CAN 2.0B, Standard or Extended ID, set to 250kbaud, can run at 500kbaud	CAN2-	A32	32	Brown	To GM CAN Network	

Appendix B

Hybrid Test Stand Labview Screenshots

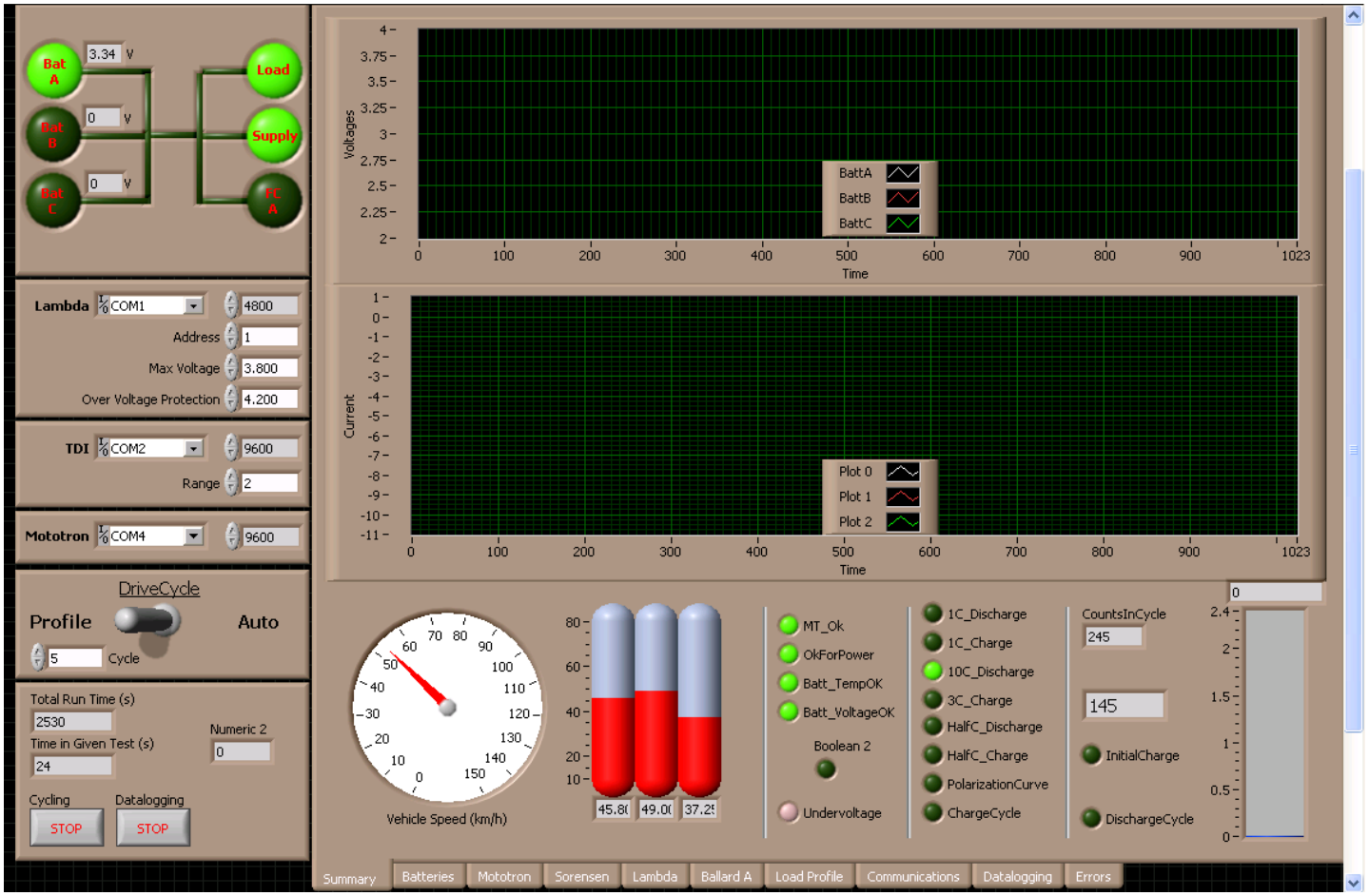

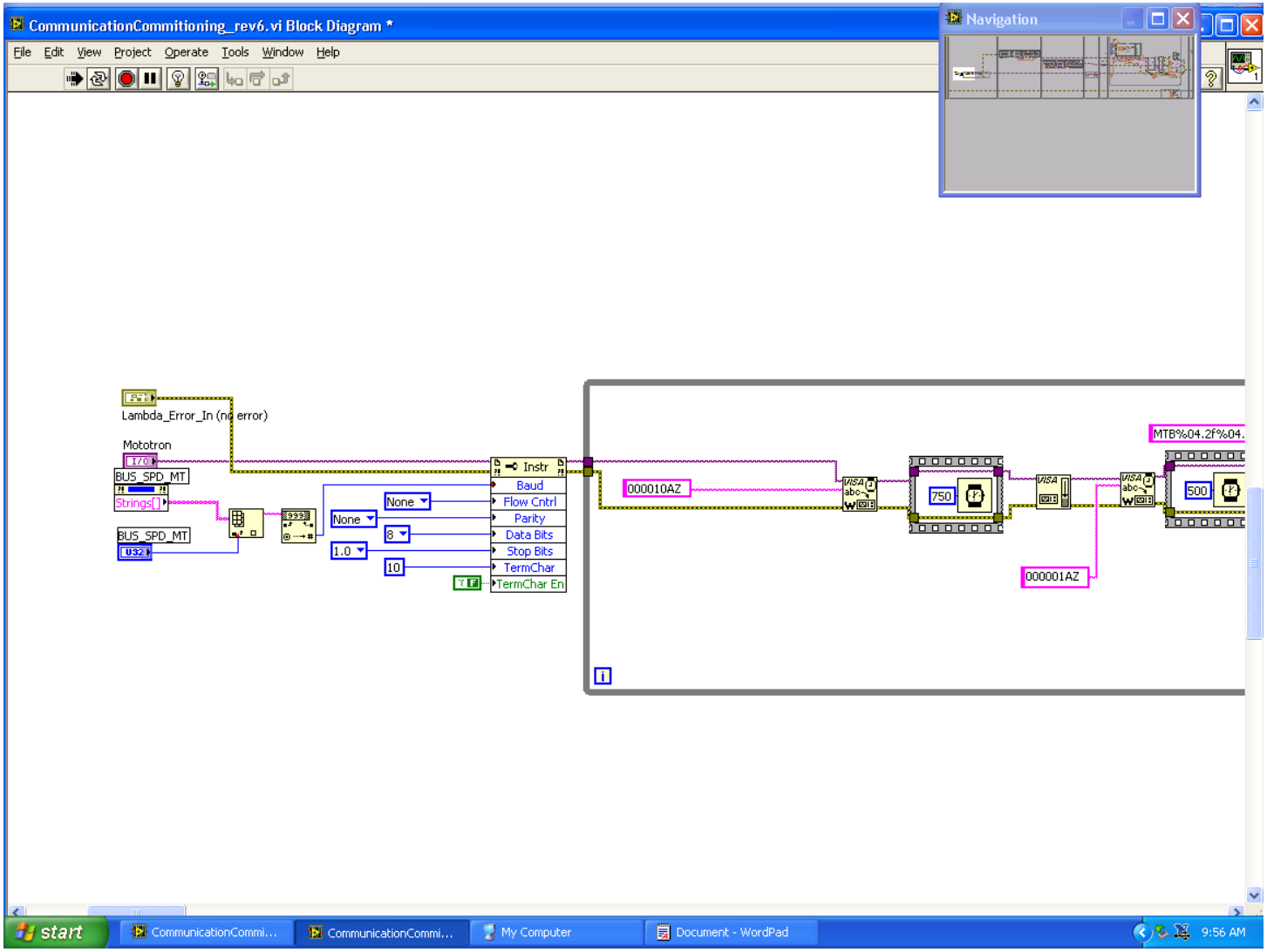
CommunicationCommitioning_rev6.vi Block Diagram *
File Edit View Project Operate Tools Window Help
Navigation
Lambda_Error_In (no error)
Mototron
I/O
BUS_SPD_MT
Strings[]
BUS_SPD_MT
U32
None
None
8
1.0
10
Instr
Baud
Flow Cntrl
Parity
Data Bits
Stop Bits
TermChar
TermChar En
000010AZ
750
000001AZ
500
MTB%04.2f%04.
start
CommunicationCommi...
CommunicationCommi...
My Computer
Document - WordPad
9:56 AM

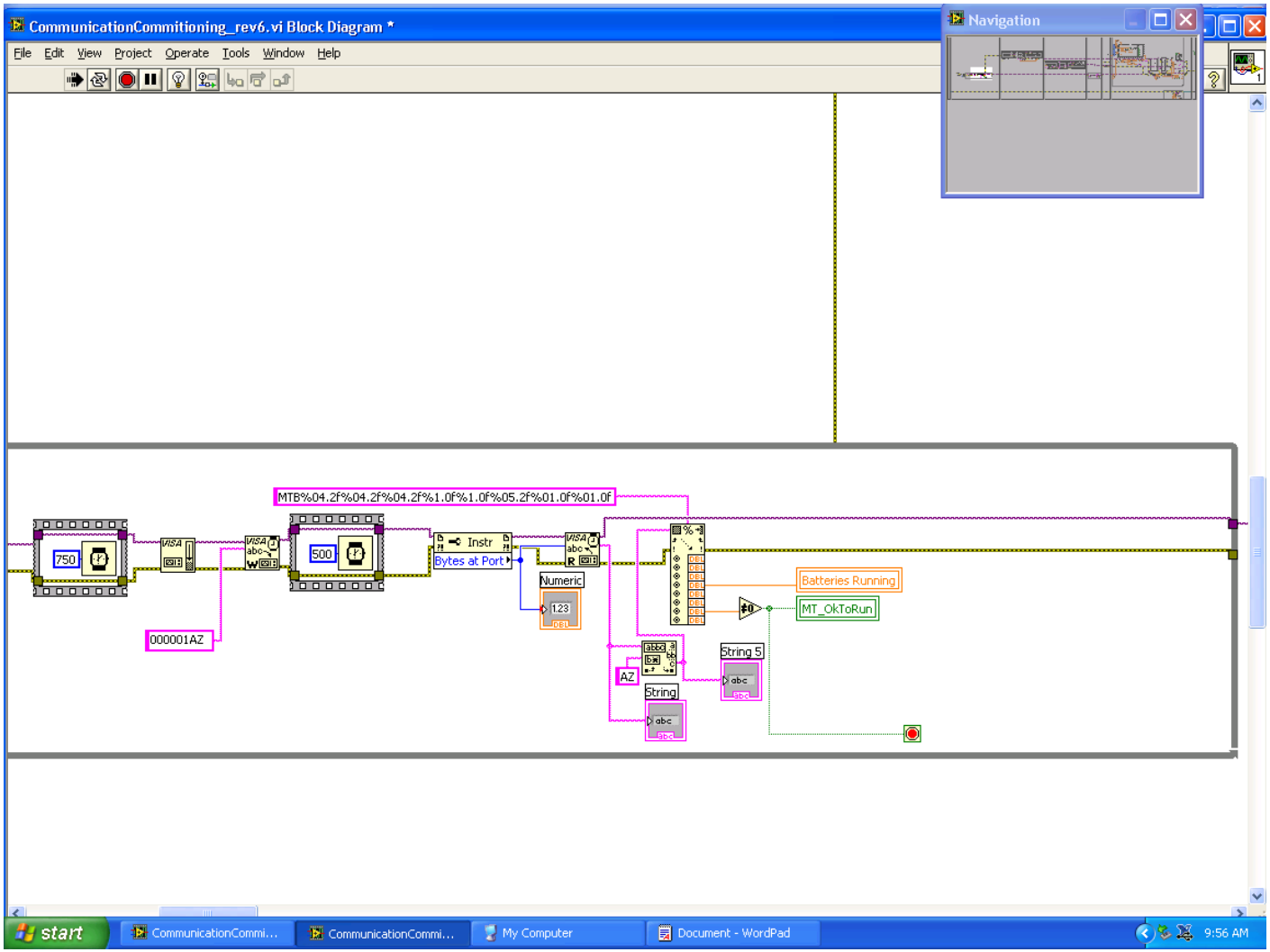
CommunicationCommitioning_rev6.vi Block Diagram *
File Edit View Project Operate Tools Window Help
Navigation
MTB%04,2f%04,2f%04,2f%1,0f%1,0f%05,2f%01,0f%01,0f
750
VISA
500
Instr
Bytes at Port
Numeric
000001AZ
Batteries Running
MT_OkToRun
String 5
AZ
String
start
CommunicationCommi...
CommunicationCommi...
My Computer
Document - WordPad
9:56 AM

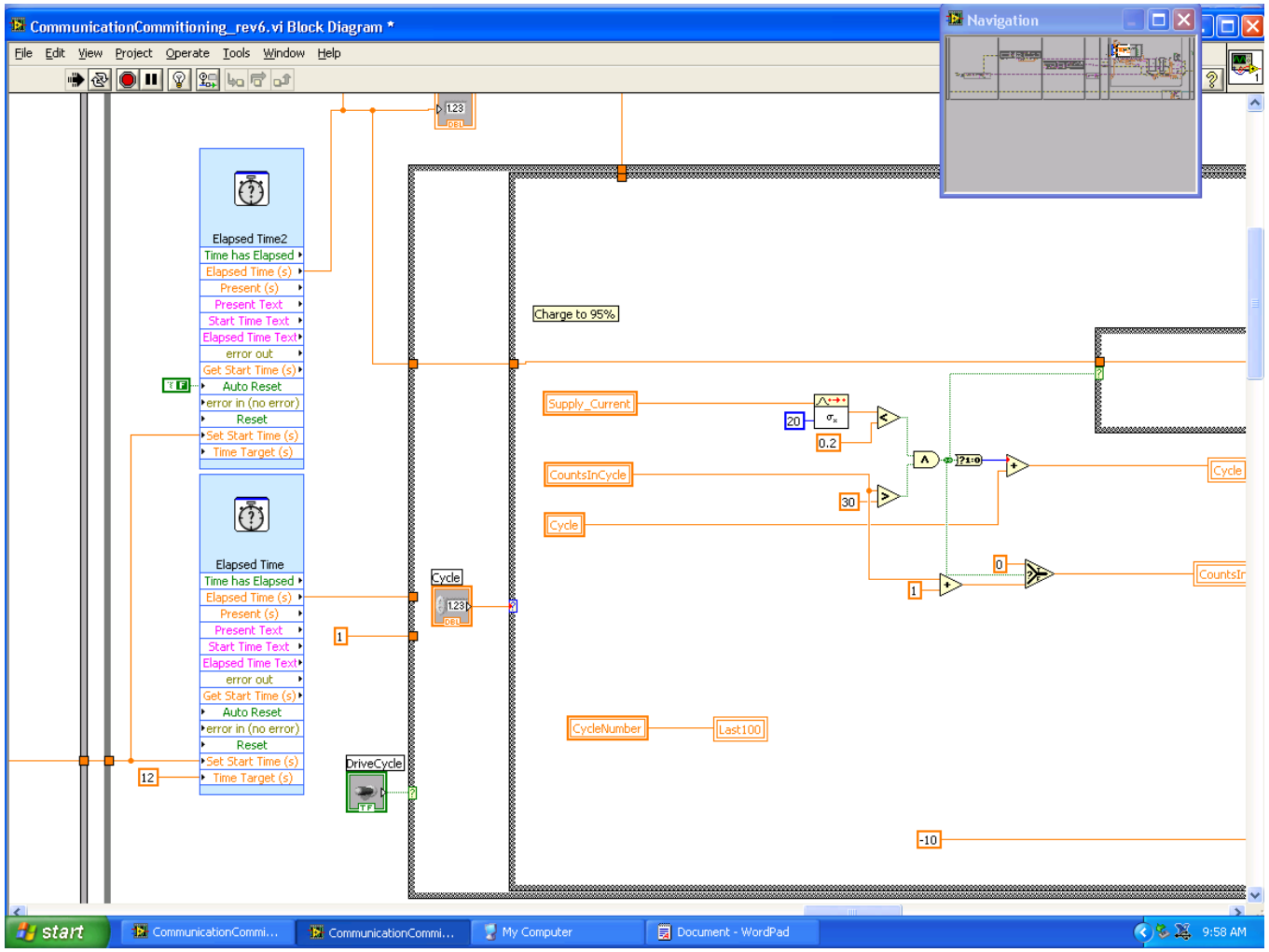

Please note, the code is truncated due to size. The full code is available upon request.

Appendix C

AC Impedance Data

A123_4wire_Galv700mA_30s_FreshBatteryB_02387

Freq	Z' (a)	Z'' (b)	Mag	Phase	Ampl (A)	Time (s)
10000	0.0064073	0.0023919	0.0068392	20.471	0.7	32.67
7196.857	0.0062021	0.0016358	0.0064142	14.775	0.7	63.45
5179.475	0.0061616	0.001054	0.0062511	9.707	0.7	94.2
3727.594	0.0061161	0.00065017	0.0061506	6.068	0.7	124.89
2682.696	0.0061405	0.00031091	0.0061484	2.8986	0.7	155.64
1930.698	0.0061918	6.00E-05	0.0061921	0.55519	0.7	186.39
1389.495	0.0062749	-0.0001448	0.0062766	-1.3221	0.7	217.14
1000	0.006384	-0.0003046	0.0063913	-2.7317	0.7	247.89
719.6857	0.0065071	-0.0004338	0.0065215	-3.8138	0.7	278.64
517.9474	0.0066305	-0.0005823	0.006656	-5.0189	0.7	309.39
372.7594	0.0067808	-0.0006708	0.0068139	-5.65	0.7	340.14
268.2696	0.0069368	-0.0007994	0.0069827	-6.574	0.7	372.64
193.0698	0.0070991	-0.0009179	0.0071582	-7.3675	0.7	403.39
138.9496	0.0072808	-0.0010266	0.0073528	-8.0259	0.7	434.14
100	0.0074864	-0.0011617	0.007576	-8.8205	0.7	464.89
71.96857	0.0077246	-0.0013102	0.0078349	-9.6265	0.7	495.64
51.79475	0.0079932	-0.0014401	0.0081219	-10.213	0.7	526.39
37.27594	0.0083301	-0.0015835	0.0084793	-10.763	0.7	557.14
26.82696	0.0087085	-0.0017063	0.0088741	-11.086	0.7	587.89
19.30698	0.0091173	-0.0017847	0.0092903	-11.076	0.7	618.64
13.89496	0.0095329	-0.0018207	0.0097052	-10.813	0.7	649.39
10	0.0099327	-0.0018146	0.010097	-10.353	0.7	680.14
7.19686	0.0103	-0.0017879	0.010454	-9.8474	0.7	711.01
5.17947	0.010624	-0.0017622	0.010769	-9.4179	0.7	741.89
3.72759	0.01091	-0.0017638	0.011052	-9.1834	0.7	772.74
2.6827	0.01117	-0.0018143	0.011316	-9.2258	0.7	803.99
1.9307	0.011399	-0.0019219	0.01156	-9.5702	0.7	834.74
1.3895	0.011649	-0.0021168	0.01184	-10.299	0.7	865.62
1	0.011879	-0.0023866	0.012116	-11.36	0.7	896.37
0.71969	0.012124	-0.0028041	0.012444	-13.023	0.7	927.62
0.51795	0.012525	-0.0033328	0.012961	-14.901	0.7	959.62
0.37276	0.012738	-0.0040334	0.013361	-17.57	0.7	992.49
0.26827	0.013096	-0.0048483	0.013965	-20.315	0.7	1026.87
0.19307	0.013599	-0.0059935	0.014861	-23.785	0.7	1058.62
0.13895	0.01421	-0.0075989	0.016114	-28.136	0.7	1095.37
0.1	0.014852	-0.0099583	0.017882	-33.842	0.7	1127.12

A123_4wire_Galv700mA_30s_FreshBatteryB_02317

Freq	Z' (a)	Z'' (b)	Mag	Phase	Ampl	Time
10000	0.0063632	0.002393	0.0067983	20.61	0.7	32.7
7196.857	0.0061589	0.0016208	0.0063686	14.744	0.7	63.45
5179.475	0.0060523	0.0010757	0.0061472	10.078	0.7	94.2
3727.594	0.0060476	0.00064766	0.0060822	6.1127	0.7	124.95
2682.696	0.0060785	0.00032216	0.006087	3.0338	0.7	155.7
1930.698	0.0061328	6.95E-05	0.0061332	0.64945	0.7	186.45
1389.495	0.0062275	-0.00013233	0.0062289	-1.2173	0.7	217.2
1000	0.0063359	-0.00029094	0.0063426	-2.6291	0.7	247.95
719.6857	0.0064617	-0.00040751	0.0064745	-3.6086	0.7	278.7
517.9474	0.006596	-0.00053486	0.0066176	-4.6359	0.7	309.45
372.7594	0.0067498	-0.00060543	0.0067769	-5.1255	0.7	340.2
268.2696	0.006909	-0.00071416	0.0069458	-5.9015	0.7	372.7
193.0698	0.0070812	-0.00076431	0.0071223	-6.1604	0.7	403.45
138.9496	0.00726	-0.00081949	0.0073061	-6.4401	0.7	434.2
100	0.007454	-0.00084193	0.0075014	-6.4443	0.7	464.95
71.96857	0.007657	-0.00083966	0.0077029	-6.258	0.7	495.7
51.79475	0.0078389	-0.00080533	0.0078802	-5.8657	0.7	526.45
37.27594	0.0080309	-0.00077274	0.008068	-5.4961	0.7	557.2
26.82696	0.0082015	-0.00072632	0.0082336	-5.0609	0.7	587.95
19.30698	0.0083524	-0.00068303	0.0083803	-4.675	0.7	618.7
13.89496	0.0084833	-0.00063902	0.0085073	-4.3078	0.7	649.45
10	0.0085995	-0.00060861	0.008621	-4.0482	0.7	680.2
7.19686	0.0087077	-0.00059422	0.008728	-3.9039	0.7	710.95
5.17947	0.0088122	-0.00059385	0.0088322	-3.8553	0.7	741.82
3.72759	0.008919	-0.0006142	0.0089401	-3.9394	0.7	772.57
2.6827	0.0090295	-0.00065169	0.009053	-4.1281	0.7	803.7
1.9307	0.0091467	-0.00071562	0.0091747	-4.4736	0.7	834.45
1.3895	0.0092562	-0.00080799	0.0092914	-4.9888	0.7	865.32
1	0.009392	-0.00092237	0.0094372	-5.6089	0.7	896.07
0.71969	0.0095254	-0.0010653	0.0095848	-6.3813	0.7	927.32
0.51795	0.0097194	-0.0012874	0.0098043	-7.5453	0.7	959.45
0.37276	0.0098479	-0.0015155	0.0099638	-8.7487	0.7	992.32
0.26827	0.010072	-0.001872	0.010244	-10.529	0.7	1026.82
0.19307	0.010323	-0.0023433	0.010586	-12.789	0.7	1058.57
0.13895	0.010601	-0.0029144	0.010994	-15.372	0.7	1095.32
0.1	0.010943	-0.0036692	0.011542	-18.536	0.7	1127.2

A123_4wire_Galv700mA_30s_FreshBatteryB_2100

Freq	Z' (a)	Z'' (b)	Mag	Phase	Ampl	Time
10000	0.0063205	0.0024096	0.0067642	20.869	0.7	32.6
7196.857	0.006119	0.0016242	0.0063309	14.866	0.7	63.36
5179.475	0.0060173	0.001075	0.0061126	10.129	0.7	94.1
3727.594	0.0060239	0.00063364	0.0060571	6.0047	0.7	124.85
2682.696	0.006046	0.00032547	0.0060548	3.0814	0.7	155.61
1930.698	0.0061085	5.72E-05	0.0061088	0.53668	0.7	186.35
1389.495	0.0062031	-0.00014798	0.0062049	-1.3666	0.7	217.1
1000	0.0063232	-0.00030176	0.0063304	-2.7322	0.7	247.86
719.6857	0.0064572	-0.00041733	0.0064707	-3.6979	0.7	278.6
517.9474	0.0065945	-0.00054251	0.0066168	-4.703	0.7	309.35
372.7594	0.0067561	-0.00060183	0.0067829	-5.0904	0.7	340.11
268.2696	0.0069257	-0.00066953	0.006958	-5.5218	0.7	372.48
193.0698	0.0070928	-0.00072166	0.0071294	-5.8096	0.7	403.23
138.9496	0.007268	-0.00073628	0.0073052	-5.7846	0.7	433.98
100	0.0074428	-0.00073687	0.0074792	-5.6541	0.7	464.73
71.96857	0.0076161	-0.00071926	0.00765	-5.395	0.7	495.48
51.79475	0.00776	-0.00065933	0.007788	-4.8565	0.7	526.23
37.27594	0.0079107	-0.00062302	0.0079352	-4.5031	0.7	556.98
26.82696	0.0080396	-0.00056961	0.0080598	-4.0527	0.7	587.73
19.30698	0.0081491	-0.00052374	0.0081659	-3.6773	0.7	618.48
13.89496	0.0082463	-0.0004874	0.0082607	-3.3825	0.7	649.23
10	0.0083327	-0.00046027	0.0083454	-3.1616	0.7	679.98
7.19686	0.0084172	-0.00044993	0.0084292	-3.0598	0.7	710.73
5.17947	0.0085009	-0.00044744	0.0085127	-3.013	0.7	741.73
3.72759	0.008587	-0.00045917	0.0085993	-3.0608	0.7	772.6
2.6827	0.0086781	-0.0004805	0.0086914	-3.1692	0.7	803.85
1.9307	0.0087781	-0.0005256	0.0087938	-3.4266	0.7	834.6
1.3895	0.0088629	-0.00056792	0.0088811	-3.6664	0.7	865.48
1	0.008974	-0.0006363	0.0089965	-4.0558	0.7	896.23
0.71969	0.0090885	-0.00069261	0.0091149	-4.3579	0.7	927.48
0.51795	0.0092163	-0.00083832	0.0092543	-5.1974	0.7	959.48
0.37276	0.0093287	-0.00092292	0.0093742	-5.6501	0.7	992.35
0.26827	0.0095131	-0.0011525	0.0095827	-6.9076	0.7	1026.73
0.19307	0.009644	-0.0014505	0.0097525	-8.5534	0.7	1058.48
0.13895	0.0098177	-0.0017472	0.009972	-10.091	0.7	1095.23
0.1	0.010021	-0.0021067	0.01024	-11.872	0.7	1126.98

A123_4wire_Galv700mA_30s_FreshBatteryB_1883

Freq	Z' (a)	Z'' (b)	Mag	Phase	Ampl	Time
10000	0.0063156	0.0023654	0.006744	20.533	0.7	32.62
7196.857	0.0061161	0.0015877	0.0063188	14.552	0.7	63.37
5179.475	0.0060302	0.0010406	0.0061193	9.7908	0.7	94.12
3727.594	0.0060287	0.00060458	0.0060589	5.7267	0.7	124.87
2682.696	0.0060585	0.0002934	0.0060656	2.7725	0.7	155.62
1930.698	0.0061229	2.57E-05	0.006123	0.24067	0.7	186.37
1389.495	0.0062207	-0.00017478	0.0062232	-1.6094	0.7	217.12
1000	0.0063447	-0.00033125	0.0063533	-2.9886	0.7	247.87
719.6857	0.0064831	-0.00044725	0.0064985	-3.9464	0.7	278.62
517.9474	0.0066295	-0.00057217	0.0066541	-4.9328	0.7	309.37
372.7594	0.0067977	-0.00063051	0.0068269	-5.2992	0.7	340.12
268.2696	0.0069726	-0.0006953	0.0070072	-5.6946	0.7	372.5
193.0698	0.0071477	-0.00073458	0.0071853	-5.8678	0.7	403.24
138.9496	0.0073267	-0.0007544	0.0073654	-5.8788	0.7	434
100	0.0075072	-0.00075269	0.0075448	-5.7255	0.7	464.75
71.96857	0.0076811	-0.00073439	0.0077161	-5.4614	0.7	495.49
51.79475	0.0078291	-0.00067401	0.0078581	-4.9205	0.7	526.24
37.27594	0.0079816	-0.00062656	0.0080062	-4.4885	0.7	557
26.82696	0.0081115	-0.00057419	0.0081318	-4.0491	0.7	587.74
19.30698	0.0082223	-0.000523	0.0082389	-3.6395	0.7	618.49
13.89496	0.0083185	-0.00048084	0.0083324	-3.3082	0.7	649.25
10	0.0084034	-0.0004512	0.0084155	-3.0734	0.7	679.99
7.19686	0.0084833	-0.00043279	0.0084943	-2.9205	0.7	710.74
5.17947	0.0085604	-0.00042569	0.008571	-2.8468	0.7	741.62
3.72759	0.0086446	-0.00043135	0.0086554	-2.8566	0.7	772.62
2.6827	0.0087287	-0.00044697	0.0087401	-2.9314	0.7	803.75
1.9307	0.0088225	-0.00048695	0.0088359	-3.1592	0.7	834.49
1.3895	0.0088974	-0.00052116	0.0089127	-3.3522	0.7	865.37
1	0.0090079	-0.00058542	0.0090269	-3.7184	0.7	896.12
0.71969	0.009115	-0.00061937	0.009136	-3.8873	0.7	927.37
0.51795	0.0092315	-0.00074234	0.0092613	-4.5975	0.7	959.24
0.37276	0.0093138	-0.00081084	0.009349	-4.9755	0.7	992.12
0.26827	0.009491	-0.0010143	0.009545	-6.1	0.7	1026.62
0.19307	0.0096265	-0.0012687	0.0097097	-7.5079	0.7	1058.37
0.13895	0.0097536	-0.0015278	0.0098725	-8.9024	0.7	1095.12
0.1	0.0099435	-0.0018109	0.010107	-10.322	0.7	1127.12

A123_4wire_Galv700mA_30s_FreshBatteryB_1717

Freq	Z' (a)	Z'' (b)	Mag	Phase	Ampl	Time
10000	0.006319	0.0023662	0.0067475	20.529	0.7	32.71
7196.857	0.0061183	0.0015867	0.0063207	14.539	0.7	63.46
5179.475	0.0060354	0.00103	0.0061227	9.6848	0.7	94.21
3727.594	0.0060383	0.0005998	0.006068	5.6727	0.7	124.96
2682.696	0.0060636	0.00027992	0.0060701	2.6431	0.7	155.71
1930.698	0.0061338	1.48E-05	0.0061338	0.13782	0.7	186.46
1389.495	0.0062313	-0.0001888	0.0062342	-1.735	0.7	217.21
1000	0.0063605	-0.0003459	0.0063699	-3.1126	0.7	247.96
719.6857	0.0065025	-0.0004632	0.006519	-4.0748	0.7	278.71
517.9474	0.0066518	-0.0005898	0.0066779	-5.0668	0.7	309.46
372.7594	0.0068242	-0.0006486	0.0068549	-5.4289	0.7	340.21
268.2696	0.0070002	-0.0007155	0.0070367	-5.8362	0.7	372.59
193.0698	0.0071822	-0.0007514	0.0072214	-5.9726	0.7	403.34
138.9496	0.0073647	-0.0007721	0.0074051	-5.9851	0.7	434.09
100	0.0075453	-0.0007705	0.0075845	-5.8305	0.7	464.84
71.96857	0.0077261	-0.0007548	0.0077629	-5.5799	0.7	495.59
51.79475	0.007878	-0.0006878	0.007908	-4.9899	0.7	526.34
37.27594	0.0080325	-0.0006364	0.0080577	-4.53	0.7	557.09
26.82696	0.0081655	-0.0005808	0.0081861	-4.0684	0.7	587.84
19.30698	0.0082781	-0.000528	0.0082949	-3.6495	0.7	618.59
13.89496	0.0083745	-0.0004837	0.0083885	-3.3057	0.7	649.34
10	0.0084604	-0.0004511	0.0084724	-3.0519	0.7	680.09
7.19686	0.0085393	-0.0004277	0.00855	-2.8671	0.7	710.84
5.17947	0.0086144	-0.0004179	0.0086245	-2.7775	0.7	741.84
3.72759	0.0086931	-0.0004181	0.0087032	-2.7538	0.7	772.71
2.6827	0.0087746	-0.0004336	0.0087853	-2.8287	0.7	803.96
1.9307	0.0088602	-0.0004646	0.0088724	-3.0013	0.7	834.71
1.3895	0.0089339	-0.0004933	0.0089475	-3.1606	0.7	865.59
1	0.0090301	-0.0005558	0.0090472	-3.5221	0.7	896.34
0.71969	0.0091586	-0.0005954	0.0091779	-3.7193	0.7	927.59
0.51795	0.0092565	-0.0007014	0.009283	-4.3332	0.7	959.34
0.37276	0.0093434	-0.0007602	0.0093743	-4.6512	0.7	992.21
0.26827	0.0094993	-0.0009511	0.0095468	-5.7177	0.7	1026.71
0.19307	0.0096182	-0.0011831	0.0096907	-7.0125	0.7	1058.59
0.13895	0.0097302	-0.0014089	0.0098317	-8.239	0.7	1095.34
0.1	0.0099097	-0.0016782	0.010051	-9.6118	0.7	1126.96

A123_4wire_Galv700mA_30s_FreshBatteryB_1550

Freq	Z' (a)	Z'' (b)	Mag	Phase	Ampl	Time
10000	0.0063415	0.0023632	0.0067675	20.438	0.7	32.6
7196.857	0.0061418	0.0015775	0.0063412	14.405	0.7	63.35
5179.475	0.0060737	0.0010106	0.0061572	9.4469	0.7	94.1
3727.594	0.0060693	0.000584	0.0060973	5.4959	0.7	124.85
2682.696	0.0060966	0.000263	0.0061023	2.4702	0.7	155.62
1930.698	0.0061686	-5.45E-06	0.0061686	-0.050641	0.7	186.35
1389.495	0.0062647	-0.000212	0.0062683	-1.9422	0.7	217.1
1000	0.0063985	-0.000371	0.0064092	-3.3164	0.7	247.85
719.6857	0.0065461	-0.000491	0.0065645	-4.2867	0.7	278.6
517.9474	0.0066998	-0.000618	0.0067283	-5.2738	0.7	309.35
372.7594	0.0068781	-0.000679	0.0069115	-5.6377	0.7	340.1
268.2696	0.0070622	-0.000744	0.0071013	-6.0167	0.7	372.48
193.0698	0.0072444	-0.000787	0.007287	-6.1983	0.7	403.23
138.9496	0.0074319	-0.000807	0.0074755	-6.1941	0.7	433.98
100	0.007621	-0.000796	0.0076625	-5.9656	0.7	464.73
71.96857	0.0078034	-0.000776	0.0078419	-5.6815	0.7	495.48
51.79475	0.0079586	-0.000709	0.0079901	-5.0918	0.7	526.23
37.27594	0.0081152	-0.000665	0.0081424	-4.6822	0.7	556.98
26.82696	0.0082497	-0.000601	0.0082716	-4.1663	0.7	587.73
19.30698	0.0083631	-0.000544	0.0083808	-3.7246	0.7	618.48
13.89496	0.00846	-0.000495	0.0084745	-3.3498	0.7	649.23
10	0.0085442	-0.000459	0.0085565	-3.0733	0.7	679.98
7.19686	0.0086198	-0.000433	0.0086307	-2.878	0.7	710.85
5.17947	0.0086922	-0.000421	0.0087024	-2.7709	0.7	741.73
3.72759	0.0087693	-0.000418	0.0087792	-2.726	0.7	772.73
2.6827	0.0088467	-0.000431	0.0088572	-2.7875	0.7	803.85
1.9307	0.0089307	-0.000464	0.0089427	-2.9721	0.7	834.6
1.3895	0.0089998	-0.000491	0.0090132	-3.122	0.7	865.48
1	0.0091007	-0.000552	0.0091174	-3.4685	0.7	896.23
0.71969	0.0092078	-0.000579	0.009226	-3.596	0.7	927.5
0.51795	0.0093039	-0.000692	0.0093296	-4.2543	0.7	959.35
0.37276	0.0093857	-0.000752	0.0094158	-4.5806	0.7	992.23
0.26827	0.0095322	-0.000929	0.0095774	-5.567	0.7	1026.73
0.19307	0.0096359	-0.001194	0.0097096	-7.0624	0.7	1058.48
0.13895	0.0097456	-0.001394	0.0098448	-8.1415	0.7	1095.23
0.1	0.00994	-0.001644	0.010075	-9.3918	0.7	1126.85

A123_4wire_Galv700mA_30s_FreshBatteryB_1333

Freq	Z' (a)	Z'' (b)	Mag	Phase	Ampl	Time
10000	0.006322	0.0023703	0.0067517	20.552	0.7	32.67
7196.857	0.0061204	0.0015884	0.0063232	14.549	0.7	63.42
5179.475	0.0060497	0.0010276	0.0061364	9.6402	0.7	94.17
3727.594	0.0060428	0.00060496	0.006073	5.717	0.7	124.92
2682.696	0.0060637	0.00028384	0.0060703	2.68	0.7	155.67
1930.698	0.0061341	2.03E-05	0.0061341	0.18948	0.7	186.42
1389.495	0.0062243	-0.00018343	0.006227	-1.688	0.7	217.17
1000	0.0063529	-0.00033662	0.0063618	-3.0331	0.7	247.92
719.6857	0.0064932	-0.00045235	0.0065089	-3.9851	0.7	278.67
517.9474	0.0066412	-0.00057218	0.0066658	-4.9242	0.7	309.42
372.7594	0.0068082	-0.00062763	0.0068371	-5.2671	0.7	340.17
268.2696	0.006984	-0.00068502	0.0070175	-5.6019	0.7	372.67
193.0698	0.0071546	-0.00071968	0.0071907	-5.7441	0.7	403.42
138.9496	0.0073217	-0.0007342	0.0073584	-5.7263	0.7	434.17
100	0.0074955	-0.00072229	0.0075302	-5.5042	0.7	464.92
71.96857	0.007659	-0.00069711	0.0076907	-5.2006	0.7	495.67
51.79475	0.0077956	-0.00062896	0.0078209	-4.6127	0.7	526.42
37.27594	0.0079335	-0.00058326	0.0079549	-4.2047	0.7	557.17
26.82696	0.0080502	-0.00052303	0.0080672	-3.7173	0.7	587.92
19.30698	0.0081466	-0.00047182	0.0081603	-3.3147	0.7	618.67
13.89496	0.0082289	-0.00042819	0.00824	-2.9787	0.7	649.42
10	0.0082997	-0.00039459	0.0083091	-2.7219	0.7	680.17
7.19686	0.0083646	-0.00037164	0.0083729	-2.544	0.7	711.04
5.17947	0.0084266	-0.00036259	0.0084344	-2.4639	0.7	741.92
3.72759	0.0084921	-0.00036288	0.0084998	-2.4468	0.7	772.92
2.6827	0.0085617	-0.00037595	0.00857	-2.5143	0.7	804.04
1.9307	0.0086374	-0.00040607	0.0086469	-2.6917	0.7	834.79
1.3895	0.0086969	-0.00042963	0.0087075	-2.8281	0.7	865.67
1	0.0087843	-0.00049207	0.0087981	-3.2062	0.7	896.29
0.71969	0.0088843	-0.00051579	0.0088993	-3.3227	0.7	927.54
0.51795	0.0089773	-0.00062415	0.008999	-3.9771	0.7	959.54
0.37276	0.0090478	-0.00066983	0.0090726	-4.234	0.7	992.42
0.26827	0.0091905	-0.00085666	0.0092303	-5.3252	0.7	1026.92
0.19307	0.0092875	-0.0010796	0.00935	-6.6304	0.7	1058.79
0.13895	0.0094023	-0.0013008	0.0094919	-7.8768	0.7	1095.54
0.1	0.0095385	-0.0015186	0.0096586	-9.046	0.7	1127.04

A123_4wire_Galv700mA_30s_FreshBatteryB_1167

Freq	Z' (a)	Z'' (b)	Mag	Phase	Ampl	Time
10000	0.0063145	0.0023641	0.0067425	20.526	0.7	32.64
7196.857	0.0061131	0.0015901	0.0063165	14.58	0.7	63.39
5179.475	0.0060464	0.0010305	0.0061336	9.6721	0.7	94.14
3727.594	0.0060333	0.00061136	0.0060642	5.7861	0.7	124.89
2682.696	0.0060555	0.00029184	0.0060625	2.7592	0.7	155.64
1930.698	0.0061214	2.68E-05	0.0061215	0.25088	0.7	186.39
1389.495	0.0062113	-0.00017282	0.0062137	-1.5938	0.7	217.14
1000	0.0063374	-0.00032516	0.0063457	-2.9372	0.7	247.89
719.6857	0.0064764	-0.00043929	0.0064913	-3.8804	0.7	278.64
517.9474	0.0066196	-0.00055904	0.0066432	-4.8273	0.7	309.39
372.7594	0.0067862	-0.00061176	0.0068137	-5.1512	0.7	340.14
268.2696	0.0069565	-0.00066937	0.0069886	-5.4962	0.7	372.51
193.0698	0.0071197	-0.00070024	0.0071541	-5.6171	0.7	403.26
138.9496	0.0072898	-0.00071557	0.0073248	-5.6062	0.7	434.01
100	0.0074573	-0.00070097	0.0074902	-5.3699	0.7	464.76
71.96857	0.0076167	-0.00067484	0.0076465	-5.0632	0.7	495.51
51.79475	0.0077466	-0.00060594	0.0077703	-4.4726	0.7	526.26
37.27594	0.0078799	-0.00056162	0.0078999	-4.0767	0.7	557.01
26.82696	0.0079913	-0.00050223	0.0080071	-3.5961	0.7	587.76
19.30698	0.0080834	-0.00045006	0.0080959	-3.1868	0.7	618.51
13.89496	0.008162	-0.0004076	0.0081722	-2.8589	0.7	649.26
10	0.0082274	-0.00037523	0.008236	-2.6113	0.7	680.01
7.19686	0.0082907	-0.00035436	0.0082983	-2.4474	0.7	710.89
5.17947	0.0083482	-0.00034327	0.0083553	-2.3546	0.7	741.76
3.72759	0.0084137	-0.00034512	0.0084208	-2.3489	0.7	772.64
2.6827	0.0084784	-0.00035665	0.0084859	-2.4088	0.7	803.89
1.9307	0.0085525	-0.00039101	0.0085614	-2.6177	0.7	834.64
1.3895	0.0086087	-0.00041705	0.0086188	-2.7735	0.7	865.51
1	0.0086995	-0.00047361	0.0087124	-3.1162	0.7	896.14
0.71969	0.0087745	-0.00049245	0.0087883	-3.2122	0.7	927.39
0.51795	0.0088768	-0.00060517	0.0088974	-3.9001	0.7	959.51
0.37276	0.0089418	-0.00064282	0.0089649	-4.1119	0.7	992.39
0.26827	0.0090855	-0.00082607	0.009123	-5.1952	0.7	1026.89
0.19307	0.0091835	-0.0010468	0.009243	-6.5029	0.7	1058.64
0.13895	0.0092899	-0.0012524	0.0093739	-7.6779	0.7	1095.39
0.1	0.00943	-0.0014696	0.0095438	-8.8579	0.7	1127.14

A123_4wire_Galv700mA_30s_FreshBatteryB_1000

Freq	Z' (a)	Z'' (b)	Mag	Phase	Ampl	Time
10000	0.0063234	0.0023643	0.0067509	20.501	0.7	32.6
7196.857	0.0061228	0.0015898	0.0063258	14.556	0.7	63.35
5179.475	0.0060546	0.0010271	0.0061411	9.628	0.7	94.1
3727.594	0.006047	0.00060809	0.0060775	5.7424	0.7	124.85
2682.696	0.0060677	0.00028723	0.0060745	2.7102	0.7	155.6
1930.698	0.0061319	1.90E-05	0.0061319	0.17734	0.7	186.35
1389.495	0.0062271	-0.0001794	0.0062297	-1.6502	0.7	217.1
1000	0.0063515	-0.0003337	0.0063603	-3.0077	0.7	247.85
719.6857	0.0064928	-0.0004476	0.0065082	-3.9432	0.7	278.6
517.9474	0.0066391	-0.0005676	0.0066633	-4.8864	0.7	309.35
372.7594	0.0068046	-0.0006212	0.0068329	-5.2163	0.7	340.1
268.2696	0.0069767	-0.0006737	0.0070092	-5.5159	0.7	372.6
193.0698	0.0071455	-0.0007079	0.0071805	-5.6577	0.7	403.35
138.9496	0.0073123	-0.0007173	0.0073474	-5.6027	0.7	434.1
100	0.0074805	-0.0007068	0.0075138	-5.3978	0.7	464.85
71.96857	0.00764	-0.0006796	0.0076702	-5.0834	0.7	495.6
51.79475	0.0077694	-0.000612	0.0077935	-4.5037	0.7	526.35
37.27594	0.0079032	-0.0005592	0.007923	-4.047	0.7	557.12
26.82696	0.0080142	-0.0005063	0.0080302	-3.615	0.7	587.87
19.30698	0.0081052	-0.0004518	0.0081178	-3.1902	0.7	618.6
13.89496	0.0081813	-0.0004073	0.0081914	-2.8504	0.7	649.35
10	0.0082476	-0.000376	0.0082562	-2.6105	0.7	680.1
7.19686	0.0083083	-0.0003513	0.0083157	-2.4211	0.7	710.98
5.17947	0.0083637	-0.0003405	0.0083706	-2.3316	0.7	741.85
3.72759	0.0084244	-0.0003422	0.0084313	-2.3264	0.7	772.73
2.6827	0.0084876	-0.0003534	0.008495	-2.384	0.7	803.98
1.9307	0.0085586	-0.0003836	0.0085672	-2.5663	0.7	834.73
1.3895	0.008614	-0.0004126	0.0086239	-2.742	0.7	865.6
1	0.008702	-0.0004645	0.0087144	-3.0555	0.7	896.35
0.71969	0.0087889	-0.0004861	0.0088023	-3.166	0.7	927.6
0.51795	0.0088717	-0.0005955	0.0088917	-3.8403	0.7	959.6
0.37276	0.0089501	-0.0006392	0.0089729	-4.0848	0.7	992.48
0.26827	0.009074	-0.0008134	0.0091104	-5.1224	0.7	1026.85
0.19307	0.0091737	-0.00102	0.0092302	-6.3445	0.7	1058.73
0.13895	0.0092573	-0.0012219	0.0093376	-7.5192	0.7	1095.48
0.1	0.0093897	-0.0014473	0.0095006	-8.7624	0.7	1126.98

A123_4wire_Galv700mA_30s_FreshBatteryB_0833

Freq	Z' (a)	Z'' (b)	Mag	Phase	Ampl	Time
10000	0.0063188	0.0023709	0.006749	20.567	0.7	32.64
7196.857	0.0061174	0.0015944	0.0063218	14.608	0.7	63.39
5179.475	0.0060538	0.0010304	0.0061409	9.6596	0.7	94.14
3727.594	0.0060424	0.00061366	0.0060735	5.799	0.7	124.89
2682.696	0.0060659	0.00028925	0.0060728	2.7301	0.7	155.64
1930.698	0.0061307	2.35E-05	0.0061307	0.21936	0.7	186.39
1389.495	0.0062267	-0.00017834	0.0062293	-1.6406	0.7	217.14
1000	0.0063523	-0.00033161	0.0063609	-2.9883	0.7	247.89
719.6857	0.006494	-0.00044635	0.0065093	-3.9319	0.7	278.64
517.9474	0.0066415	-0.0005649	0.0066655	-4.8617	0.7	309.39
372.7594	0.0068071	-0.00061752	0.0068351	-5.1835	0.7	340.14
268.2696	0.0069773	-0.00067723	0.0070101	-5.5439	0.7	372.64
193.0698	0.0071456	-0.00070353	0.0071801	-5.623	0.7	403.39
138.9496	0.0073142	-0.00071426	0.007349	-5.5775	0.7	434.14
100	0.0074803	-0.00069909	0.0075129	-5.3392	0.7	464.89
71.96857	0.0076389	-0.00067301	0.0076685	-5.0349	0.7	495.64
51.79475	0.0077669	-0.00060279	0.0077903	-4.4378	0.7	526.39
37.27594	0.0078971	-0.00055261	0.0079164	-4.0028	0.7	557.14
26.82696	0.0080076	-0.00050003	0.0080232	-3.5732	0.7	587.89
19.30698	0.0080987	-0.00044646	0.008111	-3.1554	0.7	618.64
13.89496	0.0081752	-0.00040301	0.0081851	-2.8222	0.7	649.39
10	0.008242	-0.00037131	0.0082504	-2.5795	0.7	680.14
7.19686	0.0083014	-0.00034932	0.0083087	-2.4096	0.7	710.89
5.17947	0.008357	-0.00033798	0.0083638	-2.3159	0.7	741.76
3.72759	0.0084189	-0.00034146	0.0084258	-2.3226	0.7	772.76
2.6827	0.0084823	-0.0003538	0.0084897	-2.3884	0.7	803.89
1.9307	0.0085554	-0.00038482	0.0085641	-2.5754	0.7	834.64
1.3895	0.0086078	-0.00041127	0.0086176	-2.7354	0.7	865.51
1	0.0086982	-0.00046429	0.0087106	-3.0554	0.7	896.14
0.71969	0.0087697	-0.00048051	0.0087829	-3.1362	0.7	927.39
0.51795	0.0088787	-0.00059728	0.0088988	-3.8486	0.7	959.51
0.37276	0.0089457	-0.00062908	0.0089678	-4.0225	0.7	992.39
0.26827	0.0090842	-0.0008075	0.00912	-5.0797	0.7	1026.89
0.19307	0.0091873	-0.0010177	0.0092435	-6.321	0.7	1058.64
0.13895	0.0092744	-0.0012264	0.0093551	-7.5328	0.7	1095.39
0.1	0.0094112	-0.0014254	0.0095185	-8.6124	0.7	1127.26

A123_4wire_Galv700mA_30s_FreshBatteryB_667

Freq	Z' (a)	Z'' (b)	Mag	Phase	Ampl	Time
10000	0.0063185	0.002394	0.0067568	20.751	0.7	32.67
7196.857	0.0061185	0.0016133	0.0063276	14.771	0.7	63.42
5179.475	0.0060552	0.0010429	0.0061444	9.7723	0.7	94.17
3727.594	0.0060367	0.00062516	0.006069	5.9125	0.7	124.92
2682.696	0.0060692	0.00029811	0.0060765	2.812	0.7	155.67
1930.698	0.0061265	2.94E-05	0.0061266	0.2751	0.7	186.42
1389.495	0.0062233	-0.0001715	0.0062257	-1.5784	0.7	217.17
1000	0.0063475	-0.0003258	0.0063559	-2.9378	0.7	247.92
719.6857	0.006487	-0.0004387	0.0065018	-3.8691	0.7	278.67
517.9474	0.0066324	-0.0005553	0.0066556	-4.7856	0.7	309.42
372.7594	0.0067983	-0.0006085	0.0068255	-5.115	0.7	340.17
268.2696	0.0069654	-0.0006648	0.0069971	-5.4519	0.7	372.54
193.0698	0.0071332	-0.0006925	0.0071667	-5.5449	0.7	403.29
138.9496	0.0072972	-0.0006943	0.0073302	-5.4348	0.7	434.04
100	0.0074608	-0.000683	0.007492	-5.2309	0.7	464.79
71.96857	0.0076126	-0.0006643	0.0076415	-4.9873	0.7	495.54
51.79475	0.0077366	-0.0005868	0.0077588	-4.3376	0.7	526.29
37.27594	0.0078623	-0.0005371	0.0078806	-3.9078	0.7	557.04
26.82696	0.0079685	-0.0004836	0.0079832	-3.4728	0.7	587.79
19.30698	0.0080568	-0.0004348	0.0080685	-3.0891	0.7	618.54
13.89496	0.0081316	-0.0003941	0.0081411	-2.7748	0.7	649.29
10	0.0081964	-0.0003647	0.0082045	-2.5479	0.7	680.04
7.19686	0.0082574	-0.0003456	0.0082646	-2.3965	0.7	710.92
5.17947	0.0083133	-0.0003376	0.0083202	-2.3256	0.7	741.79
3.72759	0.0083759	-0.0003396	0.0083828	-2.3218	0.7	772.79
2.6827	0.00844	-0.000356	0.0084475	-2.4152	0.7	803.92
1.9307	0.0085144	-0.0003861	0.0085231	-2.5963	0.7	834.67
1.3895	0.0085689	-0.000416	0.008579	-2.7795	0.7	865.54
1	0.0086574	-0.0004745	0.0086704	-3.1374	0.7	896.29
0.71969	0.0087553	-0.0004963	0.0087694	-3.2442	0.7	927.54
0.51795	0.0088451	-0.0006049	0.0088658	-3.9123	0.7	959.42
0.37276	0.0089104	-0.0006354	0.008933	-4.0787	0.7	992.29
0.26827	0.0090514	-0.0008089	0.0090875	-5.1065	0.7	1026.79
0.19307	0.0091529	-0.0010335	0.0092111	-6.4423	0.7	1058.54
0.13895	0.0092605	-0.0012272	0.0093415	-7.5488	0.7	1095.29
0.1	0.0094056	-0.0014235	0.0095127	-8.6062	0.7	1127.17

A123_4wire_Galv700mA_30s_FreshBatteryB_0333

Freq	Z' (a)	Z'' (b)	Mag	Phase	Ampl	Time
10000	0.0063268	0.0023949	0.0067649	20.733	0.7	32.67
7196.857	0.0061257	0.0016131	0.0063345	14.753	0.7	63.42
5179.475	0.0060678	0.0010392	0.0061561	9.7185	0.7	94.17
3727.594	0.0060467	0.00061947	0.0060783	5.8494	0.7	124.92
2682.696	0.0060795	0.00028675	0.0060863	2.7005	0.7	155.67
1930.698	0.0061396	1.88E-05	0.0061396	0.17551	0.7	186.42
1389.495	0.0062383	-0.00018382	0.006241	-1.6878	0.7	217.17
1000	0.0063659	-0.00034117	0.006375	-3.0677	0.7	247.92
719.6857	0.0065101	-0.00045587	0.006526	-4.0056	0.7	278.67
517.9474	0.0066595	-0.00057442	0.0066842	-4.9299	0.7	309.42
372.7594	0.0068293	-0.0006275	0.0068581	-5.2498	0.7	340.17
268.2696	0.0070012	-0.00068246	0.0070344	-5.5675	0.7	372.67
193.0698	0.0071725	-0.00071532	0.0072081	-5.6953	0.7	403.42
138.9496	0.0073423	-0.00071649	0.0073772	-5.5735	0.7	434.17
100	0.0075063	-0.0007023	0.0075391	-5.3451	0.7	464.92
71.96857	0.007666	-0.00067931	0.007696	-5.0639	0.7	495.67
51.79475	0.0077944	-0.00060173	0.0078176	-4.4145	0.7	526.42
37.27594	0.0079233	-0.00055014	0.0079424	-3.9719	0.7	557.17
26.82696	0.0080312	-0.00049633	0.0080465	-3.5364	0.7	587.92
19.30698	0.0081207	-0.00044473	0.0081329	-3.1347	0.7	618.67
13.89496	0.0081959	-0.00040329	0.0082058	-2.817	0.7	649.42
10	0.0082608	-0.00037179	0.0082692	-2.5769	0.7	680.17
7.19686	0.0083217	-0.00035144	0.0083291	-2.4183	0.7	710.92
5.17947	0.0083801	-0.00034332	0.0083871	-2.346	0.7	741.92
3.72759	0.0084423	-0.0003466	0.0084494	-2.351	0.7	772.79
2.6827	0.0085063	-0.00036199	0.008514	-2.4368	0.7	803.92
1.9307	0.0085889	-0.00038756	0.0085976	-2.5836	0.7	834.67
1.3895	0.0086512	-0.00042836	0.0086618	-2.8347	0.7	865.54
1	0.0087365	-0.0004745	0.0087494	-3.1088	0.7	896.29
0.71969	0.0087961	-0.00049463	0.00881	-3.2185	0.7	927.54
0.51795	0.0089158	-0.00060219	0.0089361	-3.864	0.7	959.79
0.37276	0.0089962	-0.00063798	0.0090188	-4.0564	0.7	992.67
0.26827	0.0091208	-0.00081556	0.0091572	-5.1097	0.7	1027.04
0.19307	0.0092246	-0.001033	0.0092823	-6.3895	0.7	1058.79
0.13895	0.0093083	-0.0012231	0.0093883	-7.4857	0.7	1095.54
0.1	0.0094632	-0.0014158	0.0095685	-8.509	0.7	1127.29

A123_4wire_Galv700mA_30s_FreshBatteryB_0000

Freq	Z' (a)	Z'' (b)	Mag	Phase	Ampl	Time
10000	0.0062572	0.0024305	0.0067127	21.228	0.7	32.59
7196.857	0.0060592	0.0016343	0.0062757	15.095	0.7	63.34
5179.475	0.0059969	0.0010647	0.0060907	10.067	0.7	94.09
3727.594	0.0059857	0.00062264	0.006018	5.9386	0.7	124.84
2682.696	0.0060236	0.00026631	0.0060295	2.5315	0.7	155.59
1930.698	0.006114	2.13E-06	0.006114	0.019953	0.7	186.34
1389.495	0.0062089	-0.00020523	0.0062123	-1.8932	0.7	217.09
1000	0.0063425	-0.00036661	0.0063531	-3.3081	0.7	247.85
719.6857	0.006493	-0.000484	0.006511	-4.263	0.7	278.59
517.9474	0.0066509	-0.0006149	0.0066793	-5.2822	0.7	309.34
372.7594	0.0068295	-0.00066951	0.0068622	-5.5989	0.7	340.1
268.2696	0.0070079	-0.00075577	0.0070485	-6.1553	0.7	372.59
193.0698	0.0071924	-0.00078158	0.0072347	-6.2019	0.7	403.34
138.9496	0.0073734	-0.00079464	0.0074161	-6.1511	0.7	434.09
100	0.0075525	-0.00080779	0.0075956	-6.105	0.7	464.84
71.96857	0.0077297	-0.00078051	0.007769	-5.7659	0.7	495.59
51.79475	0.0078764	-0.00073383	0.0079105	-5.3228	0.7	526.34
37.27594	0.0080318	-0.00070712	0.0080629	-5.0314	0.7	557.09
26.82696	0.0081716	-0.00068077	0.0081999	-4.7623	0.7	587.84
19.30698	0.0083024	-0.00066462	0.008329	-4.5769	0.7	618.59
13.89496	0.0084253	-0.00065906	0.008451	-4.4728	0.7	649.34
10	0.0085409	-0.00066769	0.008567	-4.47	0.7	680.09
7.19686	0.0086561	-0.00069354	0.0086838	-4.5808	0.7	710.96
5.17947	0.0087717	-0.00074134	0.008803	-4.8309	0.7	741.84
3.72759	0.008893	-0.00081837	0.0089306	-5.2578	0.7	772.71
2.6827	0.0090222	-0.00092973	0.00907	-5.8835	0.7	803.96
1.9307	0.0091695	-0.0010928	0.0092344	-6.7963	0.7	834.71
1.3895	0.0093133	-0.0012954	0.009403	-7.9185	0.7	865.59
1	0.0095035	-0.001585	0.0096348	-9.4687	0.7	896.34
0.71969	0.0097238	-0.0019096	0.0099095	-11.111	0.7	927.59
0.51795	0.0099635	-0.00241	0.010251	-13.598	0.7	959.46
0.37276	0.010235	-0.0029616	0.010655	-16.138	0.7	992.34
0.26827	0.010605	-0.0038069	0.011268	-19.747	0.7	1026.84
0.19307	0.011007	-0.0048804	0.01204	-23.912	0.7	1058.59
0.13895	0.011485	-0.0061838	0.013044	-28.299	0.7	1095.34
0.1	0.01209	-0.0078765	0.014429	-33.084	0.7	1127.09

A123_4wire_Galv700mA_30s_FreshBatteryB_0000_Repeat

Freq	Z' (a)	Z'' (b)	Mag	Phase	Ampl	Time
10000	0.0062222	0.0024315	0.0066804	21.344	0.7	32.64
7196.857	0.0060188	0.0016482	0.0062404	15.315	0.7	63.39
5179.475	0.0059544	0.0010858	0.0060526	10.334	0.7	94.14
3727.594	0.0059344	0.00064887	0.0059698	6.24	0.7	124.89
2682.696	0.0059656	0.00029912	0.0059731	2.8705	0.7	155.64
1930.698	0.0060476	4.20E-05	0.0060477	0.3976	0.7	186.39
1389.495	0.0061376	-0.000161	0.0061397	-1.5026	0.7	217.14
1000	0.006261	-0.00031552	0.0062689	-2.885	0.7	247.89
719.6857	0.0064032	-0.00042734	0.0064174	-3.8182	0.7	278.64
517.9474	0.006548	-0.0005519	0.0065712	-4.8178	0.7	309.39
372.7594	0.006714	-0.00059956	0.0067407	-5.103	0.7	340.14
268.2696	0.0068764	-0.00067946	0.0069099	-5.6431	0.7	372.51
193.0698	0.007045	-0.00070383	0.0070801	-5.7052	0.7	403.26
138.9496	0.0072101	-0.00071579	0.0072455	-5.6695	0.7	434.01
100	0.0073745	-0.00072444	0.00741	-5.6105	0.7	464.76
71.96857	0.0075339	-0.00069984	0.0075663	-5.3071	0.7	495.51
51.79475	0.0076643	-0.00065565	0.0076923	-4.8895	0.7	526.26
37.27594	0.0078023	-0.00063387	0.007828	-4.6446	0.7	557.01
26.82696	0.0079263	-0.00061216	0.0079499	-4.4163	0.7	587.76
19.30698	0.008042	-0.00060222	0.0080645	-4.2826	0.7	618.51
13.89496	0.0081508	-0.00059951	0.0081728	-4.2067	0.7	649.26
10	0.0082569	-0.00061262	0.0082796	-4.2433	0.7	680.01
7.19686	0.0083647	-0.00064305	0.0083894	-4.3961	0.7	710.89
5.17947	0.0084706	-0.0006898	0.0084986	-4.6556	0.7	741.76
3.72759	0.0085848	-0.00076795	0.0086191	-5.1118	0.7	772.64
2.6827	0.0087093	-0.00087582	0.0087532	-5.7424	0.7	803.89
1.9307	0.0088488	-0.0010359	0.0089092	-6.677	0.7	834.64
1.3895	0.0089836	-0.0012271	0.009067	-7.7781	0.7	865.51
1	0.0091688	-0.0015088	0.0092921	-9.3447	0.7	896.26
0.71969	0.0093816	-0.0018131	0.0095552	-10.938	0.7	927.51
0.51795	0.0096142	-0.0022873	0.0098825	-13.382	0.7	959.39
0.37276	0.0098748	-0.0027987	0.010264	-15.824	0.7	992.26
0.26827	0.010241	-0.003624	0.010863	-19.487	0.7	1026.76
0.19307	0.010611	-0.0046577	0.011588	-23.699	0.7	1058.51
0.13895	0.011064	-0.0058975	0.012538	-28.059	0.7	1095.26
0.1	0.011634	-0.0074821	0.013832	-32.746	0.7	1127.01

A123_4wire_Galv700mA_30s_FreshBatteryB_0000_SecondRepeat

Freq	Z' (a)	Z'' (b)	Mag	Phase	Ampl	Time
10000	0.0061931	0.0024323	0.0066536	21.442	0.7	32.68
7196.857	0.0059889	0.0016575	0.006214	15.47	0.7	63.43
5179.475	0.0059222	0.0010897	0.0060216	10.426	0.7	94.18
3727.594	0.0059007	0.00065942	0.0059374	6.3765	0.7	124.93
2682.696	0.005926	0.00032052	0.0059347	3.0959	0.7	155.68
1930.698	0.0060089	6.33E-05	0.0060092	0.60387	0.7	186.43
1389.495	0.0060922	-0.00013567	0.0060937	-1.2757	0.7	217.18
1000	0.0062104	-0.00028555	0.006217	-2.6326	0.7	247.93
719.6857	0.0063424	-0.00039399	0.0063546	-3.5546	0.7	278.68
517.9474	0.0064824	-0.0005127	0.0065026	-4.5222	0.7	309.43
372.7594	0.0066365	-0.00055875	0.00666	-4.8126	0.7	340.18
268.2696	0.0067878	-0.00063211	0.0068172	-5.3203	0.7	372.56
193.0698	0.0069429	-0.0006549	0.0069737	-5.3886	0.7	403.31
138.9496	0.0070962	-0.00067151	0.0071279	-5.4058	0.7	434.06
100	0.0072464	-0.00066028	0.0072764	-5.2063	0.7	464.81
71.96857	0.0073861	-0.00066367	0.0074159	-5.1345	0.7	495.56
51.79475	0.0075019	-0.00060239	0.007526	-4.5909	0.7	526.31
37.27594	0.0076281	-0.00058397	0.0076504	-4.3777	0.7	557.06
26.82696	0.0077414	-0.00056898	0.0077623	-4.2036	0.7	587.81
19.30698	0.0078475	-0.00056059	0.0078675	-4.086	0.7	618.56
13.89496	0.0079482	-0.00056445	0.0079682	-4.0621	0.7	649.31
10	0.0080473	-0.0005788	0.0080681	-4.1139	0.7	680.06
7.19686	0.0081428	-0.00061	0.0081656	-4.2842	0.7	710.81
5.17947	0.0082425	-0.00066222	0.0082691	-4.5934	0.7	741.68
3.72759	0.0083503	-0.00073864	0.0083829	-5.055	0.7	772.68
2.6827	0.0084647	-0.00084546	0.0085068	-5.7038	0.7	803.81
1.9307	0.0086026	-0.0010015	0.0086607	-6.6404	0.7	834.56
1.3895	0.0087216	-0.0012001	0.0088038	-7.8348	0.7	865.43
1	0.0089036	-0.0014618	0.0090228	-9.3237	0.7	896.18
0.71969	0.0090858	-0.0017467	0.0092522	-10.882	0.7	927.43
0.51795	0.0093053	-0.0022257	0.0095678	-13.452	0.7	959.43
0.37276	0.009548	-0.0027222	0.0099285	-15.913	0.7	992.31
0.26827	0.009908	-0.0035377	0.010521	-19.649	0.7	1026.81
0.19307	0.010254	-0.0045417	0.011215	-23.89	0.7	1058.56
0.13895	0.01067	-0.0057308	0.012112	-28.24	0.7	1095.31
0.1	0.011196	-0.0072585	0.013343	-32.956	0.7	1127.18

Due to the number of data files the datasets for the other batteries are not included but available upon request.

Appendix D

Base Vehicle Model Simulink Models and Initialization Files

Battery – Top Level

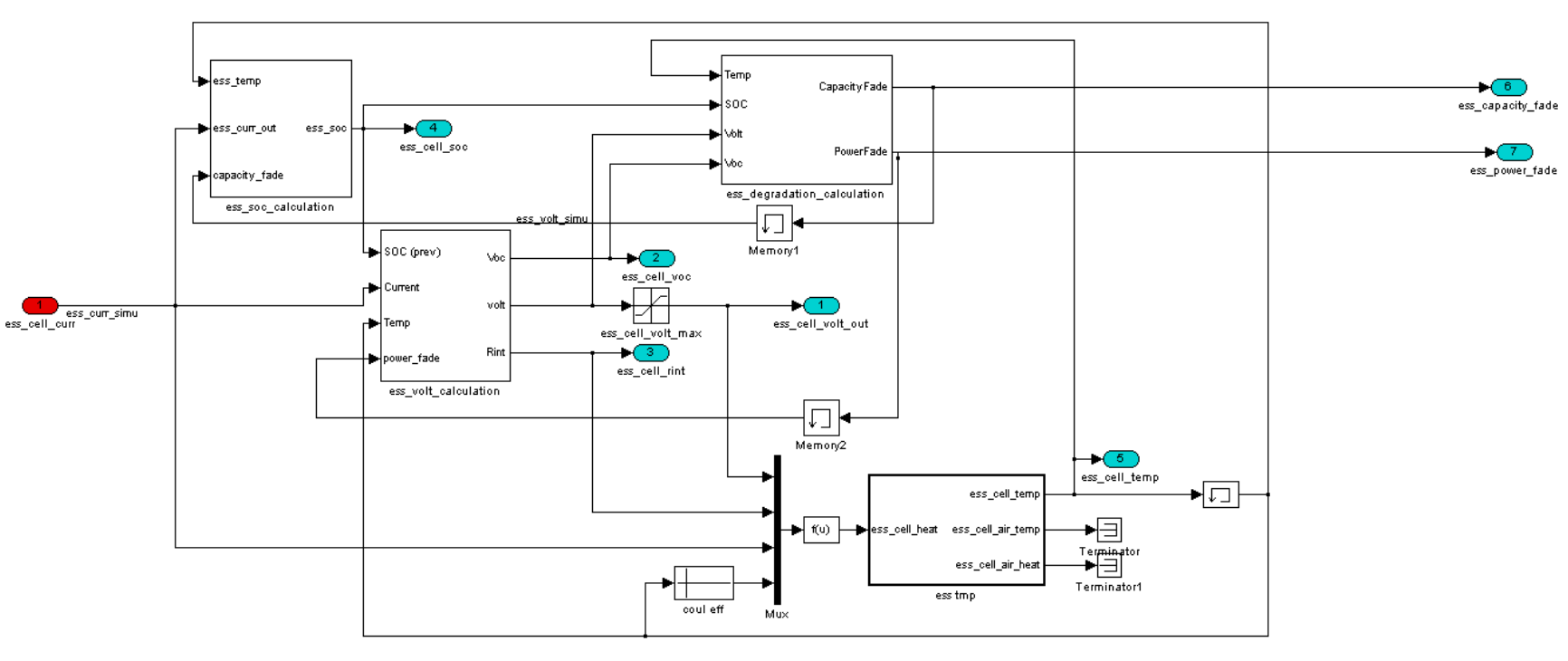

Battery – Degradation Block (ess_degradation_calculation)

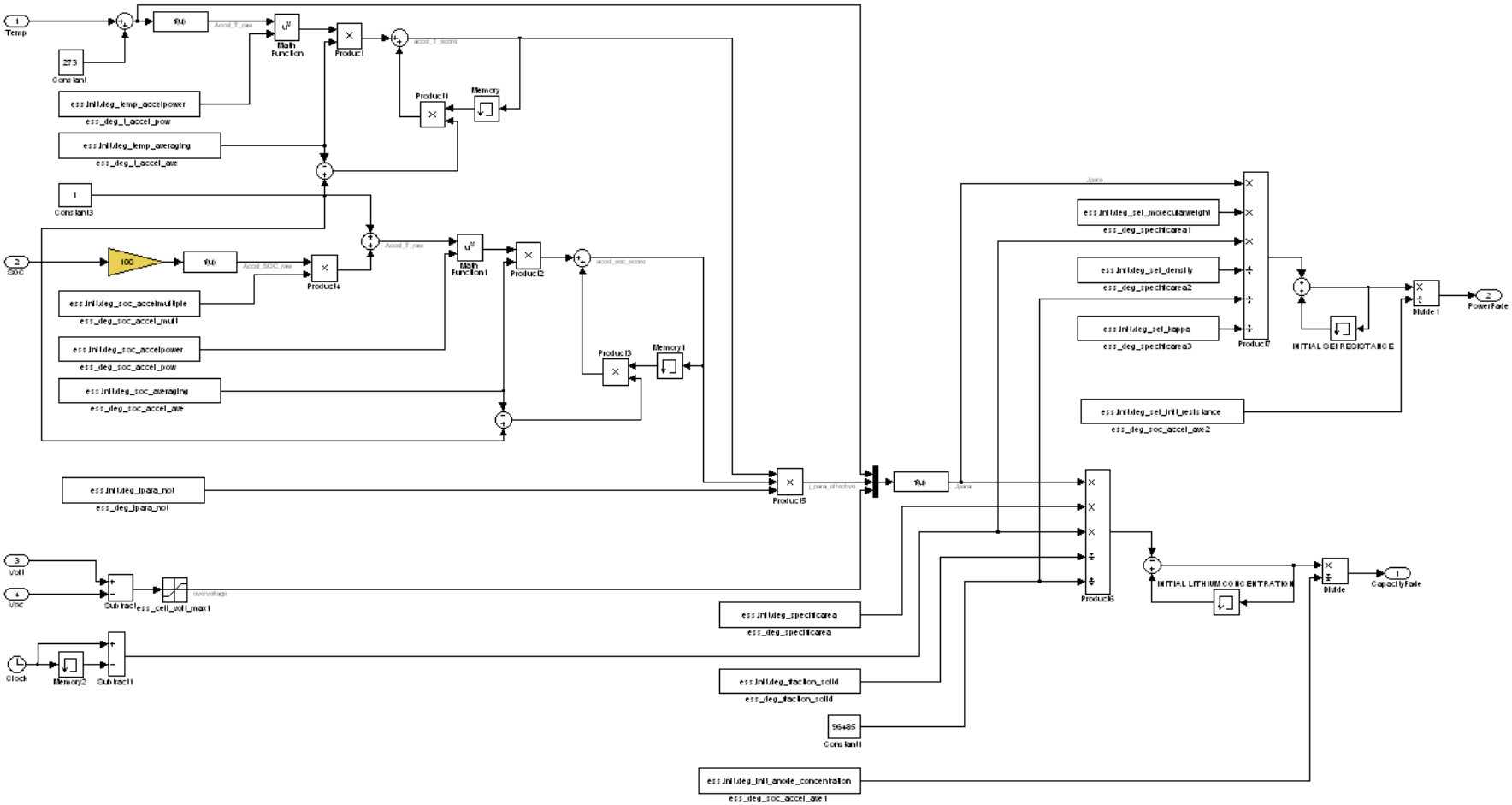

Battery – Modified Voltage Block (ess_volt_calculation)

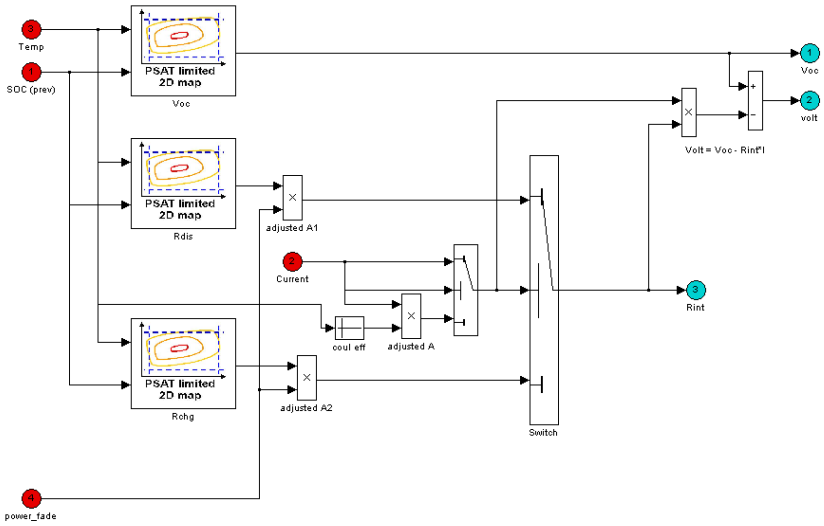

Battery – Modified SOC Block (ess_soc_calculation)

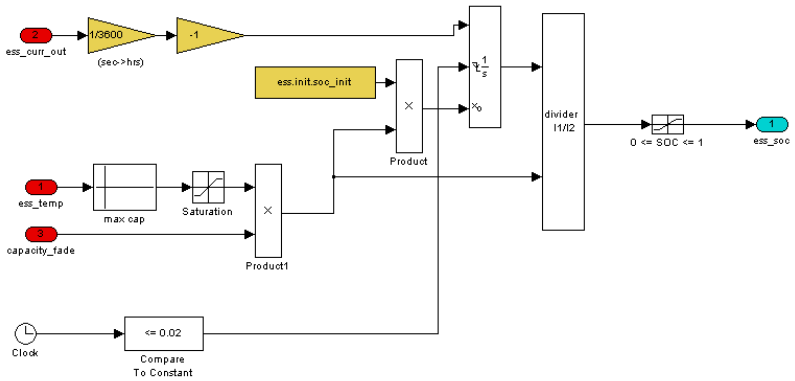

Fuel Cell – Top Level

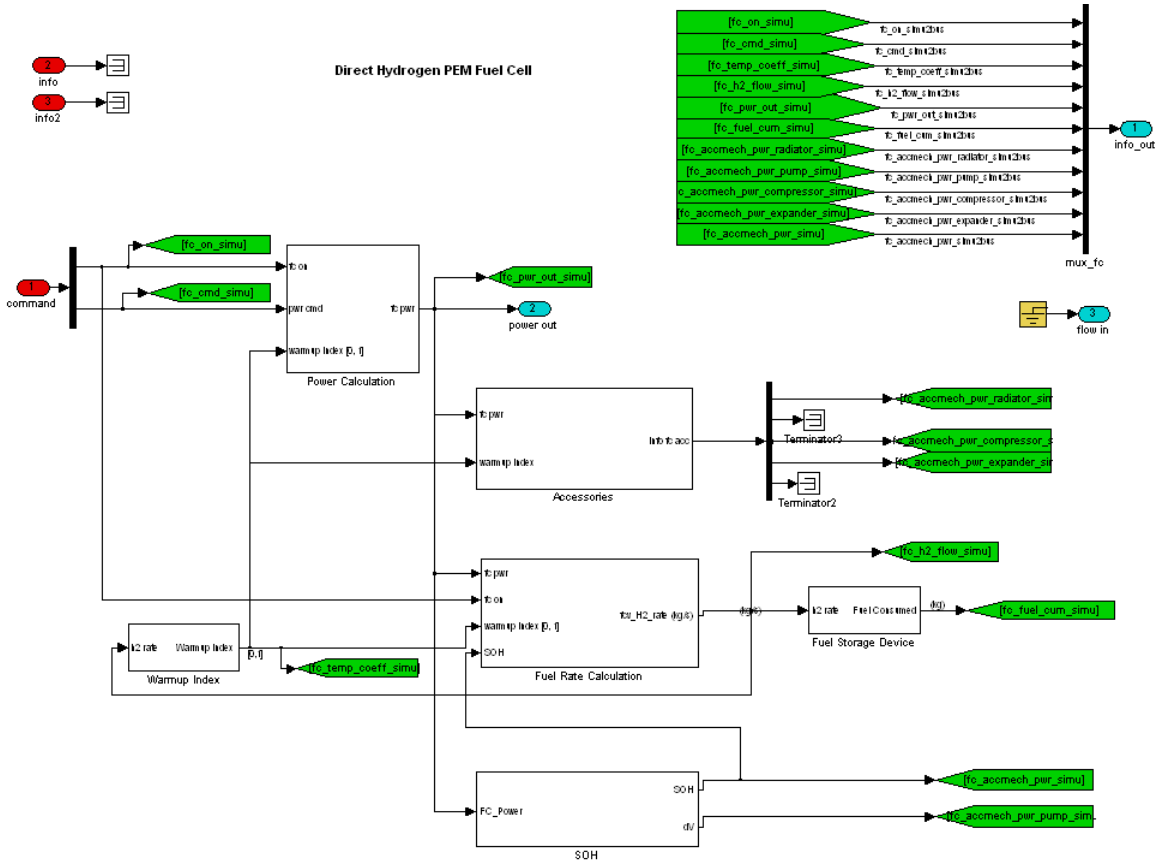

Fuel Cell – Fuel Cell Degradation Block (SOH)

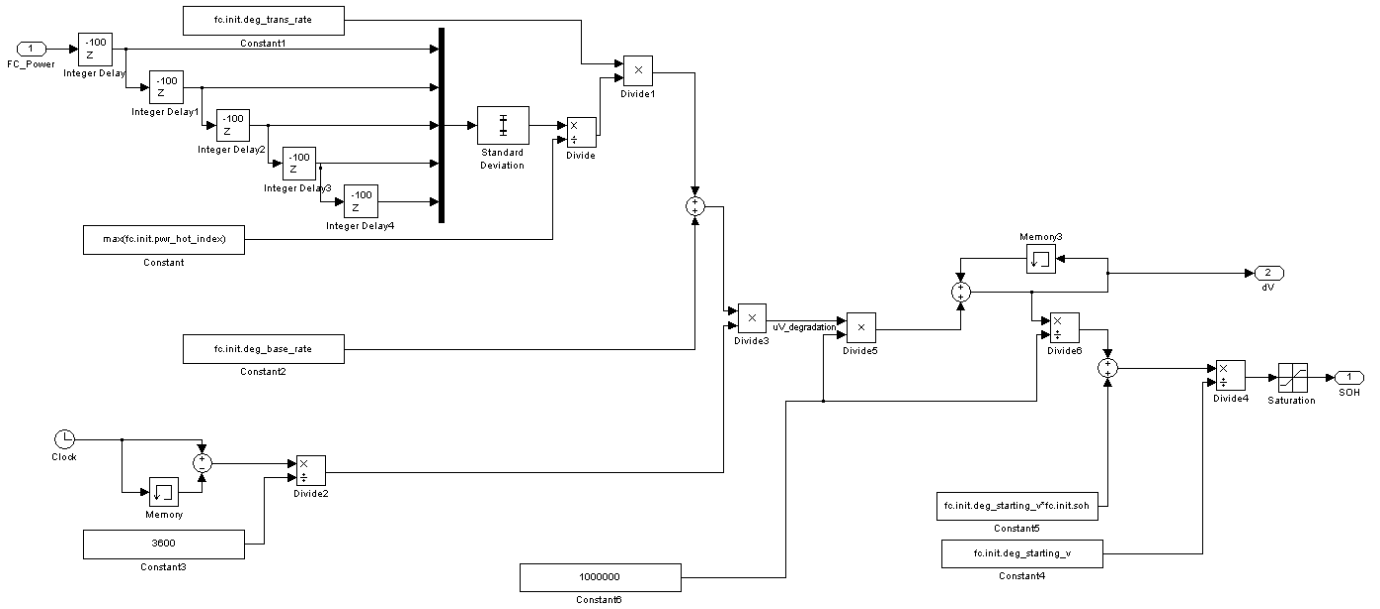

Fuel Cell – Fuel Cell Degradation Block (SOH)

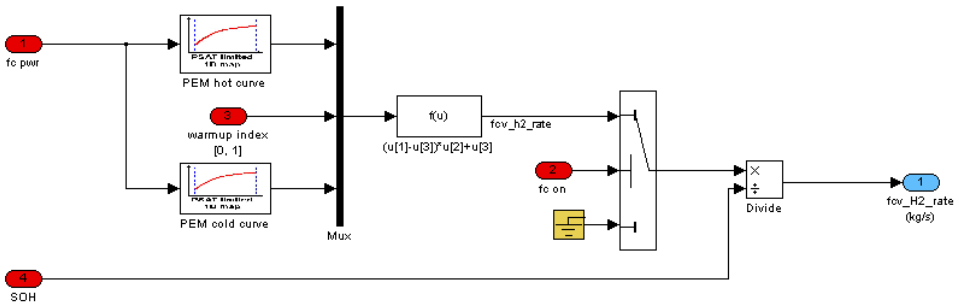

DC/DC Fuel Cell – Top Level (Included Fuel Cell Blower Load)

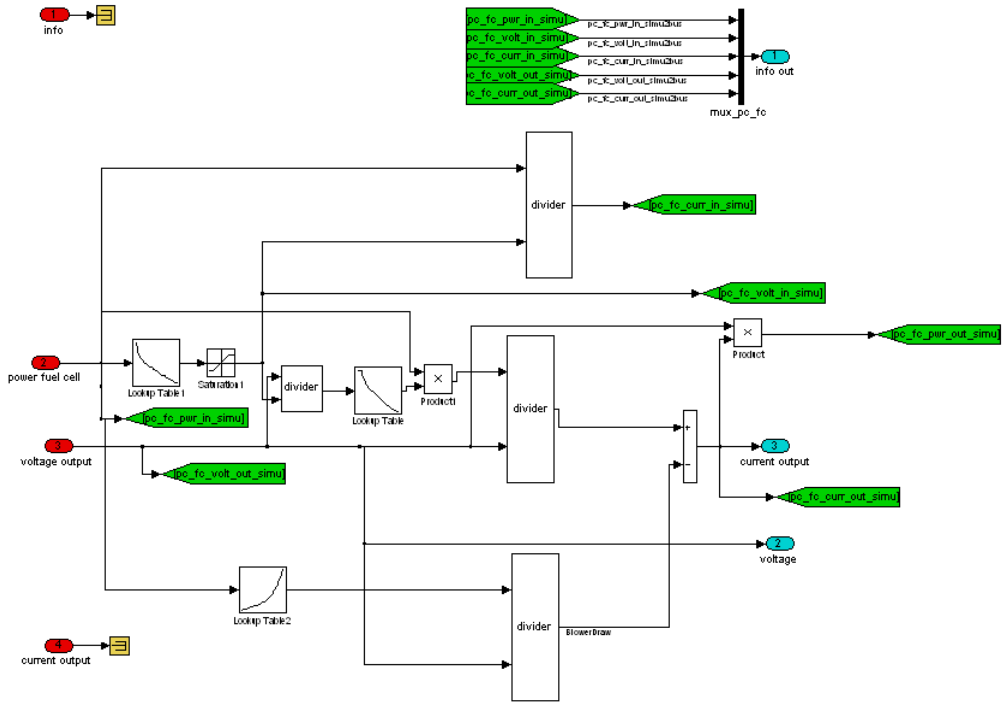

Powertrain Controller (Rule Based Version)

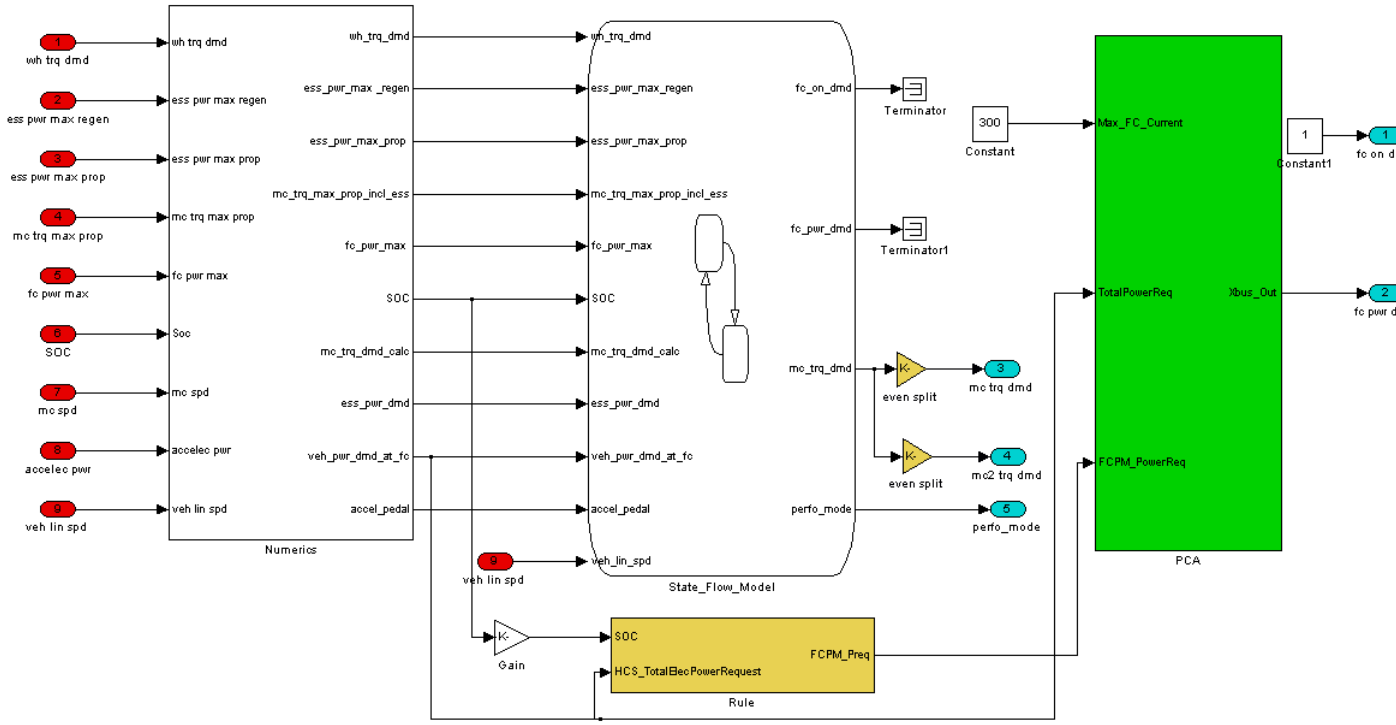

Powertrain Controller (Rule Based Version)

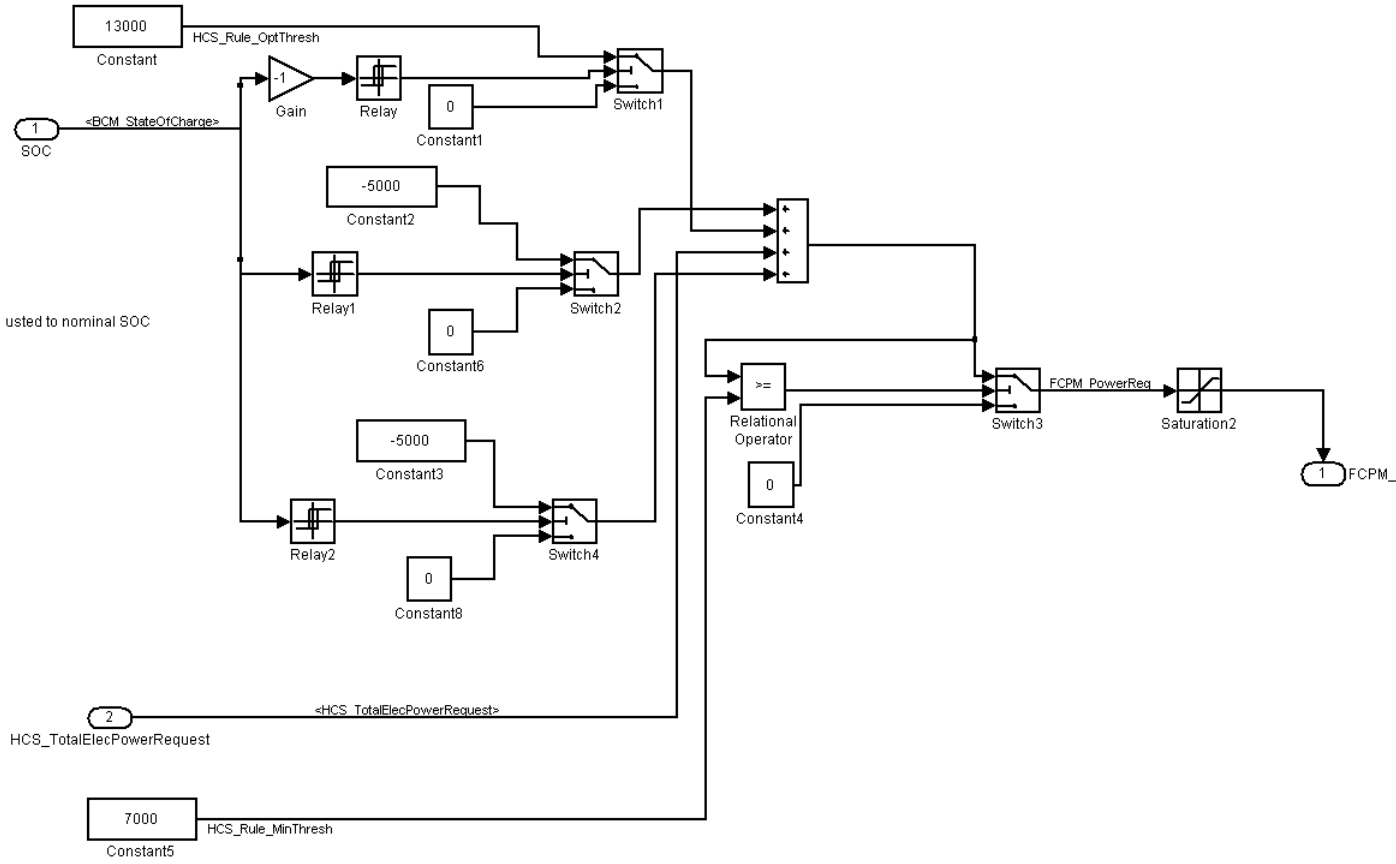

Motor Model – Initialization File

```
%% File description
% Name : mc_id_45_65_ballard_uwaft
% Author : Original file by A.Rousseau, Modified by M.Stevens
% Description : Initialize the Ballard AC induction motor/controller
for the UWAFT Equinox
% Continuous Power = 32kW, Peak Power = 67kW
% Model : lib_mc_map_Pelec_funTW_volt_multiple_in,
lib_mc_map_Pelec_funTW_volt_in,lib_mc_map_Pelec_funTW_pwr_in
% Technology : id, id
% Vehicle Type : a, Light

%% File content
mc.list.init = {'inertia','tau','coeff_regen','volt_min','curr_max'};
mc.list.parametric = {'inertia','tau','coeff_regen'};

mc.init.inertia             = 0.024;    % rotor's rotational inertia,
kg-m^2
mc.init.coeff_regen         = 1.0;
mc.init.time_response       = 0.05;
mc.init.volt_min            = 250; % (V), minimum voltage allowed by
the controller and motor
```

```
mc.init.tau                 = 0.05; % from 0 to 100 % of the torque in
50 ms
mc.init.t_max_trq           = 180; % Time the motor can remain at max
torque
mc.init.mass                = 90;% Weight of motor power/sum of motor
and controller mass
mc.init.curr_max            = 350; % (A), maximum current allowed by
the controller and motor
mc.init.spd_base            =
conversion_calc('rotational_speed','rpm','rad/s',2665);% rad/s

mc.init.motor_mass          = 50;
mc.init.controller_mass     = 20;

mc.init.curr_max            = 480; % (A), maximum current allowed by
the controller and motor
mc.init.spd_base            =
conversion_calc('rotational_speed','rpm','rad/s',2000);% rad/s

mc.init.spd_cont_index      =
conversion_calc('rotational_speed','rpm','rad/s',[0   500 1000    2000
3000    4000    5000    6000    7000    8000    9000    10000   11000
12000   13000   13500]);
mc.init.trq_cont_map        = [112.57   112.57  112.57  112.57  112.57
107.43  85.94   71.62   61.39   53.71   47.75   42.97   39.07   35.81
33.06   31.83];

mc.init.spd_max_index       = mc.init.spd_cont_index;
mc.init.trq_max_map         = [225.14   225.14  225.14  225.14  206.9
155.18  124.14  103.45  88.67   77.59   68.97   62.07   56.43   51.73
47.75   45.98];

mc.init.spd_min_index       = mc.init.spd_max_index; % rad/s
mc.init.trq_min_map         = [-112.57  -112.57 -112.57 -112.57 -103.45
-77.59  -62.07  -51.725 -44.335 -38.795 -34.485 -31.035 -28.215 -25.865
-23.875 -22.99];

mc.init.spd_eff_index       =
conversion_calc('rotational_speed','rpm','rad/s',[0   500 1000    2000
3000    4000    5000    6000    7000    8000    9000    10000   11000
12000   13000   13500]);
mc.init.trq_eff_index       = [0    10  20  30  40  50  60  70  80  90
100 110 120 130 140 160 170 200 210 220 230];
mc.init.eff_trq_map             = [...
0.01    0.01    0.01    0.01    0.01    0.01    0.01    0.01    0.01
0.01    0.01    0.01    0.01    0.01    0.01    0.01;
0.01    0.534365962 0.670710344 0.762957806 0.809509636 0.826190524
0.840437215 0.854642352 0.860834752 0.868386115 0.877018789 0.881151996
0.888813759 0.8920889   0.897237912 0.899360656;
0.01    0.590620777 0.709530399 0.790266462 0.822073193 0.840234359
0.853005197 0.863647475 0.869525231 0.875644515 0.882755928 0.889561702
0.899191677 0.910001091 0.918776516 0.923542323;
0.01    0.598132677 0.733643537 0.807370905 0.83332383  0.849857883
0.861925636 0.872629999 0.880187597 0.885583407 0.89323392  0.900035393
0.918075606 0.926796367 0.937695719 0.938513162;
```

```
0.01    0.616404168 0.747423091 0.813608925 0.841659779 0.858656653
0.870781889 0.87910672  0.884957417 0.89277709  0.90483865  0.918827292
0.929659497 0.939139538 0.945625676 0.947360278;
0.01    0.626266232 0.740472876 0.823419481 0.847383505 0.861194839
0.871671601 0.881869066 0.887350263 0.899162788 0.915699604 0.928251398
0.938143263 0.943357511 0.953904811 0.956724496;
0.01    0.614504786 0.752134252 0.819459632 0.850244016 0.866300774
0.875234204 0.883597882 0.889843214 0.904478777 0.92371109  0.934889359
0.943141408 1   1   1;
0.01    0.611706574 0.748662239 0.821728164 0.855481448 0.868066472
0.878701916 0.888828071 0.896524507 0.907159432 0.928069865 1   1   1
1   1;
0.01    0.611080814 0.742290186 0.822331072 0.856427809 0.870162154
0.882067278 0.890571936 0.90310897  0.919632086 1   1   1   1   1   1;
0.01    0.615177694 0.735803821 0.821990908 0.857953958 0.871822796
0.884333652 0.89255783  0.905555918 1   1   1   1   1   1   1;
0.01    0.598618448 0.732912405 0.822190267 0.857477876 0.873037662
0.88539588  0.894030893 1   1   1   1   1   1   1   1;
0.01    0.592699443 0.736441419 0.825215578 0.85509761  0.874503114
0.885851921 1   1   1   1   1   1   1   1   1;
0.01    0.596745905 0.726409843 0.819660645 0.853994449 0.876592386
0.886338722 1   1   1   1   1   1   1   1   1;
0.01    0.582315351 0.723947708 0.81881486  0.856838633 0.875221251 1
1   1   1   1   1   1   1   1   1;
0.01    0.582585152 0.726157453 0.819579753 0.857253636 0.878062016 1
1   1   1   1   1   1   1   1   1;
0.01    0.57646907  0.720686745 0.818922538 0.857761741 0.880357475 1
1   1   1   1   1   1   1   1   1;
0.01    0.573565904 0.715985876 0.816269113 0.856050774 1   1   1   1
1   1   1   1   1   1   1;
0.01    0.549301053 0.699012369 0.806426882 0.850305826 1   1   1   1
1   1   1   1   1   1   1;
0.01    0.540544597 0.694273365 0.803303424 0.848407962 1   1   1   1
1   1   1   1   1   1   1;
0.01    0.532646547 0.69051265  0.80073136  1   1   1   1   1   1   1
1   1   1   1   1;
0.01    0.526200618 0.682867691 0.799314997 1   1   1   1   1   1   1
1   1   1   1   1;
]';


mc.init.spd_prop_cont_index = [-fliplr(mc.init.spd_cont_index(2:end)) -
eps 0 eps mc.init.spd_cont_index(2:end)];
mc.init.trq_prop_cont_map   = [-fliplr(mc.init.trq_cont_map(2:end))  -
mc.init.trq_cont_map(2) mc.init.trq_cont_map(2) mc.init.trq_cont_map(2)
mc.init.trq_cont_map(2:end)];
mc.init.pwr_prop_cont_map =
mc.init.spd_prop_cont_index.*mc.init.trq_prop_cont_map;


mc.init.spd_prop_max_index  = [-fliplr(mc.init.spd_max_index(2:end)) -
eps 0 eps mc.init.spd_max_index(2:end)];
mc.init.trq_prop_max_map    = [-fliplr(mc.init.trq_max_map(2:end))   -
mc.init.trq_max_map(2) mc.init.trq_max_map(2) mc.init.trq_max_map(2)
mc.init.trq_max_map(2:end)];
```

```
mc.init.pwr_prop_max_map    =
mc.init.spd_prop_max_index.*mc.init.trq_prop_max_map;

mc.init.spd_reg_cont_index  = [-fliplr(mc.init.spd_cont_index(2:end)) -
eps 0 eps mc.init.spd_cont_index(2:end)];
mc.init.trq_reg_cont_map    = [fliplr(mc.init.trq_cont_map(2:end))
mc.init.trq_cont_map(2) mc.init.trq_cont_map(2) -
mc.init.trq_cont_map(2)  -mc.init.trq_cont_map(2:end)];
mc.init.pwr_reg_cont_map =
mc.init.spd_reg_cont_index.*mc.init.trq_reg_cont_map;

mc.init.spd_reg_max_index   = [-fliplr(mc.init.spd_max_index(2:end)) -
eps 0 eps mc.init.spd_max_index(2:end)];
mc.init.trq_reg_max_map     = [fliplr(mc.init.trq_max_map(2:end))
mc.init.trq_max_map(2) mc.init.trq_max_map(2) -mc.init.trq_max_map(2) -
mc.init.trq_max_map(2:end)];
mc.init.pwr_reg_max_map     =
mc.init.spd_reg_max_index.*mc.init.trq_reg_max_map;

mc.init.spd_eff_index       = [-fliplr(mc.init.spd_eff_index(2:end))
mc.init.spd_eff_index];
mc.init.trq_eff_index       = [-fliplr(mc.init.trq_eff_index(2:end))
mc.init.trq_eff_index];
mc.init.eff_trq_map         =
[flipud(fliplr(mc.init.eff_trq_map(2:end,2:end)))
flipud(mc.init.eff_trq_map(2:end,:));fliplr(mc.init.eff_trq_map(:,2:end
)) mc.init.eff_trq_map];
```

Battery Model – Initialization File

```
%% File description
% Name : ess_li_48_297_A123_Degrading
% Author : Matthew Stevens, University of Waterloo
% Description : Initialize the parameters used in the A123 degradation
% Capacity = 8 Ah, Cell number = 90
% Cell type =
% Nominal Voltage = 297V
% Nominal Capacity (rate not specified) = 8Ah
% Dimensions (L * W * H) =
% Pack Weight = 50 kg       (360 cells X 0.07 kg/cell X 1.4 packaging)
% Volume (modules only) =
% Nominal Energy (C) = 2376 Wh
% Peak Charge Power (10s pulse @ 60%DOD @ 30 deg. C 434V min) =
% Peak Discharge Power (10s pulse @50%DOD @ 30 deg. C 108V min) =
% Data provided by  :
% Model : lib_ess_generic_map_uwaft, lib_ess_generic_map,
lib_ess_generic_map_degrade
% Technology : liion
% Vehicle Type : Light, Heavy

%% File content
```

```
ess.list.init =
{'soc_min','soc_max','soc_init','num_cell','packaging_factor','soh_powe
r','soh_capacity'};
ess.list.parametric = {'soc_init','num_cell'};

ess.init.num_module_parallel = 4;

ess.init.soc_init           = 0.6;
ess.init.element_per_module = 10;
ess.init.num_module         = 9;                                    %
value for number of modules
ess.init.num_cell           = ess.init.num_module *
ess.init.element_per_module;
ess.init.volt_nom           = 3.3;
ess.init.volt_min           = 2;                                 % from
data sheet (8.7V/module)
ess.init.volt_max           = 3.8;                                  %
from data sheet (1.55V per cell)
ess.init.mass_module        = 0.07.*10;
% (kg), calculated from pack weight of 88kg
ess.init.mass_cell          =
ess.init.mass_module/ess.init.element_per_module;
ess.init.soc_min            = 0.001;
ess.init.soc_max            = 0.999;
ess.init.num_cell_series            = ess.init.num_module *
ess.init.element_per_module;



% Degradation Variables
ess.init.deg_temp_accelpower            =   0.25;           %unitless
ess.init.deg_temp_averaging             =   0.001;          %unitless
ess.init.deg_soc_accelmultiple          =   2;              %unitless
ess.init.deg_soc_accelpower             =   4;              %unitless
ess.init.deg_soc_averaging              =   0.001;          %unitless
ess.init.deg_jpara_not                  =   0.00000008;     %A/m2
ess.init.deg_specificarea               =   735000;         %m2/m3
ess.init.deg_fraction_solid             =   0.49;           %unitless
ess.init.deg_init_anode_concentration   =   9;              %mol/m3
(from model - actual is believed to be less)
ess.init.deg_sei_molecularweight        =   0.100;            %g/mol
ess.init.deg_sei_density                =   2100;           %g/m3
ess.init.deg_sei_kappa                  =   0.000000379;    %S/m
ess.init.deg_sei_init_resistance        =   0.008;          %Ohm
ess.init.deg_overvoltage_max            =   0.15;           %V
ess.init.soh_power                      =   1;              %unitless
ess.init.soh_capacity                   =   1;              %unitless

%Because the Mass is given for a module.
ess.init.packaging_factor  = 1.0;              % from another model,
not sure of correct number, taken to be 1 as module weight was
calculated from total weight

% LOSS AND EFFICIENCY parameters
%%%%%%%%%%%%%%%%%%%%%%%%%%%%%%%%%%%%%%%%%%%%
```

```
ess.init.soc_index           = [0   0.004   0.01    0.02    0.03
0.05    0.06    0.07    0.08    0.1 0.12    0.14    0.16    0.18    0.2
0.22    0.24    0.26    0.28    0.3 0.32    0.34    0.36    0.38    0.4
0.42    0.44    0.46    0.48    0.5 0.52    0.54    0.56    0.58    0.6
0.62    0.64    0.66    0.68    0.7 0.72    0.74    0.76    0.78    0.8
0.82    0.84    0.86    0.88    0.9 0.92    0.94    0.96    0.98    1];
% SOC RANGE over which data is defined
ess.init.temp_index          = [-10 10 20 35 55];  % Temperature range
over which data is defined (C)
ess.init.cap_max_map         = [2 2 2 2 2]; % Changed, originally 8.5
but adjusted due to results of validation
ess.init.eff_coulomb         = [0.99 0.99 0.99 0.99 0.99];  % average
coulombic (a.k.a. amp-hour) efficiency below, indexed by
ess.init.temp_index

% 288-60 pack's resistance to being discharged, indexed by
ess.init.soc_index and ess.init.temp_index
% converted to per cell
ess.init.rint_dis_map=[0.008    0.008   0.008   0.008   0.008   0.008
0.008   0.008   0.008   0.008   0.008   0.008   0.008   0.008   0.008
0.008   0.008   0.008   0.008   0.008   0.008   0.008   0.008   0.008
0.008   0.008   0.008   0.008   0.008   0.008   0.008   0.008   0.008
0.008   0.008   0.008   0.008   0.008   0.008   0.008   0.008   0.008
0.008   0.008   0.008   0.008   0.008   0.008   0.008   0.008   0.008
0.008   0.008   0.008   0.008
                        0.008   0.008   0.008   0.008   0.008   0.008
0.008   0.008   0.008   0.008   0.008   0.008   0.008   0.008   0.008
0.008   0.008   0.008   0.008   0.008   0.008   0.008   0.008   0.008
0.008   0.008   0.008   0.008   0.008   0.008   0.008   0.008   0.008
0.008   0.008   0.008   0.008   0.008   0.008   0.008   0.008   0.008
0.008   0.008   0.008   0.008   0.008   0.008   0.008   0.008   0.008
0.008   0.008   0.008   0.008
                        0.008   0.008   0.008   0.008   0.008   0.008
0.008   0.008   0.008   0.008   0.008   0.008   0.008   0.008   0.008
0.008   0.008   0.008   0.008   0.008   0.008   0.008   0.008   0.008
0.008   0.008   0.008   0.008   0.008   0.008   0.008   0.008   0.008
0.008   0.008   0.008   0.008   0.008   0.008   0.008   0.008   0.008
0.008   0.008   0.008   0.008   0.008   0.008   0.008   0.008   0.008
0.008   0.008   0.008   0.008
                        0.008   0.008   0.008   0.008   0.008   0.008
0.008   0.008   0.008   0.008   0.008   0.008   0.008   0.008   0.008
0.008   0.008   0.008   0.008   0.008   0.008   0.008   0.008   0.008
0.008   0.008   0.008   0.008   0.008   0.008   0.008   0.008   0.008
0.008   0.008   0.008   0.008   0.008   0.008   0.008   0.008   0.008
0.008   0.008   0.008   0.008   0.008   0.008   0.008   0.008   0.008
0.008   0.008   0.008   0.008
                        0.008   0.008   0.008   0.008   0.008   0.008
0.008   0.008   0.008   0.008   0.008   0.008   0.008   0.008   0.008
0.008   0.008   0.008   0.008   0.008   0.008   0.008   0.008   0.008
0.008   0.008   0.008   0.008   0.008   0.008   0.008   0.008   0.008
0.008   0.008   0.008   0.008   0.008   0.008   0.008   0.008   0.008
0.008   0.008   0.008   0.008   0.008   0.008   0.008   0.008   0.008
0.008   0.008   0.008   0.008]; % (ohm)
```

```
% 288-60 pack's resistance to being charged, indexed by
ess.init.soc_index and ess.init.temp_index
% converted to per cell
ess.init.rint_chg_map=[0.008    0.008   0.008   0.008   0.008   0.008
0.008   0.008   0.008   0.008   0.008   0.008   0.008   0.008   0.008
0.008   0.008   0.008   0.008   0.008   0.008   0.008   0.008   0.008
0.008   0.008   0.008   0.008   0.008   0.008   0.008   0.008   0.008
0.008   0.008   0.008   0.008   0.008   0.008   0.008   0.008   0.008
0.008   0.008   0.008   0.008   0.008   0.008   0.008   0.008   0.008
0.008   0.008   0.008   0.008
                        0.008   0.008   0.008   0.008   0.008   0.008
0.008   0.008   0.008   0.008   0.008   0.008   0.008   0.008   0.008
0.008   0.008   0.008   0.008   0.008   0.008   0.008   0.008   0.008
0.008   0.008   0.008   0.008   0.008   0.008   0.008   0.008   0.008
0.008   0.008   0.008   0.008   0.008   0.008   0.008   0.008   0.008
0.008   0.008   0.008   0.008
                        0.008   0.008   0.008   0.008   0.008   0.008
0.008   0.008   0.008   0.008   0.008   0.008   0.008   0.008   0.008
0.008   0.008   0.008   0.008   0.008   0.008   0.008   0.008   0.008
0.008   0.008   0.008   0.008   0.008   0.008   0.008   0.008   0.008
0.008   0.008   0.008   0.008   0.008   0.008   0.008   0.008   0.008
0.008   0.008   0.008   0.008   0.008   0.008   0.008   0.008   0.008
0.008   0.008   0.008   0.008
                        0.008   0.008   0.008   0.008   0.008   0.008
0.008   0.008   0.008   0.008   0.008   0.008   0.008   0.008   0.008
0.008   0.008   0.008   0.008   0.008   0.008   0.008   0.008   0.008
0.008   0.008   0.008   0.008   0.008   0.008   0.008   0.008   0.008
0.008   0.008   0.008   0.008   0.008   0.008   0.008   0.008   0.008
0.008   0.008   0.008   0.008   0.008   0.008   0.008   0.008   0.008
0.008   0.008   0.008   0.008]; % (ohm)

% 288-60 pack's open-circuit (a.k.a. no-load) voltage, indexed by
ess.init.soc_index and ess.init.temp_index
% converted to per cell
ess.init.voc_map=  [2.09    2.6 2.78    2.9 2.98    3.08    3.12
3.15    3.19    3.23    3.25    3.25    3.26    3.28    3.29    3.295
3.3 3.31    3.31    3.32    3.325   3.33    3.33    3.335   3.335
3.335   3.335   3.335   3.34    3.345   3.35    3.35    3.35    3.355
3.355   3.355   3.36    3.365   3.365   3.37    3.37    3.375   3.375
3.375   3.38    3.38    3.39    3.395   3.4 3.4 3.41    3.43    3.47
3.61    3.8
                    2.09    2.6 2.78    2.9 2.98    3.08    3.12
3.15    3.19    3.23    3.25    3.25    3.26    3.28    3.29    3.295
3.3 3.31    3.31    3.32    3.325   3.33    3.33    3.335   3.335
3.335   3.335   3.335   3.34    3.345   3.35    3.35    3.35    3.355
3.355   3.355   3.36    3.365   3.365   3.37    3.37    3.375   3.375
3.375   3.38    3.38    3.39    3.395   3.4 3.4 3.41    3.43    3.47
3.61    3.8
```

```
                    2.09    2.6 2.78    2.9 2.98    3.08    3.12
3.15    3.19    3.23    3.25    3.25    3.26    3.28    3.29    3.295
3.3 3.31    3.31    3.32    3.325   3.33    3.33    3.335   3.335
3.335   3.335   3.335   3.34    3.345   3.35    3.35    3.35    3.355
3.355   3.355   3.36    3.365   3.365   3.37    3.37    3.375   3.375
3.375   3.38    3.38    3.39    3.395   3.4 3.4 3.41    3.43    3.47
3.61    3.8
                    2.09    2.6 2.78    2.9 2.98    3.08    3.12
3.15    3.19    3.23    3.25    3.25    3.26    3.28    3.29    3.295
3.3 3.31    3.31    3.32    3.325   3.33    3.33    3.335   3.335
3.335   3.335   3.335   3.34    3.345   3.35    3.35    3.35    3.355
3.355   3.355   3.36    3.365   3.365   3.37    3.37    3.375   3.375
3.375   3.38    3.38    3.39    3.395   3.4 3.4 3.41    3.43    3.47
3.61    3.8
                    2.09    2.6 2.78    2.9 2.98    3.08    3.12
3.15    3.19    3.23    3.25    3.25    3.26    3.28    3.29    3.295
3.3 3.31    3.31    3.32    3.325   3.33    3.33    3.335   3.335
3.335   3.335   3.335   3.34    3.345   3.35    3.35    3.35    3.355
3.355   3.355   3.36    3.365   3.365   3.37    3.37    3.375   3.375
3.375   3.38    3.38    3.39    3.395   3.4 3.4 3.41    3.43    3.47
3.61    3.8]; % (V)


% Max current and power when charging/discharging
%%%%%%%%%%%%%%%%%%%%%%%%%%%%%%%%%%%%%%%%%%%%%%%%%%%%%%%%%%%%%%%%%%%%%%%
%%%
ess.init.curr_chg_max      = -max(max((ess.init.volt_max-
ess.init.voc_map)./ess.init.rint_chg_map));
ess.init.curr_dis_max      = max(max((ess.init.voc_map-
ess.init.volt_min)./ess.init.rint_dis_map));

%check the ess.calc.pwr_chg & ess.calc.pwr_dis because they're a vector
and in the database for the plot we
%need maps
ess.calc.pwr_chg           = -max((ess.init.volt_max-
ess.init.voc_map).*ess.init.volt_max./ess.init.rint_chg_map);%per cell
ess.calc.pwr_dis           = max((ess.init.voc_map-
ess.init.volt_min).*ess.init.volt_min./ess.init.rint_dis_map);%per cell



% gain factor to modify ess.calc.pwr_chg and ess.calc.pwr_dis
% discharge is brought to 0 at low SOC and charge is brought to 0 at
high
% SOC
temp=find(ess.init.soc_min>=ess.init.soc_index);
temp1=ones(size(ess.init.soc_index));
temp1(1:temp(end))=0;
temp1(temp(end)+1)=0.5;
temp=find(ess.init.soc_max>=ess.init.soc_index);
temp2=ones(size(ess.init.soc_index));
temp2(temp(end):end)=0;
temp2(temp(end)-1)=0.5;
ess.calc.pwr_chg            = ess.calc.pwr_chg.* temp2;
ess.calc.pwr_dis            = ess.calc.pwr_dis.* temp1;
clear temp temp1 temp2
```

```
ess.init.pwr_chg     = max(max((ess.init.volt_max-
ess.init.voc_map).*ess.init.volt_max./ess.init.rint_chg_map));%per cell
ess.init.pwr_dis     = max(max((ess.init.voc_map-
ess.init.volt_min).*ess.init.volt_min./ess.init.rint_dis_map));%per
cell



% battery thermal model
%%%%%%%%%%%%%%%%%%%%%%%%%%%%%%%%%%%%%%%%%%%%
ess.init.therm_on           = 0;
% --     0=no ess thermal calculations, 1=do calc's
ess.init.therm_cp_module        = 830;
% J/kgK  ave heat capacity of module (estimated for NiMH)
ess.init.temp_reg           = 35;
% C      thermostat temp of module when cooling fan comes on
ess.init.area_mod           = 1.6*(ess.init.mass_module/11)^0.7;
% --     if module dimensions are unknown, assume rectang shape and
scale vs PB25
ess.init.area_module            = 2*(0.195*0.081+0.102*0.081);
% m^2    total module surface area exposed to cooling air (typ rectang
module)
ess.init.flow_air_mod       = 0.01;
% kg/s   cooling air mass flow rate across module (20 cfm=0.01 kg/s at
20 C)
ess.init.mod_flow_area      = 0.005*2*(0.195+0.102);
% m^2    cross-sec flow area for cooling air per module (assumes 10-mm
gap btwn mods)
ess.init.case_thk           = 2/1000;
% m      thickness of module case (typ from Optima)
ess.init.therm_case_cond        = 0.2;
% W/mK   thermal conductivity of module case material (typ polyprop
plastic - Optima)
ess.init.speed_air          =
ess.init.flow_air_mod/(1.16*ess.init.mod_flow_area);
% m/s  ave velocity of cooling air
ess.init.therm_air_htcoef   = 30*(ess.init.speed_air/5)^0.8;
% W/m^2K cooling air heat transfer coef.
ess.init.therm_res_on       =
((1/ess.init.therm_air_htcoef)+(ess.init.case_thk/ess.init.therm_case_c
ond))/ess.init.area_module; % K/W  tot thermal res key on
ess.init.therm_res_off      =
((1/4)+(ess.init.case_thk/ess.init.therm_case_cond))/ess.init.area_modu
le; % K/W  tot thermal res key off (cold soak)
ess.init.flow_air_mod       = max(ess.init.flow_air_mod,0.001);
ess.init.therm_res_on       =
min(ess.init.therm_res_on,ess.init.therm_res_off);

if isfield(ess,'tmp')
ess = rmfield(ess,'tmp');
end

% Battery density
%%%%%%%%%%%%%%%%%%%%%%%%%%%%%%%%%%%%%%%%%%%%
```

```
ess.init.pwr_dis_nom        = max(max((ess.init.volt_nom-
ess.init.volt_min).*ess.init.volt_min./ess.init.rint_dis_map));%per
cell
ess.init.pwr_density        = ess.init.pwr_dis_nom/ess.init.mass_cell;
ess.init.energy_density     =
mean((ess.init.volt_nom*ess.init.cap_max_map))/ess.init.mass_cell;
%Values should only be used to calculate the number of cells
ess.init.num_cell_series            =
overwrite_parameters('simulation.drivetrain.ess','num_cell_series',ess.
init.num_cell_series);% need to update to make sure we have 0 power at
SOC_min
ess.init.num_module_parallel        =
overwrite_parameters('simulation.drivetrain.ess','num_module_parallel',
ess.init.num_module_parallel);% need to update to make sure we have 0
power at SOC_min
ess.init.num_cell =
ess.init.num_module_parallel.*ess.init.num_cell_series;
```

Fuel Cell – Initialization File

```
%% File description
% Name : fc_65_hydrogenics_uwaterloo_dyno
% Author : Matthew Stevens - University of Waterloo
% Description : 65kW direct hydrogen fuel cell initialization file
% Data from dynamometer testing of Waterloo's Challenge X hybrid fuel
cell
% vehicle at Argonne National Lab advanced powertrain test facility
% Proprietary : Public
% Model : lib_fc_H2_map_hot_and_cold,lib_fc_H2_trifecta,
,lib_fc_H2_trifecta_degrade
% Vehicle Type : Light

%% File content
fc.list.init =
{'tau','fuel_mass','tank_mass','temp_tau_hot','temp_tau_cold','warmup_i
nit'};

fc.init.tau                 = 0.2;                  % transient load
delay for first order lag
fc.init.temp_tau_hot        = 600;                  % MS - kept the
same
fc.init.temp_tau_cold       = 1800;                 % MS - kept the
same
fc.init.warmup_init         = 1;
fc.init.time_response       = 0.2;
fc.init.fuel_density_val    = 0.018;            % kg/m3 or g/L
fc.init.fuel_heating_val    = 120000000;     % J/kg; specific LHV of
Hydrogen

% Define the following variable to satisfy the series power
controller's dependency on an optimal point
fc.init.pwr_opt             = 15000 ;

% Hot power
```

```
fc.init.pwr_hot_index       = [0    1500    3000    4500    6000
7500    9000    10500   12000   13500   15000   16500   18000   19500
21000   22500   24000   25500   27000   28500   30000   31500   33000
34500   36000   37500   39000   40500   42000   43500   45000   46500
48000   49500   51000   52500   54000   55500   57000   58500   60000
61500   63000   64500];
fc.init.pwr_hot_max         = max(fc.init.pwr_hot_index);           %
Max DC power of fuel cell, W
fc.init.h2_hot_map          = [0.032618208  0.047020973 0.062798194
0.079868765 0.098151582 0.11756554  0.138029534 0.159462458 0.181783208
0.204910679 0.228763766 0.253261364 0.278322368 0.303865672 0.329810173
0.356074765 0.382578342 0.409239801 0.435978035 0.462711941 0.489360413
0.515842346 0.542076635 0.567982175 0.593477861 0.618482589 0.642915253
0.666694748 0.689739969 0.711969812 0.733303171 0.753658942 0.772956018
0.791113297 0.808049671 0.823684037 0.83793529  0.850722324 0.861964035
0.871579317 0.879487066 0.885606176 0.889855543 0.892154062] /1000;   %
kg/s, taken at 50C;
fc.init.h2_hot_max          = max(fc.init.h2_hot_map) ;

fc.init.fc_mass             = 200;
fc.init.tank_mass           = 100;
fc.init.fuel_mass           = 4;

% Cold power
fc.init.pwr_cold_index      = [0    1500    3000    4500    6000
7500    9000    10500   12000   13500   15000   16500   18000   19500
21000   22500   24000   25500   27000   28500   30000   31500   33000
34500   36000   37500   39000   40500   42000   43500   45000   46500
48000   49500   51000   52500   54000   55500   57000   58500   60000
61500   63000   64500];          % W
fc.init.pwr_cold_max        = max(fc.init.pwr_cold_index); % Max DC
power of fuel cell, W
fc.init.h2_cold_map         = [0.039802304  0.05183112  0.065578309
0.080962767 0.097903389 0.11631907  0.136128704 0.157251188 0.179605415
0.203110281 0.227684682 0.253247511 0.279717664 0.307014036 0.335055522
0.363761017 0.393049417 0.422839615 0.453050508 0.483600989 0.514409955
0.5453963   0.57647892  0.607576708 0.638608561 0.669493373 0.700150039
0.730497455 0.760454515 0.789940115 0.818873149 0.847172512 0.8747571
0.901545807 0.927457529 0.952411161 0.976325597 0.999119732 1.020712462
1.041022682 1.059969286 1.077471171 1.093447229 1.107816358] /1000;   %
kg/s, taken at 30C;

% Polarization Curves
fc.init.stck_pwr_hot_index = [0 29.94   296 1163.6  1974.7  2764
5298    7734    10096   12395   14646   16849   19008   21132   23210
25256   27264   29250   31192   33090   34976   36822   38646   40432
42180   43911   45628   47288   48936   50550   52130   53703   55244
56753   58230];
fc.init.stck_curr_hot_index = [ 0   0.1 1   4   7   10  20  30  40  50
60  70  80  90  100 110 120 130 140 150 160 170 180 190 200 210 220 230
240 250 260 270 280 290 300 ];      % A
fc.init.stck_volt_hot_map   = [ 300 299.4 296   290.9   282.1   276.4
264.9   257.8   252.4   247.9   244.1   240.7   237.6   234.8   232.1
229.6   227.2   225.0   222.8   220.6   218.6   216.6   214.7   212.8
210.9   209.1   207.4   205.6   203.9   202.2   200.5   198.9   197.3
195.7   194.1];          % V
```

```
fc.init.stck_curr_cold_index= [0    0.1 1   4   7   10  20  30  40  50
60  70  80  90  100 110 120 130 140 150 160 170 180 190 200 210 220 230
240 250 260 270 280 290 300];
fc.init.stck_volt_cold_map  = [ 300 299.4 296   285.8   277.5   272.2
261.3   254.5   249.4   245.2   241.5   238.3   235.3   232.6   230.0
227.6   225.3   223.1   221.0   218.9   216.9   215.0   213.1   211.3
209.5   207.7   206.0   204.3   202.6   201.0   199.3   197.7   196.1
194.6   193.0];
fc.init.volt_map_increasing = [194.1    195.7   197.3   198.9   200.5
202.2   203.9   205.6   207.4   209.1   210.9   212.8   214.7   216.6
218.6   220.6   222.8   225 227.2   229.6   232.1   234.8   237.6
240.7   244.1   247.9   252.4   257.8   264.9   276.4   282.1   290.9
296 299.4   300];     %V
fc.init.pwr_hot_index_increasing = [58230   56753   55244   53703
52130   50550   48936   47288   45628   43911   42180   40432   38646
36822   34976   33090   31192   29250   27264   25256   23210   21132
19008   16849   14646   12395   10096   7734    5298    2764    1974.7
1163.6  296 29.94   0]; %W


% Degradation
fc.init.deg_trans_rate      = -0.000225;            %V
fc.init.deg_base_rate       = -0.000010;            %V
fc.init.deg_starting_v      = 1.223;                %V
fc.init.soh                 = 1;                    %unitless

% Power vs Voltage values     \
%fc.init.power_index        = [ 0.443 0.7107 0.9662 1.481 2.046 5.165
10.12 19.67 36.44 52.51 67.71 80.00]* 1000;                % W
%fc.init.ucell_volt_map         = [ 0.9260 0.9190 0.9120 0.9059 0.9041
0.8936 0.8761 0.8409 0.7829 0.7554 0.7280 0.7004 ];        % V/cell
%fc.init.nb_cell            = 400;  % later put it in the test file
(fc.init.nb_cell = gui_*)


% In the hydrogenic's power module the pumps are run off the fuel cell
% current, therefore that load is captured in the h2 consumption
numbers.
% There is no expander.  The radiator fan is on the 12V auxiliary bus.
% Hot accessory power
fc.init.accmech_pwr_hot_pump        = [0    0   0   0   0   0   0   0
0   0   0   0   0   0   0   0   0   0   0   0   0   0   0   0   0   0
0   0   0   0   0   0   0   0   0   0   0   0   0   0   0   0   0   0];
% W; pump/fan
fc.init.accmech_pwr_hot_compressor  = [161.5    232.6   296.9   355.1
408.0   456.1   500.1   540.8   578.8   614.8   649.4   683.4   717.4
752.1   788.2   826.4   867.2   911.5   959.9   1013.0  1071.6  1136.3
1207.8  1286.8  1373.9  1469.9  1575.4  1691.1  1817.6  1955.7  2106.1
2269.3  2446.1  2637.2  2843.2  3064.9  3302.8  3557.7  3830.3  4121.2
4431.1  4760.7  5110.6  5481.6];   % W; compressor
fc.init.accmech_pwr_hot_expander    = [0    0   0   0   0   0   0   0
0   0   0   0   0   0   0   0   0   0   0   0   0   0   0   0   0   0
0   0   0   0   0   0   0   0   0   0   0   0   0   0   0   0   0   0];
% W; expander
fc.init.accmech_pwr_hot_radiator    = [0    0   0   0   0   0   0   0
0   0   0   0   0   0   0   0   0   0   0   0   0   0   0   0   0   0
```

```
0   0   0   0   0   0   0   0   0   0   0   0   0   0   0   0   0   0
];   % W; radiator duty

% Cold accesory power
fc.init.accmech_pwr_cold_pump       = [0    0   0   0   0   0   0   0
0   0   0   0   0   0   0   0   0   0   0   0   0   0   0   0   0   0
0   0   0   0   0   0   0   0   0   0   0   0   0   0   0   0   0   0
]*1000;           % W; pump/fan
fc.init.accmech_pwr_cold_compressor = [ 161.5   232.6   296.9   355.1
408.0   456.1   500.1   540.8   578.8   614.8   649.4   683.4   717.4
752.1   788.2   826.4   867.2   911.5   959.9   1013.0  1071.6  1136.3
1207.8  1286.8  1373.9  1469.9  1575.4  1691.1  1817.6  1955.7  2106.1
2269.3  2446.1  2637.2  2843.2  3064.9  3302.8  3557.7  3830.3  4121.2
4431.1  4760.7  5110.6  5481.6];        % W; compressor
fc.init.accmech_pwr_cold_expander   = [0    0   0   0   0   0   0   0
0   0   0   0   0   0   0   0   0   0   0   0   0   0   0   0   0   0
0   0   0   0   0   0   0   0   0   0   0   0   0   0   0   0   0   0
]*1000;        % W; expander
fc.init.accmech_pwr_cold_radiator   = [0    0   0   0   0   0   0   0
0   0   0   0   0   0   0   0   0   0   0   0   0   0   0   0   0   0
0   0   0   0   0   0   0   0   0   0   0   0   0   0   0   0   0   0
]*1000;        % W; radiator by-passed

%calculate the maximum efficiency
fc.init.eff_hot=fc.init.pwr_hot_index/fc.init.fuel_heating_val./fc.init
.h2_hot_map;
fc.init.eff_cold=fc.init.pwr_cold_index/fc.init.fuel_heating_val./fc.in
it.h2_cold_map;
fc.init.eff_hot(find(fc.init.eff_hot<0))=0;
fc.init.eff_cold(find(fc.init.eff_cold<0))=0;
fc.init.eff_max=max(max(fc.init.eff_hot));

fc.init.pwr_max = fc.init.pwr_hot_max; %<- Needed for control strategy
compatibility in the absence of scaling.


% fc.init.accmech_mass      = 20;
```

Powertrain Controller – Initialization File

Appendix E

Lifetime Vehicle Script

```
%% Scripting FCV lifetime test

%  Author:  Matthew Stevens - University of Waterloo
%  This script runs the fuel cell vehicle for 200,000km

%initialize battery and fuel cell count
num_batt=1;
num_fc=1;

x_thous=20;
sol_matrix=zeros(x_thous,15);

for i=1:1:x_thous

    %Run a single simulation
    sim('ser_fc_2t2wd_p2')

    %Initialize vector components (note that the ess_temp_air and
    %fc_acc_mech and ess_heat are used for degradation variables)
    fc.init.soh_old=fc.init.soh;
    fc.init.soh_new = fc_accmech_pwr_simu(end);
    ess.init.soh_power_old = ess.init.soh_power;
    ess.init.soh_power_new = ess_heat_simu(end);
    ess.init.soh_capacity_old=ess.init.soh_capacity;
    ess.init.soh_capacity_new= ess_temp_air_simu(end);

    %Determine /km degradation rates
    distance_travelled=sum(veh_lin_spd_out_simu(:))*0.1*0.001;
    fc_soh_per_km=(fc_accmech_pwr_simu(end)-
fc_accmech_pwr_simu(1))./distance_travelled;
    ess_soh_pwr_per_km=(ess_heat_simu(end)-
ess_heat_simu(1))./distance_travelled;
    ess_soh_cap_per_km=(ess_temp_air_simu(end)-
ess_temp_air_simu(1))./distance_travelled;

    %Check if fuel cell needs replacement
    if (fc.init.soh_old + fc_soh_per_km*10000)<0.2
        fc.init.soh=1;
        num_fc=num_fc+1;
    else
        fc.init.soh = fc.init.soh_old + fc_soh_per_km*10000;
    end

    %Check if battery needs replacement
    if (ess.init.soh_capacity_old + ess_soh_cap_per_km*10000)<0.2
        ess.init.soh_capacity=1;
        ess.init.soh_power=1;
        num_batt=num_batt+1;
```

```
    else
        ess.init.soh_power=ess.init.soh_power_old +
ess_soh_pwr_per_km*10000;
        ess.init.soh_capacity=ess.init.soh_capacity_old +
ess_soh_cap_per_km*10000;
    end

    %Write to results matrix
    sol_matrix(i,1)=fc_accmech_pwr_simu(1);
    sol_matrix(i,2)=fc_accmech_pwr_simu(end);
    sol_matrix(i,3)=ess_heat_simu(1);
    sol_matrix(i,4)=ess_heat_simu(end);
    sol_matrix(i,5)=ess_temp_air_simu(1);
    sol_matrix(i,6)=ess_temp_air_simu(end);
    sol_matrix(i,7)=fc_fuel_cum_simu(end);
    sol_matrix(i,8)=ess_soc_simu(end);
    sol_matrix(i,9)=distance_travelled;

    %Calculated addition results variables
    fc_energy_out=sum(fc_pwr_out_simu(:))*0.1;

fc_eff=sum(fc_pwr_out_simu(:))*0.1/(fc_fuel_cum_simu(end)*120000000);
    ess_elec_pwr_out=max(ess_curr_out_simu,0).*ess_volt_out_simu;
    ess_elec_pwr_in=min(ess_curr_out_simu,0).*ess_volt_out_simu;
    ess_elec_energy_out=sum(ess_elec_pwr_out(:)).*0.1;
    ess_elec_energy_in=sum(ess_elec_pwr_in(:)).*0.1;

    %Write calculated variables to the result matrix
    sol_matrix(i,10)=fc_energy_out;
    sol_matrix(i,11)=fc_eff;
    sol_matrix(i,12)=ess_elec_energy_out;
    sol_matrix(i,13)=ess_elec_energy_in;
    sol_matrix(i,14)=num_fc;
    sol_matrix(i,15)=num_batt;

    %Input degradation variables for re-intialization of the simulink
model
    ess.init.soh_capacity =
overwrite_parameters('simulation.drivetrain.ess','soh_capacity',ess.ini
t.soh_capacity);% need to update to make sure we have 0 power at
SOC_min
    ess.init.soh_power =
overwrite_parameters('simulation.drivetrain.ess','soh_power',ess.init.s
oh_power);% need to update to make sure we have 0 power at SOC_min
    fc.init.soh =
overwrite_parameters('simulation.drivetrain.fc','soh',fc.init.soh);%
need to update to make sure we have 0 power at SOC_min

    i
end
```

Appendix F

Battery Operating Ranges

Battery Voltage Limits of 288V Cobasys Pack

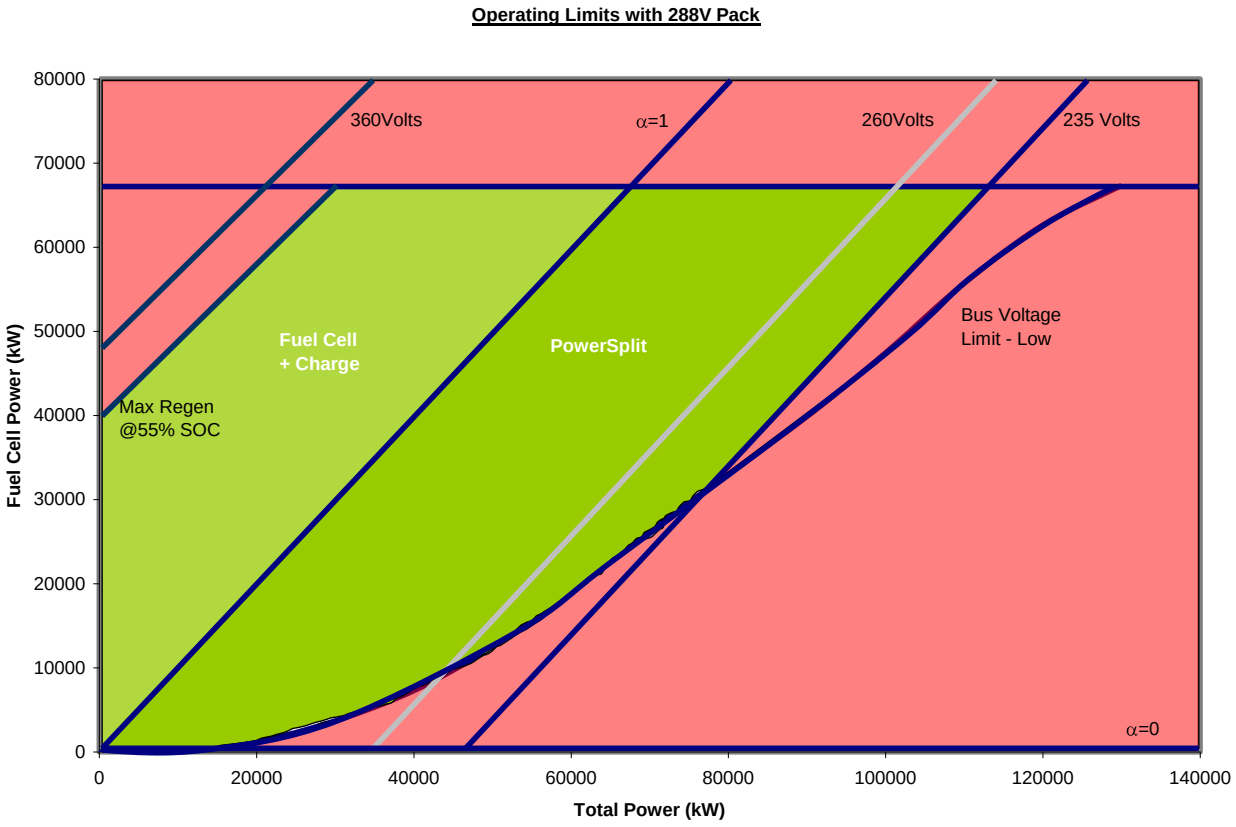

Battery Voltage Limits of 336V Cobasys Pack

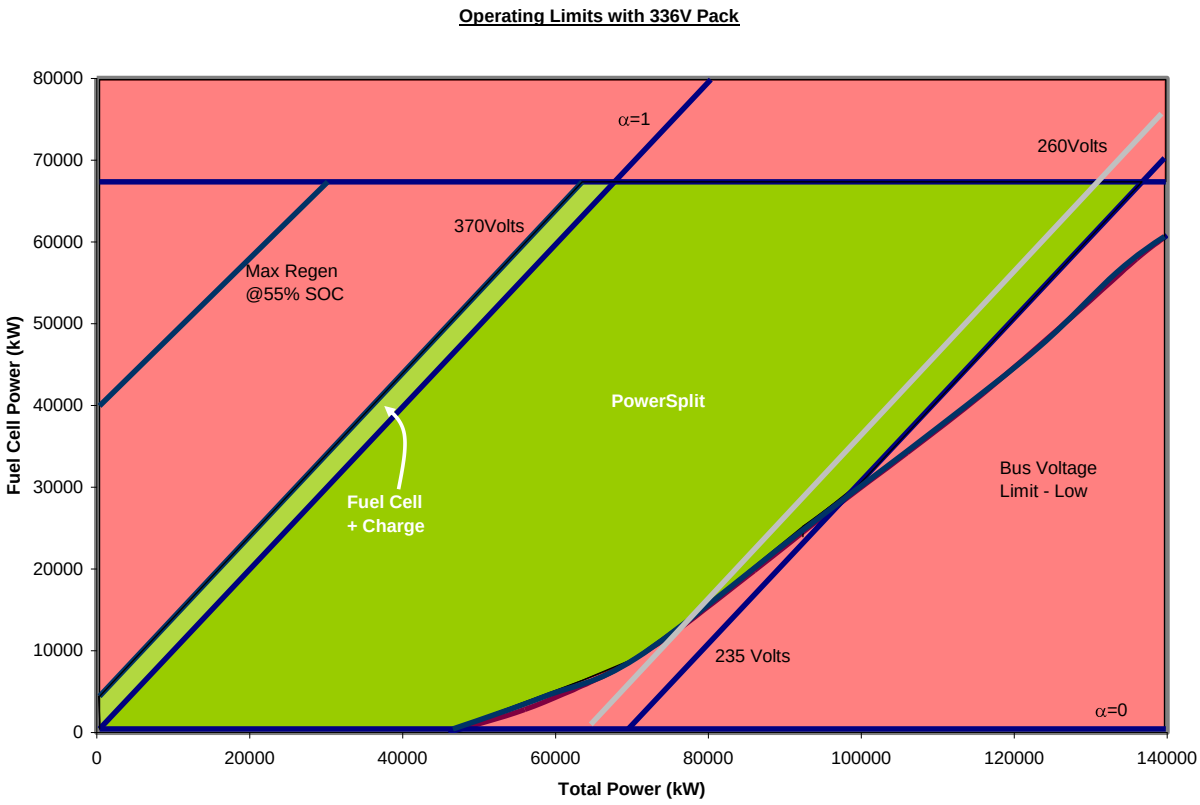

Desired Operating Points (simulation) with 336V Cobasys Pack

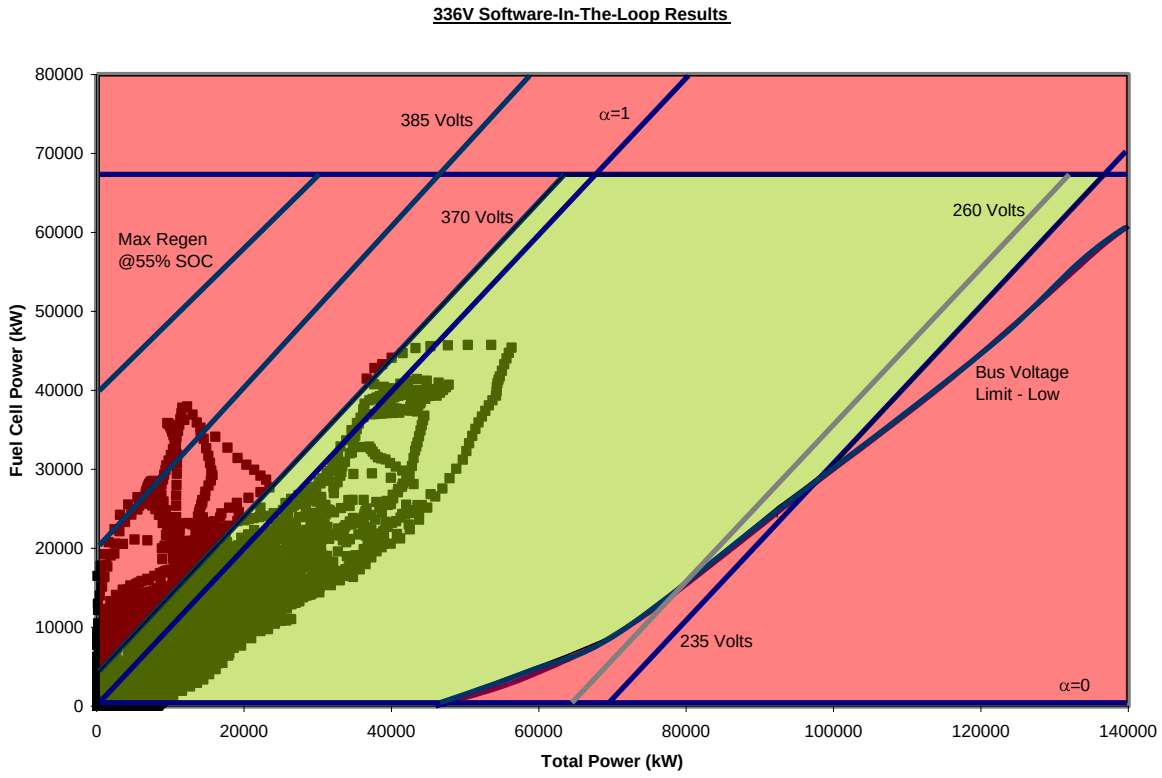

Desired Operating Points (simulation) with 288V Cobasys Pack